Microfluidic Synthesis of Colloidal Nanomaterials

by

Saif A. Khan

B. Chem. Engg. (2001)
University of Mumbai, Institute of Chemical Technology

Submitted to the Department of Chemical Engineering
in partial fulfillment of the requirements for the degree of

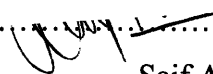Doctor of Philosophy in Chemical Engineering

at the

MASSACHUSETTS INSTITUTE OF TECHNOLOGY

September 2006

Author...
Saif A. Khan
Department of Chemical Engineering
July 5, 2006

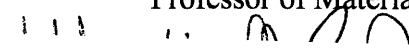Certified by...
Klavs F. Jensen
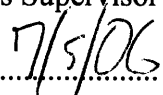Lammot duPont Professor of Chemical Engineering
Professor of Materials Science and Engineering
Thesis Supervisor

Certified by...
Martin A. Schmidt
Professor of Electrical Engineering and Computer Science
Thesis Supervisor

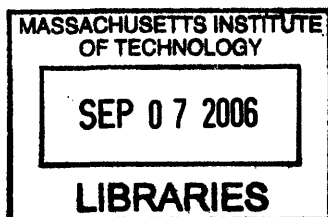Accepted by...
William M. Deen
Carbon P. Dubbs Professor of Chemical Engineering
Chairman, Committee for Graduate Students

Microfluidic Synthesis of Colloidal Nanomaterials
by
Saif A. Khan

Abstract

This thesis focuses on microfluidics based approaches for synthesis and surface-engineering of colloidal particles. Bottom-up assembly through colloidal nucleation and growth is a popular route to the controlled synthesis of nanomaterials. Standard bench-scale synthetic chemistry techniques often involve non-uniform spatial and temporal distributions of concentration and temperature, and are not readily scalable. Photolithography-based microfabrication enables the application of classical techniques of chemical reaction engineering to design chemical reactors that cannot be realized easily at the macroscale, and that closely approach theoretical 'idealized' reactor configurations. In addition, the microfluidic format allows precisely controlled reaction conditions such as rapid mixing, and concentration and temperature uniformity. The goal of this thesis was to design microfluidic reactors for synthesis of core-shell colloidal particles with tunable sizes.

Microscale segmented gas-liquid flows overcome the large axial dispersion effects associated with single-phase laminar flows. Microchannel devices that yielded uniform, stable gas-liquid segmented flows over three orders of magnitude in flow velocity were first developed. Extensive experimental studies of the transport, dynamics and stability of such flows were then conducted with pulsed-laser fluorescent microscopy, optical stereomicroscopy and micro particle image velocimetry (μ-PIV). Flow segmentation not only reduces axial dispersion, but also allows rapid micromixing of miscible liquids through internal recirculations in the liquid phase. This added functionality is especially useful in syntheses involving colloidal particles that, due to inherently low diffusivity, cannot be rapidly mixed by laminar diffusive techniques. Continuous segmented flow reactors were then developed for the synthesis of colloidal silica and titania particles by sol-gel chemistry. Particle sizes could be tuned by varying the rates of flow of reactants, or by varying the chip temperature. Particle size distributions comparable to or narrower than the corresponding stirred-flask synthesis, with little agglomeration or shape distortion were obtained.

Coating of colloidal particles with one or more layers of different materials is used to modify their optical, chemical or surface properties. Core-shell particles are often prepared by controlled precipitation of inorganic precursors onto core particles. Synthesis of such structures requires precise control over process parameters to prevent precipitation of secondary particles of shell material and agglomeration of primary particles. Particles coated with titania are exceptionally difficult to synthesize due to the high reactivity of the titania precursors, which makes controlled precipitation difficult. A

novel continuous flow microfluidic reactor with sequential multi-point precursor addition was developed for colloidal overcoating processes. Silica particles were coated with uniform titania layers of tunable thickness by the controlled hydrolysis of titanium ethoxide, with no secondary particle formation or agglomeration. An integrated reactor for continuous silica synthesis and *in-situ* series overcoating with titania was then developed using a two-level stacked reactor fabrication process. Finally, multi-step nanomaterials synthesis and surface coating with incompatible chemistries requires the development of microfluidic 'unit operations' equivalent to particle filtration. In this context, rapid, continuous microfluidic particle separation was demonstrated using transverse free-flow electrophoresis.

Thesis Supervisor: Klavs F. Jensen
Title: Lammont du Pont Professor of Chemical Engineering
    Professor of Materials Science and Engineering

Thesis Supervisor: Martin A. Schmidt
Title: Professor of Electrical Engineering and Computer Science

To my grandfather Mohammed

and my mother Yasmin

with love

Acknowledgements

My five years in Cambridge have been filled with learning, fun and fond memories. I sincerely thank my advisor, Professor Klavs Jensen, for the wonderful opportunity to work in his research group and for his wisdom and guidance through the years. Klavs, thank you for treating me as an equal from day one, and for always encouraging me to think creatively. I have been fortunate to have Professor Martin Schmidt as a thesis advisor. Thank you Marty for your advice, encouragement, and for helping me develop an appreciation for smart, practical engineering to solve real-world problems. I also thank my thesis committee members, Professor Daniel Blankschtein, and Professor Alice Gast for their insightful feedback throughout my PhD. Professor Blankschtein, I aspire one day to teach classes as well as you do.

It has been a rewarding experience working alongside several extremely talented people. I owe many thanks to Dr. Axel Günther and Franz Trachsel for a wonderful and fruitful collaboration during my initial years in the lab. I also thank Dr. Yasuhiro Wada and Dr. Thomas Gervais for their guidance in the initial stages, Nicolas Imlinger for introducing me to synthetic chemistry techniques, and Jacob Albrecht, Hemant Sahoo and Veronique Gondoin for their collaboration in the latter stages of my PhD. Thanks to Professors Hang Lu and Michiel Kreutzer for their mentorship. Many thanks to Dr. Jamil El-Ali, for being my co-conspirator in developing a robust fabrication process, and for all the insightful discussions.

The KFJ group has been a wonderfully diverse, sometimes idiosyncratic and always fun workplace. Special thanks to Jason and Ed for their friendship, the baseball, the coffee, the movies, and their perspective on all things *Americana*. Joan Chisholm, thank you for always being there for us, for all the Red Sox memorabilia, and for the unlimited supply of sugary treats.

Boston would not have been the same without my friends, to whom I owe many thanks: Mahju, for everything, Harsh and Harpreet for the wonderful couple of years as room-mates, Zeeshan, Ebad, Zaid, and Zubair for all the fun we've had despite the Indo-Pak divide. Special thanks to my friends from home, especially Bala for always being my role model.

I am grateful to be blessed with a wonderful family. Thank you Sadaf, you are the light of my life. Thanks to Sajid and Noor for their unending love, to my grandparents, aunts Razia and Sabiha, and uncle Imtiaz for their support and encouragement through the years.

Finally, I gratefully thank my mother Yasmin, for all her love, sacrifices and prayers. She is the reason I am here today.

Table of Contents

List of Figures

13

14

16

18

List of Tables

1 Introduction

1.1 Colloidal particles: Fascinating properties

Colloidal particles (~1 nm to ~10 μm) are some of the most commonly encountered forms of materials in nature and in the physical sciences. In chemistry, typical examples include polymer macromolecules, gold colloids, and spherical latex particles. Proteins, viruses and cells are examples of biological colloids. Nature abounds in hierarchically assembled structures of colloidal particles over multiple length scales. A natural opal, for instance, is beautifully iridescent in color because silica colloids (colorless by themselves) have been organized into a three-dimensionally ordered array with a lattice constant that is comparable to the wavelength of visible light (300-800 nm).[1] Colloidal particles and their suspensions exhibit several fascinating physical and chemical properties. Colloidal particle sizes are comparable to the dimensions of visible light, giving rise to unique optical and scattering properties not observed in their bulk matter counterparts.[2] Several forces such as viscous, gravitational, brownian, dispersive, steric and electrostatic forces become comparable at the colloidal length scale, thus giving rise to a rich variety of physical interactions, phase behavior and dynamics. Small changes in the relative magnitudes of these forces often lead to dramatic effects in suspension behavior and properties.

1.1.1 'Colloids are everywhere'

Colloidal particles, their suspensions and assemblies have been used for a wide spectrum of scientific, industrial, medical and consumer applications in the last century. Inorganic colloidal particles of silica and titania, the focus of this thesis, are classical materials with a wide variety of applications. These include adhesion and lubrication technology, pigments, catalysts, thin films for photovoltaic, electrochromic, photochromic and electro-luminescence devices, sensors, foods, health-care, anti-reflective coatings, chromatography and ceramics manufacture.[3-5] Spherical latex colloids are now standard substrates in several biological and immunological assays and sensor

applications.[6] Metallic colloidal particles such as platinum dispersed on inorganic supports are some of the most common catalytic materials used in the chemical industry.[7] Colloids in the form of emulsions and foams are also ubiquitous in food science and technology.[8,9]

In addition to the established applications, colloidal particles are also being studied as candidates for emerging applications such as controlled drug delivery and advanced photonic materials. Both these applications involve tuning the structure of individual particles as well as their ensembles. Sub-micron spherical colloids that consist of an encapsulated hydrophobic drug core covered by a water-soluble shell are being explored as potential candidates for effective drug delivery vehicles.[10] The surface properties of the shells may be tuned to target specific organs or tissues within the body. By manipulating size and surface properties it is possible to control the biological fate of particles in the body, and thereby deliver drug to their target sites with much greater efficiency. The ability to assemble colloidal nanoparticles into two- or three-dimensional crystalline structures is directly useful in many areas. Colloidal crystalline lattices have been used as model systems to study fundamental thermodynamic phenomena such as crystallization, phase transition and fracture mechanics. The last decade has seen increased interest in the use of three-dimensional assemblies of monodisperse, spherical colloidal particles to manufacture photonic band-gap materials. By tuning the relative refractive index of the particles and the host medium, photonic band-gaps in the visible region of the electromagnetic spectrum have been demonstrated.[11,12]

1.1.2 Colloid physics: forces, stability and dynamics

The interactions and forces between colloidal particles have been investigated intensively for almost two centuries due to their profound effect on the behavior of colloidal dispersions, especially with respect to stability, phase behavior and flow.[8] Much of colloid science, that involves understanding colloidal stability, dynamics and phase behavior, is based on the study of *individual* particles in isolation, or interacting in a pairwise manner. The principal forces that govern colloid stability are Brownian forces that arise due to the interaction between colloidal particles and the surrounding medium, and inter-particle forces that act between two (or more) particles. The Derjaguin-Landau-

Vervey-Overbeek (DLVO) theory of colloidal stability represents the total inter-particle potential as a sum of repulsive and attractive components. The pairwise potential energy of interaction consists of three terms: the short-range repulsive interaction, the longer range attractive interaction, usually referred to as the Van der Waals (or London dispersion, or Hamaker) force, and the long-range Coulomb repulsion shielded by electrolytes (the Yukawa potential).

Colloidal dynamics is the study of colloid behavior under the action of external fields such as hydrodynamic, electrical and magnetic fields. Colloidal suspensions display complex, non-Newtonian rheological behavior that is intimately linked to stability and suspension microstructure. For example, concentrated suspensions stabilized electrostatically form ordered layers when a shear stress is applied, and undergo an order-to-disorder transition beyond a critical value of applied shear. The science of electrokinetic phenomena deals with interaction of colloidal particles and electric fields. The phenomenon of electrophoresis, for example, is the movement of charged colloidal particles relative to the fluid in a DC electric field and can be used to determine the net electric charge on particle. Colloidal dynamics is therefore a rich, interdisciplinary field of research with several fundamental and practical challenges.[8]

1.2   Nanoscience and Nanotechnology

In the past decade, there has been an explosion of research efforts in the area of *'nanotechnology'*, which deals with the synthesis and assembly of matter larger than the molecular scale but smaller than that typically produced by microfabrication techniques (~1 nm to 100 nm). Nanotechnology involves development of structures, devices and materials with organizational features on the above length scales, with novel *tailored* properties and functions.[13] One vision of the nanotechnology revolution is the possibility of fabricating tiny 'machines' that imitate single-celled organisms, and can perform a host of functions, from assembling computer components to destroying tumors. The underlying science, also called *'nanoscience'* essentially deals with studying and harnessing the (often unexpected) *size-dependent* optical and electronic properties of matter in the nanometer size regime. It is the size-dependence of fundamental physical

properties that sets nano-scale materials apart from their molecular-scale and bulk-scale counterparts.

1.2.1 Nanoparticles

Nanometer-sized particles with at least one critical dimension in the ~1 nm to 1 μm size range, such as carbon black, have been synthesized for several thousand years. Such particles have attracted renewed interest as the building blocks of nanoscience and technology. The term 'nanoparticle' generally encompasses several forms of matter dispersed at such small length scales, including dense solid particles (amorphous or crystalline) such as semiconductor nanocrystals or magnetic ferrite particles, and macromolecular assemblies, such as micelles. The optical, electrical and chemical properties of nanoparticles are fundamentally different from their bulk-scale counterparts. These properties exhibit strong size-dependence due to quantum confinement effects, especially at length scales below 10 nm, thereby enabling tailoring of these properties to achieve specific functions. For example, semiconductor nanocrystals, also known as 'quantum dots', exhibit luminescence properties that may be tuned over the entire UV-visible spectrum by simply varying particle size.[14,15] In addition, several different physical phenomena have length scales comparable to the size of the nanoparticles, thus giving rise to unique, tunable interaction effects. In this respect, there is considerable overlap with traditional colloid science as described in the previous section. For example, gold sols exhibit size-dependent colors, an effect that was first documented by Faraday in the 19th century.[16] Nanoparticles and their macroscale assemblies have a broad range of high-impact applications in the fields of advanced functional materials,[17] optoelectronics,[18] biotechnology,[19] neuroscience,[20,21] oncology,[22] pharmaceuticals and drug delivery,[23] chemical catalysis,[7] dispersions and pigments,[24] environmental remediation and miniaturized sensors.[25]

1.2.2 Synthetic approaches and challenges

There are two primary approaches toward the synthesis of nanoparticles and other nanostructured materials. The 'top-down' approach, as the name suggests, involves starting with a bulk material and, through suitable processing, 'sculpting' new functionality from it. This is the approach successfully followed by the semi-conductor

industry, where complex integrated circuits have been fabricated from silicon substrates by micromachining and optical pattern transfer processes (lithography) with sub-micron resolution. The 'bottom up' approach involves assembling nanoscale building blocks such as nanoparticles from their molecular precursors through physical and/or chemical processes. Nucleation and growth of nanoparticles and colloids from solution-based precursors through synthetic chemistry is one of the most popular routes to nanomaterials synthesis, and is the focus of this thesis. Both liquid-phase and gas-phase synthetic chemistry techniques for fabricating several different classes of functional nanomaterials have been developed and extensively characterized. These techniques include vapor-phase processes such as chemical vapor condensation,[26,27] combustion and flame/spray pyrolysis,[28,29] and liquid-phase processes such as dispersion polymerization,[30] hydrothermal synthesis,[31,32] and sol-gel synthesis.[3,4] Vapor-phase synthesis is usually carried out in fast, continuous flow reactors, and is a popular industrial technique for the production of powders for pigments and coatings.

Liquid-phase synthetic chemistry techniques for nanoparticle synthesis are the focus of this thesis. These inherently 'bottom-up' techniques are standard, versatile and easy to execute on the lab-bench scale. However, due to the nature of the processing (details in 1.3.1), particle size distributions narrower than 5% are rarely obtained, and some form of post-synthesis size classification is inevitably required for most final applications. In addition, scale-up to larger amounts of production while still maintaining product quality (uniform size, size distribution) is often difficult to accomplish, and remains one of the outstanding challenges in the field of nanotechnology.

1.3 Role of Chemical Engineering

As nanotechnology moves from mere academic curiosity and simple demonstrations to the more serious issues of large-scale manufacturing, there are still several challenges that provide opportunities to chemical engineers for both scientific and technological innovation. Manufacturing well-defined and controllable nanoscale structures through synthetic chemistry requires precise concentration and temperature control over very small length and time scales. Such control is very difficult to achieve in conventional macroscale synthetic chemistry techniques. Other challenges that have attracted a lot of

interest but still remain largely unresolved are the elucidation of the general physical mechanisms of nanostructure formation and growth, as well as the sensitivity of particle morphology, composition and size to processing conditions.[5]

1.3.1 Limitations of bench-scale synthesis

Bench-scale synthetic chemistry for nanoparticle synthesis is typically carried out in batch mode in stirred flasks. Such syntheses often involve heterogeneous spatial and temporal distributions of concentration and temperature. For rapidly nucleating systems, as are often encountered in colloid synthesis, homogeneity of concentration and temperature are critical for monodisperse (<5% polydispersity) particle size distributions due to the sensitivity of colloidal nucleation and morphology to local temperature and composition. The details of the mixing process also affect colloidal growth. Stirring is conventionally used to rapidly mix reactants and to keep growing particles in suspension. Colloidal aggregation in such high-shear flow fields is a well studied phenomenon.[8] In addition, batch-to-batch variations are a frequent occurrence. All the above factors make it very difficult to scale-up bench-scale stirred flask synthesis to larger amounts of production. Synthesis of multi-layered core-shell particles is typically accomplished by controlled addition of secondary reactants to pre-formed core particle suspensions. Details of the (inherently semi-batch) addition process, such as addition rate and mixing speed dictate the presence or absence of secondary particle nucleation, homogeneity of shell growth and state of aggregation of the final mixture.

1.3.2 Chemical reactor engineering

Continuous flow chemical reactors overcome some of the drawbacks of stirred-flask synthesis. Plug flow reactors ensure spatial homogeneity of concentration and temperature. Such reactors may be constructed, for example, from long narrow tubes.[33] Micromixing still remains an issue, and inline micromixers such as static mixers or packed beds may be used. However, multi-step particle synthesis, requiring multi-point addition is problematic. Plug flow reactors with multiple reactant additions would require an inline micromixer at every point of addition, adding additional complexity to the system at every step. Monodisperse particle size distributions require narrow residence time distributions (RTD). The overall RTDs of dynamic systems consisting of multiple

units in series are convolutions of the RTDs of individual units.[33,34] Consequently, multi-unit arrangements as suggested above can have wide RTDs, thus leading to polydisperse particle size distributions.

1.4 Motivation: Microreactors for Particle Synthesis

1.4.1 Microfluidic chemical systems

Scientific and commercial interest in microfluidic systems for analysis,[35,36] synthesis,[37] catalyst testing,[38-40] kinetic studies,[41,42] rapid reaction optimization,[43] process intensification and production has increased tremendously since the early 1990's. Microreactors for single and multi-phase chemistry have been successfully demonstrated and characterized.[44-48] The main driving forces are the advantages of rapid heat and mass transfer, small reactor volumes, less use of resources and waste generation, and integration of online monitoring and detection.[49] Recent research has demonstrated the feasibility of scaling microreactor syntheses to larger amounts of production.[50-52]

1.4.2 Microreactors for nanoparticles

Microfluidic reactors for nanomaterials synthesis have multiple advantages that overcome the drawbacks associated with bench-scale processing (1.3.1). There have been several reports of nanoparticle synthesis in microfluidic reactors since 2002, when the work on this thesis began. Rapid heat transfer is possible in these reactors due to small characteristic dimensions and high surface-to-volume ratios, enabling fast heating and cooling of reaction mixtures. This intrinsic advantage of reactor size-reduction has been used by several research groups for the synthesis of semiconductor nanocrystals ('quantum dots') through high-temperature reaction of organometallic precursors. The main requirement for narrow particle size distributions in such syntheses is the rapid and uniform heating of precursor mixtures to high-temperatures, thus ensuring a well-defined, temporally confined nucleation event. Both microfabricated channel reactors and small-diameter capillary reactors have been demonstrated.

Maeda et al. used capillary tube reactors immersed in oil baths for CdSe nanocrystal synthesis as well as for multi-step synthesis of CdSe-ZnS composite nanoparticles.[53-56] Yen et al. also used a similar approach with a capillary tube heated by an aluminum

block.[57] Axial dispersion associated with laminar single-phase flows led to wide liquid residence time distributions (RTD), and hence wide particle size distributions. Continuous flow chip-based microreactors with online analysis for CdS and CdSe nanoparticles were reported by deMello et al., who also quantified the effect of RTD on size distributions.[58,59] Yen et al.[60] and Chan et al.[61] presented two complementary approaches to nanocrystal synthesis using two-phase flows that overcame the axial dispersion effects associated with laminar flows. Yen et al. used a gas-liquid segmented flow reactor microfabricated in silicon (using similar principles of reactor design as are presented in this thesis) for CdSe nanocrystal synthesis.[60] This reactor had a localized hot zone that operated at 260 °C followed by a cool zone that effectively quenched the reaction at the outlet. This work demonstrated the utility of silicon microfabrication in creating and maintaining large temperature gradients on the same substrate. Chan et al. performed high-temperature CdSe synthesis inside octadecene droplets dispersed in a fluorinated polymer inside a reactor microfabricated in glass, and also demonstrated an elegant online photoluminescence detection technique.[61] Shestopalov et al. synthesized CdS particles inside aqueous droplets suspended in a fluorocarbon carrier fluid using a multi-step process that involved synchronized merging of droplets under certain conditions.[62] Among other particulate systems, metal nanoparticle synthesis was described by Köhler et al. who used a microfabricated continuous flow micromixer-reactor [63,64] and Lin et al. demonstrated silver nanoparticle synthesis in a tubular capillary reactor.[65]

Microreaction technology as a scalable alternative to large-scale batch processing for particle synthesis has attracted increased attention from major industrial producers of fine particles. Recently, researchers at Clariant GmBH developed a high throughput pilot-plant scale fine pigment synthesis process based on microreaction technology.[66,67] The synthesized pigments were found to possess superior properties as compared to large-scale batch synthesis. Stable, high-throughput production of silver halide fine particles was also demonstrated recently by researchers at Fuji Photo film company, who used a cylindrical, annular multi-lamination type microreactor.[68,69]

1.5   Thesis Objectives and Layout

This thesis focuses on microfluidics-based approaches for synthesis and surface-engineering of colloidal particles. The ultimate goal is to develop microfluidic chemical reactors for continuous synthesis of multi-layered colloids with tunable size and surface functionalization. Sol-gel derived inorganic oxide particles of silica (SiO_2) and titania (TiO_2) and their core-shell composites are studied as technologically relevant model colloids. Multiphase microfluidics, specifically gas-liquid segmented flow, is the enabling technology for the reactors developed in this thesis. The generation, dynamics and transport properties of uniform, monodisperse bubble flows in microfluidic channels is presented in Chapter 2. General design guidelines are described for generating such flows over a wide range of flow velocities and gas-to-liquid ratios. Gas-liquid flows overcome the large axial dispersion effects associated with single-phase laminar flow in microchannels. A general experimental methodology to obtain residence time distribution (RTD) information in microfluidic flows is presented in Chapter 3, and the RTD of both single-phase and two-phase gas-liquid flows are compared. As expected, gas-liquid segmented flow yields RTDs several times narrower than those from laminar flows under identical conditions. Microfluidic chemical reactors for the continuous synthesis of colloidal silica and titania particles through sol-gel chemistry are the focus of Chapter 4. Particle sizes can be tuned in the 50 nm to 1 μm size range by varying reactant flow velocities (and hence residence times) and also by varying reactor temperature. Synthesis of core-shell structures requires controlled secondary (shell) reactant addition to primary (core) particles. The design and operation of a microfluidic reactor for continuously coating thick, uniform layers of titania (30 nm) on silica particles with complete suppression of secondary nucleation and primary particle agglomeration is presented in Chapter 5. Finally, multi-step reactors for continuous colloidal synthesis and in-situ coating, as well as continuous particle separation units using free-flow electrophoresis are described in Chapter 6. These devices present initial steps towards the ultimate goal of general microfluidic systems that perform tunable, multi-step colloidal nanomaterials synthesis. Chapter 7 is a final discussion of the technology developed in this thesis, including figures of merit and bounds of operation, scale-out considerations and directions for future work.

1.6   References

1.   Sanders, J. V. Diffraction of light by opals. *Acta Crystallographica* **A24**, 427 (1968).

2.   Bohren, C. F. & Huffman, D. R. *Absorption and Scattering of Light by Small Particles* (Wiley, New York, 1983).

3.   Iler, R. K. *The Chemistry of Silica* (John Wiley and Sons, New York, 1979).

4.   Brinker, C. J. & Scherer, G. W. *Sol-Gel Science: The Physics and Chemistry of Sol-Gel Processing* (Academic Press, Boston, 1990).

5.   Matijevic, E. Uniform Inorganic Colloidal Dispersions. Achievements and Challenges. *Langmuir* **10**, 8-16 (1994).

6.   Verpoorte, E. Beads and chips: new recipes for analysis. *Lab on a Chip* **3**, 60N-68N (2003).

7.   Bonnemann, H. & Richards, R. M. Nanoscopic metal particles - Synthetic methods and potential applications. *European Journal of Inorganic Chemistry*, 2455-2480 (2001).

8.   Russell, W. B., Saville, D. A. & Schowalter, W. R. *Colloidal Dispersions* (Cambridge University Press, 1989).

9.   Morr, C. V. Colloids in Foods - Dickinson,E, Stainsby,G. *Food Technology* **37**, 155-155 (1983).

10. Panyam, J. & Labhasetwar, V. Biodegradable nanoparticles for drug and gene delivery to cells and tissue. *Advanced Drug Delivery Reviews* **55**, 329-347 (2003).

11. Hayward, R. C., Saville, D. A. & Aksay, I. A. Electrophoretic assembly of colloidal crystals with optically tunable micropatterns. *Nature* **404**, 56-59 (2000).

12. Trau, M., Sankaran, S., Saville, D. A. & Aksay, I. A. Electric-Field-Induced Pattern-Formation in Colloidal Dispersions. *Nature* **374**, 437-439 (1995).

13. *Beyond the Molecular Frontier: Challenges for Chemistry and Chemical engineering* (ed. Council, N. R.) (National Academy Press, Washington, D.C., 2003).

14. Murray, C. B., Kagan, C. R. & Bawendi, M. G. Self-Organization of Cdse Nanocrystallites into 3-Dimensional Quantum-Dot Superlattices. *Science* **270**, 1335-1338 (1995).

15. Murray, C. B., Kagan, C. R. & Bawendi, M. G. Synthesis and characterization of monodisperse nanocrystals and close-packed nanocrystal assemblies. *Annual Review of Materials Science* **30**, 545-610 (2000).

16. Faraday, M. Experimental relations of gold (and other metals) to light. *Philosophical Transactions of the Royal Society of London, Series A* **147**, 145-181 (1857).

17.   Tsukagoshi, K. et al. Carbon nanotube devices for nanoelectronics. *Physica B-Condensed Matter* **323**, 107-114 (2002).

18.   Matsui, I. Nanoparticles for electronic device applications: A brief review. *Journal of Chemical Engineering of Japan* **38**, 535-546 (2005).

19.   Pissuwan, D., Valenzuela, S. M. & Cortie, M. B. Therapeutic possibilities of plasmonically heated gold nanoparticles. *Trends in Biotechnology* **24**, 62-67 (2006).

20.   Silva, G. A. Small neuroscience: The nanostructure of the central nervous system and emerging nanotechnology applications. *Current Nanoscience* **1**, 225-236 (2005).

21.   Silva, G. A. Nanotechnology approaches for the regeneration and neuroprotection of the central nervous system. *Surgical Neurology* **63**, 301-306 (2005).

22.   Portney, N. G. & Ozkan, M. Nano-oncology: drug delivery, imaging, and sensing. *Analytical and Bioanalytical Chemistry* **384**, 620-630 (2006).

23.   Sahoo, S. K. & Labhasetwar, V. Nanotech approaches to delivery and imaging drug. *Drug Discovery Today* **8**, 1112-1120 (2003).

24.   Quinten, M. The color of finely dispersed nanoparticles. *Applied Physics B-Lasers and Optics* **73**, 317-326 (2001).

25.   Baraton, M. I. & Merhari, L. Advances in air quality monitoring via nanotechnology. *Journal of Nanoparticle Research* **6**, 107-117 (2004).

26.   Choi, C. J., Tojochko, O. & Kim, B. K. Preparation of iron nanoparticles by chemical vapor condensation. *Materials Letters* **56**, 289-294 (2002).

27.   Dong, X. L., Choi, C. J. & Kim, B. K. Structural and magnetic characterization of Fe nanoparticles synthesized by chemical vapor condensation process. *Journal of Applied Physics* **92**, 5380-5385 (2002).

28.   Teleki, A., Pratsinis, S. E., Wegner, K., Jossen, R. & Krumeich, F. Flame-coating of titania particles with silica. *Journal of Materials Research* **20**, 1336-1347 (2005).

29.   Wegner, K. & Pratsinis, S. E. Gas-phase synthesis of nanoparticles: scale-up and design of flame reactors. *Powder Technology* **150**, 117-122 (2005).

30.   Bosma, G. et al. Preparation of monodisperse, fluorescent PMMA-latex colloids by dispersion polymerization. *Journal of Colloid and Interface Science* **245**, 292-300 (2002).

31.   Wu, M. M. et al. Sol-hydrothermal synthesis and hydrothermally structural evolution of nanocrystal titanium dioxide. *Chemistry of Materials* **14**, 1974-1980 (2002).

32.   Feng, S. H. & Xu, R. R. New materials in hydrothermal synthesis. *Accounts of Chemical Research* **34**, 239-247 (2001).

33.   Levenspiel, O. *Chemical reaction engineering* (Wiley, New York, 1962).

34. Fogler, H. S. *Elements of Chemical Reaction Engineering* (Prentice-Hall, Inc., Englewood Cliffs, NJ, 1992).

35. Herzig-Marx, R., Queeney, K. T., Jackman, R. J., Schmidt, M. A. & Jensen, K. F. Infrared spectroscopy for chemically specific sensing in silicon-based microreactors. *Analytical Chemistry* **76**, 6476-6483 (2004).

36. Herzig-Marx, R., Queeney, K. T., Jackman, R. J., Schmidt, M. A. & Jensen, K. F. Integration of multiple internal reflection (MIR) infrared spectroscopy with silicon-based chemical microreactors. *Abstracts of Papers of the American Chemical Society* **223**, U196-U196 (2002).

37. Brivio, M., Verboom, W. & Reinhoudt, D. N. Miniaturized continuous flow reaction vessels: influence on chemical reactions. *Lab on a Chip* **6**, 329-344 (2006).

38. Ajmera, S. K., Delattre, C., Schmidt, M. A. & Jensen, K. F. Microfabricated differential reactor for heterogeneous gas phase catalyst testing. *Journal of Catalysis* **209**, 401-412 (2002).

39. Ajmera, S. K., Delattre, C., Schmidt, M. A. & Jensen, K. F. Microfabricated cross-flow chemical reactor for catalyst testing. *Sensors and Actuators B-Chemical* **82**, 297-306 (2002).

40. Ajmera, S. K., Delattre, C., Schmidt, M. A. & Jensen, K. F. in *Science and Technology in Catalysis 2002* 97-102 (2003).

41. Floyd, T. M., Schmidt, M. A. & Jensen, K. F. Silicon micromixers with infrared detection for studies of liquid-phase reactions. *Industrial & Engineering Chemistry Research* **44**, 2351-2358 (2005).

42. Jackman, R. J., Floyd, T. M., Ghodssi, R., Schmidt, M. A. & Jensen, K. F. Microfluidic systems with on-line UV detection fabricated in photodefinable epoxy. *Journal of Micromechanics and Microengineering* **11**, 263-269 (2001).

43. Ratner, D. M. et al. Microreactor-based reaction optimization in organic chemistry glycosylation as a challenge. *Chemical Communications*, 578-580 (2005).

44. Losey, M. W., Schmidt, M. A. & Jensen, K. F. Microfabricated multiphase packed-bed reactors: Characterization of mass transfer and reactions. *Industrial & Engineering Chemistry Research* **40**, 2555-2562 (2001).

45. Burns, J. R. & Ramshaw, C. Development of a microreactor for chemical production. *Chemical Engineering Research & Design* **77**, 206-211 (1999).

46. Chambers, R. D. et al. Elemental fluorine - Part 16. Versatile thin-film gas-liquid multi-channel microreactors for effective scale-out. *Lab on a Chip* **5**, 191-198 (2005).

47. Chambers, R. D., Fox, M. A. & Sandford, G. Elemental fluorine - Part 18. Selective direct fluorination of 1,3-ketoesters and 1,3-diketones using gas/liquid microreactor technology. *Lab on a Chip* **5**, 1132-1139 (2005).

48.   Chambers, R. D., Holling, D., Rees, A. J. & Sandford, G. Microreactors for oxidations using fluorine. *Journal of Fluorine Chemistry* **119**, 81-82 (2003).

49.   Jensen, K. F. Microreaction engineering - is small better? *Chemical Engineering Science* **56**, 293-303 (2001).

50.   de Mas, N., Guenther, A., Kraus, T., Schmidt, M. A. & Jensen, K. F. Scaled-out multilayer gas-liquid microreactor with integrated velocimetry sensors. *Ind. Eng. Chem. Res.* **44**, 8997 - 9013 (2005).

51.   de Mas, N., Guenther, A., Schmidt, M. A. & Jensen, K. F. Microfabricated multiphase reactors for the selective direct fluorination of aromatics. *Industrial & Engineering Chemistry Research* **42**, 698-710 (2003).

52.   de Mas, N., Guenther, A., Schmidt, M. A. & Jensen, K. F. Scalable microfabricated reactors for direct fluorination reactions. *Proceedings of IEEE Transducers, Boston* (2003).

53.   Nakamura, H. et al. Preparation of CdSe nanocrystals in a micro-flow-reactor. *Chemical Communications*, 2844-2845 (2002).

54.   Nakamura, H. et al. Continuous preparation of CdSe nanocrystals by a microreactor. *Chemistry Letters*, 1072-1073 (2002).

55.   Nakamura, H. et al. Application of a microfluidic reaction system for CdSe nanocrystal preparation: their growth kinetics and photoluminescence analysis. *Lab on a Chip* **4**, 237-240 (2004).

56.   Omata, T., Nose, K., Otsuka-Yao-Matsuo, S., Nakamura, H. & Maeda, H. Synthesis of CdSe quantum dots using micro-flow reactor and their optical properties. *Japanese Journal of Applied Physics Part 1-Regular Papers Short Notes & Review Papers* **44**, 452-456 (2005).

57.   Yen, B. K. H., Stott, N. E., Jensen, K. F. & Bawendi, M. G. A continuous-flow microcapillary reactor for the preparation of a size series of CdSe nanocrystals. *Advanced Materials* **15**, 1858-1862 (2003).

58.   Edel, J. B., Fortt, R., deMello, J. C. & deMello, A. J. Microfluidic routes to the controlled production of nanoparticles. *Chemical Communications*, 1136-1137 (2002).

59.   Krishnadasan, S., Tovilla, J., Vilar, R., deMello, A. J. & deMello, J. C. On-line analysis of CdSe nanoparticle formation in a continuous flow chip-based microreactor. *Journal of Materials Chemistry* **14**, 2655-2660 (2004).

60.   Yen, B. K. H., Guenther, A., Schmidt, M. A., Jensen, K. F. & Bawendi, M. G. A microfabricated gas-liquid segmented flow reactor for high-temperature synthesis: The case of CdSe quantum dots. *Angewandte Chemie-International Edition* **44**, 5447-5451 (2005).

61.   Chan, E. M., Alivisatos, A. P. & Mathies, R. A. High-temperature microfluidic synthesis of CdSe nanocrystals in nanoliter droplets. *Journal of the American Chemical Society* **127**, 13854-13861 (2005).

62. Shestopalov, I., Tice, J. D. & Ismagilov, R. F. Multi-step synthesis of nanoparticles performed on millisecond time scale in a microfluidic droplet-based system. *Lab on a Chip* **4**, 316-321 (2004).

63. Kohler, J. M., Wagner, J. & Albert, J. Formation of isolated and clustered Au nanoparticles in the presence of polyelectrolyte molecules using a flow-through Si chip reactor. *Journal of Materials Chemistry* **15**, 1924-1930 (2005).

64. Kohler, J. M., Wagner, J., Albert, J., Mayer, G. & Hubner, U. Formation of gold nano-particles and nano-particle aggregates in static micromixers in the presence of bovine serum albumin (BSA). *Chemie Ingenieur Technik* **77**, 867-873 (2005).

65. Lin, X. Z., Teng, X. W. & Yang, H. Direct synthesis of narrowly dispersed silver nanoparticles using a single-source precursor. *Langmuir* **19**, 10081-10085 (2003).

66. Kim, H., Saitmacher, K., Unverdorben, L. & Wille, C. Pigments with improved properties - Microreaction technology as a new approach for synthesis of pigments. *Macromolecular Symposia* **187**, 631-640 (2002).

67. Wille, C. et al. Synthesis of pigments in a three-stage microreactor pilot plant-an experimental technical report. *Chemical Engineering Journal* **101**, 179-185 (2004).

68. Nagasawa, H., Aoki, N. & Mae, K. Design of a new micromixer for instant mixing based on the collision of micro segments. *Chemical Engineering & Technology* **28**, 324-330 (2005).

69. Nagasawa, H. & Mae, K. Development of a new microreactor based on annular microsegments for fine particle production. *Industrial & Engineering Chemistry Research* **45**, 2179-2186 (2006).

2 Microfluidics with Bubbles: Dynamics and Transport

This chapter describes the design and operation of microfluidic devices for uniform, stable gas-liquid segmented flow over a wide range of flow conditions. We characterize the dynamics and transport properties of these flows using pulsed-laser fluorescence microscopy, optical stereomicroscopy and micro particle image velocimetry (μPIV). We specifically focus on low superficial gas and liquid velocities which yield liquid-phase residence times of several minutes.

We first describe the experimental techniques for fabrication, visualization and characterization of the microscale gas-liquid flow systems. Gas-liquid microflows at low superficial liquid and gas velocities are obtained by syringe-pump delivery of both gas and liquid to the microfluidic devices. We then analyze the important scaling relations for forces and time scales in these multiphase flows. Interfacial forces dominate over inertial, gravity and viscous forces under the conditions used in this work. The rectangular cross-sectional geometry in our microfluidic devices leads to interesting gas-liquid interface shapes. Under dynamic conditions of pressure-driven flow, adjacent liquid segments are connected through thick menisci at the sharp channel corners and thin liquid films at the center of the walls. We describe the relevant parameters that influence these dynamic interfaces. We then summarize experimental studies of the different flow regimes obtained by varying liquid and gas superficial velocities. In the segmented flow regime, the ratio of the lengths of bubbles to liquid segments depends on the relative flow rates of gas and liquid. However, the actual lengths depend on the mechanism of bubble break-up. This fact is highlighted by experimental observations of bubble break-up dynamics in three different gas-injection geometries. We present bubble and liquid segment length measurements for three inlet geometries at several different gas-liquid flow ratios and explain the observed trends. Under certain conditions of operation, large oscillations in bubble size are observed, and the amplitude of these oscillations increases with gas flow rate, for a given liquid flow rate. We describe the conditions under which such oscillating

flows are obtained. We then describe the start-up procedure and key time-scales for flow experiments to generate uniform, non-coalescing gas-liquid flows. The recirculation motion in the liquid segments associated with gas-liquid flows as well as their symmetry characteristics are quantified for straight and meandering channel networks using micro particle image velocimetry (μPIV). Even minor surface roughness effects and gas phase compressibility induce loss of symmetry and enhance mixing across the centerline in straight channels. Mixing is further accelerated in meandering channels by the periodic switching of recirculation patterns across the channel center. We illustrate how such recirculatory motion can be used to mix miscible liquid streams, and describe a simple surface tension driven technique for removing the gas after mixing has been achieved.

2.1 Introduction

2.1.1 Macroscale multiphase flow

Multiphase systems, ubiquitous in chemical process applications, are more complex than their single-phase counterparts. Multiphase reactor design and operation involves the complex interaction of several physicochemical phenomena, including hydrodynamics of fluids with free surfaces, turbulence (in large systems), heat and mass transport, surface phenomena and chemical reaction. Macroscale units (characteristic dimensions ranging from a few millimeters to several meters) involve widely different length and time scales. Successful design requires a thorough understanding of the interaction of transport phenomena and chemical kinetics at different spatial and temporal scales in each phase, and also between phases. In macroscale systems, the large disparity in scales makes first-principles numerical predictions difficult and experimental information is inevitably required. For example, design of three-phase reactors such as trickle beds and slurry bubble columns requires information on multi-phase fluid dynamics, in the form of flow regimes, pressure drops, phase holdups and inter-phase mass transfer coefficients. A large body of chemical engineering literature is devoted to these topics.[1,2] Experimental techniques to determine design parameters are well-established and used to develop macroscopic systems.[3,4] For macroscale units, it is generally desirable to operate in uniform flow regimes with large specific interfacial areas, and thus large mass transfer.[5]

2.1.2 Multi-phase flow in microchannels

The ability to fabricate microfluidic channel networks of significant complexity and with length scales of tens to hundreds of microns creates opportunities for microfluidic systems for several applications.[6,7] Based on the ability to deliver, react, separate and detect small fluid volumes a range of applications have emerged in biology and biotechnology, in cooling of IC chips, and in chemical and material synthesis.[8,9] Single-phase microflows were extensively studied initially, and multiphase fluid systems were often reduced to steady co-flows of two phases, e.g., by stabilizing fluid-fluid interfaces.[10] Multiphase microreactors have also been considered for solid catalyzed reactions, such as hydrogenation[11,12] and in challenging gas-liquid reactions, such as fluorination.[13-15] Air-water or refrigerant-vapor flows in conventionally machined microchannels were among the first transient systems to be considered because of their relevance to micro heat exchanger applications.[16-18] Segmented liquid-liquid (droplet) flows through capillaries[19] and microfabricated channel networks[20,21] have since been exploited in enhanced mixing and kinetic studies of fast reactions.

Microfluidic multiphase systems differ from their macroscopic counterparts in two principal aspects, (i) no turbulence and (ii) a smaller disparity in length and time scales - both effects are direct consequences of shrinking reactor dimensions to the micron scale. Characteristic length scales are typically comparable to those at which interfacial and diffusive forces are dominant. Gas-liquid flows result in segmented flows over a wide range of flow conditions and channels dimensions. In segmented flow, gas bubbles are located between two adjacent liquid segments. The multiphase flow terminology used in the microfluidics literature has two sources of nomenclature; it is either borrowed from viscous flows (Taylor flow) or from macroscopic multiphase pipe flows (plug/slug flow). We will use the terms "gas-liquid segmented flow" or "plug/slug flow" interchangeably.

Taylor characterized the velocity profile in segmented low-Reynolds number flows,[22] among other low-Reynolds number flows, nearly half a century ago. In this chapter, we show that 'classical' low Reynolds number fluid mechanics results can be directly translated into the microscale to provide unique multiphase mixing and reaction solutions. Direct numerical simulation of the overall multiphase reactor behavior is, however, still a difficult task due to non-linearity introduced by the interaction between phases and partial

wetting of channel wall surfaces. This necessitates use of experimental tools to evaluate multiphase microfluidic reactor behavior, analogous to the approach for macroscale reactors. 'Classical' design information e.g., flow-regime maps, hold-up information, and residence time distributions therefore have to be used for a thorough understanding of multiphase microfluidic reactors.[11,12] This is the focus of this chapter and Chapter 3.

2.2 Experimental

2.2.1 Microfluidic devices: design and fabrication

Microchannel networks used in this work were 300 μm or 400 μm wide and approximately 150-250 μm deep and their configurations are schematically shown in Figure 2-1. Design 1 uses straight channel segments that are interconnected by bends, while design 2 consists of meandering channels (the bending radius of the channel center line is 600 μm). Microchannel lengths between 0.15 m and 3 m were used. The specific dimensions of all microchannels are provided with the results for individual experiments.

Microfluidic devices were fabricated in poly (dimethylsiloxane) (PDMS) by using standard soft-lithographic techniques.[23] PDMS (Dow Corning Sylgard Brand 184 Silicone Elastomer, Essex-Brownell Inc.) was molded on masters fabricated on silicon wafers using SU-8 (2050) (Negative photoresist, Microchem Corporation, MA). Typically, 150 μm thick SU-8 films were spun on 100 mm diameter silicon wafers (Silicon Quest International). Photolithography was used to define negative images of the microfluidic channels, and finally the wafers were developed using SU-8 Developer (Microchem Corporation). Packaging of the microreactors was accomplished by the following sequence of steps. PDMS was molded on the SU-8 masters described above at 70°C for 2-3 hours. In some cases (Figure 2-1(b),(c)) a small amount (~1 g) of carbon black (acetylene, 80 m²/g, Alfa Aesar) was added to the PDMS mixture before curing and thoroughly mixed. The resulting mold was opaque black in color and provided a uniform contrast background for microscopic observation of flow. The devices were peeled off the mold, cut and cleaned. Inlet and outlet holes (1/16-in. o.d.) were punched into the material. Individual devices were sealed to precleaned microscope slides (25x75 mm or 50x75mm, VWR Scientific Inc.). Both surfaces were activated in an oxygen plasma

37

(Harrick Co., PDC-32G) for 35 seconds prior to sealing. PEEK tubing (1/16-in. o.d., 508 μm i.d., Upchurch Scientific.) was inserted in the inlet and outlet holes, and glued in place with 5-min epoxy (Devcon). The outer surface of the device was activated in the same oxygen plasma for 45 seconds prior to gluing the tubes. This was found to increase epoxy adhesion significantly. The epoxy was cured either at room temperature for 24-36 hours, or at 70°C for 4-12 hours, prior to use.
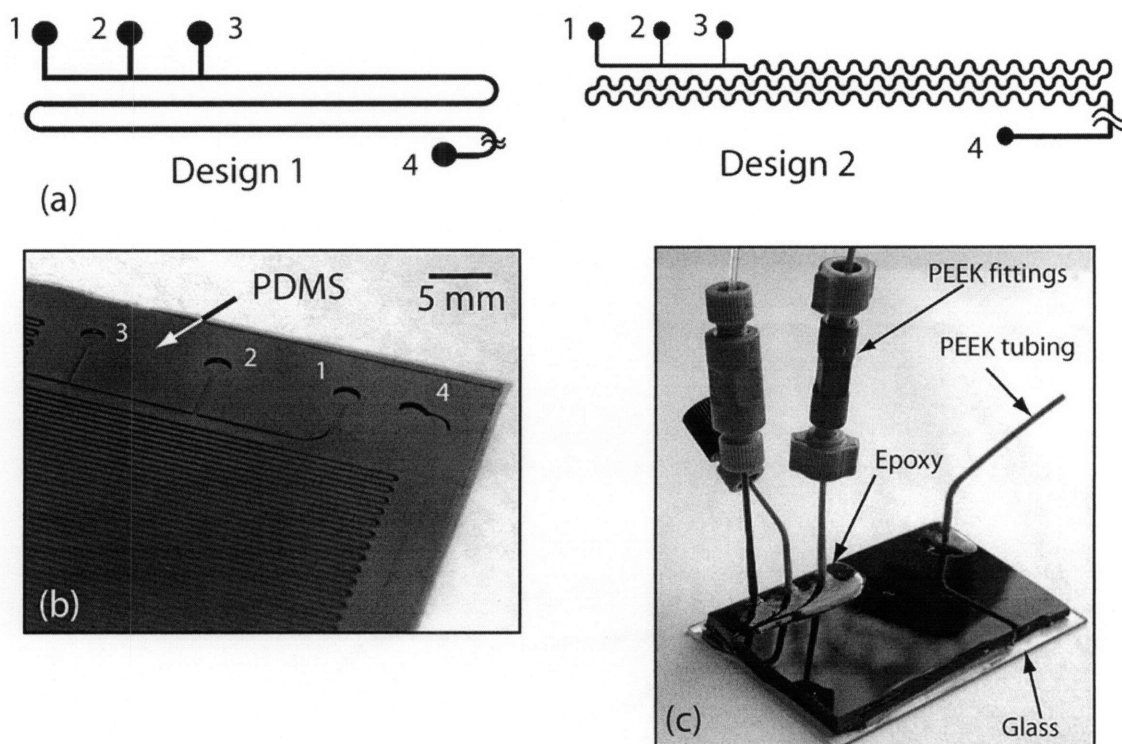
Figure 2-1 (a) Schematics of microfluidic channel configurations used in this work: design 1 consists of straight-walled channel segments and device 2 consists of meandering channels. In both cases, "1" and "2" denote liquid inlets, "3" is the gas inlet, and "4" is the common outlet. (b) Example of microchannel molded in PDMS. Microchannel length is 3 m, channel width is 300 μm and channel depth is approximately 250 μm. (c) Photograph of device packaging scheme: PEEK tubing (Upchurch Scientific) is inserted into holes punched into the PDMS, and glued in place with 5-min epoxy (Devcon). Devices are interfaced with syringes through standard PEEK fittings.

2.2.2 Experimental setup

Liquids and gases were delivered into the microfluidic devices using syringe pumps from Harvard Apparatus (PHD 2000 Infusion/Withdraw pumps), and Cole-Parmer

(74900 Series). Devices were interfaced with the pumps using PEEK fittings (Upchurch Scientific.), and Teflon tubing (1/16-in. o.d., Cole-Parmer). Air was used as the segmenting fluid in the experiments, and was pumped in through Hamilton Gastight syringes (1 mL: 1700 series TTL, 2.5 mL: 1002 series TTL and 25 mL. 1025 series TTL). The experimental set-up is schematically depicted in Figure 2-2.
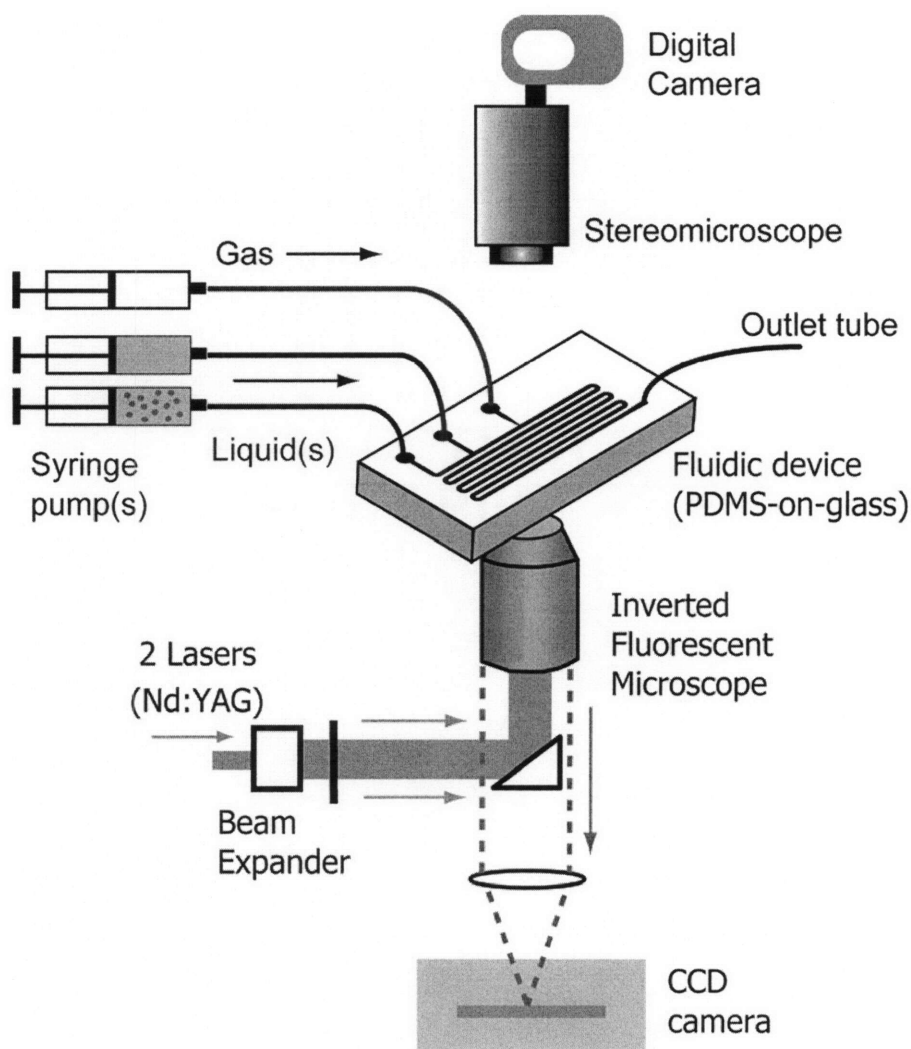
Figure 2-2 Schematic of experimental set-up: Liquids and gases were delivered using syringe pumps. An inverted fluorescent microscope or optical stereomicroscope was used for flow visualization (further details in 2.2.3).

2.2.3 Flow visualization†

Segmented gas-liquid flows are transient and impose requirements on the temporal resolution of the imaging equipment. We fluorescently labeled the liquid phase with either a continuous dye (Rhodamine B) or by dispersing dyed microspheres in the liquid (ethanol). An inverted fluorescence microscope with 5X (numerical aperture 0.12), 10X (0.3), and 20X (0.5) air objectives was used for imaging. Two independent Nd:YAG lasers (BigSky Ultra, pulse energy 30mJ/pulse, duration 7ns) served as light sources for pulsed microscopy and a sensitive full frame CCD camera (PCO Sensicam double shot QE) captured the digital images at a rate of up to 10 frames per second. When the liquid phase was dyed with Rhodamine B, the phase-distribution could be computed from micrographs. For µ-PIV measurements, fluorescent microspheres (Molecular probes, 700 nm) were dispersed in the liquid phase, and two subsequent image frames with a temporal separation that was much shorter than the camera frame rate were captured. A standard particle image velocimetry (PIV) cross correlation algorithm[24] then computed vector fields of the liquid velocity from the local displacement of tracer particles between the two frames. Further details of this technique are provided in 2.3.5. Optical stereomicroscopy was carried out using a Leica stereomicroscope and images/movies (15 fps) were captured on a digital camera (Nikon CoolPix). Image analysis was carried out on NIH ImageJ software.

2.3 Results and Discussion

2.3.1 Scaling analysis of transport parameters

This main focus of this chapter is the flow of small bubbles under strong geometric constraints in long channels of rectangular cross-section. The presence of confining solid walls significantly alters bubble shapes and dynamics from the free-surface cases in larger systems, and both size and material properties of the walls influence the final outcomes.

---

† The pulsed-laser fluorescence microscopy-based flow visualization and µ-PIV measurements in this study were carried out in collaboration with Dr. Axel Günther, who at the time was a post-doctoral associate in Prof. Jensen's research group.

In this section we describe the dimensionless parameters that characterize the significance of the various forces present in the system. These include inertial forces, gravity, surface tension, and viscous forces. For the discussion that follows we assume channels of rectangular cross-section with characteristic dimension $d \sim 200$ μm. We work with organic liquids such as ethanol, that almost completely wet the microchannel surface (contact angle $\theta \sim 0°$), and hence assume fluid properties of viscosity (μ), density (ρ) and surface tension (σ) of ethanol in the following analysis. For dynamic parameters we assume a flow velocity U of 10^{-4} m/s. The analysis is carried out for isothermal conditions.

The dimensionless stress ratios of interest are listed below, along with their typical values calculated using the above parameters.

$$Re = \frac{inertial}{viscous} = \frac{dU\rho}{\mu} \sim 10^{-2} \tag{2.1}$$

$$Bo = \frac{gravity}{interfacial} = \frac{\Delta\rho d^2 g}{\sigma} \sim 10^{-2} \tag{2.2}$$

$$We = \frac{inertial}{interfacial} = \frac{\rho U^2 d}{\sigma} \sim 10^{-8} \tag{2.3}$$

$$Ca = \frac{viscous}{interfacial} = \frac{\mu U}{\sigma} \sim 10^{-6} \tag{2.4}$$

Small values of Reynolds number (Re) indicate that inertial forces are negligible in these flows, as expected. Small values of Bond number (Bo), Weber number (We) and Capillary number (Ca) indicate that viscous, inertial and gravity forces are completely dominated by interfacial forces.

2.3.2 Gas-liquid interfaces: Effect of channel geometry and wetting properties

Zero Ca corresponds to static conditions, and gas-liquid interface shapes may be obtained from the equations of capillary statics. For the special case of perfectly wetting liquids constrained by rectangular channels under negligible gravity conditions, liquid tends to collect as thick menisci in the sharp corners throughout the channel. Computation of these interface shapes is described in detail by Wong[25-28], and reviewed by Ajaev and Homsy.[29]

The shapes of constrained bubbles under dynamic conditions of pressure-driven flow differ from the static shapes due to the presence of viscous forces. Hence the Capillary number is the key dimensionless parameter that is used to describe the dynamics. Wong et al.[25-28] investigated dynamic shapes of moving bubbles in rectangular microchannels in the low Ca limit. Their numerical simulations reveal thick liquid menisci in the channel corners (as in the statics case). However, there are no dry areas on the walls of the channels, and macroscopic films of non-uniform thickness are present, as schematically shown in Figure 2-3(a). Wong et al. have also characterized these shapes as a function of Ca.[25-28] They conclude that thickness of the menisci in the channel corners scales as $Ca^{2/3}$, and this will have important repercussions when discussing bubble and liquid segment lengths in 2.3.5.
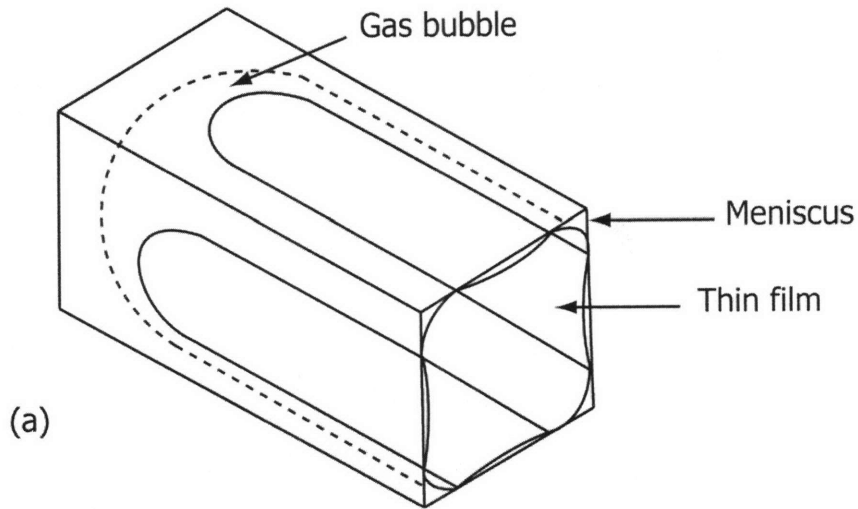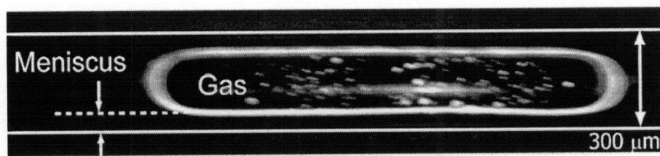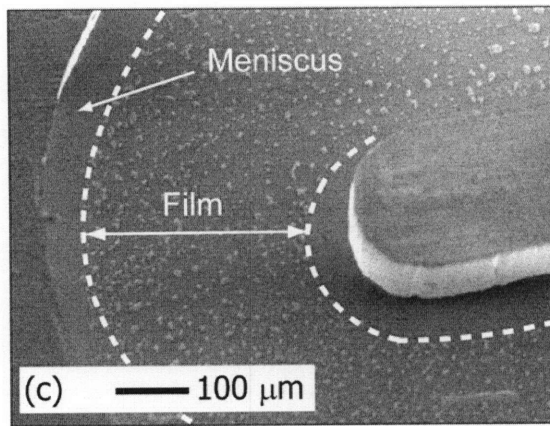
Figure 2-3 (a) Sketch of gas-liquid interface shapes in pressure-driven flow. (b) Optical stereomicrograph of gas-liquid flow showing a top-view of the thick menisci. (Ca ~ 10^{-3}) The white spots in the center of the gas bubble indicate thin film breakage (c) Preferential deposition of nanoparticles in regions of the microchannel (partially) covered by thin liquid films (Further details in Chapter 4).

Figure 2-3(b) shows an optical stereomicrograph of gas-liquid flow in our microchannel devices. As anticipated, we observe the presence of thick menisci (~ 60 μm) at the channel corners. In practice, due to finite, non-zero solid-liquid contact angles, the thin films at the wall centers are observed to break up during the passage of gas

bubbles, as seen in Figure 2-3(b). The presence and break-up of thin liquid films at the channel centers is confirmed by the preferential deposition of a thin film (<2 μm thick) of nanoparticles away from the microchannel corners in the SEM micrograph of Figure 2-3(c). Further details and description of this phenomenon are discussed in the following chapters. The presence of menisci and thin films provides a means of communication between adjacent liquid segments separated by a gas bubble. Detailed studies of axial dispersion and liquid phase residence time distribution, which quantify the communication and mass-transport between interconnected liquid segments, are reported in Chapter 3.

2.3.3 Gas-liquid flow regimes

Depending on the gas and liquid flow rates, different spatial distributions of the two phases are obtained. We refer to the different phase distributions as "flow regimes", in accordance with macroscale multiphase flow terminology. We define the superficial gas and liquid velocities, j_G and j_L, as volumetric flow rates divided by the cross sectional area of the channel. Figure 2-4(a) shows the sharp images obtained from pulsed-laser fluorescence microscopy. Parameters in this diagram (Figure 2-4(b)) are the gas and liquid superficial velocities. We distinguish the segmented flow patterns (bubbly and slug/plug flow) and annular flow. In segmented flow, gas bubbles are located between two liquid segments. The liquid segments are interconnected through menisci in the channel corners and thin liquid films at the walls that together cover approximately 5% of the channel cross section.[26] Annular flow is a steady flow regime, with a continuous gas core in the channel center, thin liquid films at the walls, and menisci in the channel corners. Depending on the volatility of the liquid, the liquid film can evaporate from wall surfaces at high gas flow rates.[14] The dashed rectangle in Figure 2-4(b) indicates the typical conditions in the slug and annular flow regimes under which multiphase microreactors (in which both liquid and gas phases are reactants) are typically operated.

Segmented gas-liquid flows are obtained for a large range of superficial gas and liquid velocities. In particular, such flows are feasible on a reaction chip at small superficial gas velocities, conditions that are required to accommodate liquid-phase reactions with residence times of several minutes. Such conditions that are the focus of this thesis are

shown as the shaded region in Figure 2-4(b). The covered range of superficial liquid velocities is similar to the one used for gas-liquid microreactors. However, significantly smaller amounts of gas are used in order to increase the mean residence time of the liquid but still allow for regularly sized gas and liquid segments to be formed. We consider gas and liquid superficial velocities as low as 0.1 mm/s. As discussed in 2.3.1, at these flow rates, interfacial forces dominate by two orders of magnitude over gravity and by three to four orders of magnitude over viscous forces.

Taylor characterized segmented flow of two phases through tubes of circular cross section at low Reynolds numbers for macroscale systems.[22] He predicted that liquid phase internal recirculation would occur at a moderate slip between the liquid and the gas phases, corresponding to values of the parameter $m = (U_b - U_{bulk})/U_b < 0.5$ (U_b is bubble velocity and U_{bulk} is the bulk liquid velocity in a liquid segment). For our conditions, m is approximately 0.02 for the range of considered Capillary numbers. Figure 2-4(c) shows the Capillary number range for the considered experiments. We thus expect and observe internal recirculation in the liquid phase, and quantify it in 2.3.5.
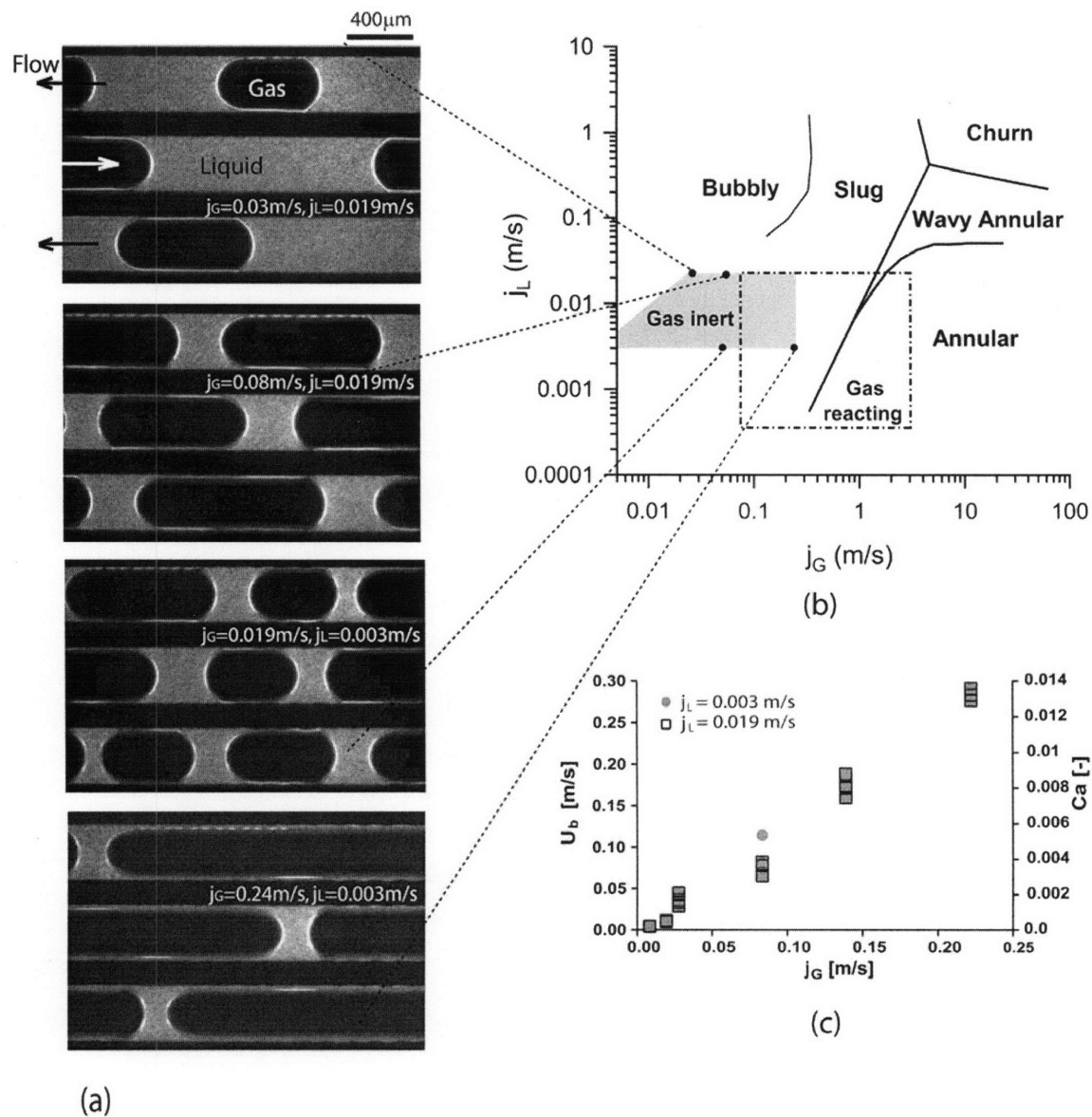
Figure 2-4 (a) Pulsed-laser fluorescence micrographs taken at different flow conditions in a center plane (depth of field: 66.4 μm) through three neighboring lanes in design 1; (b) is the associated gas-liquid flow regime diagram. Present conditions where the introduction of inert gas into a liquid stream creates a segmented gas-liquid flow to improve mixing and the residence time distribution are shaded. The dash-dotted line indicates operating conditions for multiphase microreactors with reacting gases. (c) Variation of bubble velocity and capillary (Ca) number with superficial gas velocity.

2.3.4 Bubble break-up dynamics

We describe experimental observations of breakup dynamics of bubbles in microfluidic channels of rectangular cross-section in this section. We consider two main gas inlet geometries, the T-junction and a J-shaped inlet, as shown in Figure 2-5, and two

different inlet widths for the T-junction. Although the mechanism of bubble breakup is the same in all cases (as described below), the differing geometries yield different bubble and liquid segment lengths under similar conditions of superficial gas and liquid velocities. This is discussed further in section 2.3.5.
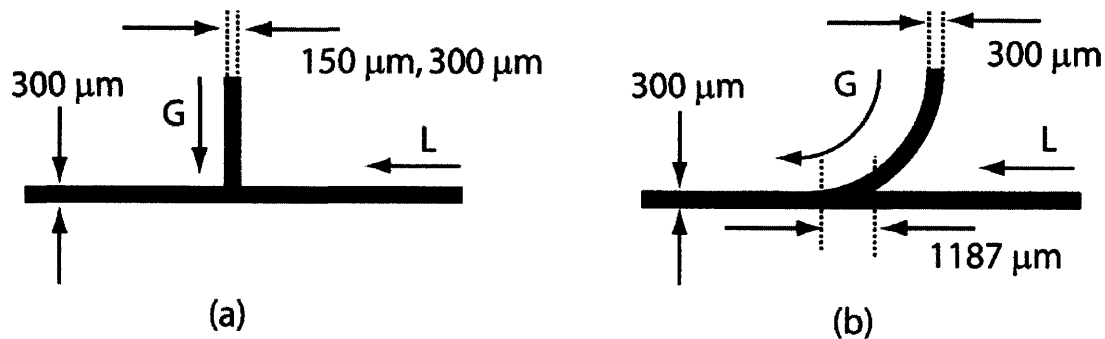
Figure 2-5 Schematics of gas inlet geometries used: (a) T-junction and (b) J-shaped inlet. Dimensions are indicated in the figure.

Figure 2-6 shows a series of real-time snapshots of gas bubble breakup in the T-junction geometry. The gas is the dispersed phase and liquid (ethanol) is the continuous phase. The breakup process begins when the gas-liquid interface advances into the main liquid flow (Figure 2-6(b)) and almost entirely blocks the channel (Figure 2-6(c)). It is important to note that since ethanol readily wets the channel walls, thick liquid menisci are present in the gas inlet as well as the main flow channel. Hence even though the growing bubble blocks the channel cross-section, a small amount of liquid still flows through the menisci. The gas bubble now starts growing in length while the gas-liquid interface situated upstream advances forward (Figure 2-6(d), (e)). The advancing gas-liquid interface narrows the neck of the growing bubble (Figure 2-6(f), (g)), until it collapses when the advancing interface contacts the wetting film on the downstream edge of the gas inlet (Figure 2-6(h)). The gas-liquid interface retracts back to its initial position after the neck collapses, and the process repeats itself. This retraction is especially prominent for the case of the 150 µm gas inlet, where the interface retracts more than 1.5 mm into the gas inlet, as shown in Figure 2-7. Retraction distance is a direct function of the ratio of main channel width to gas inlet width, and larger ratios yield larger retraction distances due to increased capillary action.
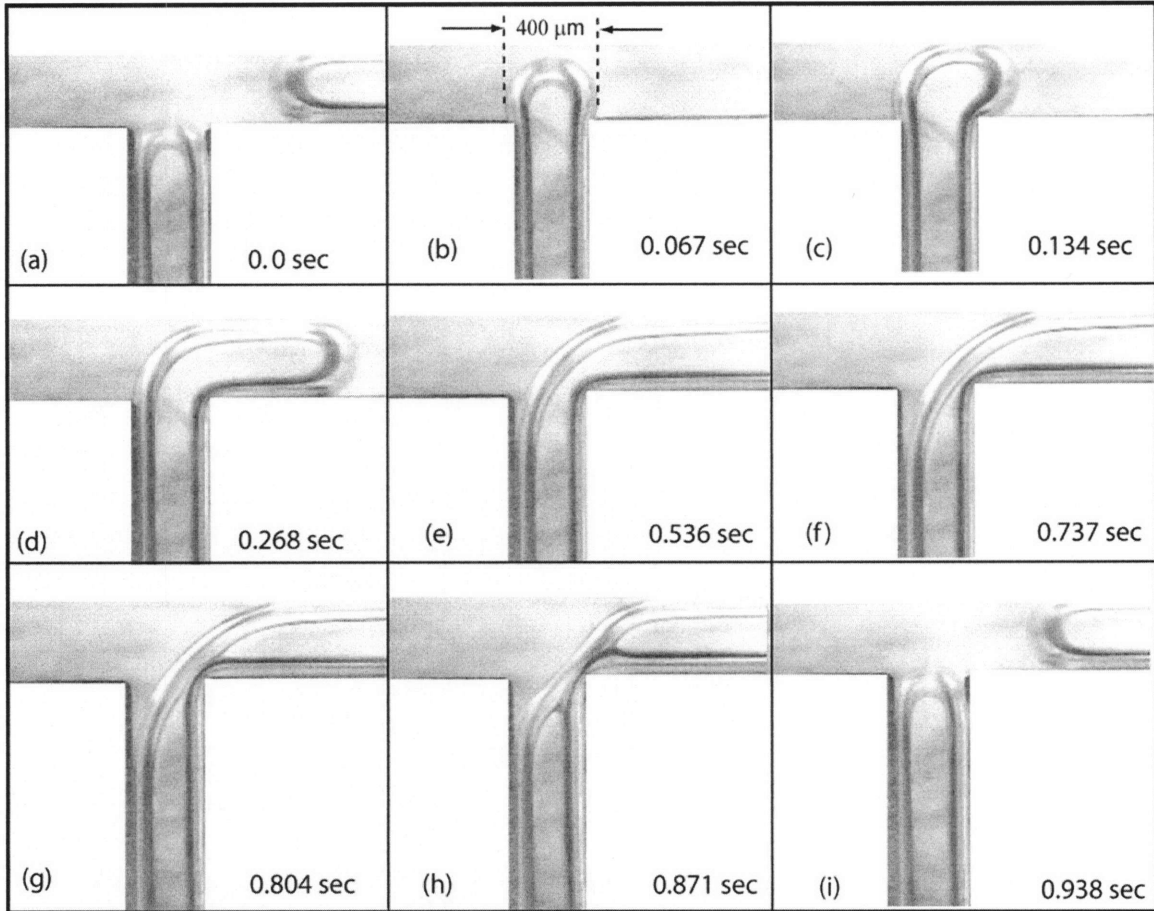
Figure 2-6 Snapshots of gas bubble breakup in a T-junction: 300 μm wide gas-inlet, Q_G = 10 μL/min, Q_L = 5 μL/min. Note the thick (~25 μm) liquid menisci present in the gas-inlet. The flow channel is 300 μm wide and 250 μm deep.

Bubble breakup in the J-shaped gas-inlet geometry also takes place through the mechanism described above, as shown in Figure 2-8. There is, however, an important difference. In general, the lengths of gas bubbles formed at the junction are dependent on both the rate of bubble growth (and hence on Q_G) as well as on the rate at which the gas-liquid interface advances across the inlet (and hence on Q_L). Since the gas-liquid interface has to travel across a greater distance in a J-shaped inlet before neck collapse occurs, under similar conditions of gas and liquid flow rates, longer bubbles (~4x) are formed in the J-shaped inlet than in the standard T-junction. Inlet geometry may therefore be used to control bubble lengths for similar conditions of superficial gas and liquid velocities. Detailed discussion of bubble and liquid segment lengths in both geometries follows in the next section.
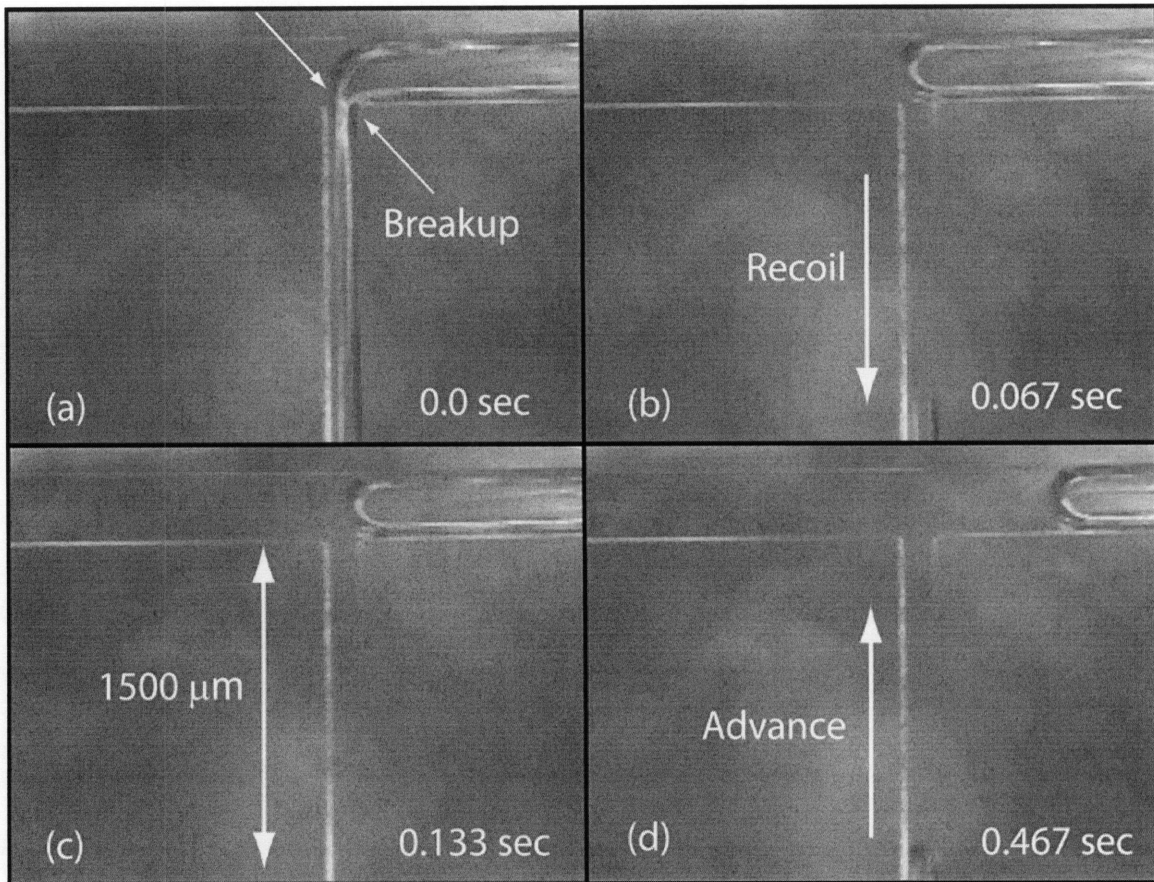
Figure 2-7 Snapshots of bubble breakup at 150 μm wide gas inlet; Q_G = 10 μL/min, Q_L = 5 μL/min. Note that the gas-liquid interface retracts more than 1.5 mm after breakup. The flow channel is 300 μm wide and 250 μm deep. Note also the presence of thin liquid 'islands' at the channel centers in regions occupied by bubbles.

Garstecki et al.[30] have recently documented breakup at microfabricated T-junction geometries for both bubbles and droplets, and presented a scaling analysis to predict the size of the dispersed bubbles or droplets as a function of flow rates of dispersed and continuous phases. They describe two regimes of bubble breakup. In the first regime, the flow rate of the liquid is much greater than that of the gas (Q_L/Q_G >10), and the resulting bubble size is essentially independent of the rates of flow of either phase. In the second regime where Q_L is comparable to Q_G, the bubble size increases approximately linearly with increasing Q_G. The crossover between the two regimes occurs at approximately Q_L= Q_G. In this study, we are interested in flow regimes where the gas to liquid flow ratio is between 0.5 to about 5, and this range falls into the linear regime described by Garstecki

et al.[30] In addition to gas bubble lengths, we also measure the lengths of liquid segments between bubbles and explain the observe trends in the following section.
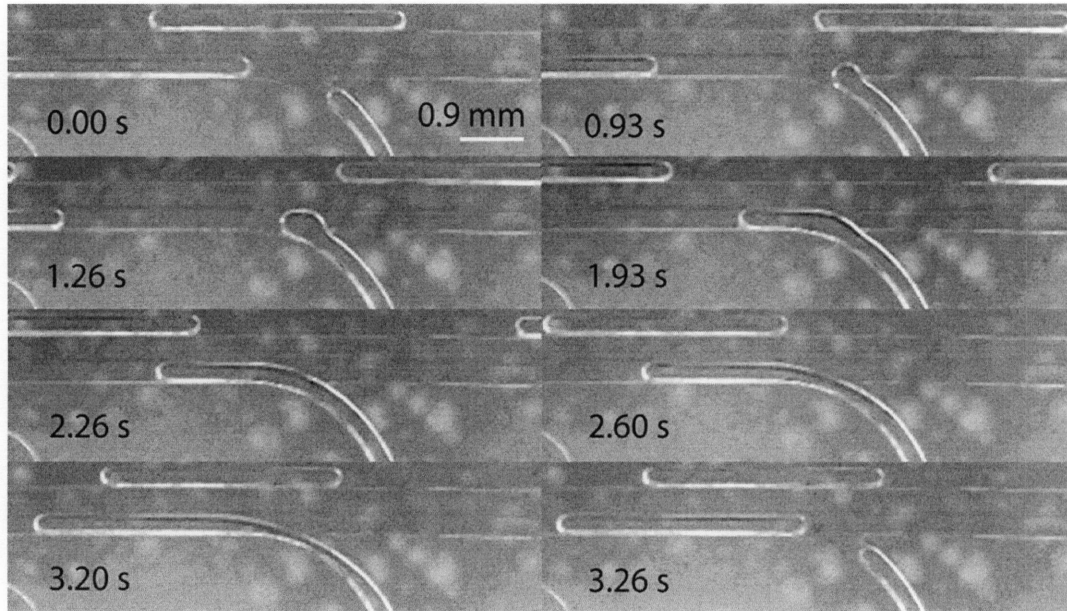
Figure 2-8 Snapshots of break-up in J-shaped tangential gas injection. Q_G = 5 µL/min, Q_L = 6 µL/min. The flow channel is 300 µm wide and 250 µm deep.

2.3.5 Bubble and slug lengths

In this section, we present bubble and liquid segment length measurements for two inlet geometries (T-junction and J-junction) at several different gas-liquid flow ratios. We captured a series of consecutive stereomicroscope images for each flow condition and analyzed the bubble and liquid segments as shown in Figure 2-9. Bubble length was measured from the upstream bubble tip to the downstream one, and liquid segment length was measured as the distance between the leading and trailing tips of two consecutive bubbles. At least 50 consecutive bubbles and liquid segments were measured for each condition.

Figure 2-9(b) shows a graphical summary of bubble and liquid segment lengths for breakup from a J-shaped gas inlet. For a given Q_L, bubble length increases linearly with Q_G while liquid segment length decreases non-linearly with Q_G. We perform non-linear least squares regression and fit the liquid segment data to a power law function of the following type:

$$L_L = A \left(\frac{Q_G}{Q_L} \right)^{-n} \tag{2.5}$$

where L_L is the liquid segment length (in μm), and A, n are the two fitting parameters. The n values obtained using the Levenberg-Marquardt method are summarized in Table 2-1.
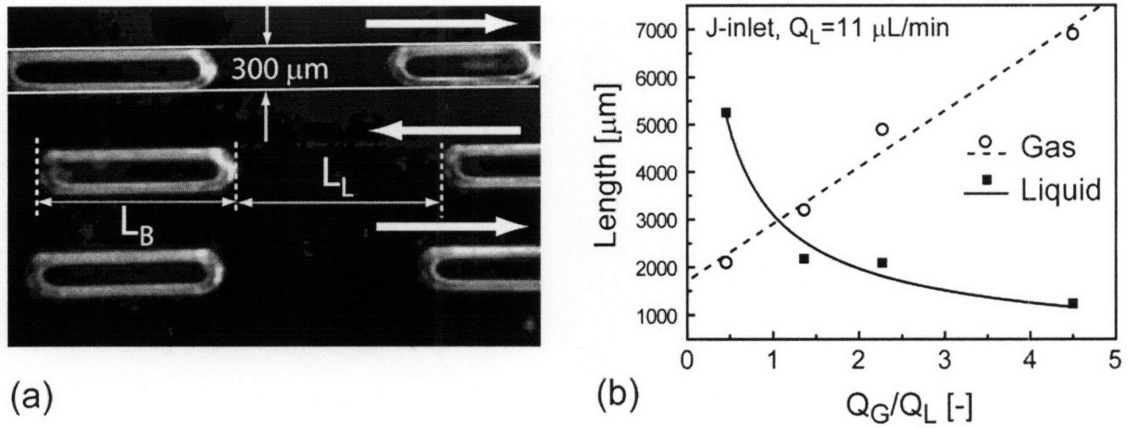
Figure 2-9 (a) Typical stereomicrograph used for measurement of bubble and liquid segment lengths. Thick arrows represent alternating flow direction due to the serpentine nature of the channel. The microchannels used in this study were 3 m long and 300 μm wide and approximately 250 μm deep (b) Gas and liquid segments lengths (mean values) measured for breakup at a J-junction ($Q_L = 11 \mu L/min$). The dotted line is a linear fit to the gas bubble length data and the solid line is a power-law fit to the liquid segment data. Further details in the text.

Figure 2-10 summarizes the same measurements for a 300 μm wide T-junction gas-inlet. Similar trends to the J-inlet are observed for both liquid segments and gas bubbles. Comparing the raw data from Figure 2-10 to those in Figure 2-9(b), we observe that the J-shaped gas inlet yields bubble and liquid segment sizes nearly *double* those in the T-junction at comparable Q_L and Q_G. Gas inlet geometry may therefore be used as a means of tuning bubble and liquid segment sizes under similar flow conditions, as previously noted in 2.3.4. Table 2-1 summarizes the results of non-linear least squares fitting performed on the data in Figure 2-10(a) using Equation (2.5). In the following paragraphs, we analyze and explain the physical mechanisms underlying the observed trends.

51
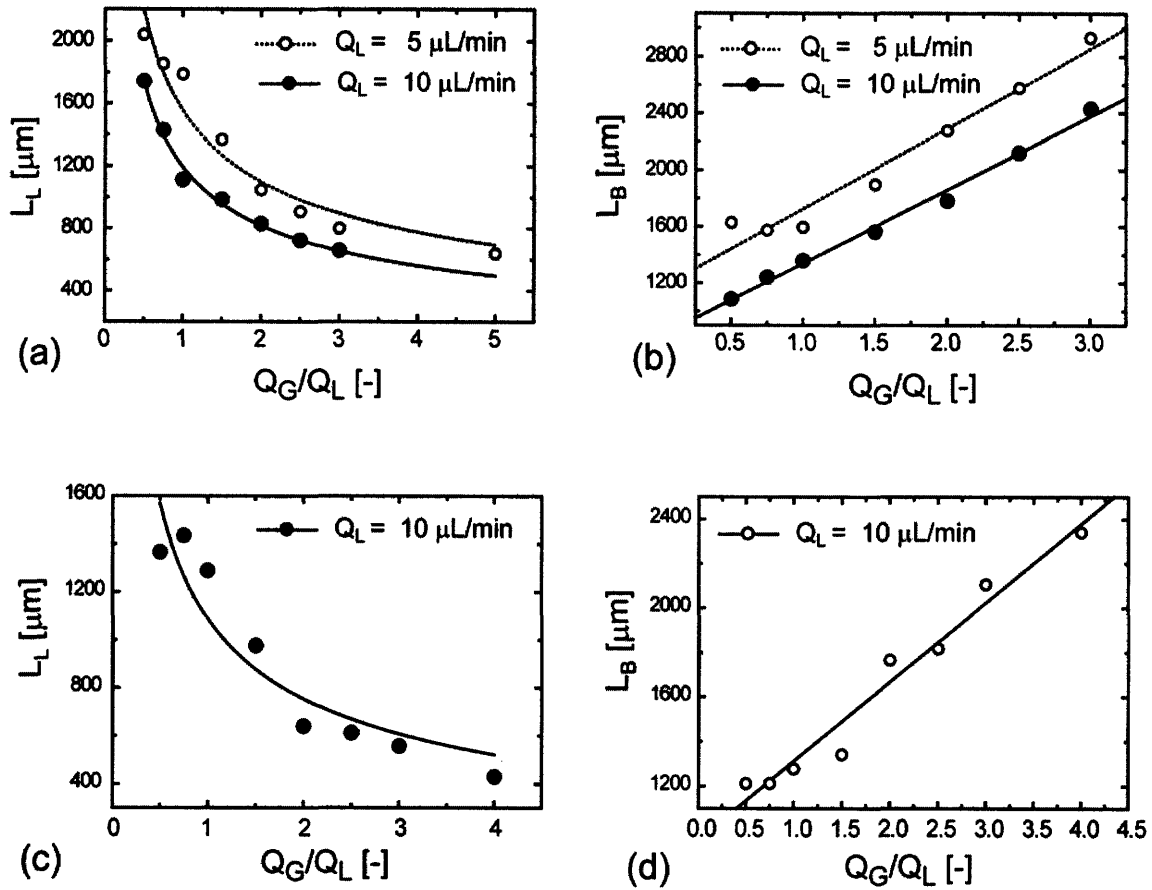
Figure 2-10 Graphs of liquid segment (L_L) and gas bubble (L_B) lengths (mean values) for breakup at T-junction for 300 μm wide gas inlet ((a),(b)) and for 150 μm wide gas inlet ((c),(d)) Solid lines are power-law fits to the data in (a) and (c) and are linear fits to the data in (b) and (d). Further details in the text.

Q_L (μL/min)	n
5 (T, 300 μm)	0.500 ± 0.054
10 (T, 300 μm)	0.544 ± 0.024
10 (T, 150 μm)	0.529 ± 0.089
11 (J-inlet)	0.610 ± 0.072

Table 2-1 Summary of non-linear fitting of data in Figure 2-9(b) and Figure 2-10 to Equation (2.5)

Bubble length increases linearly with Q_G, for all values of Q_L used in the study. The dependence is of the type:

$$L_B = A + B\left(\frac{Q_G}{Q_L}\right) \tag{2.6}$$

where the constant A varies between 400 to 600 μm for the T-junction. To explain these trends, we revisit the breakup mechanism described in 2.3.4 (Figure 2-6, Figure 2-7 and Figure 2-8). Bubble growth and breakup take place in two stages. In the first stage the gas-liquid interface advances from the gas-inlet into the main flow channel, and a symmetric gas bulb (>400 μm) fills the microchannel cross section (Figure 2-6(b)). This explains the presence of the constant term A in Equation (2.6). Following this, in the second stage of growth, the gas-liquid interface at the downstream end starts advancing upstream. During this stage, the bubble elongates at a rate proportional to Q_G and leads to the presence of the second term in Equation (2.6). Growth proceeds until the gas-liquid interface neck snaps at the downstream edge of the gas inlet.

The ratio of bubble length to liquid segment length (L_B/L_L) is consistently *larger* than the ratio of Q_G to Q_L, and this discrepancy increases with Q_G/Q_L. This is explained by the fact that adjacent liquid segments are connected by thick menisci (~30 μm size) in the channel corners under all flow conditions (2.3.2). The microchannel volume occupied by these menisci increases with Q_G/Q_L, leading to a corresponding increase in L_B/L_L well beyond the value of Q_G/Q_L. For a fixed value of Q_L, liquid segment length L_L decreases with Q_G, and the dependence is of the form given by Equation (2.5). Meniscus thickness scales as $Ca^{2/3}$. For fixed Q_L, meniscus thickness therefore scales approximately as $Q_G^{0.6}$. In addition, the lengths of the regions occupied by the menisci scale as Q_G. Hence the total volume of the menisci scales approximately as $Q_G^{1.6}$. This provides a possible explanation for the observed decreasing trend of L_L with Q_G. Increasing meniscus volume scaling as $Q_G^{1.6}$ implies decreasing liquid segment length with approximately the same scaling (i.e. $Q_G^{-0.6}$).

2.3.6 Size oscillations and pressure drop

In this section we describe the effect of two phase flow pressure drop on the stability of gas-liquid segmented flow in microchannels. Since we work at low superficial gas and

liquid velocities, all our experiments are conducted with syringe pump driven liquid and gas flows. It is possible to obtain perfectly uniform, non-coalescing monodisperse flows with less than 5% variation in bubble and liquid segment length distributions. Examples of uniform distributions at different liquid and gas flows are presented in Figure 2-11. However, under certain conditions of operation, large oscillations in bubble size are observed, and the amplitude of these oscillations increases with Q_G/Q_L. In this section we discuss the conditions to obtain both kinds of flows: steady and oscillating, the origin of oscillations and approaches to reducing their amplitude.
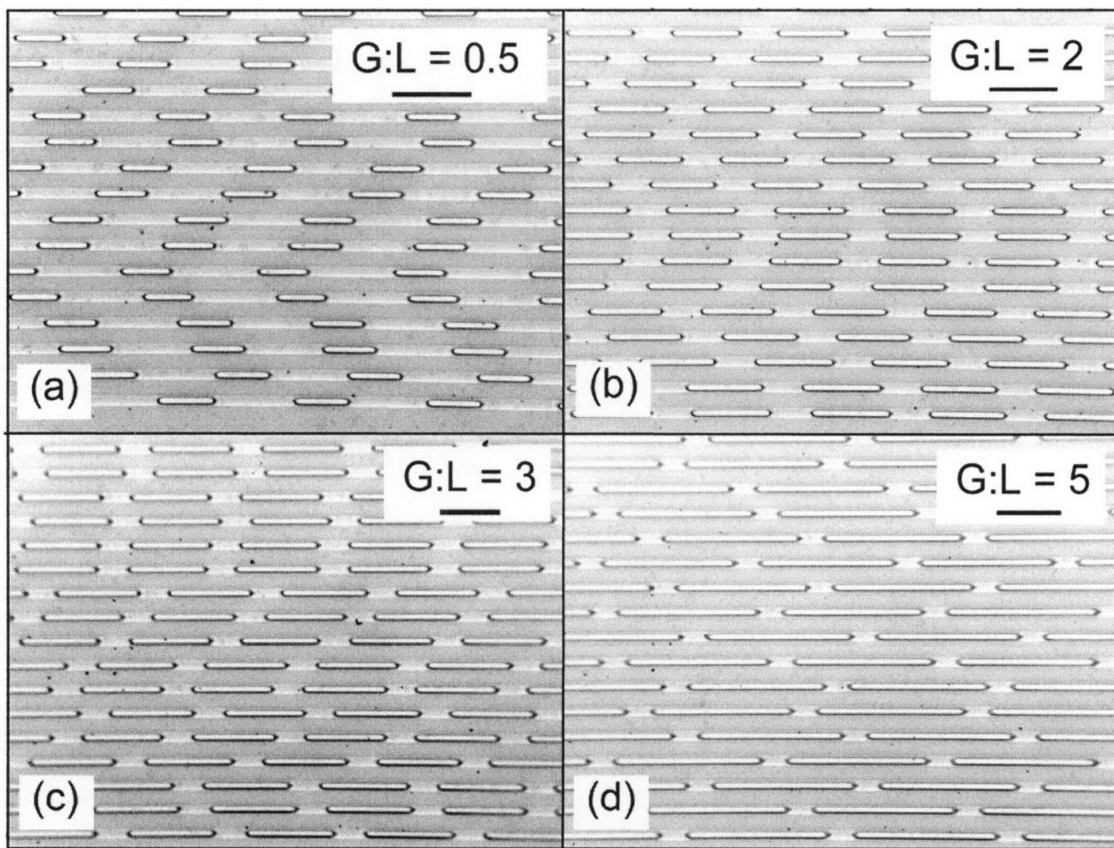
Figure 2-11: Uniform bubble flow in microfluidic devices. Q_L=5 µL/min, various Q_G. Scale bar in each case corresponds to 2 mm.

Figure 2-12(a) is a graphical summary of bubble size oscillations for a fixed Q_L of 15 µL/min and three different gas flow rates for a 300 µm T-junction gas-inlet. We measured the length of 50 consecutive bubbles at the gas inlet and bubble length was plotted as a function of bubble serial number. Oscillations in bubble size are observed for

all three gas flow rates, and the amplitude of the oscillations increases from less than 200 μm for Q_G=7.5 $\mu L/min$ to about 1000 μm for Q_G=45 $\mu L/min$. Similar measurements were made for all the flow conditions of 2.3.5, and the same trends were observed. Figure 2-12(b) summarizes both liquid and gas phase oscillations for Q_L=5 $\mu L/min$ and Q_G=10 $\mu L/min$. Liquid segment size oscillates with the same frequency as gas bubble size, with am amplitude less than 200 μm.

Figure 2-12 Observed oscillations in size of consecutive bubble and liquid segments (a) Bubble size oscillations for Q_L=15 µL/min and different Q_G. Oscillation amplitude increases with Q_G (b) Bubble and liquid segment size oscillations for Q_L=5 µL/min and Q_G=10 µL/min. Liquid segment size oscillates with the same frequency as gas bubble size, with an amplitude less than 200 µm.

To explain the origin of the oscillations, we note the details of the experimental setup in Figure 2-13(a). Gas was delivered from a syringe (25 mL Hamilton 1025 TTL) with an inner diameter of 23 mm. The syringe was interfaced to the microfluidic device via capillary tubing and a high pressure union (Upchurch Scientific, 250 µm through-hole). Two tubes were used (labeled Tube 1 and Tube 2 in Figure 2-13(a)), one from the syringe

to the union (Tube 1), and the other from the union to the device (Tube 2). The tube 1 material used was either PTFE or PEEK (1/16-in o.d.) The presence or absence of oscillations was critically dependent on the inner diameter of tube 2. In this study, tube 2 had an inner diameter of 65 μm or 500 μm (1/16-in o.d., PEEK) and a length of 10 mm. Large oscillations in bubble sizes were obtained for the 500 μm tube, and not for the 65 μm tube (Figure 2-13).
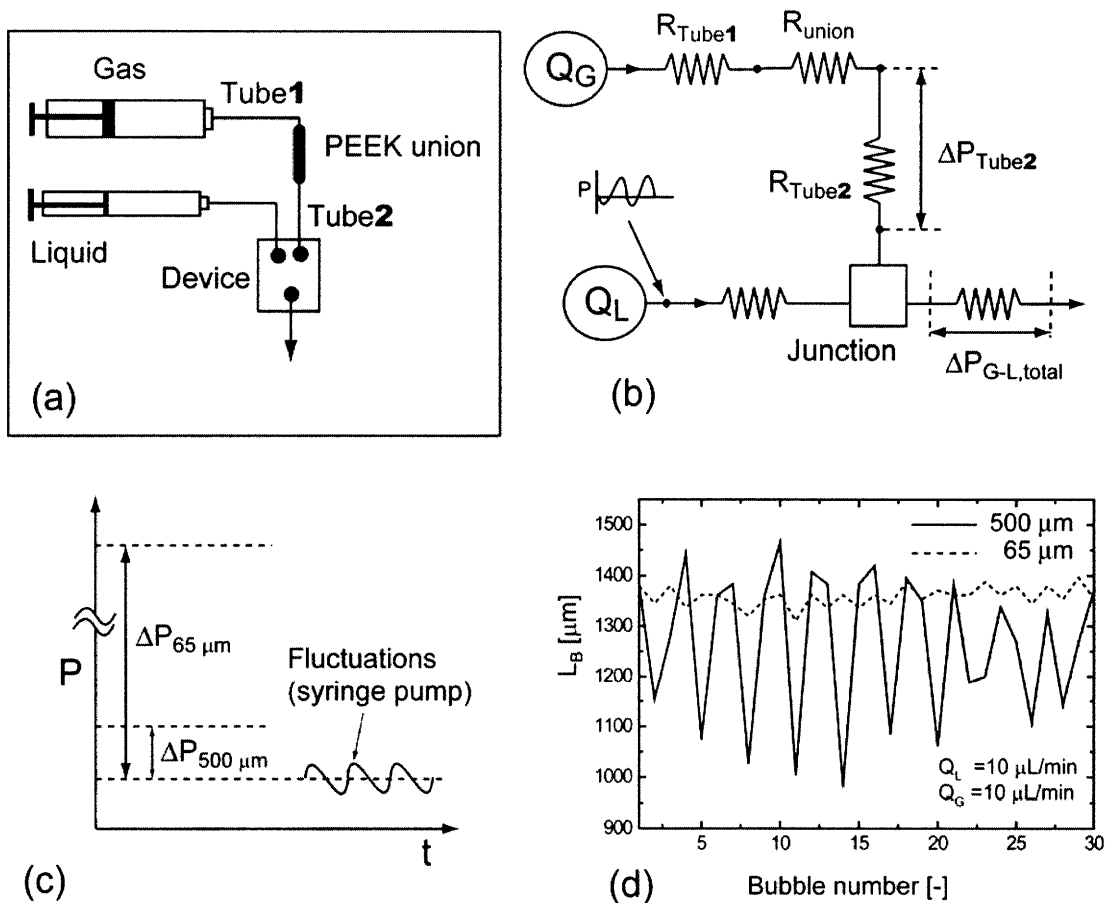
Figure 2-13 (a) Experimental setup showing how the gas syringe is connected to the device through a union and capillary tubing. (b) Equivalent circuit model of the gas-liquid flow device. (c) Illustration of how the change in diameter of tube 2 affects pressure drop and sensitivity to fluctuations (details in text). (d) Graph comparing bubble size oscillations for two different inner diameters (500 μm and 65 μm) of tube 2, at the same Q_G and Q_L.

An equivalent circuit model of the fluidic systems is schematically depicted in Figure 2-13(b). For single phase (gas or liquid flow), the volumetric fluid flow between two points in the circuit is given by the Hagen-Poiseulle equation as:

$$Q = \frac{\Delta P}{R} \qquad (2.7)$$

where R is the hydraulic resistance given by:

$$R = \frac{8\mu L}{\pi r^4} \qquad (2.8)$$

The hydraulic resistance of the tubing thus scales as the inverse fourth power of the radius. Hence the resistance (R_{65}) of the 65 μm tubing is approximately 3500 times that of the 500 μm tubing (R_{500}). For a given flow rate Q_G delivered to the device from the syringe pump, the pressure drop ΔP across the 65 μm tube is therefore 3500 times larger than across the 500 μm tubes. This makes the 500 μm tube much more sensitive to fluctuations in pressure downstream from it. Extreme sensitivity to environmental fluctuations is a key criterion for a non-linear dynamical system exhibiting chaotic behavior. Such fluctuations may arise, for example, from the syringe pump delivery of liquid into the microfluidic device as is the case in this study (Figure 2-13(c)). Even small pressure fluctuations in the pumping mechanism will immediately transfer to the gas inlet due to the incompressibility of the liquid, resulting in a corresponding fluctuation in gas flow rate, and hence bubble size. Figure 2-13(d) is a graph comparing bubble size oscillations in the two cases outlined above, at the same Q_G and Q_L. As seen in this figure, large oscillations are seen in the case of the 500 μm tube, with maximum amplitude approximately ten times that in the case of 65 μm tube.

To explain the increasing amplitude of oscillations with Q_G for a given Q_L, we calculate the pressure drop of gas-liquid segmented flow through our devices. Figure 2-14 is a schematic illustration of the calculation technique.
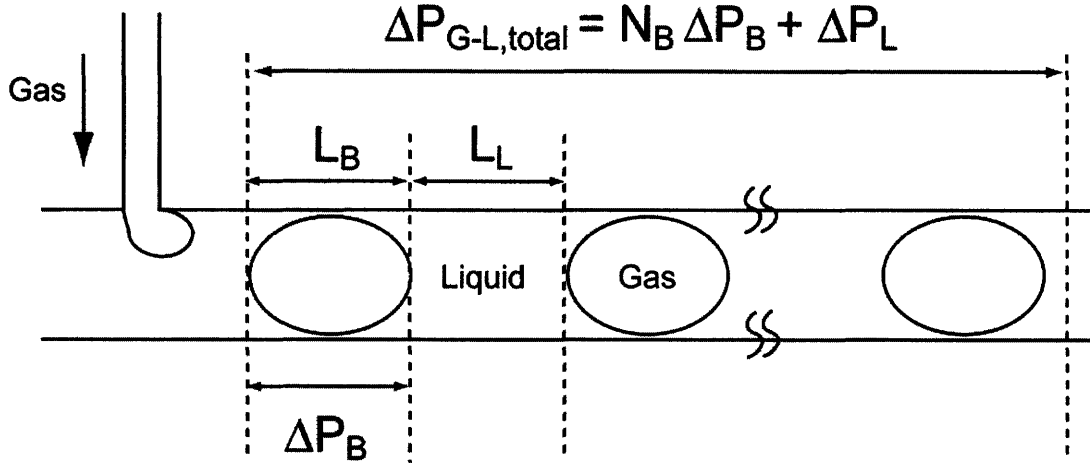
Figure 2-14 Gas-Liquid pressure drop calculation: Total pressure drop is a sum of pressure drops of individual bubbles (ΔP_B) and the total liquid phase pressure drop (ΔP_L).

In the following, we follow the approach of Stark and Manga, who modeled bubble train flows inside tubular networks of circular cross-section.[31] The pressure drop across a single bubble is given by an expression first developed by Bretherton[32]:

$$\Delta P_B = 3.58 \left(\frac{\sigma}{r_E} \right) (3Ca)^{\frac{2}{3}} \tag{2.9}$$

In the above expression, we assume the tube to be of circular cross section, an upper bound for bubble pressure drop. Due to the presence of large menisci in the rectangular cross-sectional microchannels (2.3.2), the pressure drop across a bubble is lower than that for the corresponding circular case.[29] The equivalent radius r_E for a rectangular microchannel of width w and height h is given by:

$$r_E = \frac{d_E}{2} = \frac{1}{2} \left(\frac{128wh^3}{\pi K} \right)^{\frac{1}{4}} \tag{2.10}$$

where K is a constant that depends on the aspect ratio w/h. For example, for $w/h=1.5$, K is 20.43. The bubble velocity used in the calculation of Ca is approximated (with little error) as the total gas-liquid superficial velocity:

$$U_b = \frac{Q_L + Q_G}{wh} \tag{2.11}$$

Liquid phase pressure drop is estimated by the Hagen-Poiseulle equation for laminar flow in a microchannel as follows:

$$\Delta P_L = \frac{8 \mu Q_L (\varepsilon_L L)}{\pi r_E^{4}} \qquad (2.12)$$

The number of bubbles present inside the microchannel is calculated as:

$$N_B = \varepsilon_G \frac{L}{L_B} \qquad (2.13)$$

where ε_G and ε_L are the void fractions respectively of gas and liquid phase, given by:

$$\varepsilon_G = \frac{Q_G}{Q_G + Q_L} \; ; \; \varepsilon_L = \frac{Q_L}{Q_G + Q_L} \qquad (2.14)$$

L in equations (2.12) and (2.13) is the total microchannel length. L_B is the length of a single bubble, and is taken from experimental data for each condition. The total gas-liquid pressure drop is calculated as:

$$\Delta P_{G-L,total} = N_B \Delta P_B + \Delta P_L \qquad (2.15)$$

The results of such a calculation for two different conditions are summarized in Figure 2-15. For a given Q_L, the pressure drop is found to *decrease* with increasing Q_G. This is primarily due to the fact that single bubble pressure drop given by equation (2.9) is independent of bubble length, and hence overall pressure drop is a function of the total number of bubbles present in the microchannel, which decreases at high Q_G, where fewer, longer bubbles are obtained (Figure 2-11). The calculated pressure drop is quite low (~0.075 bar) and decreases by about 30% from a gas to liquid ratio of 0.5 to 3.0. Higher Q_L leads to higher pressure drops, due to increased liquid velocity.

The decreasing trend of gas-liquid pressure drop with increasing gas flow rate at constant liquid flow rate therefore explains the general observations of Figure 2-12. As the gas flow rate is increased, the system becomes much more sensitive to any pressure fluctuations, such as those from the liquid side syringe pump delivery (Figure 2-13(b) and(c)), thus leading to oscillations of bubble size with larger amplitude than at lower gas flow rates. We note that oscillations may therefore be significantly damped by the use of pressure-driven liquid flow using, for example, a pressurized liquid container. In general, uniform non-coalescing bubble distributions will be obtained when the effect of external fluctuations is minimized, by working under high two-phase pressure-drop conditions (long microchannels) and with narrow diameter tubing at all the gas inlets.
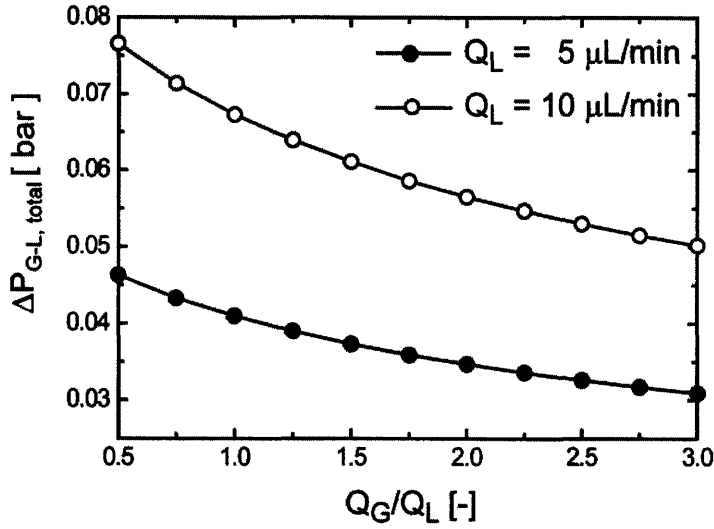
Figure 2-15 Gas-liquid pressure drop calculated for a 300 μm wide, 250 μm deep and 3 m long channel, Q_L= 5 μL/min and 10 μL/min.

2.3.7 Generating uniform bubble flows: Startup procedure

In this study, gases and liquids were delivered to the microfluidic devices using syringe pumps, as mentioned previously. At conditions of low superficial gas-velocities, the pressure required in the gas delivery line for stable, uniform segmented flow was too low (<5 psig) to control reliably using pressurized cylinder delivery. We therefore used syringe pumps to deliver gas, since very low volumetric flow-rates and gas pressure could be reliably handled with these. We followed a series of startup steps to attain uniform segmented flows, and each step had an associated time-scale. We describe the various steps and time-scales in this section.

Initially, before the gas or liquid flow was started, the entire setup of Figure 2-2 was at atmospheric pressure. Gas flow was first started to pressurize the gas line. Typically, gas flow-rates (~500 μL/min) much higher than the final desired rates were used. Gas flow was observed at the outlet once the gas line had enough built-up pressure to overcome the pressure drop of gas flow through empty microchannels. The time-scale (τ_1) for gas line pressurization was experimentally observed to be:

$$\tau_1 = \frac{1}{2}\frac{V_{0,s}}{Q_G} \qquad (2.16)$$

61

$V_{0,S}$ is the starting volume of the syringe and Q_G is the initial volumetric gas flow rate. This expression essentially gives the time required for the syringe volume to decrease to 50% of its starting volume. For example, for a starting syringe volume of 10 mL, and gas flow rate of 500 μL/min, this time scale was approximately 10 min.

Liquid flow was started at a rate equal to or near the final desired rate (~10 μL/min) when regular gas bubbling was observed at the outlet. Liquid segments were immediately formed, and flowed in succession through the microchannels. The first few segments were observed to thin and eventually disappear along the channel since that liquid was used to wet the (initially dry) microchannel walls. An unstable segmented flow was observed once the entire microchannel was filled with alternating liquid segments and gas bubbles. This flow comprised of thin liquid segments (shorter than one channel width) separated by very long gas bubbles (>50 mm). The time scale (τ_2) for this initial segmented flow condition was observed to be about two reactor residence times:

$$\tau_2 = 2\frac{V_R}{(Q_L + Q_G)} \tag{2.17}$$

V_R is the total reactor volume and Q_L and Q_G are volumetric flow rates. For example, for a typical reactor volume of 250 μL and liquid and gas flow rates of 5 and 500 μL/min respectively, this time scale was approximately 2 min.

At this stage, the gas flow was reduced to the final desired value and allowed to stabilize to its final condition. The time scale (τ_3) for this final segmented flow condition was once again observed to be about two reactor residence times (given by Equation (2.17)). For a final gas flow rate of 5 μL/min, τ_3 was approximately 50 min. An additional 15 min were provided in all experiments to ensure attainment of stable flows.

2.3.8 Liquid-phase velocity profiles

We performed μ-PIV measurements by seeding the working liquid ethanol with 1 μm diameter polystyrene particles (carboxylate-modified microspheres, nile red, Molecular Probes) and imaging through 10X (depth of field 11.2 μm) and 20X (5 μm) air objectives. A series of 200 image pairs was obtained with a time delay of 1 ms between the first and the second frames. Vector fields were obtained by locally cross correlating the image pairs with a spot size of 128 x 128 pixels and 50% overlap (64 pixels) resulting in 20 x 15

velocity vectors for each image pair in the plane. Since the cameras field of view (FOV) contained not only the desired particle intensities within liquid segments, but also reflections from gas-liquid interfaces, gas segments, and locations outside of the microchannel walls, a validation step was required to remove spurious (erroneous) velocity vectors. Locations outside the microchannels were detected by averaging the intensities of all acquired images. Since the gas and liquid segments were randomly distributed within the channel, the channel was characterized by a significantly higher intensity in such an averaged distribution, and an intensity threshold reliably excluded locations outside of the microchannel walls. Spurious vectors within the channel, typically associated with reflections at the gas-liquid interfaces or within gas bubbles, were excluded using criteria described by Westerweel.[33]

Figure 2-16 shows fluorescent micrographs (top, one frame of an image pair), and the corresponding velocity fields (center) and contour lines for the stream function inside a liquid segment when passing through the straight channel sections in design 1 (Figure 2-16(a)) and the meandering sections in design 2, (Figure 2-16(b)). The bulk velocity in the liquid segment was subtracted for velocity vector and streamline plots to reveal the recirculation motion. The maximum velocity in the direction normal to the flow, a measure of the recirculation motion, was found to be approximately 25% of U_{bulk}.

The velocity vectors and streamline contours obtained for the straight-walled channels at a gas flow rate of 30 µL/min and a liquid flow rate 10 µL/min show an overall symmetry with respect to the channel center (Figure 2-16(a)). The recirculation motion and the stagnation points found in the streamline contours are consistent with Taylor's prediction and shows that mixing improvement would be expected for segmented gas-liquid flow. However, they also indicate that even though the walls are parallel, slightly non-symmetric flow fields can be observed. We attribute this effect to the compressibility of the gas phase and the micron sized roughness of the channel side walls which becomes important when walls are only partially wetted. It marks a distinct difference to the strictly symmetric patterns observed in segmented liquid-liquid (droplet) flows through straight microchannels.[21]

As expected, non symmetric liquid velocity fields with respect to the channel centerline are obtained when the channel walls bend, i.e., for design 2. Figure 2-16(b)

shows the velocity vectors and streamline contours corresponding to such a segmented gas-liquid flow (The projection of the liquid bulk velocity to the mean flow direction was subtracted locally). From the (typically 200) instantaneous velocity fields obtained for each flow condition we observed that streamlines in the recirculation region were not closed, consistent with an increased three-dimensional nature of the recirculating flow. Further, statistical information on the length of liquid and gas segments can be obtained from the set of instantaneous fluorescence images.

inverted fluorescence image

velocity vector field

velocity streamlines

(a)

(b)
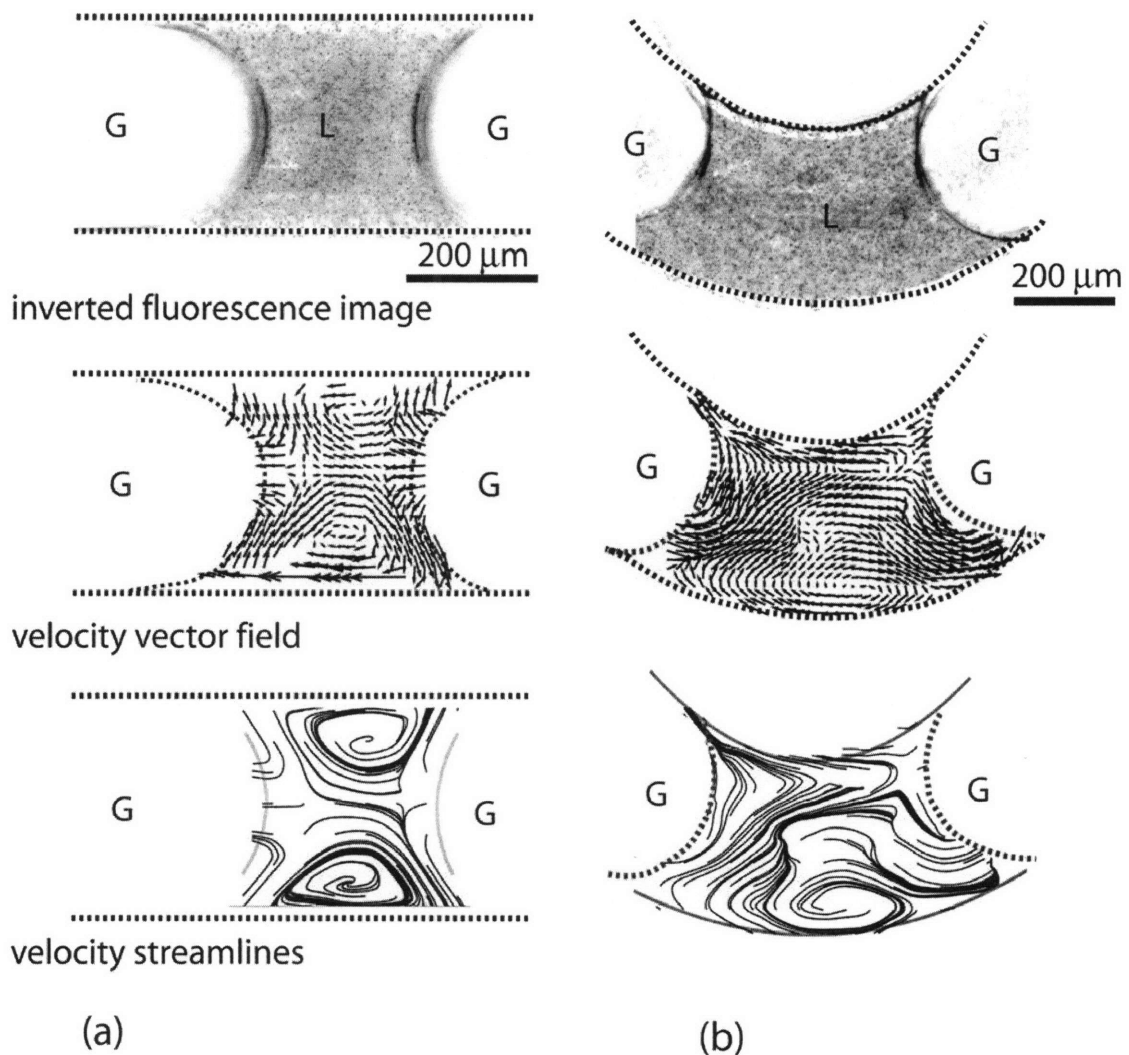
Figure 2-16 Representative fluorescence micrographs (inverted) showing liquid segments (top), the corresponding velocity vector fields (center), and streamline contours (bottom) from µPIV measurements of gas (G) - liquid (L) flow in design 1, (a), the straight channel design (G: 30 µL/min, L: 10 µL/min), and (b), the meandering channel design 2 (G: 70µL/min, L: 10 µL/min). A series of 200 dual-frame images was acquired and the bulk velocity of the liquid was subtracted in both cases. Flow through the channels with rectangular cross sections (w = 400 µm, depth = 150 µm, d_h = 220 µm) is from left to right, and the curvature radius of channel center line for (b) is 600 µm at the air and ethanol flow rates: 30 µL/min (j_G = 8 mm/s), 10 µL/min (j_L = 3 mm/s).

2.3.9 Liquid-liquid mixing by segmented flow‡

We now take advantage of the recirculation motion inside the liquid segments to enhance mixing between two miscible liquid streams. We inject gas into the co-flowing liquid streams to be mixed. One advantage of this continuous mixing strategy over several microfabricated chaotic mixers[34,35] and over mixing in individual liquid segments[36] is that it does not require any patterning of wall surfaces. As an example of this procedure, a segmented flow between an air stream (30 μL/min) and a fluorescently labeled ethanol stream (10 μL/min) is initially formed (Figure 2-17). A red labeled (Rhodamine B) ethanol stream (1 μL/min) is injected into the segmented flow with a hundredfold higher tracer concentration than in the initial liquid stream through a 50 μm wide side channel. Representative instantaneous images (Figure 2-17(a)) show the streamwise evolution of the concentration field inside a liquid segment at the location of tracer injection and for the downstream distances x / d_h of 10 and 20. Only several tens of hydraulic channel diameters (d_h) are required to observe a homogenization of the tracer concentration. It is apparent that for design 1 transport takes place across the center line, a confirmation of the non symmetry of the flow field already observed from the velocity field (Figure 2-17(a)). Figure 2-17(b) shows the corresponding results for the meandering channel design 2 (b) at three locations $x/d_h = 0$, 13, and 26. Consistent with the increased non symmetry of the flow with respect to the channel centerline (Figure 2-17(b)), we observe that the channel length required to homogenize the concentration field further decreases.

In order to quantify mixing lengths, time-resolved confocal scanning microscopy measurements were performed. We define the normalized mixing length x_{90}/d_h as the distance along the flow channel at which 90% homogeneity in the concentration field is achieved. Confocal microscopy allowed exclusive collection of local fluorescence intensities from a narrow plane through the liquid segments instead of sampling fluorescence intensities from the entire depth of the entire channel (as in the case of wide-field microscopy). These measurements are not the focus of this chapter and are reported elsewhere.[37] Figure 2-17(c) shows mixing lengths obtained following this procedure for

---

‡ This study was conducted in collaboration with Dr. Axel Günther, and for a detailed discussion and characterization of liquid-liquid mixing using inert gas bubbles we refer to his recent publication.[34]

device 1 at different superficial liquid velocities, or, Peclet numbers, $Pe = d_h j_L D^{-1}$, where D is the diffusion coefficient of Rhodamine B in ethanol,[38] $2.8 \cdot 10^{-6} cm^2/s$. For comparison, data obtained from chaotic mixers[34,35] and microdroplet flows[21,39] are included in the graph. The literature data for microdroplet mixing lengths were established with a less restrictive criterion based on time-averaged fluorescence intensities and are consistent with our segmented gas-liquid flow results. Mixing in segmented gas-liquid and liquid-liquid flows is more efficient than the homogeneous chaotic mixers.
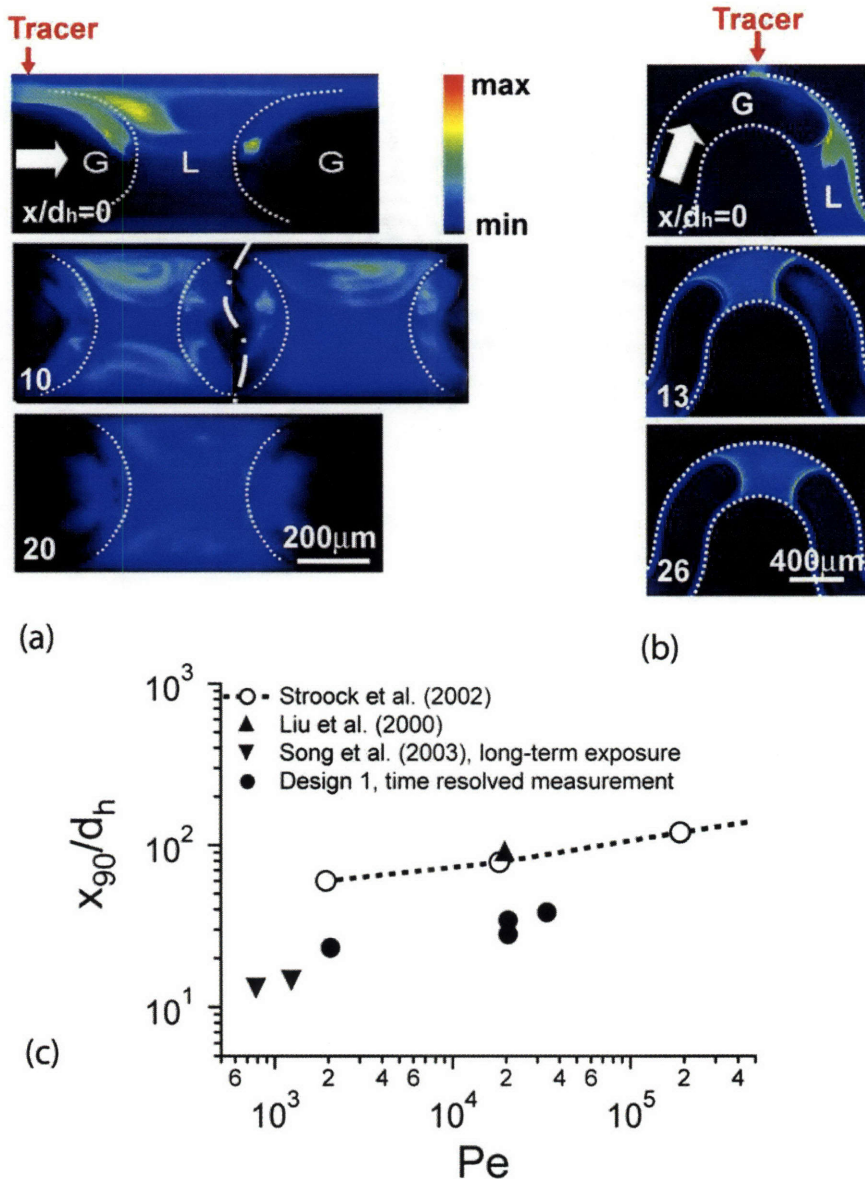
Figure 2-17 False-color images of instantaneous fluorescence micrographs for the homogenization of the concentration field in a liquid segment after continuously injecting a small amount of fluorescent tracer fluid into a segmented ethanol-air flow; (a) straight channel design 1, and (b), meandering channel design 2. Air and ethanol flow rates: 30 µL/min (j_G = 8 mm/s), 10 µL/min (j_L = 3 mm/s), microchannel depth: 150 µm, length 150 mm. (c) Mixing length x_{90}/d_h required to obtain 90% homogeneity in the concentration field for design 1. A time-resolved confocal microscopic procedure is used. Literature data for chaotic mixers or long-term exposed intensity data from a microdroplet mixer are included.

It is possible to vary the Peclet number over an order of magnitude by changing the liquid superficial velocity and adjusting the gas superficial velocity such that liquid segments of similar length are obtained. The small variation of the mixing length over

two orders of magnitude in Peclet number (Figure 2-17) has an important implication for the design of segmented flow microreactors. It implies *tunability* of micromixing time, which is not possible with conventional diffusive micromixing techniques. The mixing time is simply the ratio of mixing length (almost constant) and bubble velocity (Figure 2-4(c)). The mixing times can therefore be adjusted over at least two orders of magnitude by increasing/decreasing the gas and liquid flow rates while still preserving the segmented gas-liquid (slug) flow regime (Figure 2-17(b)). This enables flexible design of microreactors for reactions with a large range of different reaction time scales (i.e. reaction rates).

2.3.10 Planar gas-liquid separators

An apparent disadvantage of segmented flow mixers is that a two-phase mixture is produced during the mixing process. However, integration of a microfabricated capillary separator downstream of the mixing section enables the complete removal of gas from the mixed liquid stream.[37] Figure 2-18(a) shows a fluorescent micrograph of the regular ethanol-air flow in a design 1 microreactor with a 1.2 m long flow section and a capillary separator integrated at the outflow end. This simple solution does not require additional processing steps – only a modification in the lithographical mask – since the 20 μm wide capillaries are defined in the same processing step as the flow channel.

The outflow side of the capillaries is initially wetted. If a gas bubble is locally present in the flow channel, a gas-liquid-solid interface exists and the capillary pressure is sufficient to support the liquid meniscus. If a liquid segment passes by, the gas-liquid-solid interface is destroyed and liquid is drawn into the capillaries. A sufficient number of capillaries is required in order to allow liquid segments to be completely withdrawn from the mixing channel. Figure 2-18(b) shows the separation of a liquid segment in a series of subsequent fluorescent images. At the considered gas and liquid flow rates of 8 μL/min and 4 μL/min, a maximum of three (of the 16 capillaries) are active and the capacity limit is therefore far from being reached. The liquid phase is ultimately removed at the outflow side of the capillaries and the gas phase is withdrawn at the end of the flow channel.
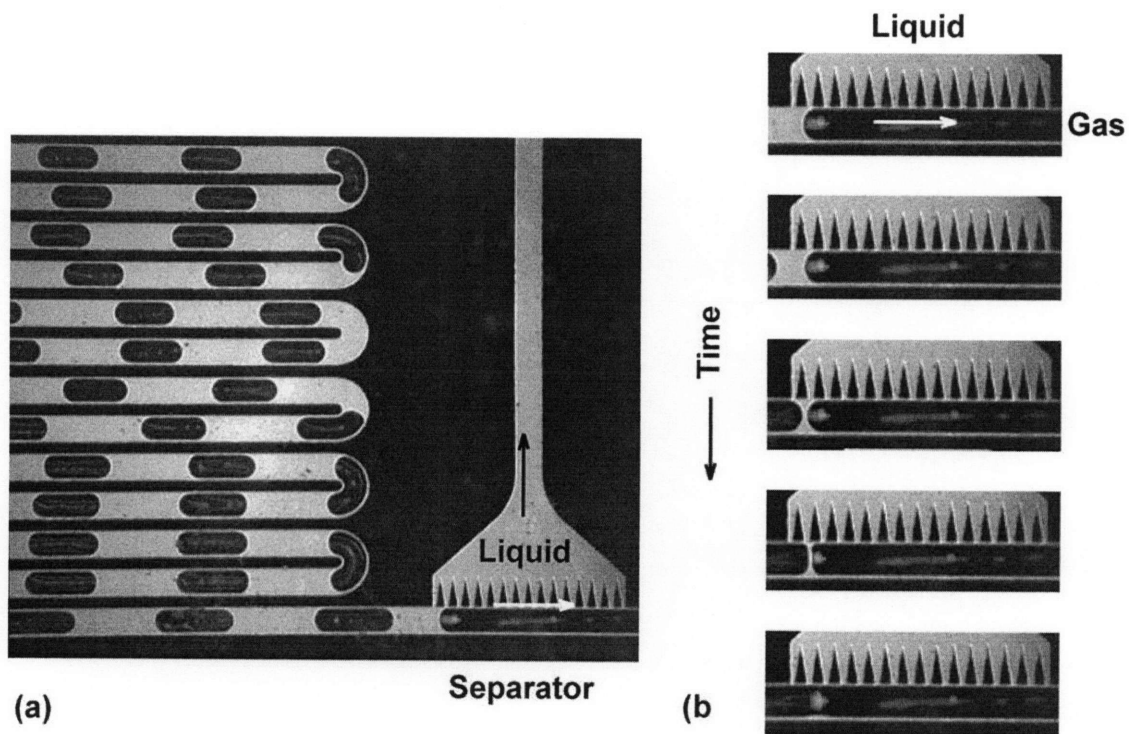
Figure 2-18 (a) Fluorescence micrograph of the segmented gas-liquid flow (gas: 8 µL/min, liquid: 4 µL/min) with the capillary separator integrated at the end of a 400 µm wide and 120 µm deep flow channel. (b) Sequence of fluorescence micrographs (temporal separation 200ms) illustrating how an ethanol segment is withdrawn through the capillary array of the planar gas - liquid separator. The separator contains 16 capillaries of 20 µm width at their tip, along which a pressure differential is applied. The gas phase remains in the flow channel and is removed at its outlet.

2.4 Summary

This chapter describes the design and operation of microfluidic devices for generating uniform gas-liquid segmented flows. Optical stereomicroscopy, micro particle image velocimetry (µPIV) and pulsed-laser fluorescence microscopy were used to characterize the dynamics and transport properties of these flows. Flow regimes, bubble and liquid segment lengths were measured for several flow conditions and inlet geometries, and the observed trends were explained. Bubble sizes exhibit oscillatory behavior under certain conditions, and this behavior was explained using considerations of single and two-phase pressure drop. The recirculation motion in the liquid segments associated with the gas-liquid flows and the symmetry of the recirculations were quantified in straight and meandering channel configurations. Surface roughness effects and the compressibility of

the gas phase induce loss of symmetry for the velocity and the concentration fields and therefore enhance mixing across the centerline of straight microchannels. Mixing is further accelerated in meandering channels by the periodically switching of recirculations across the channel center line.

2.5   References

1. Dudukovic, M. P., Larachi, F. & Mills, P. L. Multiphase reactors - revisited. *Chemical Engineering Science* **54**, 1975-1995 (1999).

2. Dudukovic, M. P., Larachi, F. & Mills, P. L. Multiphase catalytic reactors: A perspective on current knowledge and future trends. *Catalysis Reviews-Science and Engineering* **44**, 123-246 (2002).

3. AlDahhan, M. H., Larachi, F., Dudukovic, M. P. & Laurent, A. High-pressure trickle-bed reactors: A review. *Industrial & Engineering Chemistry Research* **36**, 3292-3314 (1997).

4. Chaouki, J., Larachi, F. & Dudukovic, M. P. Noninvasive tomographic and velocimetric monitoring of multiphase flows. *Industrial & Engineering Chemistry Research* **36**, 4476-4503 (1997).

5. Deckwer, W. D. *Bubble Column Reactors* (John Wiley and Sons, New York, 1991).

6. Ho, C. M. & Tai, Y. C. Micro-electro-mechanical-systems (MEMS) and fluid flows. *Annual Review of Fluid Mechanics* **30**, 579-612 (1998).

7. Stone, H. A., Stroock, A. D. & Ajdari, A. Engineering flows in small devices: Microfluidics toward a lab-on-a-chip. *Annual Review of Fluid Mechanics* **36**, 381-411 (2004).

8. Jensen, K. F. Microreaction engineering - is small better? *Chemical Engineering Science* **56**, 293-303 (2001).

9. Jahnisch, K., Hessel, V., Lowe, H. & Baerns, M. Chemistry in microstructured reactors. *Angewandte Chemie-International Edition* **43**, 406-446 (2004).

10. Zhao, B., Moore, J. S. & Beebe, D. J. Surface-directed liquid flow inside microchannels. *Science* **291**, 1023-1026 (2001).

11. Losey, M. W., Jackman, R. J., Firebaugh, S. L., Schmidt, M. A. & Jensen, K. F. Design and fabrication of microfluidic devices for multiphase mixing and reaction. *Journal of Microelectromechanical Systems* **11**, 709-717 (2002).

12. Losey, M. W., Schmidt, M. A. & Jensen, K. F. Microfabricated multiphase packed-bed reactors: Characterization of mass transfer and reactions. *Industrial & Engineering Chemistry Research* **40**, 2555-2562 (2001).

13. de Mas, N., Guenther, A., Kraus, T., Schmidt, M. A. & Jensen, K. F. Scaled-out multilayer gas-liquid microreactor with integrated velocimetry sensors. *Ind. Eng. Chem. Res.* **44**, 8997 - 9013 (2005).

14. de Mas, N., Guenther, A., Schmidt, M. A. & Jensen, K. F. Microfabricated multiphase reactors for the selective direct fluorination of aromatics. *Industrial & Engineering Chemistry Research* **42**, 698-710 (2003).

15. de Mas, N., Guenther, A., Schmidt, M. A. & Jensen, K. F. Scalable microfabricated reactors for direct fluorination reactions. *Proceedings of IEEE Transducers, Boston* (2003).

16. Zhao, T. S. & Bi, Q. C. Co-current air-water two-phase flow patterns in vertical triangular microchannels. *International Journal of Multiphase Flow* **27**, 765-782 (2001).

17. Triplett, K. A., Ghiaasiaan, S. M., Abdel-Khalik, S. I., LeMouel, A. & McCord, B. N. Gas-liquid two-phase flow in microchannels - Part II: void fraction and pressure drop. *International Journal of Multiphase Flow* **25**, 395-410 (1999).

18. Coleman, J. W. & Garimella, S. Characterization of two-phase flow patterns in small diameter round and rectangular tubes. *International Journal of Heat and Mass Transfer* **42**, 2869-2881 (1999).

19. Burns, J. R. & Ramshaw, C. The intensification of rapid reactions in multiphase systems using slug flow in capillaries. *Lab on a Chip* **1**, 10-15 (2001).

20. Link, D. R., Anna, S. L., Weitz, D. A. & Stone, H. A. Geometrically Mediated Breakup of Drops in Microfluidic Devices. *Physical Review Letters* **92**, 054503-1-0545034 (2004).

21. Song, H., Tice, J. D. & Ismagilov, R. F. A microfluidic system for controlling reaction networks in time. *Angewandte Chemie-International Edition* **42**, 768-772 (2003).

22. Taylor, G. I. Deposition of a viscous fluid on the wall of a tube. *Journal of Fluid Mechanics* **10**, 11-15 (1961).

23. Xia, Y. N. & Whitesides, G. M. Soft lithography. *Annual Review of Materials Science* **28**, 153-184 (1998).

24. Meinhart, C. D., Wereley, S. T. & Santiago, J. G. PIV measurements of a microchannel flow. *Experiments in Fluids* **27**, 414-419 (1999).

25. Wong, H. The motion of a long bubble in polygonal capillaries at low capillary numbers. *Dissertation Univertiy of California, Berkeley* (1992).

26. Wong, H., Morris, S. & Radke, C. J. 3-Dimensional Menisci in Polygonal Capillaries. *Journal of Colloid and Interface Science* **148**, 317-336 (1992).

27. Wong, H., Morris, S. & Radke, C. J. 2-Dimensional Menisci in Nonaxisymmetric Capillaries. *Journal of Colloid and Interface Science* **148**, 284-287 (1992).

28. Wong, H., Radke, C. J. & Morris, S. The motion of long bubble in polygonal capillaries. Part 1. Thin films. *Journal of Fluid Mechanics* **292**, 71-94 (1995).

29.   Ajaev, V. S. & Homsy, G. M. Modeling shapes and dynamics of confinded bubbles. *Annual Review of Fluid Mechanics* **38**, 227-307 (2006).

30.   Garstecki, P., Fuerstman, M. J., Stone, H. A. & Whitesides, G. M. Formation of droplets and bubbles in a microfluidic T-junction - scaling and mechanism of break-up. *Lab on a Chip* **6**, 437-446 (2006).

31.   Stark, J. & Manga, M. The motion of long bubbles in a network of tubes. *Transport in Porous Media* **40**, 201-218 (2000).

32.   Bretherton, F. The motion of long bubbles in tubes. *Journal of Fluid Mechanics* **10**, 166-88 (1961).

33.   Westerweel, J. Efficient Detection of Spurious Vectors in Particle Image Velocimetry Data. *Experiments in Fluids* **16**, 236-247 (1994).

34.   Stroock, A. D. et al. Chaotic mixer for microchannels. *Science* **295**, 647-651 (2002).

35.   Liu, R. H. et al. Passive mixing in a three-dimensional serpentine microchannel. *Journal of Microelectromechanical Systems* **9**, 190-197 (2000).

36.   Hosokawa, K., Fujii, T. & Endo, I. Handling of picoliter liquid samples in a poly(dimethylsiloxane)-based microfluidic device. *Analytical Chemistry* **71**, 4781-4785 (1999).

37.   Guenther, A., Jhunjhunwala, M., Thalmann, M., Schmidt, M. A. & Jensen, K. F. Micromixing of miscible liquids in segmented gas-liquid flow. *Langmuir* **21**, 1547-1555 (2005).

38.   Ko, D. S., Sauer, M., Nord, S., Muller, R. & Wolfrum, J. Determination of the diffusion coefficient of dye in solution at single molecule level. *Chemical Physics Letters* **269**, 54-58 (1997).

39.   Tice, J. D., Song, H., Lyon, A. D. & Ismagilov, R. F. Formation of droplets and mixing in multiphase microfluidics at low values of the Reynolds and the capillary numbers. *Langmuir* **19**, 9127-9133 (2003).

3 Residence Time Distribution in Microfluics†

3.1 Introduction

Microscale multiphase flows (gas-liquid and liquid-liquid) have been employed in several miniaturized chemical and biological microsystems[1,2]. Microreactors operating in segmented gas-liquid flow have been used for liquid-phase sol-gel reactions such as synthesis of colloidal silica [3] (the subject of Chapter 4) and semiconductor quantum dots[4]. As described in Chapter 2, the introduction of gas serves the dual purpose of segmenting flow and enabling mixing through recirculatory motion in the liquid segments[5]. The liquid segments behave as a succession of small batch reactors passing through a long channel, which eliminates the problem of axial dispersion as encountered in the case of single phase laminar flow reactors. However, this situation is strictly true only if adjacent segments of the phase of interest are completely disconnected from each other.

Figure 3-1 shows different possible phase distributions between the liquid phase of interest (black colored) and the segmenting fluid (white colored gas or liquid). Examples of completely disconnected flows are segmented gas-liquid flow with hydrophobic side walls (Figure 3-1 (b)), and immiscible liquid-liquid flows (Figure 3-1(c)). In this work, we consider segmented gas-liquid flow with hydrophilic walls (Figure 3-1(a)), where adjacent liquid segments are connected through thin liquid films and liquid menisci in the channel corners. The film and meniscus thickness depends on the relative magnitude of viscous to surface tension forces, the dimensionless capillary number:

$$Ca = \frac{\mu U_b}{\sigma} \tag{3.1}$$

where μ is the liquid viscosity, U_b is bubble velocity and σ is the interfacial tension.

---

† This work was done in close collaboration with Mr. Franz Trachsel, who at the time was a visiting student from ETH (Zürich), and Dr. Axel Günther, who at the time was a post-doctoral associate in Prof. Jensen's research group.
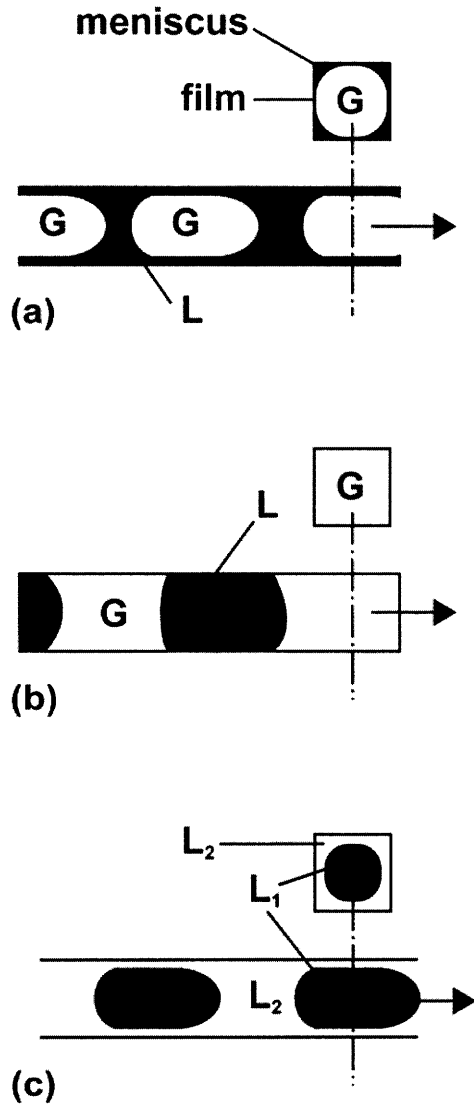
Figure 3-1 Schematic of phase distribution for (a) segmented gas-liquid flow with hydrophilic walls, (b) segmented gas-liquid or liquid-liquid flow with hydrophilic walls and (c) for liquid-liquid droplet flow at high superficial velocities. The phase of interest is colored black.

At the low capillary numbers used in this thesis ($10^{-4} < Ca < 10^{-3}$), the liquid film thickness δ in circular capillaries scales with $Ca^{2/3}$.[6-8] We consider channels with rectangular cross section that are 400 μm wide and 115 μm deep. In addition to thin liquid films, there also is confined liquid in the corners of the microchannel (menisci) that covers approximately 5.0% of the channel cross-sectional area.[9,10] In contrast, models of

circular cross-sectional capillaries predict a film thickness of 1.0 μm and a corresponding cross sectional area of only 1.5% of the channel cross section at a representative Ca = $8 \cdot 10^{-4}$.[6,7] Thus, a 2-3 fold increase in the communication between neighboring liquid slugs would be expected in rectangular channels with the considered cross section. Menisci and films allow adjacent liquid segments to intermix in the axial direction, as does the occasional merging of slugs in the microfluidic device. The communication and merging of liquid slugs is expected to widen the liquid phase residence time distribution (RTD) from the sharp peak associated with an ideal segmented flow situation. Therefore, knowledge of the prevailing RTD is required to quantify the performance of such a segmented flow reactor.

We thus address the RTD in *pressure-driven* single-phase and two-phase segmented flow in microfabricated channel networks of rectangular cross section. Dispersion in curved channels has been previously characterized for pressure driven and electrokinetic flow[11]. Low-dispersion devices with turns and junctions[12] have been designed to overcome the so-called "racetrack-effect" that is associated with a different problem, the *electro-osmotic* flow of sample analytes through devices with serpentine turns.

3.1.1 Non-ideal flow and RTD

In the classical reaction engineering literature, real systems are compared with the ideal flow cases of either completely back-mixed reactors or plug flow reactors [13]. Non-ideal flow in macro-scale multiphase reactors has been extensively characterized [14-16]. Liquid phase RTD measurements using stimulus-response techniques are common tools to evaluate the hydrodynamics of reaction systems like gas-liquid fluidized beds and bubble columns.[17,18] Tracer material is usually injected upstream as a pulse, step or periodic input function and monitored downstream. A large body of literature is devoted to the characterization of RTD in continuous reactors at steady state.[13,19-21] Recently, numerical approaches for estimating the RTD in microscale segmented flow have been undertaken.[22] However, these approaches are typically based on the simplifying assumption of circular channel cross sections that are relevant to dispersion in capillaries but neglect the substantial communication provided by liquid menisci in the corners of microfabricated channel networks with – in general – rectangular or triangular cross

sections. We therefore chose an experimental approach that allows RTD characteristics to be measured in microfluidic networks of arbitrary complexity and illustrate the method for one select flow configuration. Following the work of Levenspiel and coworkers [23], the one-dimensional axial dispersion model is used in this study to analyze the experimental RTD curves. Different solutions to this model are obtained, depending on the tracer injection technique and on the method of downstream concentration measurement used. We use a commonly employed technique which involves pulse injection of tracer followed by through-the-wall measurement of the tracer concentration near the outlet. A solution to the dispersion model under these conditions, subject to open-open boundary conditions, has been discussed elsewhere[23], and the dimensionless parameter emerging from this analysis is the vessel dispersion number $D^*/(j_L L)$, where D^* is the dispersion coefficient, j_L the superficial liquid velocity and L the channel length.

3.1.2 Miniaturized liquid injection

Miniature tracer injection devices have been previously developed for chromatography techniques[24] and separation in electro-osmotic flow.[25,26] In capillary electrophoresis (CE), small hydraulic microchannel diameters, d_h, are used. Sample volumes on the order of d_h^3 are typically produced by the on-chip electrokinetic cross-type injection technique and range from 100 picoliters to a few nanoliters. For chromatography applications, injection into a pressure-driven fluid stream is often accomplished off-chip by using miniaturized valves with sample volumes between 10 nL and 10 μL. Here we use an injection technique adopted from piezoelectrically actuated micropumps[27,28] and dispenser systems based on inkjet technology.[29-31]

3.2   Experimental

3.2.1   Tracer injector methodology

We used a microfluidic device with integrated tracer injection to characterize RTD in microfluidic single-phase and multiphase flows. A fluorescently labeled tracer pulse was injected into a liquid stream of arbitrary velocity through a transverse side stream, as shown in Figure 3-2(a). Subsequent spreading of the pulse was measured using fluorescence microscopy at three different channel lengths (Figure 3-2(b)). The

microchannel design (fabricated in poly-(dimethylsiloxane) (PDMS)) provided for a cylindrical reservoir that held the tracer material. The roof of the reservoir formed a thin membrane, which when deflected by a stacked piezoelectric bending disk element (Figure 3-2(c)), injected the tracer pulse through a transverse side channel into the main liquid channel. Piezoelectric bending disks (Piezo Systems, Inc.) with a circular cross section were sealed with 5-min epoxy (Devcon) on top of the reservoir structures in PDMS.

The maximum deflections of the piezoelectric disks (6.4 and 12.7 mm diameter) used in the injector (for an applied voltage of 170 V) were 4.7 and 19.1 μm respectively. The corresponding displaced volume for the 6.4 mm disks was approximately 0.125 μL, as obtained from finite element method calculations using ANSYS. For the considered superficial liquid velocity and residence times, the length of the initially formed pulse was seven times the channel width and 0.3% of the length of the microchannel network In the context of the overall RTD, the initial pulse approximated the ideal Dirac-δ function. The configuration of flow channels allowed the injected plug of 0.586×10^{-3} M Rhodamine B in ethanol to be observed in the same field of view (FOV) when successively passing through areas of interest (AOI) corresponding to different downstream positions (L_1, L_2, L_3).

(a)

(b)

Cross section A - A'

(c)
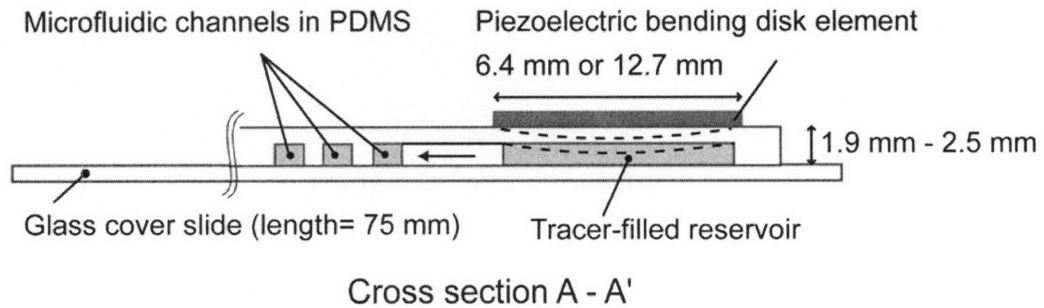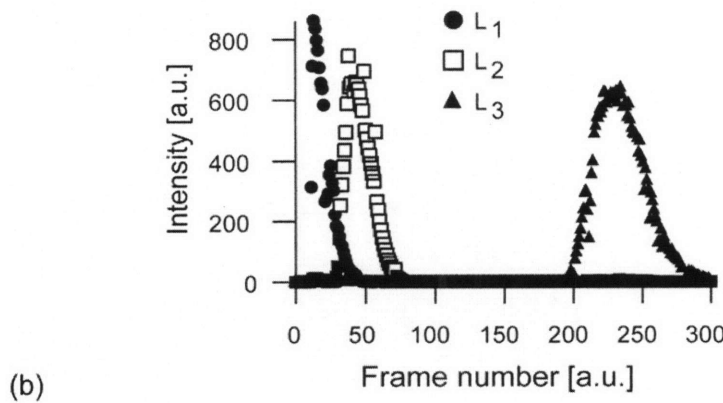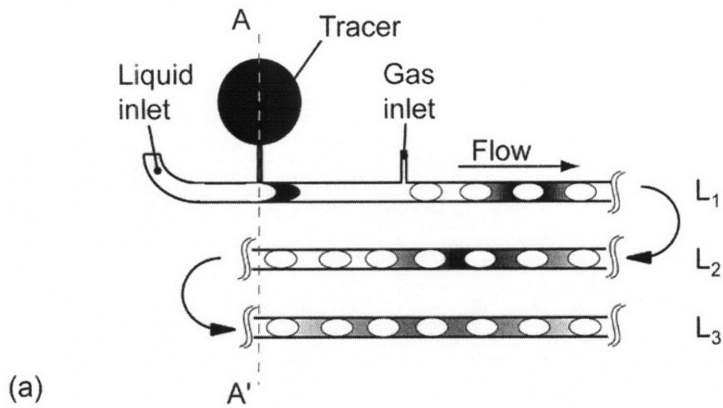
Figure 3-2 (a) Schematic of the microchannel configuration for RTD measurements. (b) Fluorescent micrographs demonstrate how the tracer spreads due to communication between neighboring liquid slugs. (c) Cross sectional schematic of the PDMS device sealed on a glass cover slide (Optical access was provided through the glass).

3.2.2 Microfluidic device design

Microfluidic devices used in this study were composed of meandering channels of rectangular cross section, 400 μm wide and 115 μm deep (d_h=178.6 μm) with bending radii of the centerline of 600 μm in the meandering sections (Figure 3-3(a) and Figure 3-3(c)). The tracer injection channels were 8.2 mm long, and their widths decreased toward the main channel from 100 to 50 μm. The fluorescence pulse formed with the injector was broadened while being convected downstream, and this broadening was quantified using fluorescence microscopy. Fluorescence microscopy measurements were taken at the following downstream distances from the point of tracer introduction: L_1=20.0 mm (112 L/d_h), L_2=149 mm (835) and L_3=1063 mm (5948) (Figure 3-3(b)). The gas and liquid flow rates used for the two-phase experiments are: Q_G=30 μL/min (condition A), 70 μL/min (condition B), and Q_L=10 μL/min, respectively. These values result in the superficial gas and liquid velocities j_G=0.0108 m/s, 0.0252 m/s and j_L=0.0036 m/s. The experimental set-up was similar to the one used in Chapter 2.

Microchannel devices were made of poly-(dimethylsiloxane) (PDMS) and sealed on a glass cover slide. All devices were fabricated using standard soft-lithographic techniques [32]. PDMS (Dow Corning Sylgard Brand 184 Silicone Elastomer, Essex-Brownell Inc.) was molded on SU-2050 masters on silicon. After PDMS was cured at 70 °C for 2 - 12 hours, the devices were peeled off the mold, cut and cleaned. Individual devices were sealed to pre-cleaned microscope slides (75 x 50 mm, 1 mm thick, Corning Glass Works), where both surfaces were treated in oxygen plasma for 35 s. Inlet and outlet PEEK tubing (1/16-in o.d., 508 μm i.d., Upchurch Scientific) was inserted and glued in place with 5-min epoxy (Devcon). The epoxy was cured at 70 °C for 12 hours or at room temperature overnight.
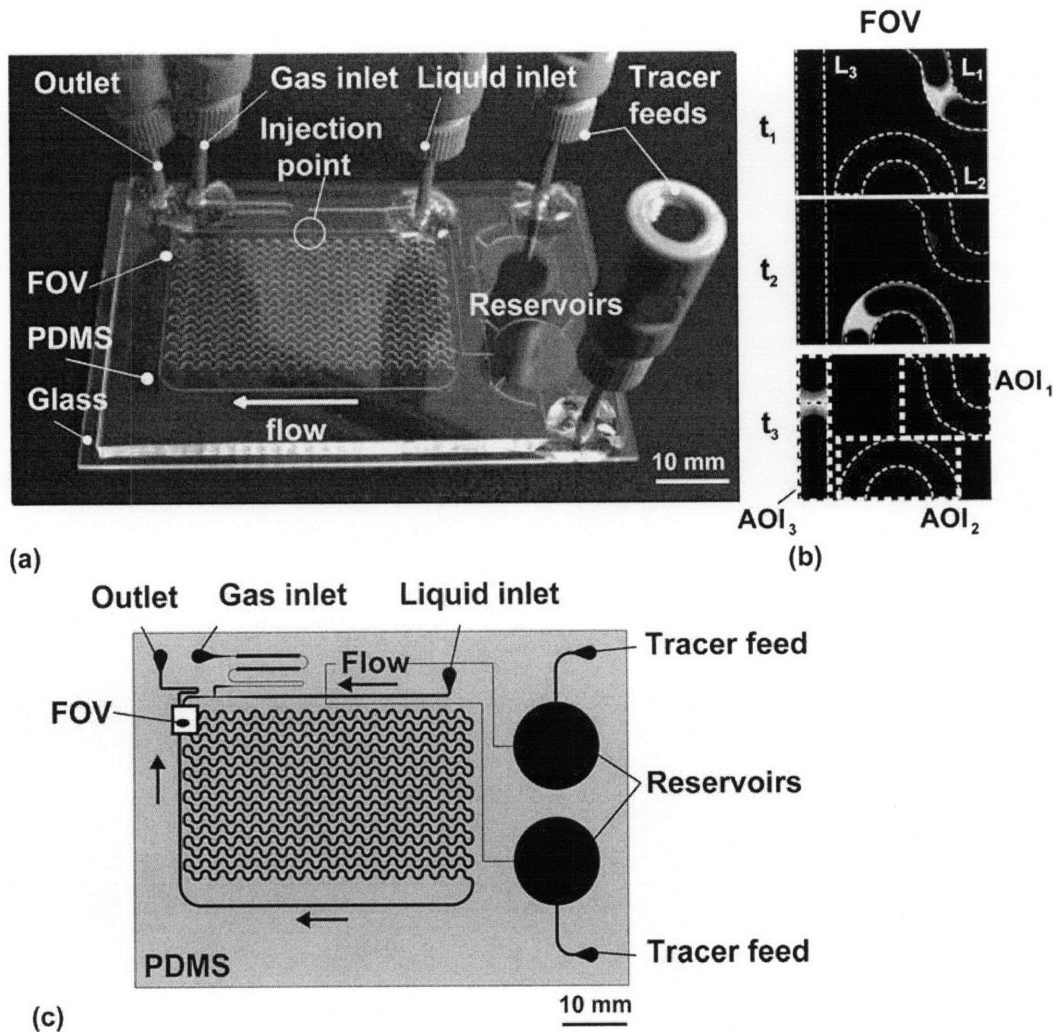
Figure 3-3 (a) Photograph of the top view of the meandering channel device with fluidic connections prior to the integration of the bending disk elements (device 2). (b) Microscopic images of the FOV at three different streamwise positions or times (t1 < t2 < t3). (c) Schematic of the microchannel network of device 2.

3.2.3 Image acquisition, processing and data analysis

A 5x microscope objective and 0.63x camera adapter (Zeiss) yielded a field of view (FOV) of 2.50 x 1.50 mm (NA=0.12). An inverted fluorescence microscope (Zeiss Axiovert 200) equipped with a full-frame CCD camera (PCO Sensicam QE doubleshot, 1280 x 1025 pixels, 9 fps) was used for the image acquisition. The light source was a mercury short arc photo optic lamp (Osram, HBO 103 W/2). Recorded images were saved as 8-bit files. The frame rate of the camera was adjusted to values between 2 and 8 frames per second (fps) by the image acquisition software (LaVision, DaVis 6.2.2). Rectangular areas of interest (AOI) (Figure 3-3(b)) within the camera's FOV, which

81

contained fluorescence intensity at the locations L_1, L_2, L_3, were selected from the recorded frames. The mean intensity determined within a given AOI at a given point in time, (i.e., I_1, I_2, I_3 corresponding to L_1, L_2, L_3) was used as a measure for the local tracer concentration Over the course of a measurement series, the transient behavior of the intensities associated with the three different streamwise positions was determined. The mean residence time at the streamwise position L_k is obtained as follows [13]:

$$\bar{t}_k = \frac{\sum_{i=1}^{n} t_i \cdot I_k(t_i) \cdot \Delta t}{\sum_{i=1}^{n} I_k(t_i) \cdot \Delta t} \tag{3.2}$$

where k corresponds to the length in the segmented-flow section of the microchannel network, n is the number of recorded frames. $I_k(t_i)$ is the observed spatially averaged intensity at the position L_k (within AOI_K) of the FOV of the microscope. The time step Δt is defined as $t_{i+1} - t_i$, and is constant for the set frame rate. The variance of the intensity distributions is calculated in discrete form as:

$$\sigma_k^2 = \frac{\sum_{i=1}^{n} (t_i - \bar{t}_k)^2 I_k(t_i)\Delta t}{\sum_{i=1}^{n} I_k(t_i)\Delta t} = \frac{\sum_{i=1}^{n} t_i^2 I_k(t_i)\Delta t}{\sum_{i=1}^{n} I_k(t_i)\Delta t} - \bar{t}_k^2 . \tag{3.3}$$

The E-curve, characterizing the residence time distribution RTD of the liquid, follows as

$$E_k(t_i) = \frac{I_k(t_i)}{\sum_{i=1}^{n} I_k(t_i) \cdot \Delta t} . \tag{3.4}$$

The calculated mean residence time $\bar{t}_k$ (Equation (3.2)) is used to non-dimensionalize the time and $E_k(t_i)$:

$$\theta_{k,i} = \frac{t_i}{\bar{t}_k}$$
$$E_k(\theta_{k,i}) = \bar{t}_k \cdot E_k(t_i). \tag{3.5}$$

We used an ensemble of 5 individual measurements to obtain the characteristic temporal concentration with a better statistics.

Deconvolution of the RTD was also performed by using discrete Fourier transforms as implemented in Matlab (The Mathworks, Natick, MA):

$$E_{k,deconv}(\theta) = FFT^{-1}\left\{\left\|\frac{FFT\{E_{k,out}(\theta)\}}{FFT\{E_{k,in}(\theta)\}}\right\|\right\}. \tag{3.6}$$

where "out" corresponded to the locations L_2 or L_3 and "in" corresponded to L_1.

3.3   Results and Discussion

We restrict ourselves to microscale segmented flows in microchannels with hydrophilic surfaces. The flow and transport properties of segmented flows in such channels have been described elsewhere[5,33-35], and summarized in Chapter 2. The prominent issue is that of communication between adjacent liquid segments through liquid menisci and films. It should be noted that gas-liquid systems that avoid such communication can be obtained under certain conditions in hydrophobic microchannels. However, it is challenging to obtain regular and short liquid segments in such systems, at the low superficial velocities that we consider in this chapter.

3.3.1 Piezoelectric injection
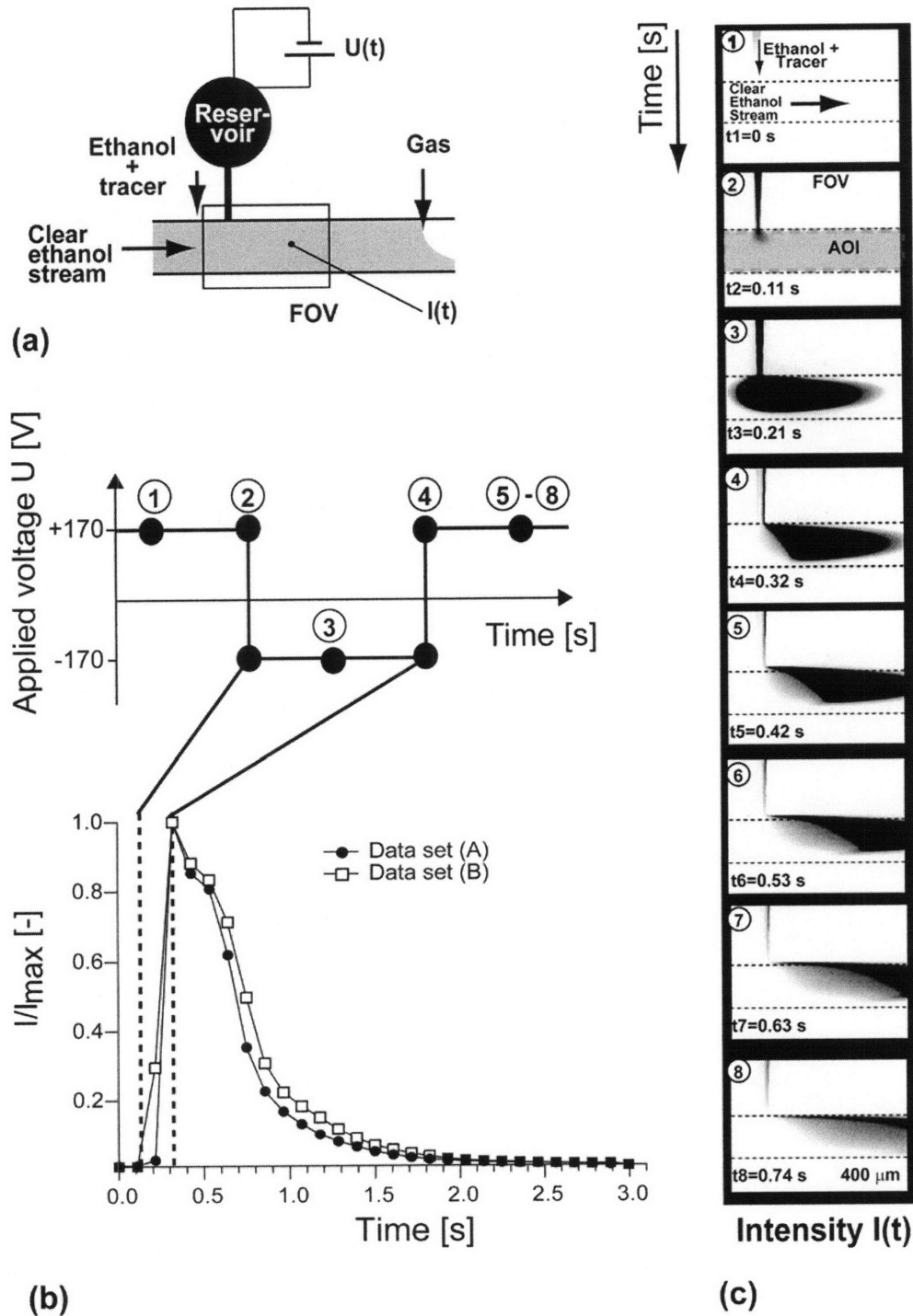
Figure 3-4 (a) Schematic of the tracer injection. (b) Average intensity distribution in AOI at the point of injection L=0 mm for two experiments (A) and (B) with the corresponding voltage profile applied to the piezoelectric bending disk element. (c) Inverted fluorescence micrographs of the pulse injection (Rhodamine B in ethanol) into a PDMS microchannel with a superficial liquid velocity j_L =0.0027 m/s in the clear ethanol stream.

Figure 3-4 summarizes experimental results of the technique used for injecting a liquid tracer plug from a liquid reservoir into the main flow channel. The voltage applied to the piezoelectric disk, $U(t)$, was switched from +170 to -170 V and back to +170 V (Figure 3-4(b)), causing an injection and subsequent suction at the tracer inlet location (to prevent the tracer from leaking out of the injection port). When we compare the injection time of about 2 s in Figure 3-4(b) with the much longer residence times (60–100 s), the injected pulse can be assumed to be a reasonable representation of the ideal Dirac δ function, and hence has no effect on the final form of the RTD. However, at small residence times, the actual shape of the inlet pulse influences the RTD, and convolution techniques have to be employed as the ideal pulse assumption is no longer valid. The time-series of micrographs in Figure 3-4(c) show a sharp pulse as the piezoelectric bending element deflects ($t=0.21$ s). Subsequently, the flow direction during the injection is reversed, partially filling the inlet channel with clear ethanol ($t=0.32$ s). The tail of the pulse is due to the nature of the laminar flow profile with a no-slip boundary condition at the channel walls. Initial attempts at injecting tracer into the two-phase flow involved injection after the segmented flow had been generated; however deflections of the PDMS membrane that were caused by local pressure fluctuations in the two-phase flow was observed. Note however that the resonant frequency of the PDMS membrane is several orders of magnitude higher than a characteristic frequency of the flow. The injection point of tracer dye was then placed upstream, before the gas inlet. This significantly reduced the oscillation of the PDMS membrane induced by local pressure fluctuations. Small piezoelectric bending disks were preferred.

3.3.2 RTD curves

In this section, we present and discuss the liquid phase residence time distribution (RTD) curves at different conditions obtained for both single phase and two-phase flow in microfluidic channels. We also compare the RTD characteristics of segmented gas-liquid flow with that of single phase flow. For the considered segmented flow conditions, the average liquid segment lengths are approximately $1 \cdot d_h$ and the average gas bubble length is approximately $4 \cdot d_h$.

The obtained RTD curves are shown in Figure 3-5, and it is seen that the curves at short channel lengths are wider and more asymmetric than those at longer lengths. These trends can be explained by comparing them to the predictions of the dispersion model, which can be used to model the single-phase flow and the segmented gas-liquid flow. For single-phase flow, we can use the simplifying assumptions of a uniform velocity distribution, vanishing wall-normal velocity component and restrict ourselves to an axisymmetric tracer distribution in the channel. Levenspiel[23] proposed an analytical solution for a plug flow superimposed by axial dispersion[36] under these conditions. The following equation represents the E-curve from a pulse experiment:

$$E_\theta = \frac{1}{\sqrt{4\pi\theta(D^* / j_L L)}} \exp\left[-\frac{(1-\theta)^2}{4\theta(D^* / j_L L)}\right], \quad (3.7)$$

where $D^*/(j_L L)$ is the vessel dispersion number. This dispersion model is appropriate for open-open boundary conditions as shown by Danckwerts[37] and through-the-wall tracer measurement [13]. We can assume open-open boundary conditions, since similar dispersion conditions exist before and after the points of tracer injection. The presented fluorescence microscopy tracer method allows us to realize a through-the-wall tracer concentration measurement downstream of the channel. The single parameter $D^*/(j_L L)$ used in the above model varies with position L along the devices, since the superficial liquid velocity j_L and the dispersion coefficient D^* are constant along the channel length. In addition, we conclude that dispersion effects caused by convective secondary fluid motion (due to the meandering channels) are negligible, by calculating the $Dn^2 Sc$ criterion based on dimensionless Dean (Dn) and Schmidt (Sc) numbers proposed by Johnson and Kamm.[38] The quantity $Dn^2 Sc$ for our measurements is approximately 3 (less than 100, where secondary flow effects start affecting the dispersion process). However, it is difficult to account quantitatively for the alternating direction of the meandering channels. The advantage of being able to perform on-chip measurements enables us to include the aforementioned nonlinear effects contributing to the RTD.
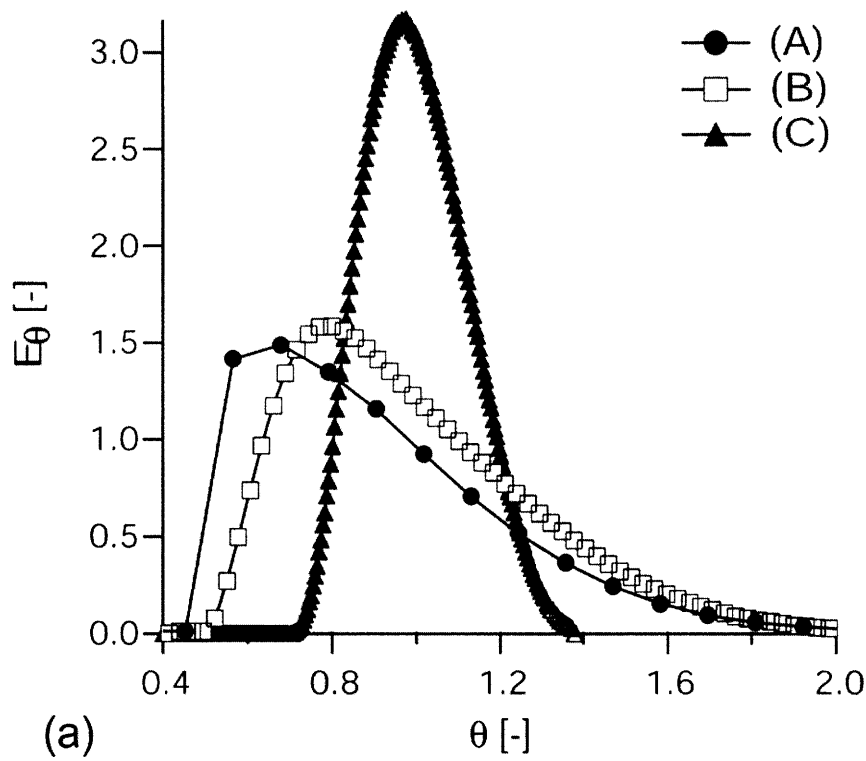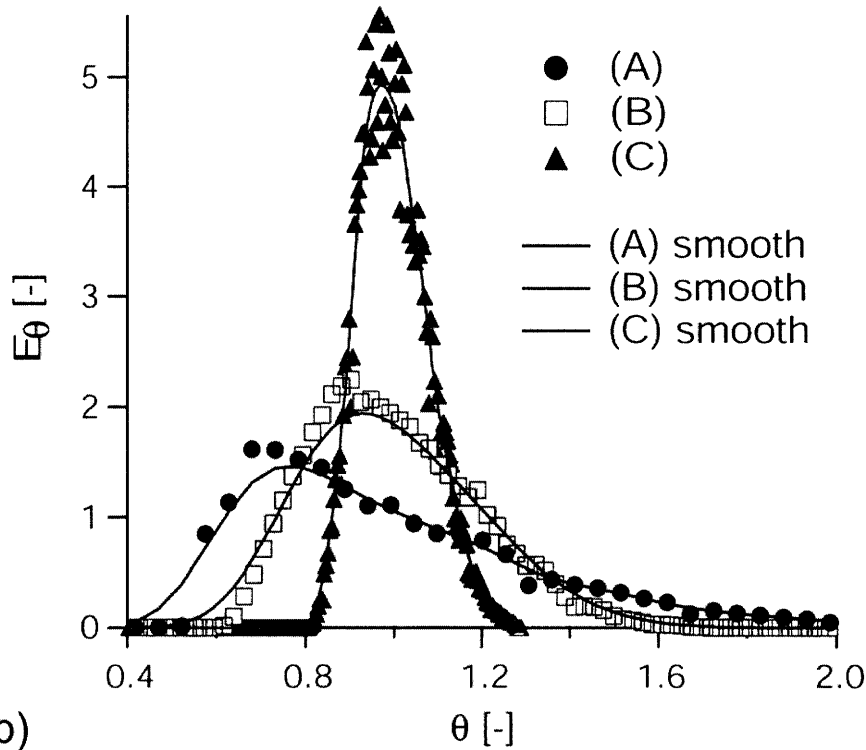
Figure 3-5 (a) RTD curves for single-phase flow, j_L =0.0096 m/s, (A) L_1=20 mm (L/d_h =112), (B) L_2=150 mm (835) and (C) L_3=1063 mm (5948), (b) RTD curves for segmented flow condition B with j_L =0.0036 m/s, j_G =0.0252 m/s, (A) L_1=20.0 mm (99 L/d_h), (B) L_2=149.2mm (738) and (C) L_3=1062.6mm (5262).

For small $D^*/(j_LL)$, as is the case for large channel lengths, a narrow, symmetric distribution is obtained. With increasing $D^*/(j_LL)$ (decreasing channel length), the RTD curves are expected to widen and become significantly asymmetric, as seen in Figure 3-5 (curve (A)). For both segmented flow (Figure 3-5 (b)) and single-phase flow (Figure 3-5 (a)), we obtain RTD curves of similar shape. The simplifying dispersion model for computing the RTD and the associated characterization assume an ideal input pulse (Dirac-δ function). To evaluate this assumption, we also perform rigorous deconvolution of the RTD from raw data using discrete Fourier transforms, for both single-phase and segmented flow. The results of these calculations are summarized in Figure 3-6. Figure 3-6(a) shows the device RTD curves for single phase flow between L_1 and L_2, and between L_1 and L_3, and Figure 3-6(b) shows the corresponding curves for segmented flow. The deconvoluted curves are, as expected, very similar to the original residence time data. This agreement confirms that the small initial length and shape of the tracer pulse are of little effect. Hence, for a sufficiently long length L, a representation of our data with the dispersion model is justified.
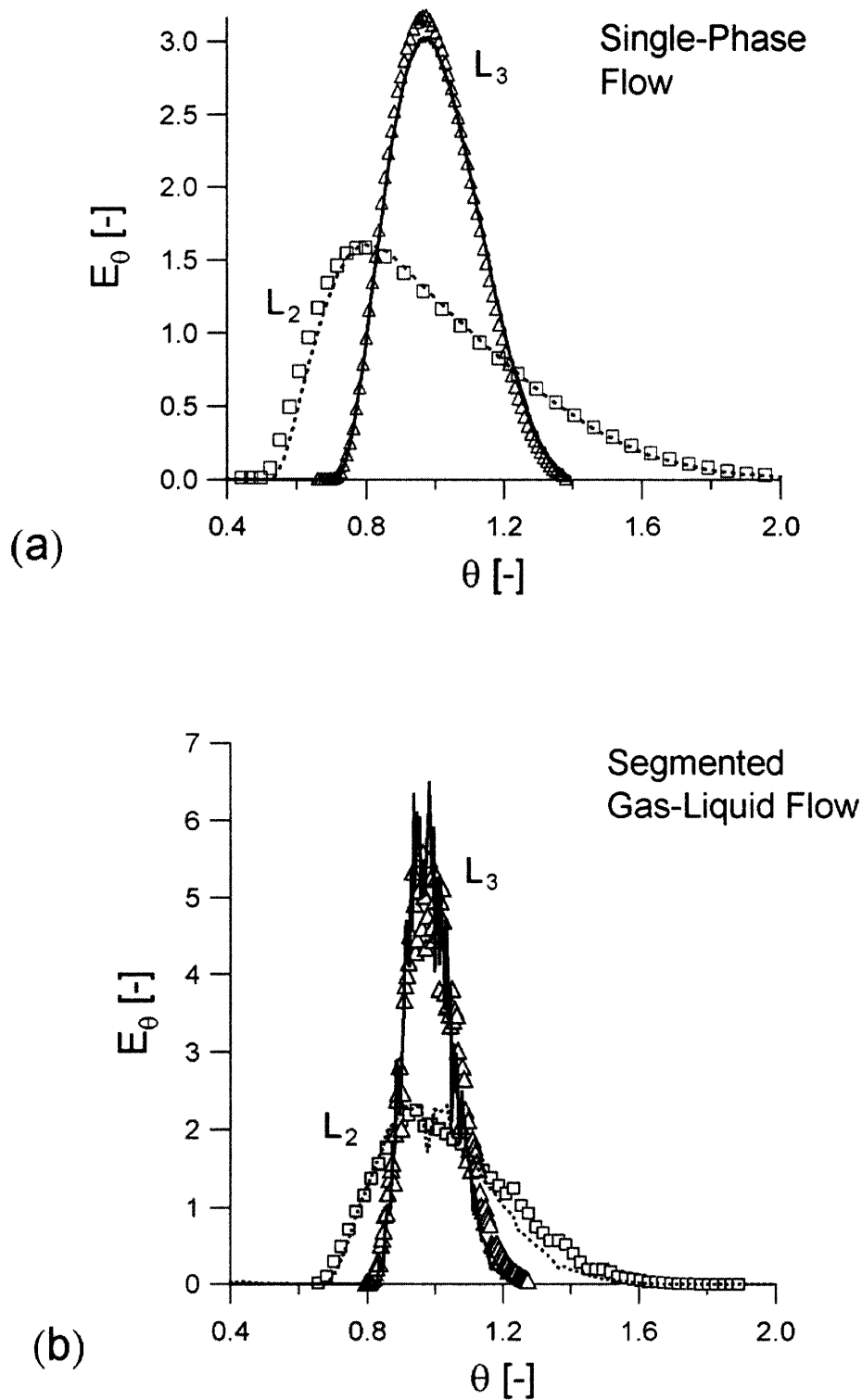
Figure 3-6 Comparison between the RTD data (symbols) and the result obtained by deconvolution (lines). The conditions are L_2=150 mm (L/d_h =835) (squares, dashed line), and L_3=1063 mm (L/d_h =5948) (triangles, straight line). (a) RTD curves for single phase flow, j_L =0.0096 m/s (b) RTD curves for segmented flow, j_L =0.0036 m/s, j_G =0.0252 m/s.
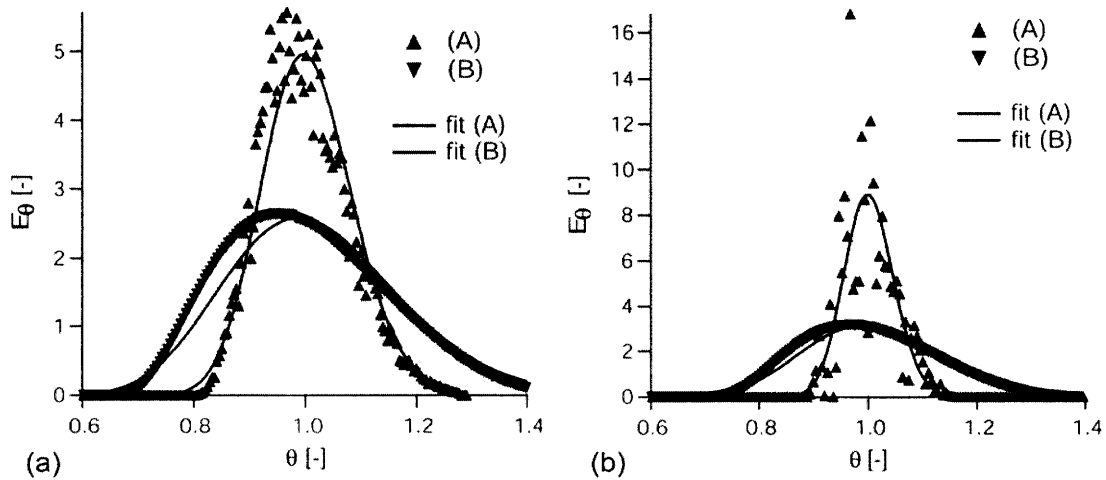
Figure 3-7 Comparison of the measured E-curves with the dispersion model for segmented flow and single-phase flow at position L_3. (a) Superficial velocities for (A) segmented flow j_L=0.0036 m/s, j_G=0.0252m/s and (B) single-phase flow: j_L =0.0149 m/s. Mean residence times: 59 s (segmented flow), 71 s (single-phase flow). (b) Superficial velocity for (A) segmented flow j_L=0.0036 m/s, j_G =0.0108 m/s and (B) single-phase flow: j_L =0.0096 m/s. Mean residence times: 98 s (segmented flow), 108 s (single-phase flow). All curves are fitted with the dispersion model (3.7) with the vessel dispersion number as fitting parameter: (a) (A): (3.247 +/- 0.034) $\cdot 10^{-3}$, (B): (1.202 +/- 0.022) $\cdot 10^{-2}$; (b) (A): (1.136 +/- 0.073) $\cdot 10^{-3}$, (B): (0.810 +/- 0.012) $\cdot 10^{-2}$.

Figure 3-7 illustrates how the variance of the RTD curve in segmented flow is narrowed (by a factor 5 in Figure 3-7(a) and a factor of 8 in Figure 3-7(b)) compared to single-phase flow with a similar mean residence time, for two different flow conditions. Since the use of the dispersion model is justified for the measuring location L_3, we include it in Figure 3-7. The experimentally obtained curves for parameter $D^*/(j_L L)$ indicate that the fit with the dispersion model improves with increasing length L, as expected since the simple 1-D model works best for sufficiently large channel lengths [13,39,40]. In both cases, the single-phase flow experiments have been carried out at slightly longer mean residence times than the segmented flow experiments. For single phase residence time to equal the two-phase residence time, operate it would be necessary to operate at a higher superficial liquid velocity. The comparisons made are therefore conservative – according to the dispersion model, for a given reactor length L, the spreading of the RTD curves ($E(\theta)$) increases with increasing superficial liquid velocity. The result illustrates a key advantage of using segmented gas-liquid flows over single-phase ones: that of narrow residence time distributions. This can be useful in many

90

reaction applications, where an improvement in the RTD directly translates into a measurable improvement in product quality, such as an improved yield or a narrowed particle size distribution in the case of particle synthesis [3,39,40].

3.4 Conclusions

A piezo-electrically activated tracer injection technique was integrated into a microchannel network and allowed to measure the spreading of a 125 nL tracer pulse in microscale segmented gas-liquid flow and single-phase liquid flow at different downstream positions. For one particular example of a microfluidic reaction network, we demonstrate the use of the injection technique to experimentally determine liquid residence time distributions. Fluorescent microscopy measurements were performed at conditions that are relevant to on-chip synthesis. Results were presented for one particular flow condition and a narrow range of Capillary numbers. The variance of the RTD was observed to be significantly smaller for segmented gas-liquid flows than for single-phase flow at similar conditions. For larger Capillary numbers, axial dispersion effects increase as a direct consequence of the increased film thickness and qualitatively follow the trends predicted by Salman et al.[22] Axial dispersion also increases with increasing slug and gas bubble lengths. However the dynamic character of multiphase flow systems couple the slug / gas bubble lengths and the Capillary number, making it difficult to vary them independently. The shape of the liquid menisci in the channel corners is dominated by the surface tension of the liquid (and less so by the channel size). Thus, if the channel size is varied at constant Capillary number, the film thickness is unaffected. Shrinking the channel size therefore increases the relative cross sectional area of the menisci and the areas covered by the films. Communication between slugs and hence a broadening of the RTD is therefore expected in smaller channels. The presented technique not only provides a viable tool to better understand the residence time characteristics of well-defined segmented flow in straight microchannels, but also to expand it to more complex configurations, e.g., multiphase flow through networks of packed or microstructured beds.

3.5 References

1. Link, D. R., Anna, S. L., Weitz, D. A. & Stone, H. A. Geometrically Mediated Breakup of Drops in Microfluidic Devices. *Physical Review Letters* **92**, 054503-1-0545034 (2004).

2. Thorsen, T., Maerkl, S. J. & Quake, S. R. Microfluidic large-scale integration. *Science* **298**, 580-584 (2002).

3. Khan, S. A., Guenther, A., Schmidt, M. A. & Jensen, K. F. Microfluidic Synthesis of Colloidal Silica. *Langmuir* **20**, 8604-8611 (2004).

4. Yen, B. K. H., Gunther, A., Schmidt, M. A., Jensen, K. F. & Bawendi, M. G. A microfabricated gas-liquid segmented flow reactor for high-temperature synthesis: The case of CdSe quantum dots. *Angewandte Chemie-International Edition* **44**, 5447-5451 (2005).

5. Guenther, A., Jhunjhunwala, M., Thalmann, M., Schmidt, M. A. & Jensen, K. F. Micromixing of miscible liquids in segmented gas-liquid flow. *Langmuir* **21**, 1547-1555 (2005).

6. Aussillous, P. & Quere, D. Quick deposition of a fluid on the wall of a tube. *Physics of Fluids* **12**, 2367-2371 (2000).

7. Bretherton, F. The motion of long bubbles in tubes. *Journal of Fluid Mechanics* **10**, 166-88 (1961).

8. Taylor, G. I. Deposition of a viscous fluid on the wall of a tube. *Journal of Fluid Mechanics* **10**, 11-15 (1961).

9. Wong, H., Radke, C. J. & Morris, S. The Motion of Long Bubbles in Polygonal Capillaries .1. Thin-Films. *Journal of Fluid Mechanics* **292**, 71-94 (1995).

10. Wong, H., Radke, C. J. & Morris, S. The Motion of Long Bubbles in Polygonal Capillaries .2. Drag, Fluid Pressure and Fluid-Flow. *Journal of Fluid Mechanics* **292**, 95-110 (1995).

11. Culbertson, C. T., Jacobson, S. C. & Ramsey, J. M. Diffusion coefficient measurements in microfluidic devices. *Talanta* **56**, 365-373 (2002).

12. Griffiths, S. K. & Nilson, R. H. Low dispersion turns and junctions for microchannel systems. *Analytical Chemistry* **73**, 272-278 (2001).

13. Levenspiel, O. *Chemical reaction engineering* (Wiley, New York, 1999).

14. Deckwer, W. D. *Bubble Column Reactors* (John Wiley and Sons, New York, 1991).

15. Joshi, J. B. Axial Mixing in Multiphase Contactors - a Unified Correlation. *Transactions of the Institution of Chemical Engineers* **58**, 155-165 (1980).

16. Joshi, J. B. & Sharma, M. M. Liquid-Phase Backmixing in Sparged Contactors. *Canadian Journal of Chemical Engineering* **56**, 116-119 (1978).

17. Badura, R., Deckwer, W. D., Warnecke, H. J. & Langeman.H. Mixing in Bubble Columns. *Chemie Ingenieur Technik* **46**, 399-399 (1974).

18. Palaskar, S. N., De, J. K. & Pandit, A. B. Liquid Phase RTD Studies in Sectionalized Bubble Column. *Chemical Engineering Technology* **23**, 61-69 (2000).

19. Stegeman, D., vanRooijen, F. E., Kamperman, A. A., Weijer, S. & Westerterp, K. R. Residence time distribution in the liquid phase in a cocurrent gas-liquid trickle bed reactor. *Industrial & Engineering Chemistry Research* **35**, 378-385 (1996).

20. Froment, G. F. & Bischoff, K. B. *Chemical Reactor Analysis and Design* (John Wiley and Sons, 1990).

21. Fogler, H. S. *Elements of Chemical Reaction Engineering* (Prentice-Hall, Inc., Englewood Cliffs, NJ, 1992).

22. Salman, W., Gavriilidis, A. & Angeli, P. A model for predicting axial mixing during gas-liquid Taylor flow in microchannels at low Bodenstein numbers. *Chemical Engineering Journal* **101**, 391-396 (2004).

23. Levenspiel, O. & Smith, W. K. Notes on the diffusion-type model for the longitudinal mixing of fluids in flow. *Chemical Engineering Science* **6**, 227-233 (1957).

24. Beard, N. R., Zhang, C. X. & deMello, A. J. In-column field-amplified sample stacking of biogenic amines on microfabricated ellectrophoresis devices. *Electrophoresis* **24**, 732-739 (2003).

25. Zhang, C. X. & Manz, A. Narrow sample channel injectors for capillary electrophoresis on microchips. *Analytical Chemistry* **73**, 2656-2662 (2001).

26. Roddy, E. S., Xu, H. W. & Ewing, A. G. Sample introduction techniques for microfabricated separation devices. *Electrophoresis* **25**, 229-242 (2004).

27. Vanlintel, H. T. G., Vandepol, F. C. M. & Bouwstra, S. A Piezoelectric Micropump Based on Micromachining of Silicon. *Sensors and Actuators* **15**, 153-167 (1988).

28. Vanderschoot, B. H., Jeanneret, S., Vandenberg, A. & Derooij, N. F. A Silicon Integrated Miniature Chemical-Analysis System. *Sensors and Actuators B-Chemical* **6**, 57-60 (1992).

29. Bassous, E. & Baran, E. Fabrication of Silicon Nozzle Arrays for Ink Jet Printing. *Journal of the Electrochemical Society* **124**, C310-C310 (1977).

30. Bassous, E., Taub, H. H. & Kuhn, L. Ink Jet Printing Nozzle Arrays Etched in Silicon. *Applied Physics Letters* **31**, 135-137 (1977).

31. Petersen, K. E. Fabrication of an Integrated, Planar Silicon Ink-Jet Structure. *Ieee Transactions on Electron Devices* **26**, 1918-1920 (1979).

32. Xia, Y. N. & Whitesides, G. M. Soft lithography. *Annual Review of Materials Science* **28**, 153-184 (1998).

33. Cubaud, T. & Ho, C. M. Transport of bubbles in square microchannels. *Physics of Fluids* **16**, 4575-4585 (2004).

34. Guenther, A. et al. Transport and reaction in segmented gas-liquid flow. *Lab on a chip* **4**, 278-246 (2004).

35. Kraus, T., Guenther, A., de Mas, N., Schmidt, M. A. & Jensen, K. F. An integrated multiphase flow sensor for microchannels. *Experiments in Fluids* (2004).

36. Taylor, G. I. Dispersion of Soluble Matter in Solvent Flowing Slowly through a tube. *Proceedings of the Royal Society of London A* **219**, 186-203 (1953).

37. Danckwerts, P. V. Continuous flow systems : Distribution of residence times. *Chemical Engineering Science* **2**, 1-13 (1953).

38. Johnson, M. & Kamm, R. D. Numerical-Studies of Steady Flow Dispersion at Low Dean Number in a Gently Curving Tube. *Journal of Fluid Mechanics* **172**, 329-345 (1986).

39. Taylor, G. Dispersion of Soluble Matter in Solvent Flowing Slowly through a Tube. *: Proceedings of the Royal Society of London. Series A, Mathematical and Physical Sciences* (1953).

40. Taylor, G. The Dispersion of Matter in Turbulent Flow through a Pipe. *: Proceedings of the Royal Society of London. Series A, Mathematical and Physical Sciences* (1954).

4   Microfluidic Synthesis of Colloidal Particles

Colloidal particles in the micron size range are some of the most commonly encountered forms of materials in nature and in the physical sciences. Monodisperse spherical colloids such as silica suspensions and their assemblies have potential applications in the manufacture of displays, optical coatings, and photocatalyst supports.[1] The engineering of such materials with enhanced properties (electrical, optical, magnetic, chemical and mechanical) depends to a large extent on the ability to successfully process a wide variety of these colloidal particulate systems. In this chapter, we describe the design, fabrication and operation of microfluidic chemical reactors for continuous controlled synthesis of colloidal silica and titania particles. Two reactor configurations are first examined for silica synthesis: single-phase laminar flow reactors (LFR) and two-phase (gas-liquid) segmented flow reactors (SFR). We examine the effect of operating variables in the two reactors on particle sizes and size distributions. Results are compared with those obtained from small-scale batch synthesis. We then use a gas-liquid segmented flow microreactor to synthesize colloidal titania particles, and use chip temperature as a parameter to obtain four-fold variation in particle size for the same reactant concentrations and reaction time. The goal of this part of the study is two-fold: to demonstrate microfluidic sol-gel processing of a more challenging class of alkoxides with much faster hydrolysis rates, as well as to examine the effect of temperature on these hydrolysis rates, and hence on particle size.

4.1   Introduction

4.1.1   Sol-gel science

This brief introduction is adapted from Brinker and Scherer's text on sol-gel science.[2] A 'colloid' is a suspension in which the dispersed phase is so small (~ 10nm-1μm) that gravitational forces are negligible and interactions are dominated by short-range forces, such as Van der Waals attraction and surface charges. The inertia of the dispersed phase is small enough that it exhibits Brownian motion, a random walk driven by momentum

imparted by collisions with molecules of the suspending medium. A *sol* is a colloidal suspension of solid particles in a liquid. In the sol-gel process, the precursors for preparation of a colloid consist of a metal or metalloid element surrounded by various ligands. Metal alkoxides are the most widely used class of precursors in sol-gel research. These precursors are members of the family of *metalorganic* compounds, which have an organic ligand attached to a metal or metalloid atom. The most thoroughly studied example is silicon tetraethoxide (or tetraethoxysilane, or tetraethyl orthosilicate, TEOS), $Si(OC_2H_5)_4$. *Organometallic* compounds are defined as having direct metal-carbon bonds, not metal-oxygen-carbon linkages as in metal alkoxides. Thus metal alkoxides are not organometallic compounds, as often referred to in the literature.

Metal alkoxides are popular precursors because they react readily with water. The reaction is called *hydrolysis*, because a hydroxyl ion becomes attached to the metal atom, as in the following reaction:

$$Si(OR)_4 + H_2O \rightarrow HO\text{-}Si(OR)_3 + ROH \qquad (4.1)$$

The R represents a proton or other ligand (if R is an alkyl, then –OR is an *alkoxy* group), and ROH is an alcohol. Depending on the amount of water and catalyst present, hydrolysis may go to completion (so that all of the OR groups are replaced by OH),

$$Si(OR)_4 + 4H_2O \rightarrow Si(OH)_4 + 4ROH \qquad (4.2)$$

or the reaction may stop while the metal is only partially hydrolyzed, $Si(OR)_{4\text{-}n}(OH)_n$. Two partially hydrolyzed molecules can link together in a condensation reaction, such as

$$(OR)_3\,Si\text{-}OH + HO\text{-}Si\,(OR)_3 \rightarrow (OR)_3Si\text{-}O\text{-}Si(OR)_3 + H_2O \qquad (4.3)$$

or

$$(OR)_3\,Si\text{-}OR + HO\text{-}Si\,(OR)_3 \rightarrow (OR)_3Si\text{-}O\text{-}Si(OR)_3 + ROH. \qquad (4.4)$$
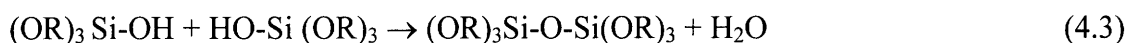
By definition, condensation liberates a small molecule, such as water or alcohol. This type of reaction can continue to build larger and larger silicon containing molecules by the process of polymerization. According to Iler,[3] condensation takes place in such a fashion as to maximize the number of Si-O-Si bonds and minimize the number of terminal hydroxyl groups through internal condensation. Thus rings are quickly formed to which monomers add, creating three-dimensional particles. These particles condense to the most compact state leaving OH groups on the outside.

4.1.2 Stöber process for silica synthesis

Colloidal silica (SiO_2) serves as a model system in the present work, since the fundamental aspects of this system have been investigated in experimental and theoretical studies.[2,4-10] Moreover, silica particles with a narrow size distribution have important industrial applications in pigments, catalysts, thin films for photovoltaic, electrochromic, photochromic and electro-luminescence devices, sensors, health-care, anti-reflective coatings, and chromatography.[2,3] Batch synthesis of particles with narrow size distributions (~5%) can be achieved by the Stöber technique[11] and its modifications. This method involves hydrolysis of tetraethyl-orthosilicate (TEOS) in a basic solution of water and alcohol. The overall hydrolysis and condensation reactions respectively can be written as:

$$Si(OC_2H_5)_4 + 4H_2O \rightarrow Si(OH)_4 + 4C_2H_5OH \tag{4.5}$$

and

$$Si(OH)_4 \rightarrow SiO_2 + 2H_2O. \tag{4.6}$$

In the preparation of particles, the ratio of water to TEOS is typically more than 20:1 and the pH is very high, and both of these factors promote condensation. This encourages the formation of compact structures, rather than extended polymeric networks of the kind generally found in alkoxide-derived gels. Typically, alcohol, ammonia and water are mixed, and then TEOS is added, resulting in visible opalescence within approximately 10 minutes. The most important parameters are silane and base concentrations, and the water-silane molar ratio. Others have studied the effects of reaction conditions and temperature with similar results.

Several theoretical studies examine the mechanisms of sol-gel silica synthesis, and offer explanations for the observed monodispersity. Matsuokas and Gulari[4-6] propose a monomer addition model, an extension of the classic LaMer model,[12] for the precipitation of uniform silica particles. In their model, nucleation occurs by the reaction of two hydrolyzed TEOS [Silicic Acid: $Si(OH)_4$] monomers. Particle growth occurs by monomer addition, through two possible pathways: diffusion or surface reaction limited addition. TEOS hydrolysis, however, is the overall rate limiting step. Bogush et al. propose a mechanism of nucleation of marginally unstable particles that grow through

aggregation.[7-10,13] According to their model, nucleation occurs through a large part of the reaction, and final monodispersity is achieved through size-dependent aggregation rates.

Working with a well-characterized materials synthesis system facilitates the systematic study of the influence of reactor design and operating variables (reactant contacting, flow-rates, mixing time etc.) on particle size distribution. Since the product from the Stöber synthesis is monodisperse, any departure from monodispersity in the product from the reactor can be attributed to some aspect of reactor design or operation. Such information is valuable for rational design of reactors for controlled synthesis of the general class of inorganic colloidal particles.

4.1.3   Titania synthesis and challenges

Colloidal particles of titania are of considerable technological importance, and are widely used in applications such as pigments, photocatalysis, optical displays and healthcare products.[14] Several chemical synthesis techniques have been developed to synthesize titania particles in the colloidal size range (10 nm to 1 μm).[15-17] Spherical particles of titania have been prepared by the controlled hydrolysis of titanium alkoxides in dilute alcoholic solutions.[18-21] The rapid hydrolysis rates of titanium alkoxides make them considerably more difficult to process than their silicon alkoxide counterparts. Particle size, morphology and size-distributions are sensitive to processing conditions such as stirring rate in batch reactors and micromixer type in continuous flow reactors.[22,23] Effective physical or chemical techniques to control these hydrolysis rates are needed to enable controlled synthesis of particles with size-based tunable properties. The effects of temperature on reaction rate (and hence particle size) in sol-gel silica synthesis have been previously reported,[24] but no analogous reports exist for sol-gel titania synthesis from alkoxides.

Coagulation is a problem in sol-gel synthesis of titania in stirred-batch reactors. Large amounts (i.e. 10 to 50%) of agglomeration occur when reactant concentrations are above 0.1% solids. Agglomeration is caused by frequent collisions in the concentrated suspensions obtained from the concentrated reactant solutions that give high nucleation rates. In order to overcome this problem, hydroxypropyl cellulose (HPC) has been used as a steric-stabilization agent[25,26] during the precipitation. Experimental results suggest

that HPC molecules are reversibly adsorbed and are not incorporated during particle formation, with most of the adsorbed HPC present on the external particle surfaces. Fast adsorption-desorption compared with the powder precipitation process prevents the HPC molecules from being incorporated into the particle structure and prevents particle agglomeration throughout growth. Jean and Ring[21] have studied the kinetics of nucleation and growth in the generation of monodisperse titania powders by the above method.

4.1.4 Review of macroscale approaches

Batch reactors are conventionally used for colloid synthesis. There are several limitations associated with industrial scale batch processing: inhomogeneous reactant and temperature distributions, inefficient mixing, and product variations from batch to batch. Continuous flow reactors are attractive because they operate at steady state and ensure greater control and reproducibility. Several methods have developed and characterized systems for macro-scale continuous synthesis of ceramic powders[23,27-30]. Ogihara et al.[27,28] demonstrated a laminar flow reactor consisting of a mixing unit for particle nucleation (packed bed, static mixer or electromagnetic stirrer) connected in series with a Teflon aging tube (2 mm-4 mm i.d.) for particle growth. Powder characteristics obtained from their reactor depended on the type of mixer used, and particles obtained had wider size distributions than those from the corresponding small-scale batch process due to axial dispersion effects, i.e. the variation in residence times caused by the fluid moving slower near the tube wall than in the center[31]. Yonemoto et al.[23] and Kaiser et al.[30] introduced segmented flow reactors consisting of mixers (packed bed or static mixers) and Teflon aging tubes for the synthesis of colloidal titania and silica respectively. In both cases gas was used as the segmenting fluid to create recirculation and mixing, and eliminate axial dispersion otherwise associated with tube flow. These reactors gave particles with narrow size distributions comparable to small-scale batch synthesis.

4.1.5 Microscale reactors

Scaling down reactor dimensions to the sub-millimeter scale provides opportunities for improved size and composition control of colloidal synthesis[32]. Microfabrication also affords increased flexibility in reactor design. Complex reactant-contacting schemes that are difficult to achieve in macroscale units can be realized[33], and flow patterns can be

accurately controlled[34]. For colloidal synthesis, the micromixing and aging units can be integrated into one unit, whereas in macro scale reactors they are typically separate units that are externally connected to each other. For example, Kubo et al.[29] demonstrated a multi-stage (macro-scale) segmented flow system for the continuous synthesis of colloidal titania that consisted of four units (mixers and aging tubes) connected in series. The capability to integrate several functional units into one device using microfabrication greatly reduces the complexity of such multi-step synthesis systems.

Multiphase microreactors employing segmented flow for chemistries other than particle synthesis have been developed and characterized. Both gas-liquid (bubble) and liquid-liquid (droplet) multiphase microreactors have been reported[35-38]. Droplet microreactors employing immiscible liquids are beneficial for reactions where both fluids contain reactants[35,36]. In these cases, there is a large enhancement in mass transfer across the phases due to internal recirculation of the liquids. Tice et al.[38] used internal recirculation in aqueous droplets separated by oil for rapid mixing in droplet-based microfluidic devices, and they elucidated mechanisms of droplet formation and mixing. Typically, one liquid phase contains the reactants, while the other liquid serves only to segment the flow and induce mixing. Gas-liquid segmented flow reactors are attractive due to the ease with which the gas can be separated from the liquid. The segmenting gas, aside from dividing the incoming liquid into small batches, can also be used to accelerate micromixing by a combination of small segment dimensions and recirculation in each segment.

Recent research in the application of microfluidic reactors for particle synthesis has focused on the synthesis of semiconductor nanoparticles[39-43], and in all cases laminar flow reactors have been used. The objective of this work is to apply microreactors to the more general class of colloidal particles obtained from sol-gel chemistry and to explore multiphase microreactors as a means of obtaining narrow particle size distributions.

Suspensions of colloidal silica prepared by the above methods range in size from 10 nm to around 500 nm, and have solid content between 1 to 10 weight percent. There are several particle-handling issues to be considered when designing microsystems to process such suspensions. These include deposition of the particles on channel walls, and blocking of channels due to irreversible agglomeration. Particle deposition can be

prevented by appropriate surface modification. For example, the aging tubes in most macro-scale reactors for synthesis[23,27-30] ranged between 2 mm to 4 mm (inside diameter), and were made of a fluoropolymer such as PTFE. Robust operation was reported in all cases. Hence, by analogy, microchannel surfaces passivated with PTFE may be used for the microreactors[44]. Irreversible agglomeration, leading to catastrophic blockage, is prevented by the inherent characteristic of sol-gel particle synthesis. A balance of repulsive electrostatic forces and attractive dispersion forces stabilizes the sol against agglomeration[2]. Aggregates are limited to low-order multiplets that are at least an order of magnitude smaller than typical channel dimensions.

4.2 Microfluidic reactors

4.2.1 Design

The microreactors used for silica synthesis are schematically depicted in Figure 4-1. Design 1 [Figure 4-1(a)] is an LFR, and consists of two liquid inlets leading into a micromixing section for silica particle nucleation and initial growth. The channel has a rectangular cross section, 50 μm wide, 150 μm deep and 40 mm long. Reactant streams introduced into the micromixing section are focused into streams of 25 μm width each, and mixing takes place by molecular diffusion across these streams. The time that is takes for reactants to diffuse across streams, and hence mix completely, has to be translated into length in a continuous flow system. Adequate length has to be provided to ensure complete micromixing over the whole range of linear flow velocities. The serpentine nature of this section is merely to pack a large mixing length within a small area of the device (in this particular design- 40 mm of mixing length within a linear distance of 7 mm). This is followed by an aging length section that is 400 μm wide, 150 μm deep and 0.975 m long in which the silica particle size can be controlled by the residence time. Design 2 [Figure 4-1(b)] is an SFR, and consists of two liquid inlets followed by a gas-injection nozzle that is 25 μm wide and 150 μm deep. Slugs of liquid thus formed flow through an ageing length section that is 400 μm wide, 150 μm deep and 0.975 m long. In Design 2, the injected gas segments the flow, and the resulting recirculation creates mixing. In Design 3 [Figure 4-1(c)], micromixing is accomplished by fluid 'layering'[45].

Four liquid inlets lead into a 50 μm wide and 56 mm long micromixing section, where 12.5 μm wide liquid layers are formed, and mixing takes place by molecular diffusion across these layers. Gas is then injected to create slugs with recirculation and mixing during the ageing process. A gas inlet (300 μm wide) is provided at the end of this section, and is followed by an ageing length section where the channels are 300 μm wide and 2.3 m long. All channels in this device are 200 μm deep.
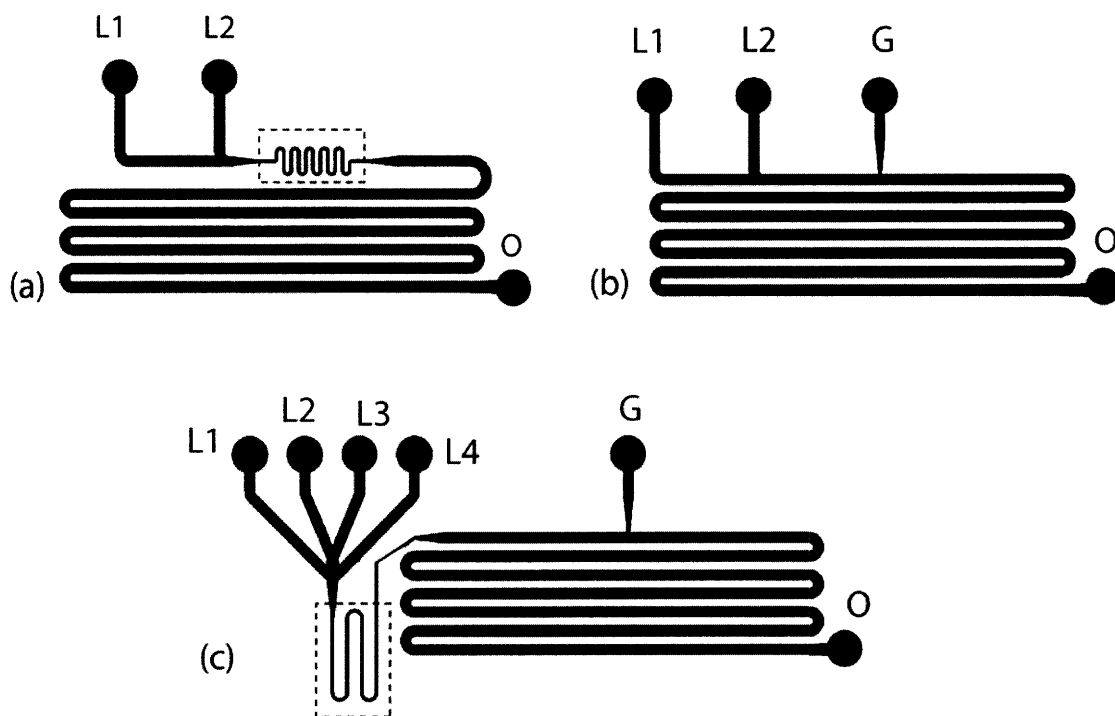
Figure 4-1. Schematics of microfluidic channels for silica synthesis: (a) Design 1 (LFR) has two liquid inlets (L1 and L2) and one outlet (O). Channels in the micromixing section (dotted) are 50 μm wide and 40 mm long, and those in the remaining device are 400 μm wide and 0.975 m long. All channels are 150 μm deep. (b) Design 2 (SFR) has two liquid inlets (L1 and L2), a gas inlet (G), and an outlet (O). The channels are 400 μm wide, 150 μm deep and 0.975 m long. (c) Design 3 (SFR) has four liquid inlets (L1-L4), a gas inlet (G) and an outlet (O). Channels in the micromixing section (dotted) are 50 μm wide and 56 mm long, and those in the remaining device are 300 μm wide and 2.3 m long. All channels are 200 μm deep.

The microreactor used for titania synthesis was designed to have two liquid reactant inlets, one gas inlet and one outlet for product (Figure 4-2(a)). The microchannels are rectangular in cross-section with a width of 300 μm, average height of 200 μm and total

length of 3 m. A (poly) tetrafluoroethylene (PTFE) tube (750 μm ID, 0.3 m long) leading to a sampling vial was connected to the microreactor outlet. The microreactor was submerged in a temperature-controlled water bath (Endocal, Neslab) which maintained temperature to within ±1.0 °C of the set-point. The sampling tube was outside the bath, at ambient temperature (22 °C) to facilitate easy sample collection.
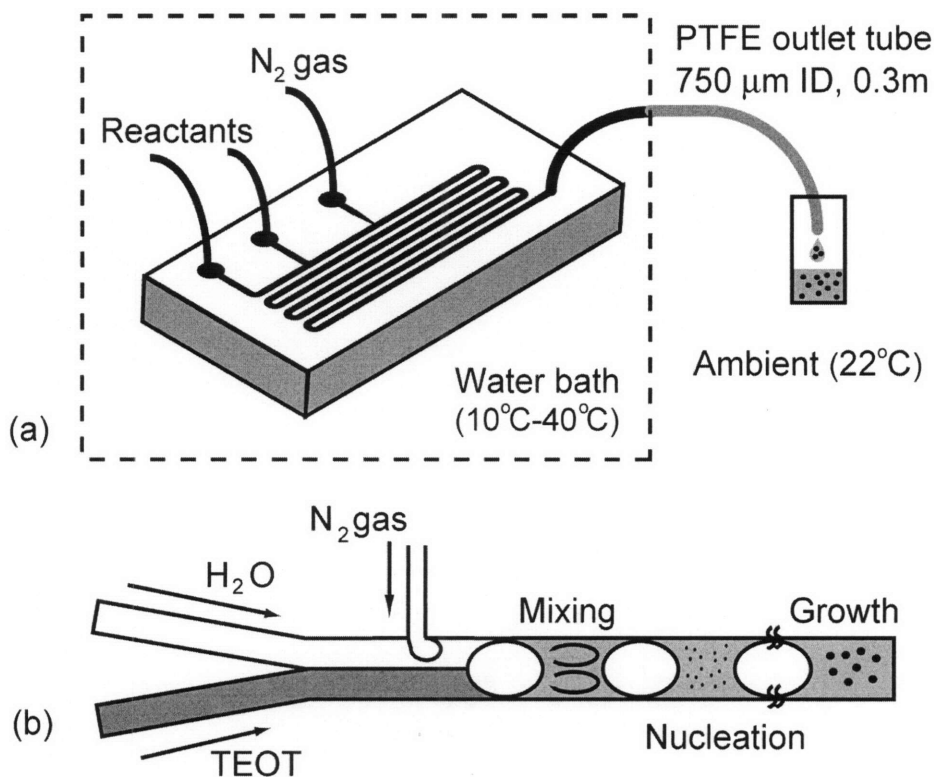
Figure 4-2. (a) Schematic of titania synthesis experimental setup. The microreactor consists of two liquid inlets and a gas inlet, and is submerged in a constant temperature water-bath. (b) Schematic of reactor operation; injection of gas rapidly mixes incoming sol-gel precursors, followed by subsequent nucleation and growth of titania particles.

4.2.2 Microfabrication and packaging

Microreactors were fabricated in poly (dimethylsiloxane) (PDMS) by using standard soft-lithographic techniques[46]. PDMS (Dow Corning Sylgard Brand 184 Silicone Elastomer, Essex-Brownell Inc.) was molded on masters fabricated on silicon wafers using SU-8 2050 (Negative photoresist, Microchem Corporation, MA). Typically, 150 μm thick SU-8 films were spun on 100 mm diameter silicon wafers (Silicon Quest International). Photolithography was used to define negative images of the microfluidic

103

channels, and finally the wafers were developed using SU-8 Developer (Microchem Corporation).
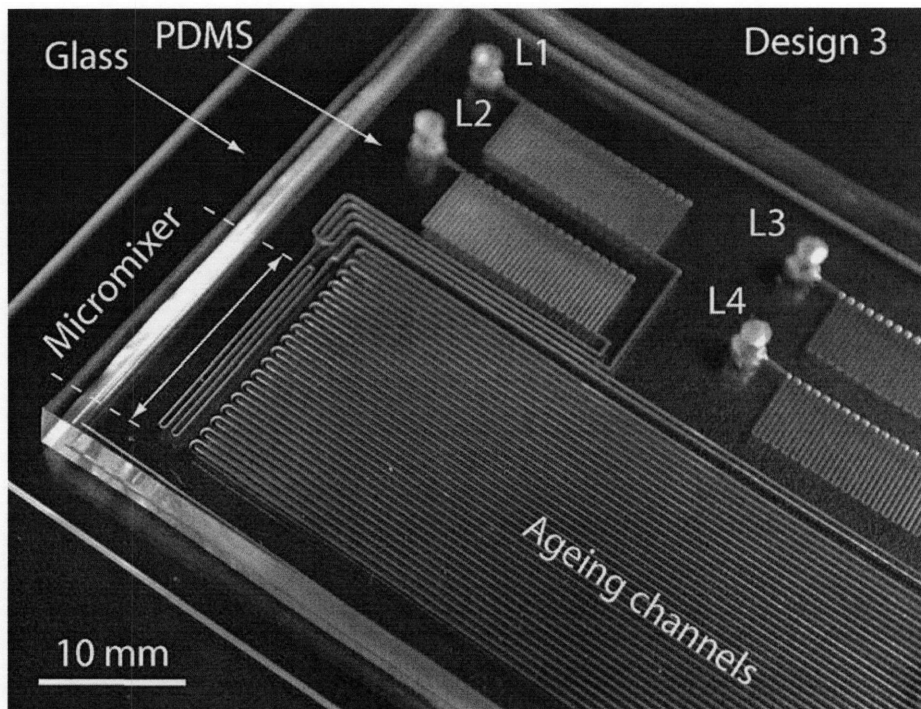
Figure 4-3. Photograph of segmented flow microreactor (Design 3) for silica synthesis: L1-L4 are the liquid inlets.

Packaging of the microreactors was accomplished by the following sequence of steps. PDMS was molded on the SU-8 masters described above at 70°C for 2-12 hours. The devices were peeled off the mold, cut and cleaned. Inlet and outlet holes (1/16-in. o.d.) were punched into the material. Individual devices were sealed to precleaned microscope slides (25 x 75 mm, 1 mm thick, VWR Scientific Inc., or 50 x 75 mm, 1 mm thick, Corning Inc.). Both surfaces were activated in an oxygen plasma (Harrick Co., PDC-32G) for 35 seconds prior to sealing. PEEK tubing (1/16-in. o.d., 508 μm i.d., Upchurch Scientific.) was inserted in the inlet and outlet holes, and glued in place with 5-min epoxy (Devcon). Figure 4-3 is a photograph of a sealed microreactor (Design 3) for silica synthesis.

4.3   Experimental

4.3.1   Stirred-batch silica synthesis

TEOS (99.999%, Aldrich Chemical Co.), ammonium hydroxide (28% NH_3 in water, 99.99+%, Aldrich Chemical Co.), ethyl alcohol (Absolute, Anhydrous, PharmCo Inc.), and deionized water (Reagent grade, 18 $M\Omega$ cm, Ricca Chemical Co.) were used as obtained without further purification. Batch synthesis of monodisperse spherical silica particles was carried out using the Stöber process (4.1.2). A typical synthesis procedure involved the preparation of two stock solutions: the first was a dilute solution of TEOS in ethyl alcohol, and second was a solution of ammonia, water and ethyl alcohol. Equal volumes of the two stock solutions were then rapidly mixed in a small glass vial (20 mL, borosilicate, precleaned; VWR Scientific). A magnetic stir bar (PTFE, VWR Scientific.) agitated the solution. In most cases, faint turbidity was observed within five minutes, and the solutions became progressively more turbid with time. A typical recipe used for comparing the performance of the microreactors with batch reactor synthesis was: 0.1M TEOS, 1.0M NH_3, and 13.0M H_2O (these concentrations corresponded to those in the final mixture obtained after mixing the stock solutions). The Stöber process and its modifications yielded monodisperse particles over a wide range of concentrations.

4.3.2   Stirred-batch titania synthesis

Titania particles were synthesized in a 10 mL glass vial (VWR Scientific) under an argon atmosphere from a Schlenk line, at ambient temperature (22 °C). Two stock solutions were prepared: (a) 0.1 M titanium tetraethoxide (TEOT) in ethyl alcohol and (b) 0.31 M H_2O in ethyl alcohol. TEOT solutions were prepared in a glove box under nitrogen in a 25 ml Schlenk tube. Briefly, 2.3 mL of TEOT (97%, Sigma-Aldrich) was added to 17.8 mL of anhydrous ethyl alcohol, and 25 mg hydroxypropyl cellulose (HPC) (M.W. 300,000, Sigma-Aldrich) was added with stirring. The water solution also contained 1 mg/mL of HPC. Transfer of solution from the Schlenk tube to gas-tight syringes was carried out under a steady stream of argon. 1 mL of TEOT solution was rapidly injected into 2 mL of water solution in ethyl alcohol, and mixed with a magnetic stirrer at 500 rpm. A bright white turbidity indicating particle nucleation was observed in

1 min, and the stirring rate was reduced to 100 rpm. Small aliquots were withdrawn from the vial and centrifuged and washed for electron microscopy observation.

4.3.3   Microreactor experiments: Silica

Stock solutions (4.3.1) were loaded into syringes, and equal flow rates of each were pumped into the reactors using syringe pumps from Harvard Apparatus (PHD 2000 Infusion/Withdraw pumps), and Cole-Parmer (74900 Series). Devices were interfaced with the pumps using PEEK fittings (Upchurch Scientific.), and Teflon tubing (1/16-in. o.d., Cole-Parmer). Air was used as the segmenting fluid in the segmented flow reactor, and was pumped in through Hamilton Gastight syringes (1 mL: 1700 series TTL, 2.5 mL: 1002 series TTL).

4.3.4   Microreactor experiments: Titania

Solutions of titanium tetraethoxide in ethyl alcohol and water in ethyl alcohol (4.3.2) were separately loaded in gas-tight syringes and delivered into the reactor (Fig. 1b). Reactant solutions and nitrogen gas were pumped into the reactors using syringe pumps from Harvard Apparatus (PHD 2000 Infusion/Withdraw pumps), and Cole-Parmer (74900 Series). The solutions were delivered to the reactor in a volumetric ratio of 1:2 TEOT/H_2O, with a total flow rate of 15 µL/min, and gas flow rate of 20 µL/min. Under these conditions, residence times of the liquid segments in the reactor were typically 5 min, and were measured by timing several liquid segments across 10 cm of channel length. Liquid residence time in the outlet tube was 3.8 min. Nitrogen gas was delivered into the third inlet, and the flow rate was adjusted so that a uniform segmented flow regime consisting of alternating segments of liquid and gas was obtained. Recirculatory motion in the liquid segments induced mixing of the reactants, followed by nucleation and subsequent particle growth, as confirmed by an increasing white turbidity along the reaction channel. Aliquots of synthesized particles were collected at the outlet, centrifuged and washed for further electron microscopy observation.

4.3.5   Sample collection and analysis

For silica synthesis, samples were collected on 200-mesh copper grids (2.3 mm diameter, Carbon coated, Ladd Research Inc.). The procedure involved collecting a drop

of the product at the outlet of the reactor and immediately wicking the fluid away with a filter paper, leaving some silica particles behind on the grid[7]. In the titania synthesis experiments, samples were collected in 0.5 mL polypropylene centrifuge tubes. Typically 75 μL aliquots were collected, immediately centrifuged and washed with ethyl alcohol. SEM samples were prepared by placing small drops of washed particle solution onto small silicon pieces (2 mm squares), and drying in an oven at 70 °C. Particle morphology, size and particle size distribution were determined from image analysis of electron micrographs taken on field emission SEMs (JEOL 6320FV and JEOL 5910). Observations from two hundred particles were used in calculations of average size and standard deviation of each sample. Images were analyzed using ImageJ software obtained from NIH, or using Adobe Photoshop.

4.4 Results and discussion

4.4.1 Batch reactors

Batch synthesis of silica is characterized by rapid initial growth, followed by slow growth with a rate that is inversely proportional to the particle size. Figure 4-4 is a summary of small-scale batch synthesis using two different recipes. Recipe 1 [Figure 4-4(a),(b)] contains 0.1M TEOS, 1.0M NH_3, and 13.0M H_2O, while Recipe 2 [Figure 4-4(c),(d)] contains 0.2M TEOS, 2.0M NH_3, and 5.9M H_2O. Recipe 1 yields a final particle size of 460 nm, while Recipe 2 yields a final particle size of 750 nm. The variance of particle size also sharpens with time, from 10% in the initial stages of particle growth to a final value of less than 5%.
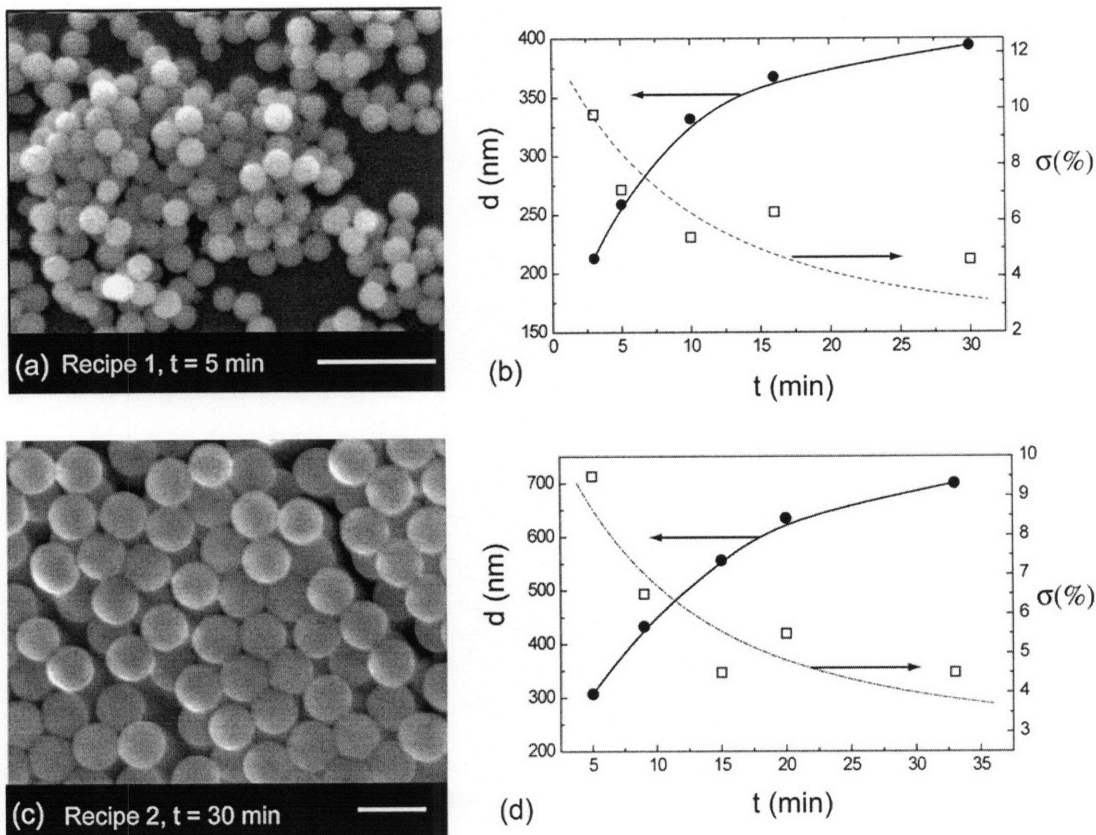
Figure 4-4. Silica batch results: (a) SEM micrograph for Recipe 1: 0.1 M TEOS, 1.0 M NH$_3$, 13.0 M H$_2$O, mean diameter = 259 nm (b) Recipe 1 summary: Graph of mean diameter ('d' nm) and standard deviation (σ) expressed as a percentage of mean diameter versus residence time ('t' min) in the batch reactor. (c) SEM micrograph for Recipe 2: 0.2 M TEOS, 2.0 M NH$_3$, 5.9 M H$_2$O, mean diameter = 695 nm (d) Recipe 2 summary: Graph of mean diameter ('d' nm) and standard deviation (σ). In both SEM micrographs, the scale-bar corresponds to 1 μm.

On the other hand, batch synthesis of titania yields irregularly shaped particles (Figure 4-5(a)), with a large percentage (>20 %) fused into doublets, triplets or higher order agglomerates through shear-induced agglomeration.[47] Such shape distortion and agglomeration caused by high shear rates limits the scalability of batch synthesis. As previously reported, the synthesized particles are amorphous.[19,20]
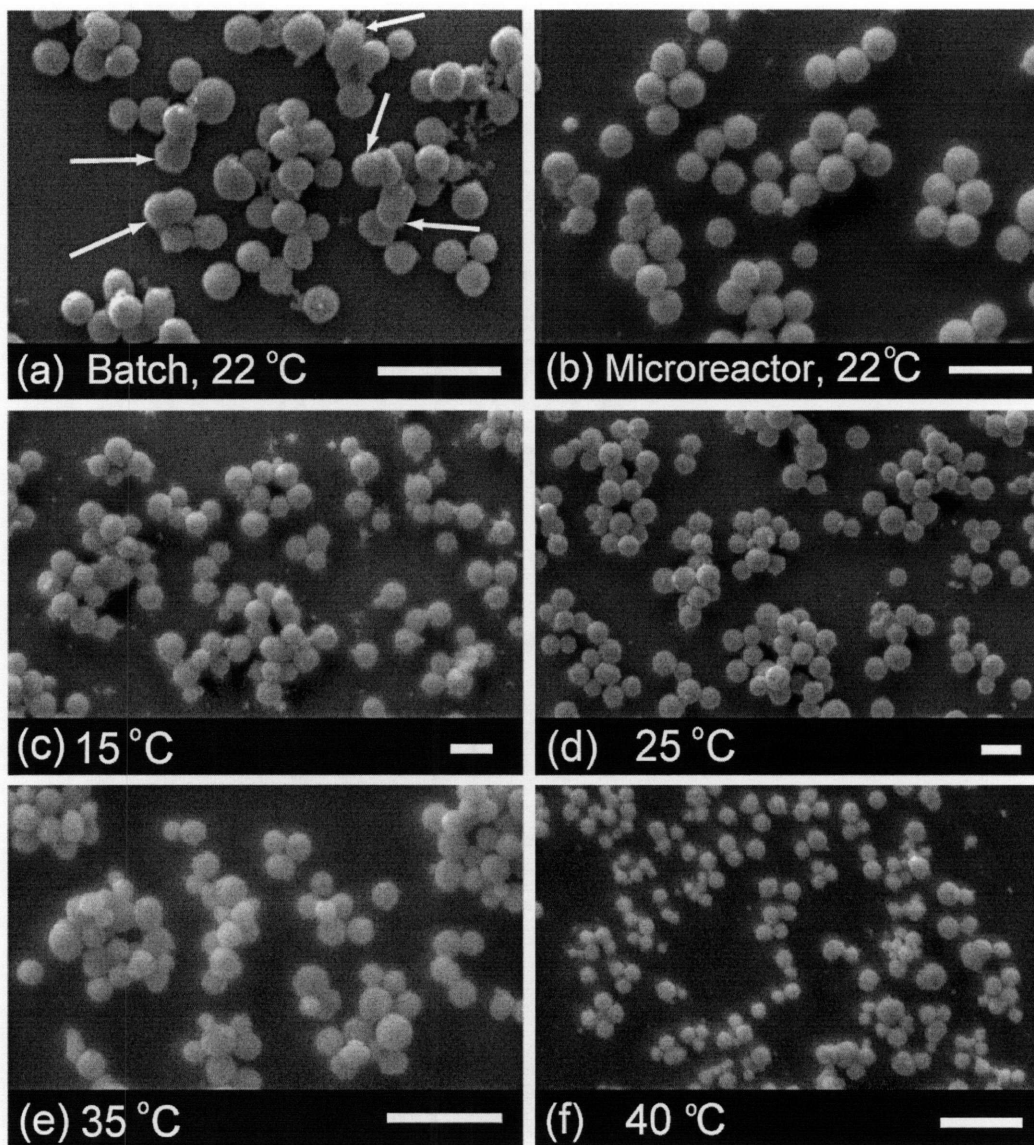
Figure 4-5. SEM of titania particles obtained from (a) Stirred-batch synthesis (agglomerates indicted with white arrows) and (b) microreactor at ambient temperature (22 °C), and from microreactor at temperatures (c) 15 °C (d) 25 °C (e) 35 °C (f) 40 °C. All scale bars are 2 μm.

4.4.2 Microreactor silica

The characteristic growth behavior of silica particles implies that synthesis in a laminar flow reactor will be particularly sensitive to residence time effects at short times. In order to delineate these flow effects, the laminar flow reactor (LFR) corresponding to Design 1 [Figure 4-1(a)] was operated over a range of linear flow velocities from 0.5 mm/s to 6 mm/s, and corresponding volumetric flow rates ranged from 2 μL/min to 20

109

μL/min. These corresponded to mean residence times ranging from 3 min to 30 min. The mean residence time is simply the ratio of the reactor volume to the total volumetric flow rate. Recipe 1 was used in all cases. Figure 4-6 shows SEM micrographs of the particles obtained from the LFR at different operating conditions, with a graphical summary of the different values of mean diameter and standard deviation at various residence times. Mean particle sizes increase with residence time in the reactor, as expected, because of the larger growth time available to the particles. The standard deviation of the mean particle size increases at high flow velocities (lower residence times). This observation is attributed to axial dispersion of the growing colloidal particles as they flow through the reactor[48]. Particles near the wall move slower than particles near the center of the channel, and thus spend more time in the reactor. The larger the amount of axial dispersion, the wider residence time distribution (RTD) becomes.

DiMarzio and Guttman[49] applied Taylor and Aris's original dispersion analysis[50,51] to evaluate longitudinal dispersion coefficients of finite-size spherical particles suspended in a viscous fluid undergoing Poiseulle flow within a cylindrical tube. They obtained a modified Taylor-Aris dispersion coefficient D^*, given by:

$$D^* = D_\infty + \left(\frac{U^2 r^2}{48 D_\infty} \right) \left(1 - \frac{r_p}{r} \right)^6 \tag{4.7}$$

where U is the area-averaged mean flow velocity, r is the radius of the tube, r_p is the particle radius, D_∞ is the particle diffusivity in an unbounded fluid, given by the Stokes-Einstein relation:

$$D_\infty = \frac{k_B T}{6 \pi \mu r_p} \tag{4.8}$$

where k_B is the Boltzmann constant, T is the absolute temperature, and μ is the fluid viscosity. The second term in the parenthesis in Eq.(4.7) accounts for the exclusion of the particle from a layer of thickness r_p around the wall.

Substituting the hydraulic radius of the microfluidic channels (54.5 μm) for the tube radius in Eq.(4.7), and assuming a radius of 200 nm for the calculation of particle diffusivity we can make the following observation on the axial dispersion effect. The small diffusivity of spherical colloidal particles ($\approx 10^{-12}$ m^2/s) implies that the axial

dispersion is dominated by the convective term in Eq.(4.7), which in turn means that the axial dispersion coefficient varies as the square of the average flow velocity. Higher dispersion coefficients lead to wide distribution of residence times, and consequently, broader particle size distributions. This phenomenon is particularly pronounced for low residence times corresponding to early stages of particle growth, as evident in Figure 4-6 (a) and (b). This behavior is consistent with the batch synthesis experiments in which the rate of particle growth is highest during the initial stages of growth (Figure 4-4). In the batch synthesis, the particle size distribution changes less rapidly after the first 15 minutes. Therefore, for sufficiently low linear velocities (corresponding to residence times greater than 15 minutes), the sharpening of the RTD that results from further decrease of linear velocity would be expected to have negligible effect on the width of the particle size distribution. This effect is observed in Figure 4-6(d).
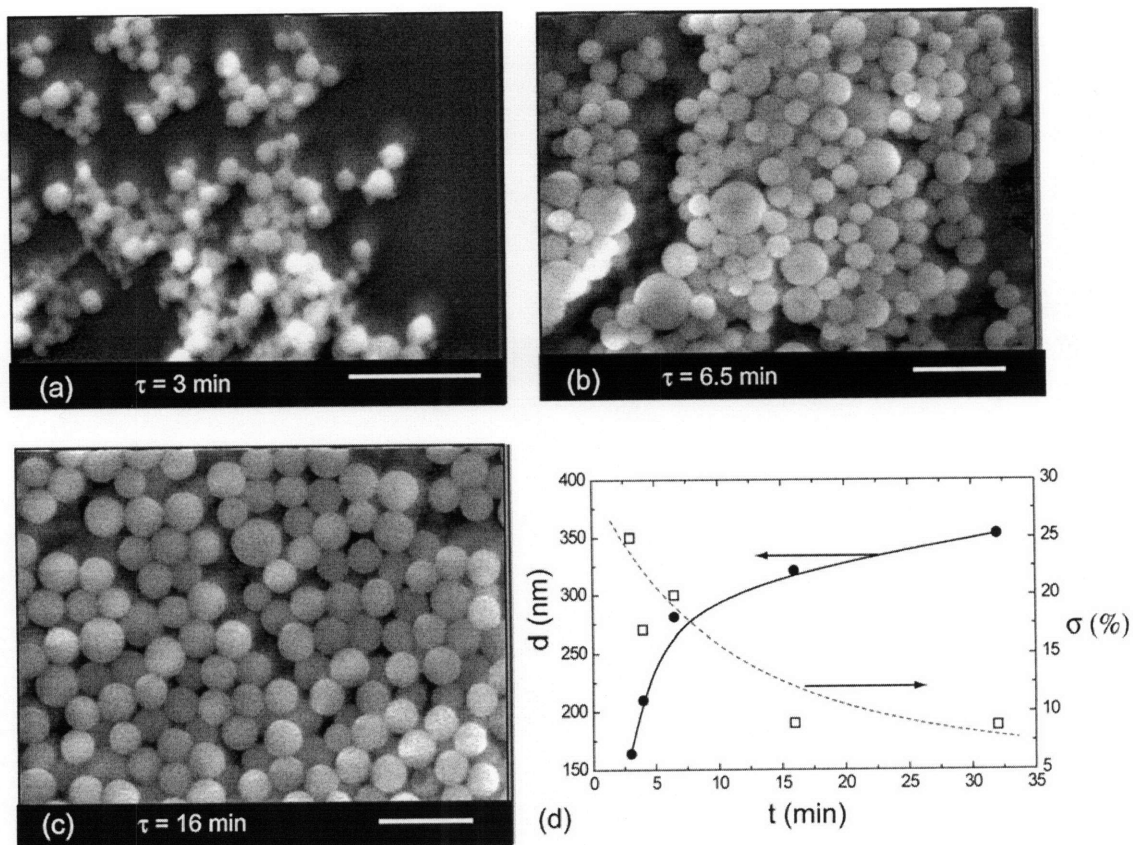
Figure 4-6. Silica synthesis in laminar flow reactor (LFR- Design 1): Sequence of SEM micrographs for recipe 0.1 M TEOS, 1.0 M NH$_3$, 13.0 M H$_2$O, and corresponding to various residence times. (a) τ = 3 min, d = 164 nm, σ = 25%. (b) τ = 6.5 min, d = 281 nm, σ = 20 %. (c) τ = 16 min, d = 321 nm, σ = 9 %. (d) Graph of mean diameter ('d' nm) and standard deviation (σ) expressed as a percentage of mean diameter versus residence time ('t' min) in the reactor. In all SEM micrographs, the scale-bar corresponds to 1 μm.

The segmented flow reactor (SFR) operates on the concept of a reacting 'macrofluid' being processed in a plug flow reactor[31]. A 'macrofluid' is defined as a fluid consisting of a large number of small sealed 'packets', each containing a large number of molecules. Hence an SFR is equivalent to a flow of small batch reactors passing in succession through a plug flow reactor, with the RTD of fluid elements approaching a delta function centered at the value of mean residence time. Since all the small batches spend the same amount of time in the reactor, the product from an SFR is equivalent to the product from a batch reactor. The SFR therefore eliminates the problem of axial dispersion as encountered in the case of the LFR.

We first examine the performance of the SFR corresponding to Design 2 [Figure 4-1(b)]. Two liquid streams containing the reactants (Recipe 1) are introduced at equal volumetric flow rates into the SFR. Total volumetric flow rates range from 4 μL/min to 30 μL/min, corresponding to residence times ranging between 16 minutes to 2 minutes. Gas is injected in 1:1 or 1:2 ratios with respect to the liquid. The gas and liquid flow rates are chosen such that an alternating flow of gas and liquid segments, a slug flow, is obtained. The injected gas segments the flow, and the resulting recirculation creates mixing. Adjacent liquid segments (plugs) are connected through thin liquid films with thicknesses depending on the relative magnitude of viscous to surface tension effects, given by the dimensionless capillary number[52];

$$Ca = \mu U_b / \sigma \qquad (4.9)$$

where μ is the liquid viscosity, U_b is bubble velocity and σ is the interfacial tension. A typical capillary number range for our flow conditions is $10^{-5} - 10^{-3}$. Two liquid segments with a gas bubble in between are connected through menisci in the channel corners that cover, for our case, approximately 5% of the channel cross section[52]. The gas-liquid flow develops downstream from the point of gas introduction with increasing slug length, due to coalescence of gas segments in the channel bends. The thin liquid films connecting the slugs could provide a mechanism for intermixing of particles in different slugs, as could the merging of adjacent slugs at bends. This would widen the RTD from the sharp peak associated with an ideal segmented, plug flow situation. The thin films can be eliminated by appropriate surface-modification of the channels walls to make the reacting mixture non-wetting. In addition, since the incoming gas segments *unmixed* liquids in Design 2, non-uniform reactant distribution between adjacent slugs could occur, thus further widening the particle size distributions.
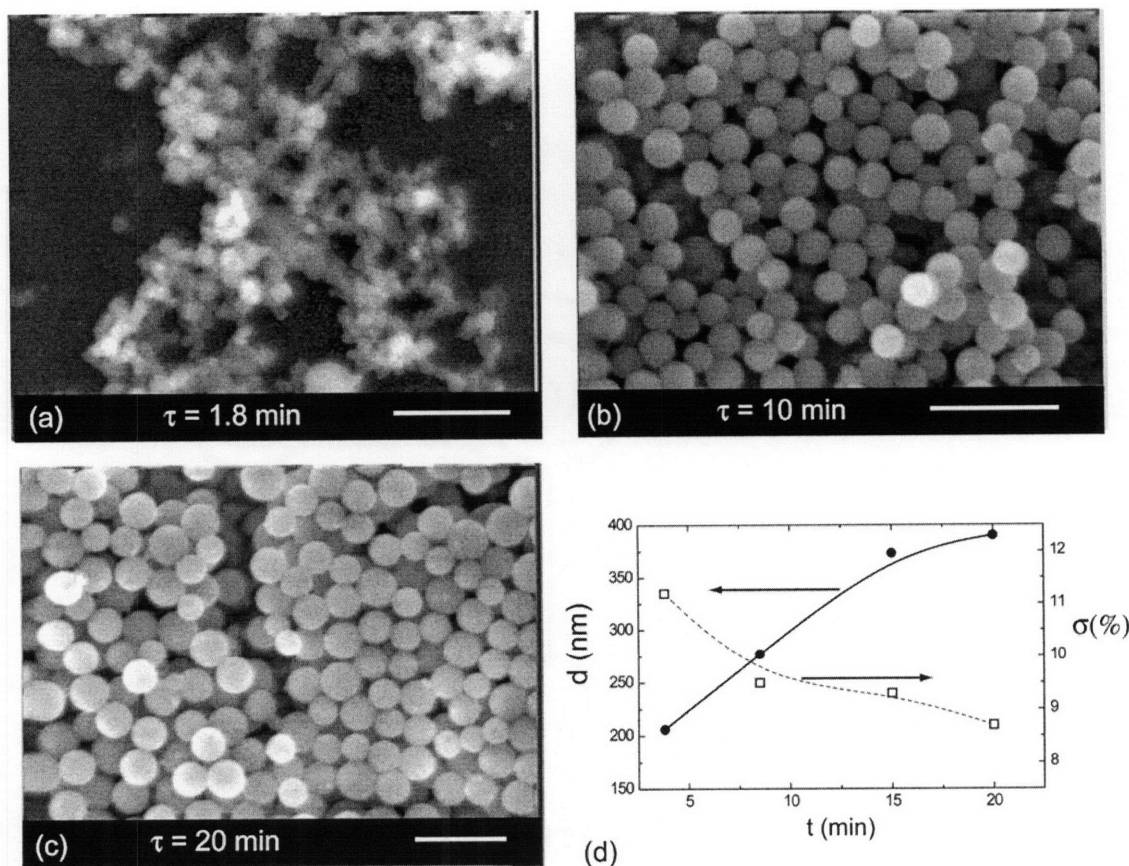
Figure 4-7. Silica synthesis in segmented flow reactor (SFR-Design 2): Sequence of SEM micrographs for recipe 0.1 M TEOS, 1.0 M NH$_3$, 13.0 M H$_2$O, and corresponding to various residence times. (a) τ = 1.8 min (b) τ = 10 min, d = 277 nm, σ = 9.5 %. (c) τ = 20 min, d = 390 nm, σ = 8.7 %. (d) Graph of mean diameter ('d' nm) and standard deviation (σ) expressed as a percentage of mean diameter versus residence time ('t' min) in the reactor. In all SEM micrographs, the scale-bar corresponds to 1 μm.

Figure 4-7 is a summary of particle synthesis results for the Design 2 SFR. As expected, the segmented flow (slug-flow) system produces sharper size distributions than the corresponding LFR in the low residence time regime. However, the narrowest size distribution that can be obtained in the Design 2 SFR ($\approx$8%) is still wider than that from batch synthesis ($\approx$5%), and is almost equal to the corresponding LFR data. We attribute the deviation from batch synthesis to two principal factors: (i). Non-uniform reactant distribution in adjacent segments at the gas inlet, and (ii). Communication between the adjacent liquid segments and their merging at channel bends.
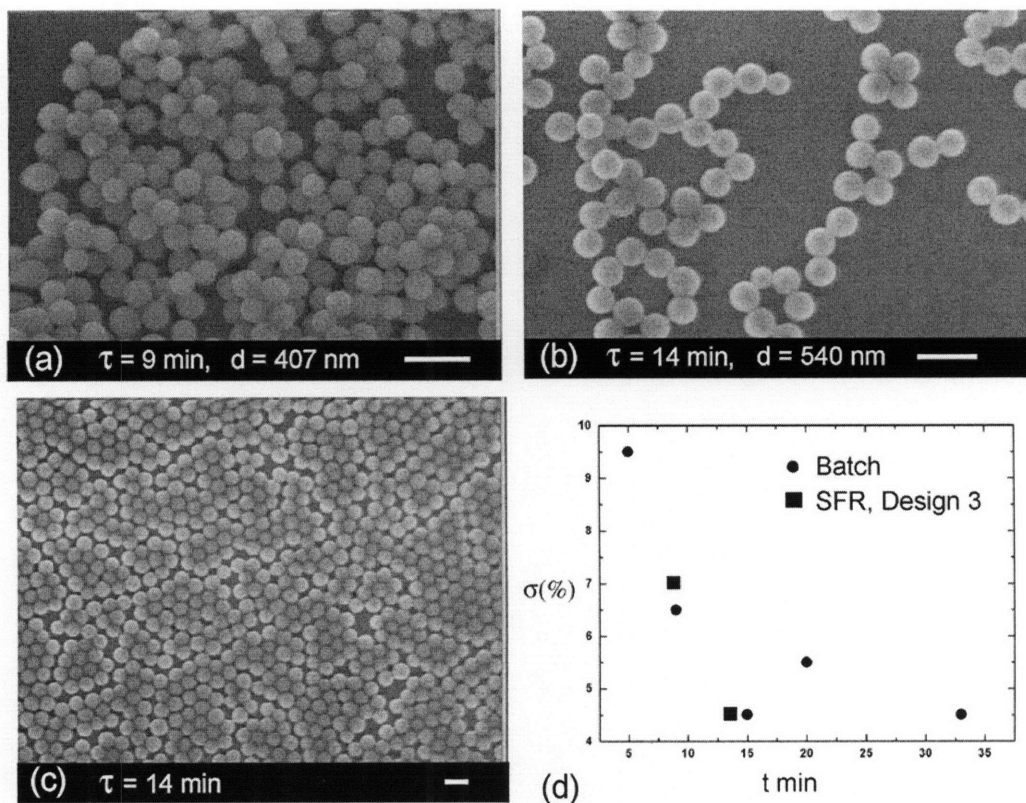
Figure 4-8. Silica synthesis in segmented flow reactor (SFR-Design 3): Sequence of SEM micrographs for recipe 0.2 M TEOS, 2.0 M NH_3, 5.9 M H_2O, and corresponding to various residence times. (a) τ = 9 min, d = 407 nm, σ = 7.1 % (b) τ = 14 min, d = 540 nm, σ = 4.5 % (c) Low magnification SEM of sample (b), the organization of particles into pseudo-crystalline domains is an indicator of the high monodispersity of the microreactor product (d) Graph of standard deviation (σ) expressed as a percentage of mean diameter versus residence time ('t' min) in the SFR as compared to batch reactor data for recipe 2. In all SEM micrographs, the scale-bar corresponds to 1 μm.

Incoming reactant liquids in the Design 3 SFR [Figure 4-1(c)] pass through a micromixing section prior to the introduction of the gas. This design thus prevents any non-uniform reactant distribution effects. In addition, the ageing section in this design is much longer (2.3 X) than those in designs 1 and 2, and stable non-coalescing slug distributions are obtained. Synthesis results from this microreactor are summarized in Figure 4-8. We obtain monodisperse particle size distributions (~ 4.5%) that are equivalent to the corresponding batch results.

4.4.3 Microreactor titania

In comparison to batch synthesis, titania particles from the microreactor are spherical in shape with relatively fewer (<5 %) particles fused into agglomerates (Figure 4-5(b)). Varying the reactor temperature, for the same reactant ratios and residence time, strongly affects the particle size and shape (Figure 4-5(c)-(f)). The average size of the produced particles varies inversely with temperature. Also, particles become irregular in shape at higher temperatures (Figure 4-5(f)). A graphical summary of the above results is presented in Figure 4-9. There is four-fold variation in particle size, from 1.2 μm to 0.3 μm, in the temperature range from 10 °C to 40 °C. Synthesis at 5 °C is an exception to this trend. As indicated in the graph (Figure 4-9), there are two modes of operation depending on reactor temperature relative to the ambient: mode 1 involves flow from a 'cold' zone (reactor) to a 'hot' zone (outlet tube) and mode 2 involves flow from a 'hot' zone (reactor) to a 'cold' zone (outlet tube).
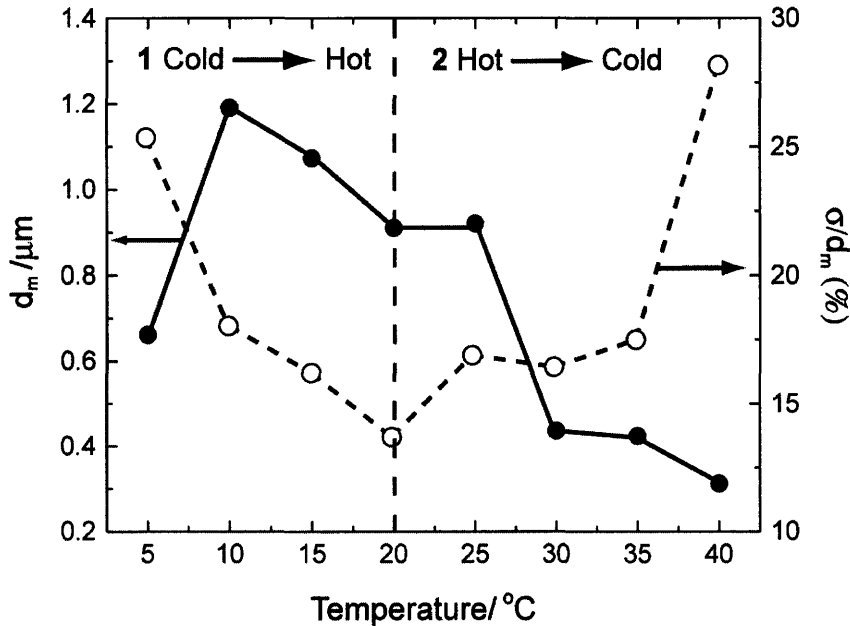
Figure 4-9. Microreactor titania synthesis: Graph of mean diameter (d_m) and standard deviation relative to mean diameter (σ/d_m %) versus temperature. The graph is divided into two regions based on reactor operation mode as indicated, depending on reactor temperature relative to the ambient temperature (22 °C).

116

As noted previously, the onset of bright white turbidity indicates titania precipitation. This occurs at different lengths along the reaction channel at various operating temperatures, indicating different reaction rates. Length is directly proportional to reaction time in a continuous flow microreactor operating at steady state. Visible turbidity appears as early as 13 s (0.12 m channel length) at 40 °C, 65 s (0.62 m channel length) at 20 °C and 260 s (2.5 m channel length) at 10 °C. It is interesting to note that at 5 °C there is no visible turbidity in the microreactor, and all precipitation occurs in the outlet tube leading to the sampling vial. The above observations indicate that hydrolysis rate increases with temperature, and offers a possible explanation for the inverse relationship of particle size with temperature. High hydrolysis rates could lead to multiple nucleation events, occurring simultaneously with growth, thus leading to smaller particles with wide size distributions. Hence we also expect an increasing trend of PSD with temperature. While we observe this trend in mode 2, the opposite trend is observed in mode 1. This can be explained by noting that particles do not grow isothermally in our setup, and are subjected to different temperature profiles depending on operation mode. In mode 1, hydrolysis rates in the reactor are low and proportional to temperature, while residence times in the reactor and tube are fixed (5 min and 3.8 min respectively). If late precipitation occurs, as is the case at low temperatures, there is little time for growth in the reactor before particles enter the outlet tube at higher temperature. Therefore, a higher concentration of unhydrolysed precursor also enters the outlet tube. We attribute the decreasing trend of PSD in mode 1 to secondary nucleation events occurring in the outlet tube due to sudden increase in temperature. The number of secondary nucleation events would increase with the temperature difference encountered by the reaction medium, due to the higher concentration of unhydrolysed precursor present. Synthesis at 5 °C did not follow the inverse trend of particle size versus temperature since particle precipitation and growth occurred primarily in the outlet tube at 22 °C.

4.4.4   Wall effects

PDMS was used as a material of construction to take advantage of rapid prototyping and a relatively simple fabrication process.   The small amount of swelling of PDMS associated with ethanol[53] was not an issue for the present application.   However, other

materials systems requiring organic solvents that swell PDMS[53] will require surface modification to make the microfluidic devices more chemically compatible. Alternatively, other materials of construction such as silicon and glass could be used. All microreactors in this work could be operated for long periods of times without agglomeration of particles on the walls and subsequent plugging. Electron microscopy of a PDMS reactor surface after a typical synthesis experiment lasting about 4 hours revealed a surface covered by a thin layer of silica particles - less than 2 μm thick (Figure 4-10). For the microreactor, we used PDMS as prepared without any surface modification beyond the oxygen plasma treatment to bond the PDMS to the glass slide. We attribute this lack of aggregation on wall to electrostatic effects of the initial thin layer of silica preventing further growth of particles on the wall - in effect stabilizing the wall particle interactions in a manner similar to the electrostatic stabilization of the sol.
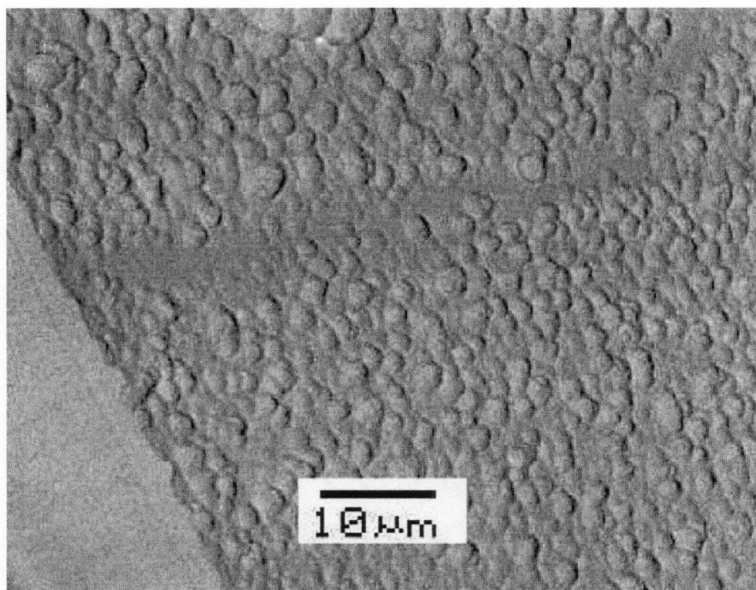
Figure 4-10. SEM micrograph of PDMS reactor wall after a 4 hour silica synthesis run (tilted view). Smooth surface represents a cut-section of the PDMS.

Figure 4-11 also illustrates preferential deposition of this thin silica film at the microchannel wall centers, away from the corners, corresponding to locations where thin liquid films are formed due to the flow of bubbles (Chapter 2). Breaking of the films

causes partial drying and hence some deposition of silica particles. Little or no deposition is seen at the channel corners, corresponding to the location of the thick liquid menisci.
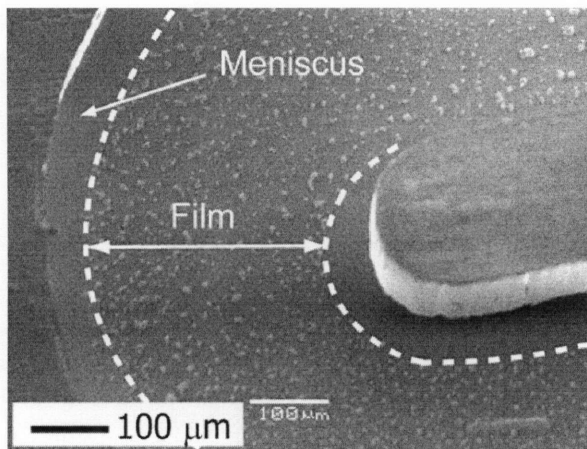
Figure 4-11 Silica particles deposit preferentially in the center of the microchannel walls, corresponding to locations where thin liquid films are formed due to the flow of bubbles (Chapter 2). Breaking of the films causes partial drying and hence some deposition of silica particles. Little or no deposition is seen at the channel corners, corresponding to the location of the thick liquid menisci.

4.5 Conclusions

We have described basic principles of operation of microfluidic reactors for synthesis of colloidal particles. It is possible to tune sizes and size distributions in a controlled fashion by varying the operating variables of linear velocity and mean residence time. For a given laminar flow reactor design, monodisperse particle distributions are only feasible under conditions that minimize axial dispersion. This requirement is especially severe for low residence times, when particle growth rate is the fastest, and wide residence time distributions lead to corresponding wide distributions of particle sizes. Segmented flow reactors eliminate axial dispersion effects and could serve as useful tools for obtaining kinetic data on growth mechanisms. Such reactors are easily scalable for synthesis of larger quantities of materials. We have used temperature as a parameter to control hydrolysis rates in titania synthesis, and hence tune particle sizes over a four-fold range, with polydispersity as low as 13%. Temperature is a powerful parameter that can be used to control colloidal nucleation and growth events, and microfluidic reactors are ideal

tools where such control can be exerted both for scalable synthesis and fundamental mechanistic studies.

4.6   References

1.   Yi, G. R. et al. Generation of uniform colloidal assemblies in soft microfluidic devices. *Advanced Materials* **15**, 1300-+ (2003).

2.   Brinker, C. J. & Scherer, G. W. *Sol-Gel Science: The Physics and Chemistry of Sol-Gel Processing* (Academic Press, Boston, 1990).

3.   Iler, R. K. *The Chemistry of Silica* (John Wiley and Sons, New York, 1979).

4.   Matsoukas, T. & Gulari, E. Dynamics of Growth of Silica Particles from Ammonia-Catalyzed Hydrolysis of Tetra-Ethyl-Orthosilicate. *Journal of Colloid and Interface Science* **124**, 252-261 (1988).

5.   Matsoukas, T. & Gulari, E. Monomer-Addition Growth with a Slow Initiation Step - a Growth-Model for Silica Particles from Alkoxides. *Journal of Colloid and Interface Science* **132**, 13-21 (1989).

6.   Matsoukas, T. & Gulari, E. Self-Sharpening Distributions Revisited Polydispersity in Growth by Monomer Addition. *Journal of Colloid and Interface Science* **145**, 557-562 (1991).

7.   Bogush, G. H. & Zukoski, C. F. in *44th Annual Meeting of the Electron Microscopy Society of America* (ed. Bailey, G. W.) 846-847 (San Francisco Press, Inc., 1986).

8.   Bogush, G. H. & Zukoski, C. F. in *Ultrastructure Processing of Advanced Ceramics* (eds. Mackenzie, J. D. & Ulrich, D. R.) 477-486 (Wiley, New York, 1988).

9.   Bogush, G. H. & Zukoski, C. F. Studies of the Kinetics of the Precipitation of Uniform Silica Particles through the Hydrolysis and Condensation of Silicon Alkoxides. *Journal of Colloid and Interface Science* **142**, 1-18 (1991).

10.   Bogush, G. H. & Zukoski, C. F. Uniform Silica Particle-Precipitation - an Aggregative Growth-Model. *Journal of Colloid and Interface Science* **142**, 19-34 (1991).

11.   Stober, W., Fink, A. & Bohn, E. Controlled Growth of Monodisperse Silica Spheres in the Micron Size Range. *Journal of Colloid and Interface Science* **26**, 62-69 (1968).

12.   LaMer, V. K. & Dinegar, R. H. Theory, production and mechanism of formation of monodispersed hydrosols. *Journnal of the American Chemical Society* **72**, 4847-4854 (1950).

13.   Bogush, G. H., Tracy, M. A. & Zukoski, C. F. Preparation of Monodisperse Silica Particles - Control of Size and Mass Fraction. *Journal of Non-Crystalline Solids* **104**, 95-106 (1988).

14. Hsu, W. P., Yu, R. & Matijevic, E. Paper Whiteners I. Titania Coated Silica. *Journal of Colloid and Interface Science* **156**, 56-65 (1993).

15. Battiston, G. A., Gerbasi, R., Porchia, M. & Rizzo, L. TiO2 coating by atmospheric pressure MOCVD in a conveyor belt furnace for industrial applications. *Chemical Vapor Deposition* **5**, 73-+ (1999).

16. Jiang, X. C., Herricks, T. & Xia, Y. N. Monodispersed spherical colloids of titania: Synthesis, characterization, and crystallization. *Advanced Materials* **15**, 1205-+ (2003).

17. Matijevic, E., Budnik, M. & Meites, L. Preparation and Mechanism of Formation of Titanium-Dioxide Hydrosols of Narrow Size Distribution. *Journal of Colloid and Interface Science* **61**, 302-311 (1977).

18. Barringer, E. A. & Bowen, H. K. Formation, Packing, and Sintering of Monodisperse Tio2 Powders. *Journal of the American Ceramic Society* **65**, C199-C201 (1982).

19. Barringer, E. A. & Bowen, H. K. High-Purity, Monodisperse Tio2 Powders by Hydrolysis of Titanium Tetraethoxide .1. Synthesis and Physical-Properties. *Langmuir* **1**, 414-420 (1985).

20. Barringer, E. A. & Bowen, H. K. High-Purity, Monodisperse Tio2 Powders by Hydrolysis of Titanium Tetraethoxide .2. Aqueous Interfacial Electrochemistry and Dispersion Stability. *Langmuir* **1**, 420-428 (1985).

21. Jean, J. H. & Ring, T. A. Nucleation and Growth of Monosized Tio2 Powders from Alcohol Solution. *Langmuir* **2**, 251-255 (1986).

22. Jean, J. H., Goy, D. M. & Ring, T. A. Continuous Production of Narrow-Sized and Unagglomerated Tio2 Powders. *American Ceramic Society Bulletin* **66**, 1517-1520 (1987).

23. Yonemoto, T., Kubo, M., Doi, T. & Tadaki, T. Continuous synthesis of titanium dioxide fine particles using a slug flow ageing tube reactor. *Chemical Engineering Research & Design* **75**, 413-419 (1997).

24. Tan, C. G., Bowen, B. D. & Epstein, N. Production of Monodisperse Colloidal Silica Spheres - Effect of Temperature. *Journal of Colloid and Interface Science* **118**, 290-293 (1987).

25. Jean, J. H. & Ring, T. A. Effect of a Sterically Stabilizing Surfactant on the Nucleation, Growth and Agglomeration of Monosized Ceramic Powders. *Colloids and Surfaces* **29**, 273-291 (1988).

26. Jean, J. H. & Ring, T. A. Processing Monosized Tio2 Powders Generated with Hpc Dispersant. *American Ceramic Society Bulletin* **65**, 1574-1577 (1986).

27. Ogihara, T., Iizuka, M., Yanagawa, T., Ogata, N. & Yoshida, K. Continuous Reactor System of Monosized Colloidal Particles. *Journal of Materials Science* **27**, 55-62 (1992).

28. Ogihara, T., Ikeda, M., Kato, M. & Mizutani, N. Continuous Processing of Monodispersed Titania Powders. *Journal of the American Ceramic Society* **72**, 1598-1601 (1989).

29. Kubo, M. & Yonemoto, T. Continuous synthesis of TiO2 fine particles and increase of particle size using a two-stage slug flow tubular reactor. *Chemical Engineering Research & Design* **77**, 335-341 (1999).

30. Kaiser, C. H., Hanson, M., Giesche, H., Kinkel, J. & Unger, K. K. in *Fine Particles Science and Technology* (ed. Pelizzetti, E.) 71-84 (Kluwer Academic Publishers, 1996).

31. Levenspiel, O. *Chemical Reaction Engineering* (John Wiley and Sons, New York, 1972).

32. Jensen, K. F. Microreaction engineering - is small better? *Chemical Engineering Science* **56**, 293-303 (2001).

33. Ajmera, S. K., Delattre, C., Schmidt, M. A. & Jensen, K. F. Microfabricated differential reactor for heterogeneous gas phase catalyst testing. *Journal of Catalysis* **209**, 401-412 (2002).

34. Jeon, N. L. et al. Generation of solution and surface gradients using microfluidic systems. *Langmuir* **16**, 8311-8316 (2000).

35. Burns, J. R. & Ramshaw, C. The intensification of rapid reactions in multiphase systems using slug flow in capillaries. *Lab on a Chip* **1**, 10-15 (2001).

36. Burns, J. R. & Ramshaw, C. A microreactor for the nitration of benzene and toluene. *Chemical Engineering Communications* **189**, 1611-1628 (2002).

37. Hessel, V. in *Fourth International Conference on Microreaction Technology* 174-186 (2000).

38. Tice, J. D., Song, H., Lyon, A. D. & Ismagilov, R. F. Formation of droplets and mixing in multiphase microfluidics at low values of the Reynolds and the capillary numbers. *Langmuir* **19**, 9127-9133 (2003).

39. Yen, B. K. H., Stott, N. E., Jensen, K. F. & Bawendi, M. G. A continuous flow microcapillary reactor for the preparation of a size series of CdSe nanocrystals. *Advanced Materials* (2003).

40. Chan, E. M., Mathies, R. A. & Alivisatos, A. P. Size-controlled growth of CdSe nanocrystals in microfluidic reactors. *Nano Letters* **3**, 199-201 (2003).

41. Edel, J. B., Fortt, R., deMello, J. C. & deMello, A. J. Microfluidic routes to the controlled production of nanoparticles. *Chemical Communications*, 1136-1137 (2002).

42. Nakamura, H. et al. Preparation of CdSe nanocrystals in a micro-flow-reactor. *Chemical Communications*, 2844-2845 (2002).

43. Nakamura, H. et al. Continuous preparation of CdSe nanocrystals by a microreactor. *Chemistry Letters*, 1072-1073 (2002).

44.   Kanai, M. et al. in *Seventh International Conference on Micro Total Analysis Systems* (eds. Northrup, M. A., Jensen, K. F. & Harrison, D. J.) 429-432 (Transducers Research Foundation, Squaw Valley, California, USA, 2003).

45.   Jackman, R. J., Floyd, T. M., Ghodssi, R., Schmidt, M. A. & Jensen, K. F. Microfluidic systems with on-line UV detection fabricated in photodefinable epoxy. *Journal of Micromechanics and Microengineering* **11**, 263-269 (2001).

46.   Xia, Y. N. & Whitesides, G. M. Soft lithography. *Annual Review of Materials Science* **28**, 153-184 (1998).

47.   Russell, W. B., Saville, D. A. & Schowalter, W. R. *Colloidal Dispersions* (Cambridge University Press, 1989).

48.   Silebi, C. A. & Dosramos, J. G. Axial-Dispersion of Sub-Micron Particles in Capillary Hydrodynamic Fractionation. *Aiche Journal* **35**, 1351-1364 (1989).

49.   Dimarzio, E. A. & Guttman, C. M. Separation by Flow. *Macromolecules* **3**, 131 (1970).

50.   Aris, R. On the dispersion of a solute in a fluid flowing through a tube. *Proceedings of the Royal Society of London A* **235**, 67-77 (1956).

51.   Taylor, G. I. Dispersion of Soluble Matter in Solvent Flowing Slowly through a tube. *Proceedings of the Royal Society of London A* **219**, 186-203 (1953).

52.   Wong, H., Radke, C. J. & Morris, S. The motion of long bubble in polygonal capillaries. Part 1. Thin films. *Journal of Fluid Mechanics* **292**, 71-94 (1995).

53.   Lee, J., Park, C. & Whitesides, G. M. Solvent Compatibility of Poly(dimethylsiloxane)-based Microfluidic devices. *Analytical Chemistry* **75**, 6544-6554 (2003).

5 Microfluidic Surface-Engineering

5.1 Introduction

This chapter describes continuous flow microfluidic reactors for coating colloidal silica particles with titania layers of tunable thickness. The goal of this work is to demonstrate a microfluidic route to surface-engineered colloidal particles, and address the challenge of producing uniform, tunable-thickness inorganic shells without aggregation or formation of secondary particles of the coating material. The ultimate vision is to integrate particle synthesis and surface-engineering on one platform, and is the subject of Chapter 6. In this work, we use the controlled hydrolysis of titanium tetraethoxide to coat colloidal silica with amorphous and crystalline titania. We describe the design, fabrication and operation of a continuous flow microfluidic reactor that enables particle coating with complete suppression of secondary nucleation, thus preserving the monodispersity of the starting silica particle size distribution. Photolithography-based microfabrication enables splitting and multi-step addition of the titanium precursor feed flow. This allows us to keep the precursor concentration in the reactor at low levels at all times, and hence suppress the formation of a secondary phase of colloidal titania. Titania coatings of two different thicknesses are obtained depending on the feed rate of titanium tetraethoxide. The size and morphology of the synthesized core-shell particles are characterized by scanning and transmission electron microscopy, and X-ray photoelectron spectroscopy.

5.1.1 Nanoparticle coatings and processes

In the last decade, there has been considerable research interest in core-shell colloidal materials with tailored structural, photonic and surface properties with potential applications in advanced materials science and technology. Core-shell materials enable tuning of physical and chemical properties over their single-component counterparts. Caruso has reviewed the extensive literature on nanocoating techniques of colloidal particles to create core-shell type materials.[1] Such materials have been utilized for a

variety of applications including coatings, pigments, electronics, catalysis, separations and diagnostics. The most commonly used core particles are polymeric (e.g. polystyrene)[2], inorganic[3] (e.g. silica) or metallic[4] (e.g. gold) in size ranges between 2 nm to 10 μm. Several coating materials and processes have been demonstrated, such as polymerization[5], layer-by-layer (LbL) self-assembly of polyelectrolytes[6], electroless plating[7] and sol-gel nanocoating[8].

5.1.2 Titania-on-silica core-shell particles

Titania-silica core-shell particles in the sub-micron size range are of potential interest for several applications, including catalysis[9], pigments (as whiteners)[10] and photonic band-gap materials.[11] The high refractive index contrast between silica and titania make sub-micron multi-layered core-shell particles promising candidates for use as optically responsive particles for biological imaging and sensing.

Several methods have been reported for titania-coated-silica synthesis. Hsu and Matijevic have coated titania layers of varying thicknesses by aging an acidified titanyl sulfate ($TiOSO_4$) solution in the presence of silica particles.[10] Thick layers were obtained via a multi-step coating process that involved repeated filtration and redispersion cycles. Kumacheva et al. have reported a modification of this technique to give thick (~40 nm) layers of amorphous titania by heterocoagulation of positively charged titanyl sulfate clusters with negatively charged silica particles.[12,13] Other methods to synthesize titania-silica particles include the use of polyelectrolyte-coated silica spheres as templates for sol-gel reactions[14], and the deposition of alternating coatings of cationic polyelectrolytes and anionic titania nanosheets on the surface of silica.[15]

Sol-gel methods to coat titania on silica via controlled hydrolysis of titanium alkoxides have been reported by several research groups. Srinivasan et al. hydrolyzed titanium n-butoxide in tetrahydrofuran to yield monolayer coatings on 270 nm silica particles.[9] Hanprasopwattana et al. demonstrated thin coatings of titania (<7 nm) on silica by the hydrolysis of titanium n-butoxide.[16] In their procedure, an ethanol solution of titanium n-butoxide containing silica particles was refluxed for several hours after a certain amount of water was added. Dong et al. extended this technique to a multi-step semi-batch process using the same precursor, and thick coatings (~46 nm) were obtained after five

coating steps.[11] Repeated centrifugation, washing and resuspension cycles were needed in between consecutive coating steps. Holgado et al. used titanium tetraethoxide (TEOT) as a precursor to obtain thick (>50 nm) coatings in a single step process.[17] Kim et al. also used a semi-batch process to obtain ~10 nm coatings using TEOT, using hydroxypropyl cellulose (HPC) as a steric stabilizer.[18] A TEOT-ethanol solution containing HPC was pumped at a controlled rate into an H_2O-ethanol solution containing silica particles. The mixture was further aged after the TEOT addition was completed. Particle size and aggregation was found to vary with rate of alkoxide addition, reaction temperature, and water and alkoxide concentrations.

5.1.3 Macroscale approaches and limitations

There are several difficulties associated with synthesizing titania-silica core-shell structures. The titanium alkoxide precursors used in sol-gel coating are highly reactive, with rapid hydrolysis rates. In general, reactivity of the precursors increases with decreasing alkoxy (-OR) group size.[19] This makes it difficult to control the particle coating process, and homogeneous nucleation of secondary titania particles, as well as severe aggregation of silica cores often occurs. In addition to these challenges, it is also difficult to reliably tune titania shell sizes by varying process parameters. Conventional sol-gel nanocoating processes reported in the literature are limited to multi-step batch or semi-batch processes involving repeated centrifugation/filtration and redispersion cycles between steps. Rapid stirring is often used for micromixing, and can cause undesired shear-induced agglomeration and shape-distortion.[20] Reproducibility is a problem due to frequent batch-to-batch product variations.[21] These bench-scale techniques are also not easily scalable to larger amounts of production. It is therefore desirable to develop continuous flow processes to overcome many of these challenges. However, to date, no continuous flow processes for sol-gel nanocoatings have been reported. In the following sections, we examine the anatomy of semi-batch (5.1.4) and continuous flow reactors (5.1.5). We then describe how microfabrication enables the facile design of continuous flow microfluidic reactors for coating processes (5.1.6).

126

5.1.4 Semi-batch reactor

Figure 5-1 illustrates a semi-batch reactor for sol-gel nanocoating of titania on silica. The main idea is to maintain low titanium alkoxide concentration at all points within the reactor at all times to formation of secondary titania particles. To accomplish this, a silica suspension in ethanol containing a small amount of water is first taken in a vessel. A titanium alkoxide solution in ethanol is fed continuously from a reservoir (e.g. a syringe) into the vessel with stirring. The incoming alkoxide solution is fed into the vessel at low flow rates, such that the volume of every incoming aliquot is much smaller than the total fluid volume in the vessel. The alkoxide concentration in the reaction vessel may thus be decreased by more than 100 times its value in the reservoir. The particles are further aged after the addition is complete. As depicted in Figure 5-1, titania shells grow progressively with time. Shell thickness may be tuned by varying inter-related operating parameters such as alkoxide and water concentrations and alkoxide addition rate. For example, for a fixed ratio of final added volumes of titanium and water solutions, increasing the feed rate of alkoxide increases its net concentration in the reaction vessel. The upper limit of alkoxide concentration is achieved when all of the alkoxide solution is added to the reaction vessel at once, in which case the reservoir alkoxide concentration is decreased by a factor equal to the ratio of added alkoxide volume to final liquid volume inside the vessel. This case simply corresponds to the single step batch process reported by most authors.
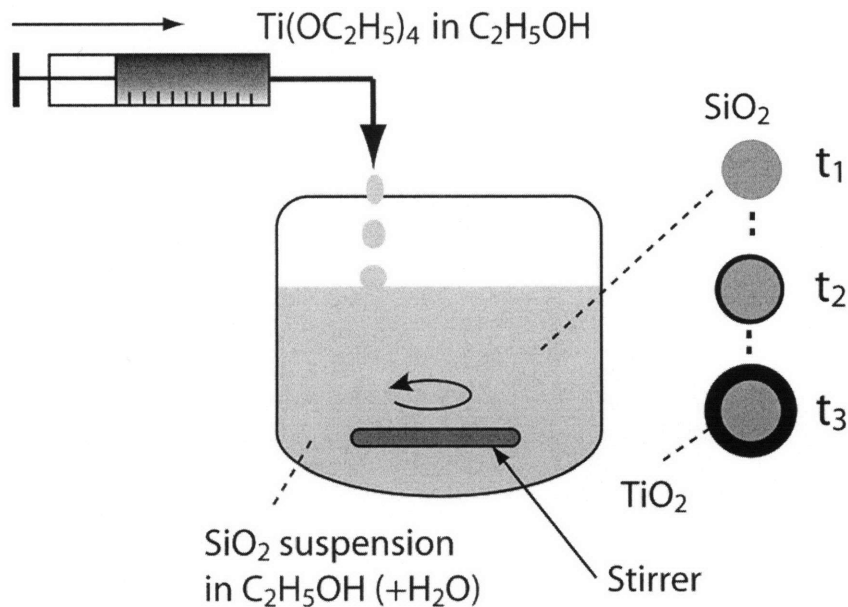
Figure 5-1 Schematic of semi-batch coating process. Titanium alkoxide is continuously fed into a vessel containing silica particles suspended in ethanol (with a small amount of added water).

5.1.5   Continuous flow reactor for sol-gel coating: General requirements

An idealized continuous flow reactor suitable for sol-gel overcoating subject to the various requirements (5.1.4) is schematically depicted in Figure 5-2. A silica suspension in ethanol containing a small amount of water is fed continuously to the inlet of a plug flow reactor. A titanium alkoxide solution is introduced at N feed points corresponding to lengths L_1, L_2, L_3,..., and L_N along the length L of the reactor. The incoming alkoxide is instantaneously mixed with the reactor contents and its concentration is thus maintained at low levels throughout the volume of the reactor. As shown in the figure, the titania shell thickness on silica particles progressively increases along the length of the reactor. The reactor contains particles with a progression of titania shell thicknesses at all times. This situation is quite different than a batch or semi-batch reactor where all particles in the reactor have (approximately) the same shell thickness at any given time. By properly adjusting reactant concentrations and feed rates, it is possible to continuously synthesize titania coated particles with uniform, predetermined shell sizes without the need for intermediate separation and redispersion steps.

128
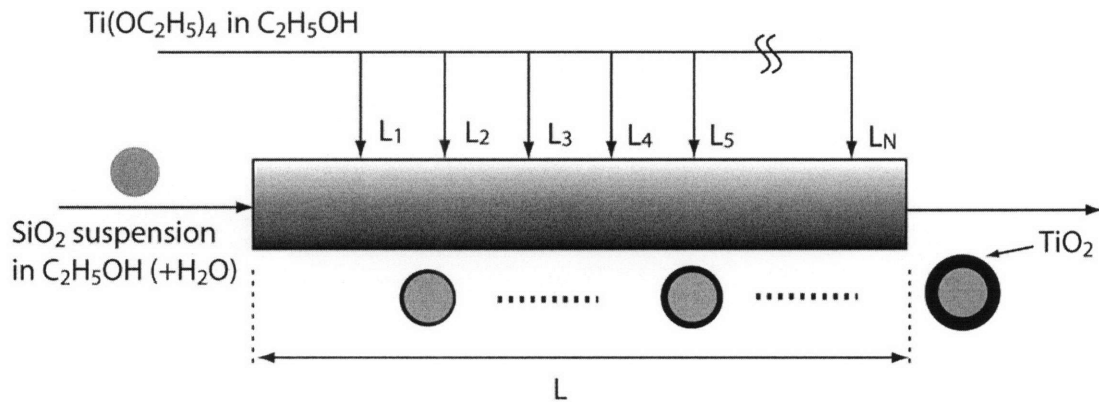
Figure 5-2 Schematic of an idealized continuous flow reactor for titania coating

In practice, a potential macroscale realization of the idealized reactor described above is shown in Figure 5-3(a). It consists of N stirred tanks in series, with an alkoxide solution feed split and introduced in equal amounts to each tank. Another alternative realization of the idealized reactor shown in Figure 5-3(b) is a series of N static mixers connected together with tubes of small internal diameter. It is apparent on examining the figure that construction of such reactors is a challenging task, and the final product may still depend on details such as stirring rate or type of micromixer used. In addition, each unit in the above assemblies has a finite residence time distribution (RTD), and the overall RTD of the assembly is a convolution of individual unit RTDs. Thus, wide RTDs may be expected from multi-unit assemblies leading to polydisperse particle size distributions.
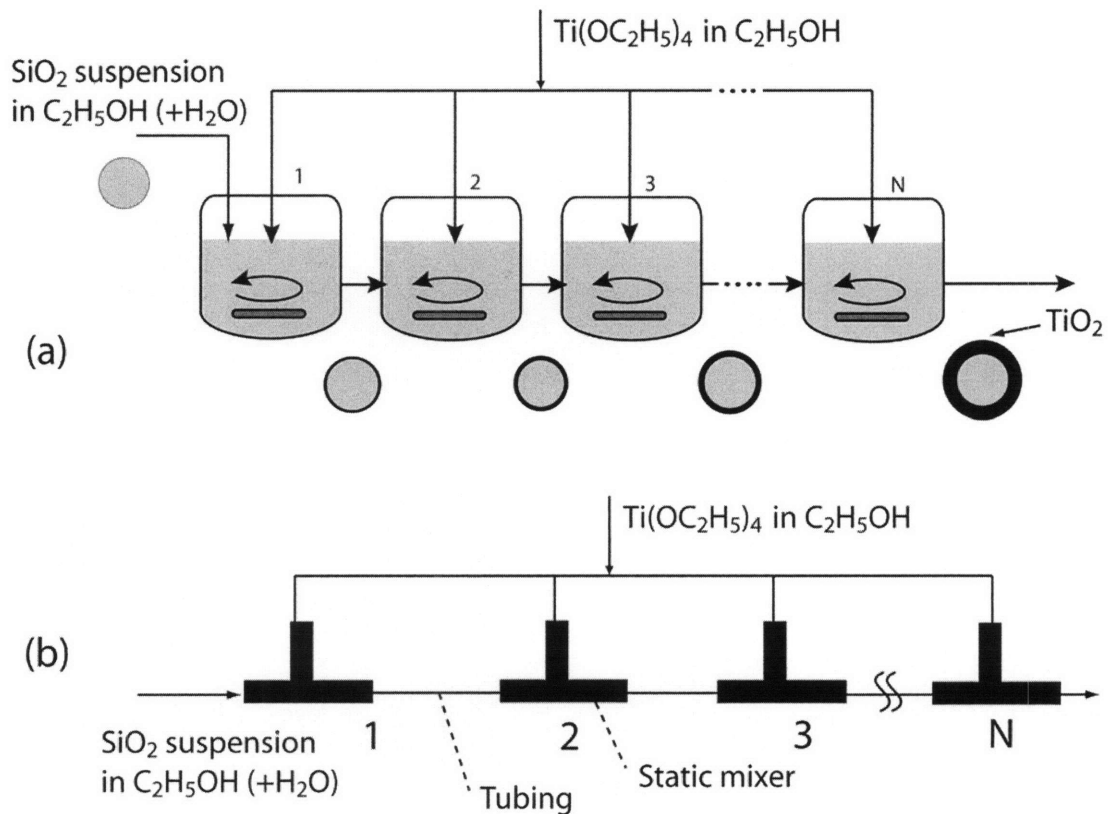
Figure 5-3 Macroscale realizations of idealized reactor in Figure 5-2 (a) N Stirred-tanks connected in series to each other, and an alkoxide feed added with stirring to each reactor. (b) N static mixers connected in series with narrow diameter tubing.

5.1.6 Microfluidic continuous flow reactor concept

The design concept for a microfluidic continuous flow coating reactor is depicted schematically in Figure 5-4. The microreactor has three inlet channels and one outlet channel for the coated particles. A silica suspension in ethanol containing a small amount of water is fed continuously to the first inlet and nitrogen gas is introduced into the second inlet. This three-phase mixture flows along the main reaction channel. A titanium alkoxide solution is introduced into the third inlet, and the flow is split into several branches that feed the alkoxide into the main reaction channel at multiple points. As shown in Figure 5-4, the gas serves two purposes: it segments the flow into alternating liquid and gas segments, thus ensuring uniform residence time distribution (Chapter 3), and also mixes the incoming alkoxide with the suspended particles via recirculatory motion inside the liquid segments (Chapter 2). Photolithography-based microfabrication

130

allows us to define complex microchannel geometries, which in combination with multiphase flows, enable the integration all of the functions required of the continuous flow reactor described in 5.1.5 onto one device.
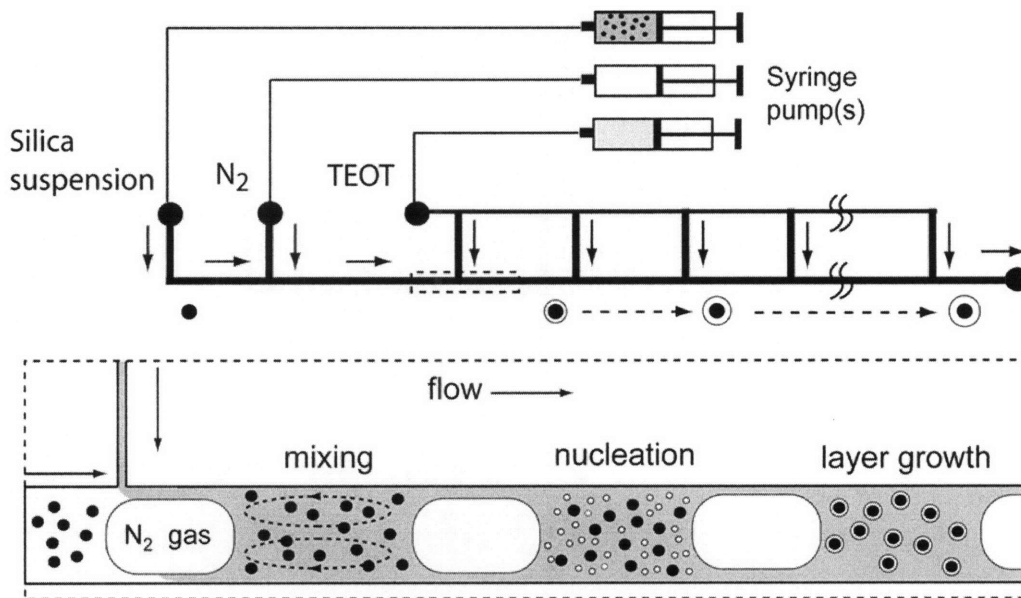
Figure 5-4 Schematic of continuous flow microfluidic reactor.

5.2   Microreactor design and fabrication

5.2.1   Design methodology and circuit model for coating reactor

In the present work, the microreactor conceptualized in 5.1.6 was designed to have eight points of titanium precursor addition at fixed intervals along the main reaction channel. The precursor feed inlet was manifolded to obviate the need for several individual feed reservoirs and inlets. Hence one inlet was designed to split into eight feed streams which fed approximately equal volumetric rates of precursor into the main reaction channel. Since this was a relatively complex fluidic network, it was critical to design the network dimensions to prevent liquid maldistribution in the various network arms. Figure 5-5 is a diagram of the microfluidic network, showing the hydraulic resistances (R) of the microchannels, flows (Q) in the channels, and pressures (P) at the various nodes.

131
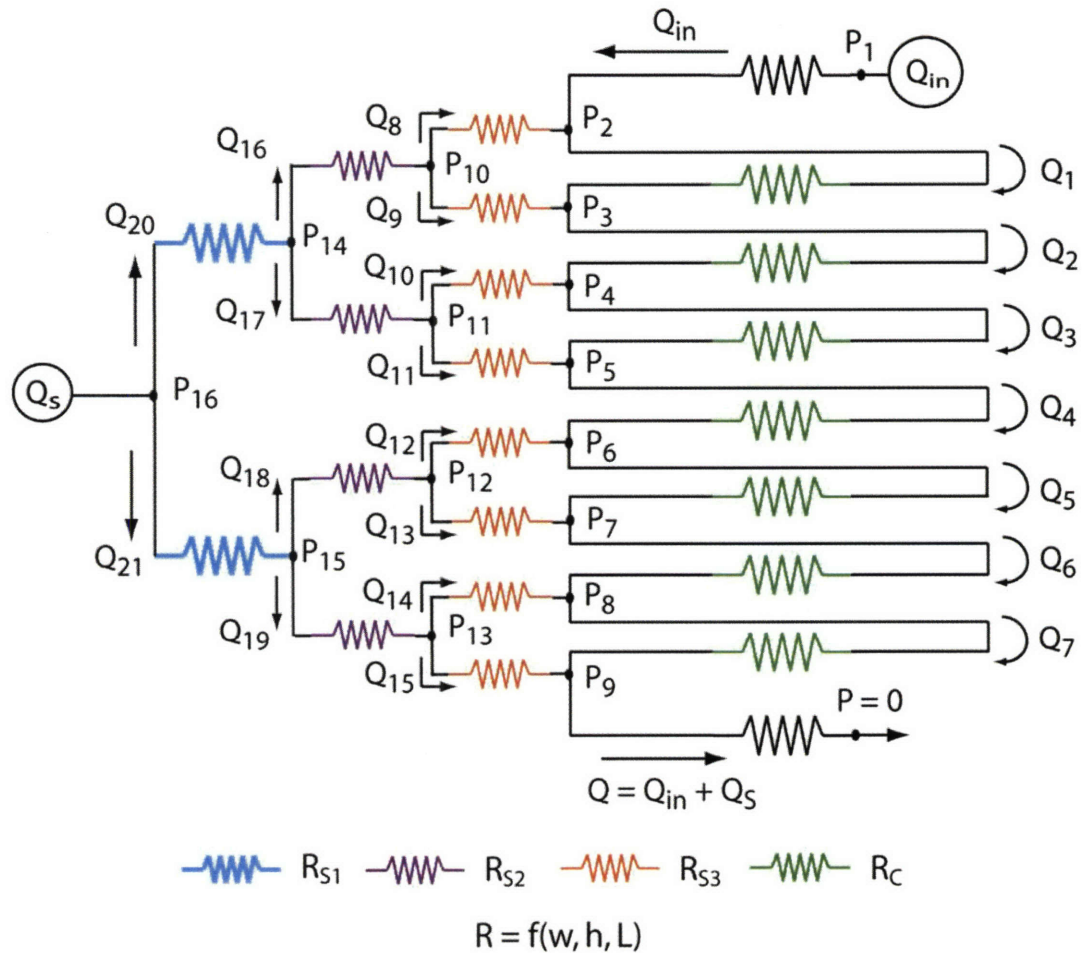
Figure 5-5 Circuit model for microfluidic coating reactor showing hydraulic resistances R, flows Q and pressures P. Further details in text.

We use the Hagen-Poiseulle (H-P) equation to model the flow of liquid through the channels of the network. Reactor design calculations are made for single-phase flow of liquid, and the validity of this design to handle gas-liquid flow is discussed in 5.2.3. The functional form of the H-P equation is shown in Equation (5.1). Liquid flow Q through a microchannel, between two pressure nodes, is directly proportional to the pressure drop ΔP, and the proportionality constant is the hydraulic resistance R of the microchannel. This is directly analogous to Ohm's Law for linear electrical circuits, where the current I is proportional to the voltage drop ΔV, and the linear proportionality constant is the electrical resistance R.

$$\Delta P = R \cdot Q \iff \Delta V = R \cdot I \qquad (5.1)$$

The microfluidic network can thus be designed as a linear electrical circuit, provided that the hydraulic resistance also has a linear functional form. This is indeed the case for laminar flow through microchannels where the hydraulic resistance is given by[22]:

$$R = \frac{8\mu L}{\pi \left(\frac{d_E}{2}\right)^4} \tag{5.2}$$

where μ is the liquid viscosity and L is the microchannel length. Also, d_E is the 'equivalent diameter' for a microchannel with rectangular cross-section, and is given by[22]:

$$d_E = \left(\frac{128wh^3}{\pi K}\right)^{1/4} \tag{5.3}$$

where w and h are respectively the width and height of the microchannel and K is a constant that depends on the aspect ratio w/h. For example, for $w/h=1.5$, K is 20.43. For a given set of dimensions (w, h, L) of the various arms of the fluidic network and incoming flows Q_{in} and Q_s, there are a total of 37 unknowns in the network, as shown in Figure 5-5. These unknowns are node pressures P_1 to P_{16} and volumetric flow rates Q_1 to Q_{21}. The H-P equation can be applied to the 23 hydraulic resistances in the network. In addition, flow is conserved at each node (for e.g. $Q_3+Q_{11}=Q_4$). Hence, 14 flow conservations equations together with the 23 H-P equations provide a set of linear equations that can be simultaneously solved using standard techniques of linear algebra to yield the unknown node pressures and flows.

The reactor is iteratively designed using the above set of equations. For a given range of desired operating flow rates Q_{in} and Q_s, the main design criterion is the requirement of positive values of Q in all arms of the network (negative Q implies undesirable back-flow). Backflow of liquid occurs from the main reaction channel into the channels of the side inlet manifold at large ratios of Q_{in} to Q_s. The width and length of the main reaction channel and height of all the microchannels are fixed at the start of the design process by materials and processing constraints, such as the maximum thickness of SU-8 films that may be uniformly spun on a wafer (~250 µm). The width and length of the various arms of the side inlet manifold are iteratively varied in the design calculations, until an

(approximately) equal distribution of Q_s into flows Q_8 to Q_{15} is obtained and no backflow into the manifold is predicted by the calculation over the entire range of Q_{in} and Q_s.

5.2.2 Microreactor dimensions

The final dimensions of the reactor used in this study are shown in Figure 5-6. Three inlets (1, 2 and 3) lead into a main reaction channel that is 300 μm wide and 2.1 m long. All microchannels are ~250 μm deep. The first side inlet (S1) feeds liquid into the main channel 0.18 m downstream of inlet M3. Thereafter, the remaining side-inlets (S2-S8) feed liquid at regular intervals 0.25 m downstream of each other. A manifold splits the side reactant feed (4) into eight streams, as shown in Figure 5-6. All manifold channels are 40 μm wide and 250 μm deep. The first two splits have a length of 0.2 m each, the next four splits have a length of 0.1 m each and the final eight splits also have a length of 0.1 m each. Figure 5-7 is a photograph of the fabricated microreactor.
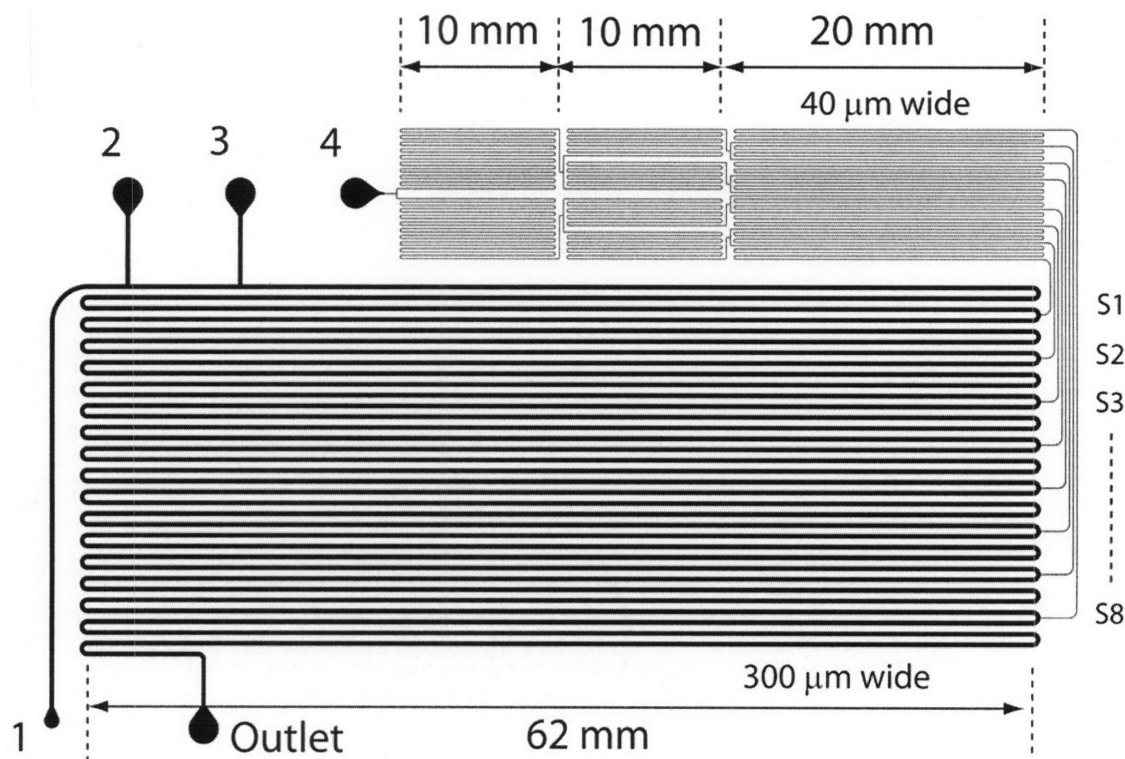
Figure 5-6 Dimensions of microreactor for titania coatings
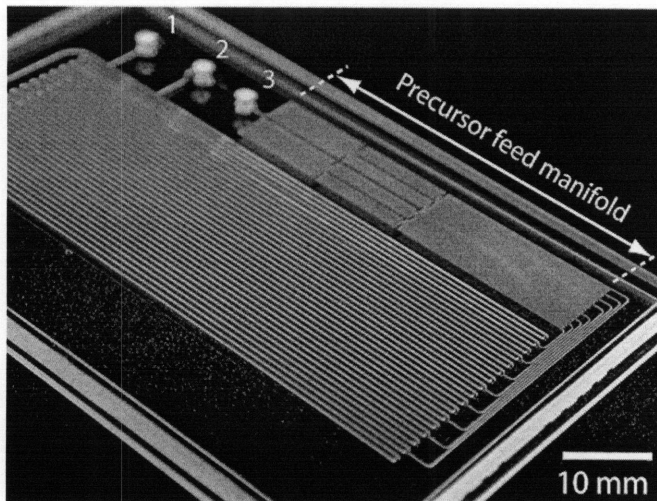
Figure 5-7 Photographs of manifolded microreactors for flow visualization (5.4.2)

5.2.3   Validity of design for two-phase flow

Using the pressure drop model for bubble trains developed in Chapter 2, we find gas-liquid pressure drops, for the same total volumetric flow rates, are typically 2-3 times greater than the corresponding liquid-phase pressure drops when the bubble sizes and liquid segment lengths are typically of the order of channel dimensions (as is the case in our study).[23] In other words, gas-liquid flow has greater flow resistance associated with it for a given flow rate than does single-phase liquid flow. For single phase flow, hydraulic resistance scales directly with length and as the inverse fourth power of characteristic channel dimension.

$$R \, \alpha \, \frac{L}{r_E^4} \tag{5.4}$$

Hence, since our side-inlet channels have equivalent diameters approximately four times smaller than the main reaction channel, their hydraulic resistance is much larger (at least 80x) than that of the main channel, for comparable flow rates. The inverse fourth power relationship with channel dimension easily offsets the factor of three increase in main channel flow resistance due to two-phase flow. Our design calculations are therefore valid for the two-phase flow case.

135

5.2.4 Microfabrication and packaging

Microreactors were fabricated in poly (dimethylsiloxane) (PDMS) by using standard soft-lithographic techniques[24]. PDMS (Dow Corning Sylgard Brand 184 Silicone Elastomer, Essex-Brownell Inc.) was molded on masters fabricated on silicon wafers using SU-8 2050 (Negative photoresist, Microchem Corporation, MA). Typically, two ~150 μm thick SU-8 films were spun on 100 mm diameter silicon wafers (Silicon Quest International). Photolithography was used to define negative images of the microfluidic channels, and finally the wafers were developed using SU-8 Developer (Microchem Corporation). Packaging of the microreactors was accomplished by the following sequence of steps. PDMS was molded on the SU-8 masters described above at 70°C for 2-12 hours. The devices were peeled off the mold, cut and cleaned. Inlet and outlet holes (1/16-in. o.d.) were punched into the material. Individual devices were sealed to precleaned microscope slides (50 x 75 mm, 1 mm thick, Corning Inc.). Both surfaces were activated in an oxygen plasma (Harrick Co., PDC-32G) for 35 seconds prior to sealing. PEEK tubing (1/16-in. o.d., 508 μm i.d., Upchurch Scientific.) was inserted in the inlet and outlet holes, and glued in place with 5-min epoxy (Devcon).

5.3 Experimental

5.3.1 Materials and methods

Silicon tetra-ethoxide (TEOS) (99.999%, Aldrich Chemical Co.), Titanium tetra-ethoxide (TEOT) (97% in anhydrous ethyl alcohol, Aldrich Chemical Co.), ammonium hydroxide (28% NH_3 in water, 99.99+%, Aldrich Chemical Co.), ethyl alcohol (Absolute, Anhydrous, PharmCo Inc.), and deionized water (Reagent grade, 18 MΩ cm, Ricca Chemical Co.) were used as obtained without further purification. Batch synthesis of monodisperse spherical silica particles was carried out using the Stöber process as described in Chapter 4. The synthesized particles were centrifuged and washed three times with anhydrous ethyl alcohol. Approximately 1% w/w particle suspensions were used in this study, as those were the typical particle concentrations obtained from the Stöber process. The TEOT stock solution for titania coatings was prepared in a glove box under nitrogen in a 25 mL Schlenk tube. Briefly, 0.7 mL of TEOT was added to 19.3 mL

of anhydrous ethyl alcohol, and 20 mg hydroxypropyl cellulose (HPC) (M.W. 300,000, Aldrich Chemical Co.) was added with stirring, thus yielding a 0.03 M TEOT solution with 1 mg/mL of dissolved HPC. A stock solution of 0.51 M water in ethyl alcohol with 2 mg/mL HPC was also prepared for semi-batch coating experiments.

5.3.2   Semi-batch titania coating on preformed silica particles

0.5 mL of washed silica stock (~1% w/w) was added to 0.5 mL of 0.51 M water solution in ethyl alcohol in a 5 mL precleaned glass vial (VWR Scientific). The net water, silica, and HPC concentration was thus 0.25 M, 0.5% w/w and 1 mg/mL respectively. To this mixture, 1 mL of TEOT stock solution as prepared above (5.3.1) was added at a constant rate of 15 µL/min from a 2.5 mL gastight glass syringe (Hamilton 1000 series) using a syringe pump (Harvard Apparatus, PHD2000 series). Transfer of solution from the Schlenk tube to the gas-tight syringe was carried out under a steady stream of argon. The mixture was gently stirred (250 rpm) with a magnetic stirrer throughout the addition process. The mixture was aged for 30 minutes after addition was complete, and then 0.5 mL aliquots were drawn, centrifuged and washed three times for further particle characterization. The final particle concentration in the washed solutions was approximately 0.25% w/w. The remaining reaction mixture was transferred to a centrifuge tube and allowed to stand for 6 hours. The coated particles settled to the bottom of the tube, and a translucent whiteness was observed in the supernatant liquid, which was analyzed by electron microscopy (5.3.5).

5.3.3   Semi-batch silica coating on titania-coated silica particles

0.9 mL of anhydrous ethyl alcohol was added to 0.1 mL of washed titania-coated silica particles as prepared above, thus diluting the particle concentration ten-fold to 0.025% w/w. To this mixture, 1 mL of 0.61 M solution of ammonia in ethyl alcohol (0.4 mL ammonium hydroxide + 9.6 mL ethyl alcohol) was added with stirring. 1 mL of 0.06 M TEOS solution was then added at a constant rate of 10 µL/min with stirring (250 rpm).

5.3.4   Microreactor setup and experiments

The microreactor set-up for the titania coating experiments is schematically depicted in Figure 5-8. 0.5 mL of washed silica stock (~1% w/w) was added to 0.5 mL of 0.51 M

water solution in ethyl alcohol as in 5.3.2. This solution and the TEOT stock solution were separately loaded in gas-tight syringes and delivered into the microreactor. Reactant solutions and nitrogen gas were pumped into the reactors using syringe pumps from Harvard Apparatus (PHD 2000 Infusion/Withdraw pumps), and Cole-Parmer (74900 Series). 200-250 µL aliquots of coated particles were collected in 0.5 mL polypropylene centrifuge tubes at the outlet, centrifuged and washed three times for further particle characterization. De-ionized water was used for the first wash, and ethyl alcohol was used for the next two washes. The particles were finally suspended in de-ionized water.
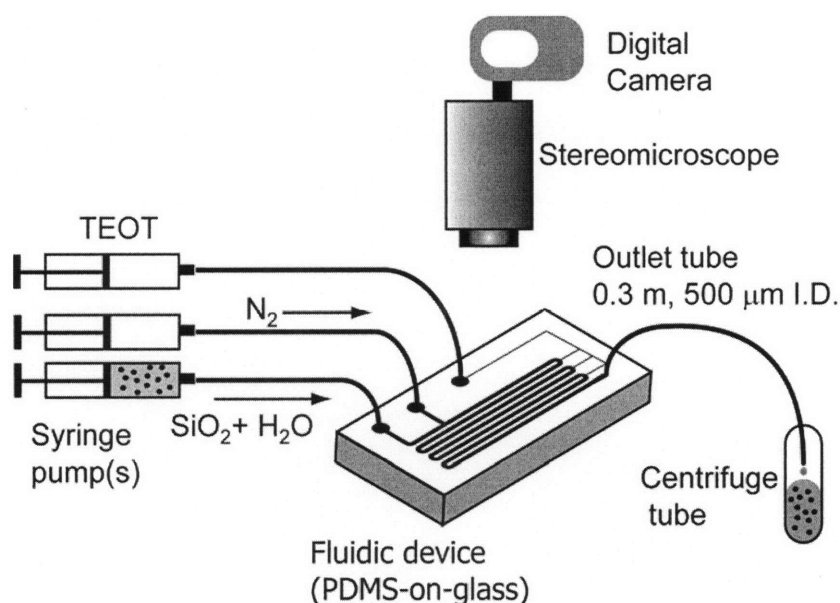
Figure 5-8 Schematic of experimental setup for microreactor titania coating experiments

5.3.5 Sample preparation and particle characterization

The as-synthesized core-shell particles were amorphous. Small amounts of the washed particles (~50 µL) were calcined in air at 500°C to convert the amorphous titania shell to crystalline anatase. Furnace temperature was ramped from 25°C to 500°C at a rate of 10°C/min and held at 500°C for 1 hour. The particles were then allowed to cool to 200°C in the furnace and then removed and quenched to room temperature. The particles to be calcined were collected in small (250 µL) glass vials or on pieces of silicon (5 mm x 5 mm) and dried at 70°C for 2 hours before calcination.

Particle morphology, size and particle size distribution were determined from image analysis of electron micrographs taken on field emission SEMs (JEOL 6320FV and JEOL 5910) at a voltage of 5kV. A drop of washed particles was placed on a piece of silicon (5 mm x 5 mm), and allowed to dry in air. Observations from at least one hundred particles were used in calculations of average size and standard deviation of each sample. Images were analyzed using ImageJ software obtained from NIH, or using Adobe Photoshop. Particle coatings were also analyzed by high resolution TEM (JEOL 2011, accelerating voltage 200 kV). A drop of colloid suspension was placed on a 200-mesh copper grid (2.3 mm diameter, Carbon coated, Ladd Research Inc.) and allowed to dry in air for 15 minutes. The remaining liquid was wicked away using a filter paper. Elemental analysis of particle surfaces by X-ray photoelectron spectroscopy (XPS) was performed using a Kratos AXIS Ultra Imaging XPS with an Al K α source. A drop of washed particles was placed on a piece of silicon (5 mm x 5 mm) that was coated with a thin layer of gold (50 nm) with an underlying titanium adhesion layer (10 nm). Metals were deposited on silicon by electron beam evaporation (Temescal Semiconductor Products e-beam evaporator) in a class 100 clean room environment.

5.4 Results and discussion

5.4.1 Semi-Batch synthesis

Figure 5-9 shows SEM micrographs of silica cores (Figure 5-9(a)) and titania-coated particles from the semi-batch experiments. Thick (~30 nm) titania coatings (Figure 5-9(b)) are obtained by the semi-batch process. The coated particles are unagglomerated, with few (<5 %) particles fused to form doublets or higher order multiplets (Figure 5-9(c)). The surface of the coated particles is rough and grainy as compared to the silica cores, indicating that hetero-coagulation is the dominant mechanism of titania coating. Small particles of titania (<10 nm) are formed by the hydrolysis of TEOT, and subsequently aggregate on the silica surface to form titania shells on the core particles. Figure 5-9(d) shows high-resolution (0.1 eV) XPS elemental scans performed on the particle surface. A strong Ti 2p signal is collected, while virtually no Si 2p signal is collected, confirming the presence and coverage of titania on the particle surface. *Small-*

scale (<5 mL reaction volume) semi-batch synthesis can thus be successfully be used to coat thick, uniform layers of amorphous titania on silica particles by sol-gel chemistry.
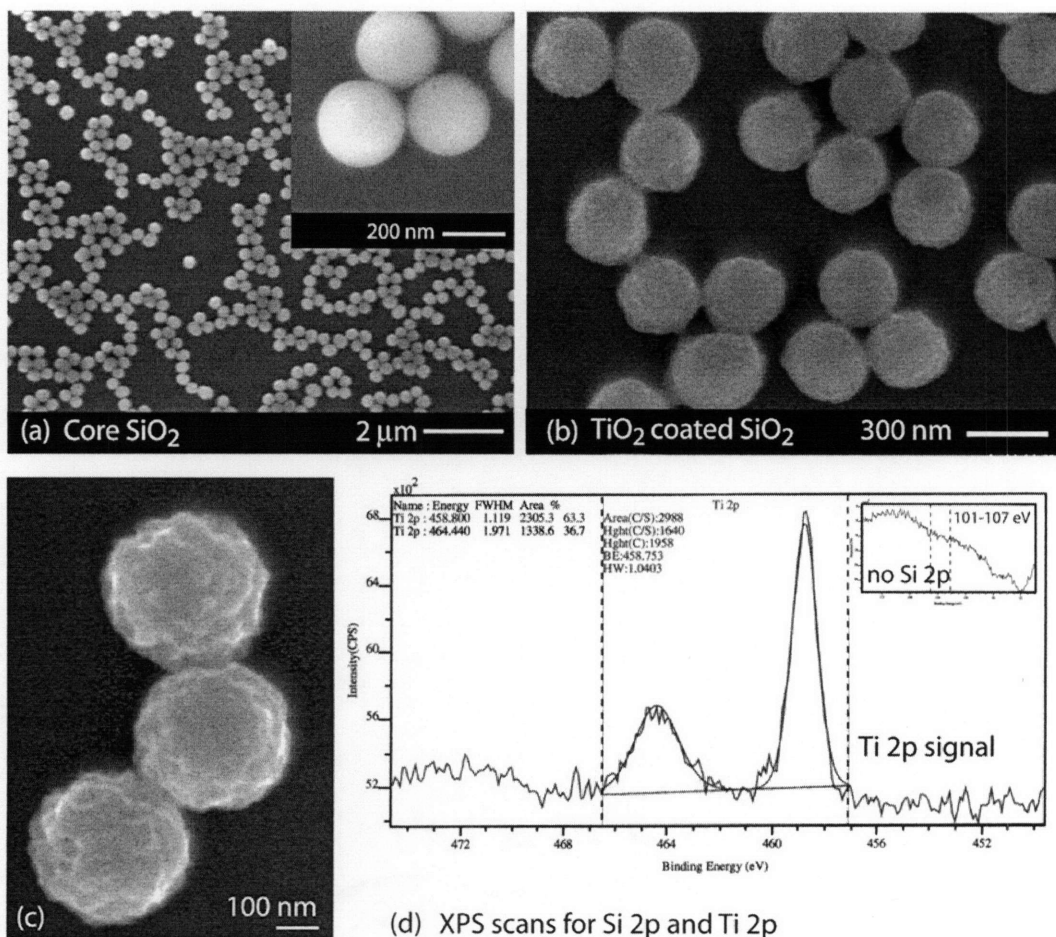
Figure 5-9 Results from semi-batch titania coating process (a) SEM of silica core particles synthesized by the Stöber process (mean diameter d_m = 280 nm). (b),(c) SEM of titania-coated silica particles (d_m = 340 nm) (d) High resolution XPS elemental scans of the surface of coated particles (scan resolution 0.1 eV): Strong Ti 2p signal obtained, no Si 2p signal (inset).

Figure 5-10(a) and (b) are SEMs of particles in the supernatant liquid obtained from the reaction mixture after the core particles were allowed to sediment at the bottom of the centrifuge tube (5.3.2). The presence of small irregularly shaped titania particles (<100 nm) indicated that TEOT concentration in the reaction mixture was above that required for titania particle nucleation at all times during the coating process. The presence of silica cores only served to prevent homogeneous aggregation of titania nuclei into larger

titania particles. Sedimentation of the silica cores resulted in homogeneous aggregation of small titania in the supernatant liquid. Further evidence for the heterocoagulation mechanism is presented by TEM analysis of coated particles presented in 5.4.2.
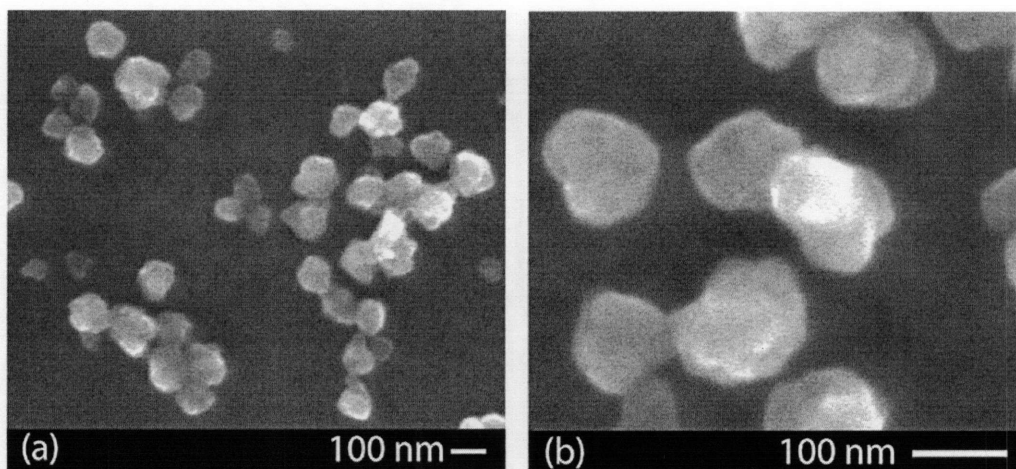
Figure 5-10 Titania particles in the supernatant from the semi-batch reaction mixture.

Silica coatings on the titania-coated particles are accomplished by the procedure described in 5.3.3. Figure 5-11 shows SEM micrographs of thin 5 nm silica coatings on titania-coated silica particles. XPS of the particle surface yielded no Ti 2p signal, and a weak Si 2p signal. Also shown in Figure 5-11 (c) and (d) are results of the silica coating procedure when particle and silica precursor concentrations were not optimized. Rapid and irreversible agglomeration occurred when particle concentration was 0.25% w/w and TEOS, water and ammonia concentration were 0.1 M, 2.0 M and 0.75 M respectively (Figure 5-11(c)). Extensive secondary nucleation was observed when the particle concentration was 0.01% w/w, for the same TEOS, water and ammonia concentrations (Figure 5-11(d)). These results underscore the importance of optimizing reactant and particle concentrations for any coating process.
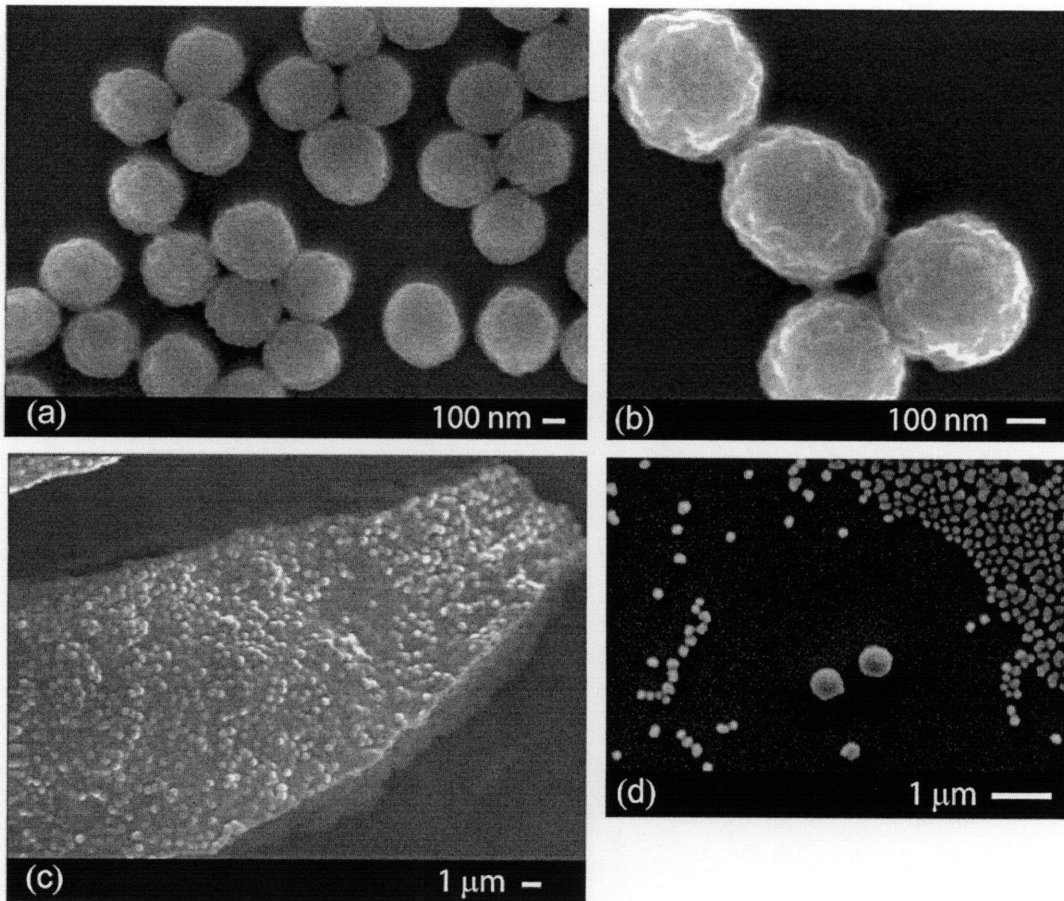
Figure 5-11 Silica overcoating on titania-coated silica (a),(b) Thin 5 nm layers of silica: particle concentration = 0.025% w/w and [TEOS] =0.02 M, [H$_2$O] =0.5 M, [NH$_3$]= 0.2 M (c) Rapid, irreversible agglomeration is observed when high particle concentrations of 0.25% w/w used, [TEOS] =0.2 M, [H$_2$O] =2.0 M, [NH$_3$]= 0.75 M (d) Secondary silica nucleation at low particle concentrations of 0.01% w/w, [TEOS] =0.2 M, [H$_2$O] =2.0 M, [NH$_3$]= 0.75 M. The apparent necking and aggregation in the SEMs is due to the sample preparation procedure, where a drop of particles suspended in ethyl alcohol is placed onto a silicon piece. Ethyl alcohol dries rapidly, and often leaves organic residue behind on the sample, which appears as necks between the particles.

5.4.2   Microfluidic coating: Single step precursor addition

Silica core particles for the microfluidic coating experiments were synthesized by the Stöber process, and had a mean diameter of 209 nm ± 11 nm (Figure 5-12). The particles had smooth surfaces.
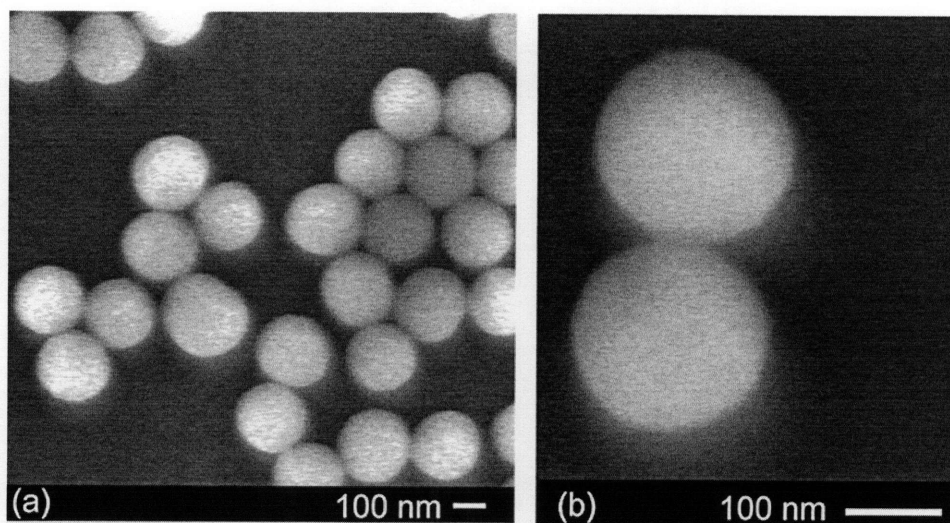
Figure 5-12 SEMs of silica core particles used in the microreactor coating experiments. [TEOS] = 0.2 M, [NH$_3$] = 1.16 M, [H$_2$O] = 2.8 M. Particles have a mean diameter (d_m) = 209 nm ± 11 nm.

The basis of the microreactor coating process is the observation that uniform thick coatings on unagglomerated particles are obtained only when the titanium precursor concentration in the reactor is low throughout the coating process. As discussed in 5.1.6, splitting of the titanium precursor feed into multiple streams which enter the reactor at regular intervals is one way to accomplish this, and thus prevent secondary titania particle formation and agglomeration of silica cores. In this section, we report a control microreactor experiment where we added TEOT in a single step to a silica particle suspension, and observed extensive agglomeration and secondary particle nucleation. Figure 5-13(a) is a schematic showing details of the experiment. TEOT and silica suspensions were fed at equal volumetric flow rates into the microreactor, and nitrogen gas was delivered into the third inlet. The incoming gas segmented the flow, and enabled rapid mixing of the two reacting streams (Chapter 2). One of the key parameters in the coating process is the ratio of TEOT to water concentration ([TEOT]/[H$_2$O]) immediately after mixing, and in this experiment it was approximately equal to 8. Figure 5-13(b)-(d) are SEMs of the particles obtained by this process. Extensive agglomeration of primary silica particles was observed. In addition, large secondary particles (> 1 μm) of titania

143

were formed. The particle surfaces are grainy, indicating heterocoagulation as the primary mechanism of coating and agglomeration, as also observed in 5.3.2.
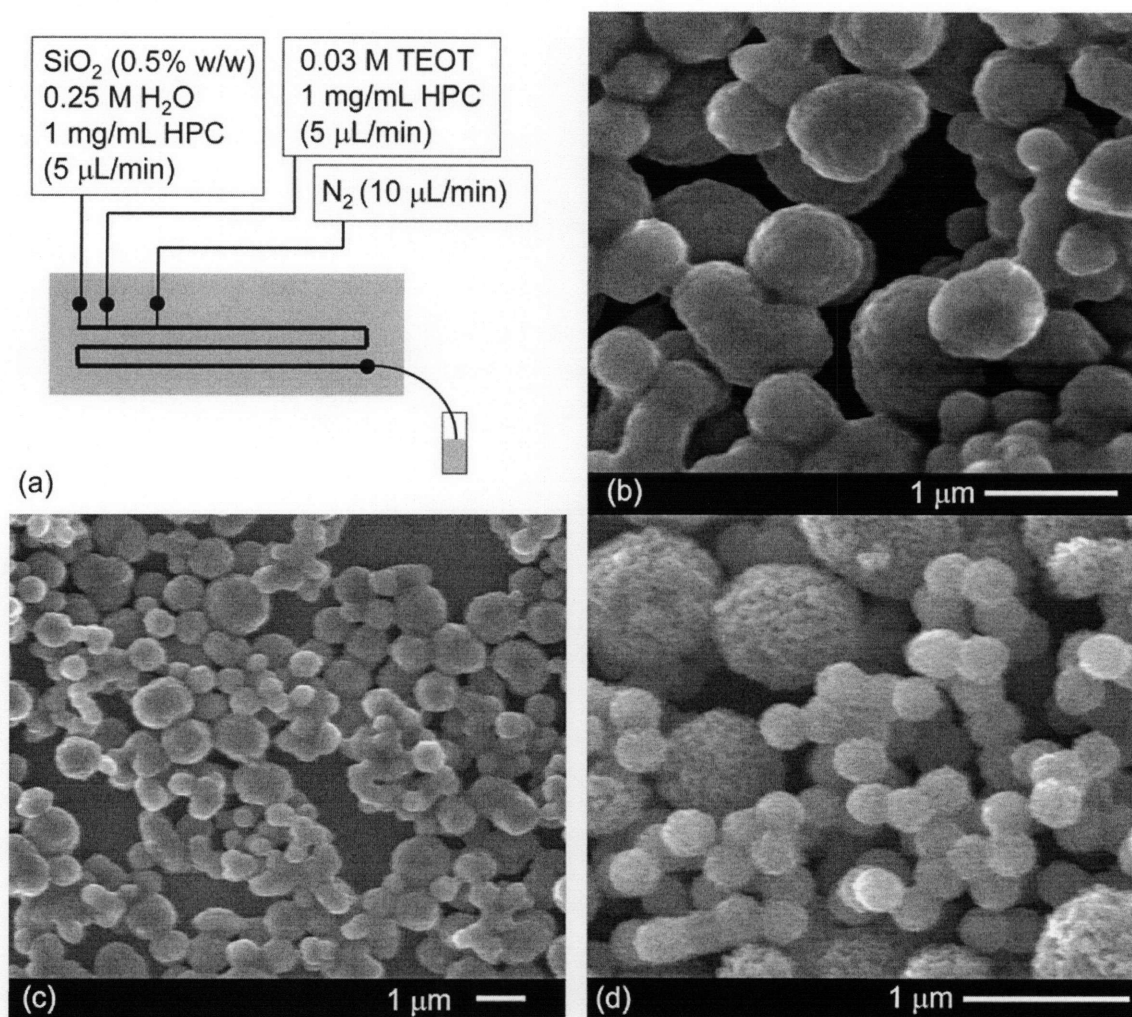
Figure 5-13 Single step TEOT addition control experiment (a) Details of the experiment, including gas and liquid flow rates and reactant concentrations (b)-(d) SEMs of particles obtained by this process. Extensive agglomeration of primary silica particles is evident, along with formation of large secondary particles of titania. Particle surfaces are grainy, consisting of nanometer sized aggregates.

5.4.3 Microfluidic coating: Manifolded multi-step precursor addition

In this section, we report the results for titania coatings on silica particles using manifolded multi-step TEOT addition to a silica particle suspension. We first demonstrate that microreactors designed using the procedure described in 5.2.1 indeed enable controlled addition of secondary liquid to a primary gas-liquid flow. Figure 5-14 is a stereomicroscope image of the microreactor of Figure 5-7 in operation. The first three

side inlets (S1, S2 and S3) from the manifold feed ethyl alcohol (dyed with black ink) into the gas-liquid flow (air-ethyl alcohol) in the main channel. The gas bubbles enable rapid mixing of the incoming liquid, as seen by the uniform intensity of black ink in the main channel 20 mm downstream of the side inlets.
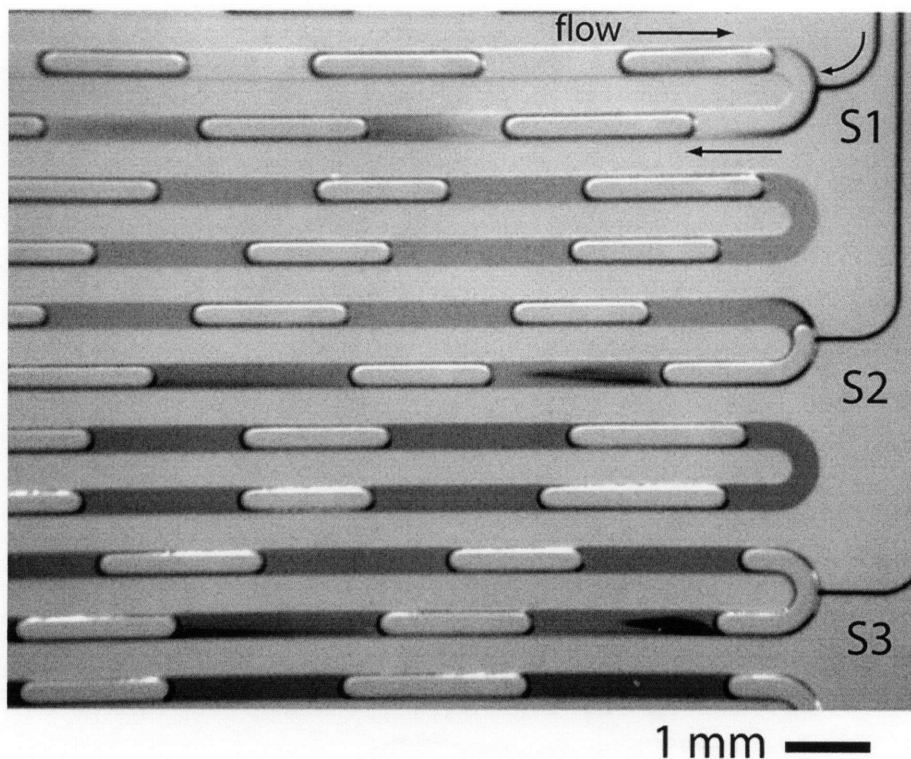
Figure 5-14 Stereomicroscope image: Operation of manifolded liquid (ethyl alcohol) addition into a gas-liquid segmented flow in the microreactor of Figure 5-7. Gas flow rate (Q_G) = 6 µL/min, liquid flow rate in main channel (Q_L) = 5 µL/min, liquid flow rate in the manifold inlet (Q_S) = 5 µL/min. The liquid entering the manifold is dyed with black ink.

Titania coating in the manifolded microreactor was carried out using the same precursor TEOT solution and silica suspension as used in the previous section, and prepared as described in 5.3.1. In this case, however, the TEOT feed was split into eight streams which entered the reactor at regular intervals. Two different volumetric flow rates of TEOT entering the manifold inlet were used, for the same gas and silica suspension flow rate, as summarized in Figure 5-15(a). The corresponding coated particles are labeled as sample A and B respectively. The TEOT to water ratio at each feed point was at least 80 for Q_{TEOT} = 5 µL/min (Sample A), and at least 140 for Q_{TEOT} =

2.5 µL/min (Sample B). Thick, uniform titania coatings (20-30 nm thick) were obtained, as seen in the SEMs of Figure 5-15(b)-(f). Secondary particle nucleation and primary particle agglomeration were completely suppressed, as is evident from Figure 5-15(d) and Figure 5-15(f), where the coated particles formed uniform close-packed crystalline arrays characteristic of perfectly monodisperse colloidal systems.
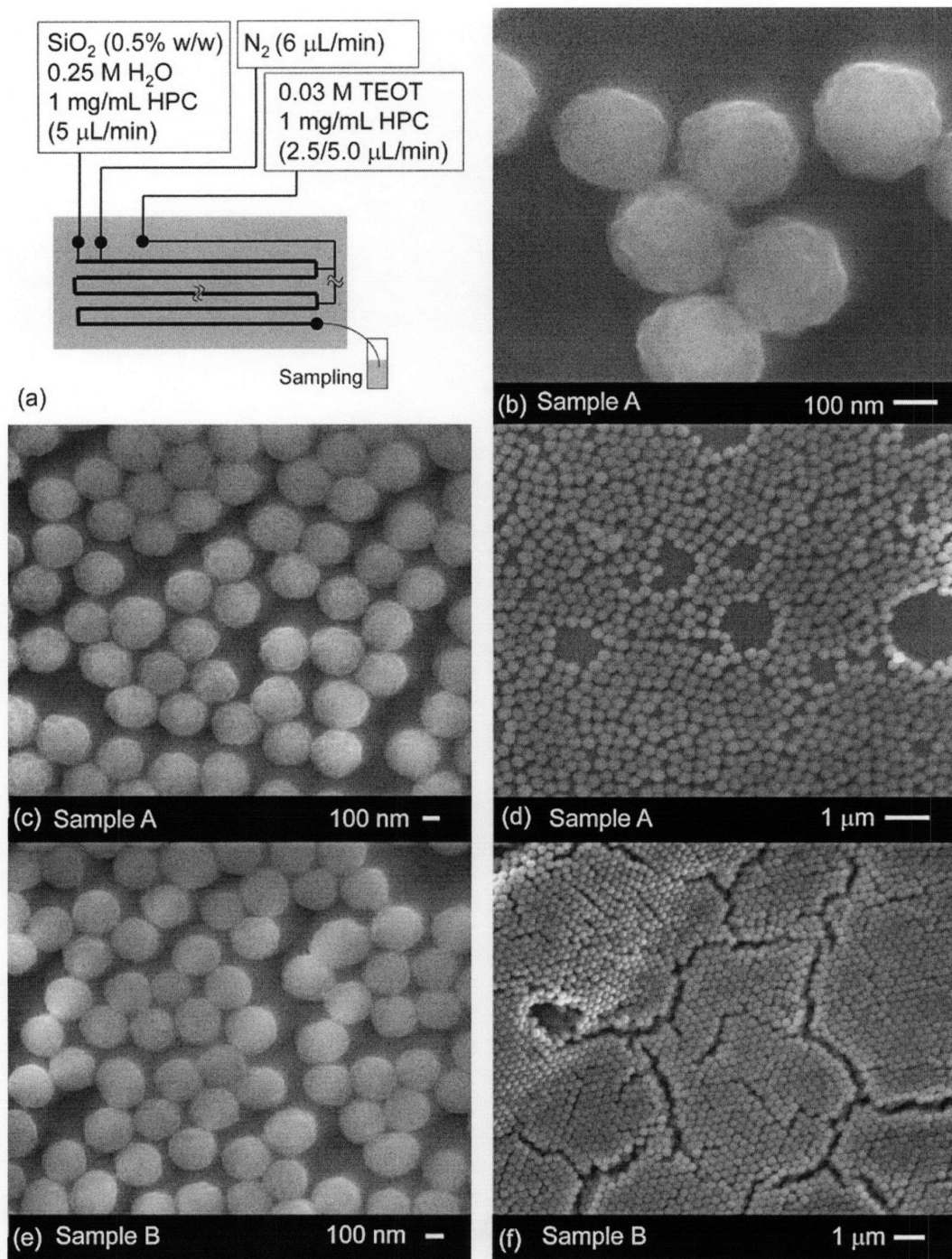
Figure 5-15 Microreactor coatings: (a) Details of the experiment, including gas and liquid flow rates and reactant concentrations (b)-(f) SEMs of particles obtained by this process.

Coated particles were also analyzed using TEM, as shown in Figure 5-16. High-resolution TEM micrographs such as those in Figure 5-16(a) and (b) were used to analyze the particle surface, and measure size and polydispersity. The core-shell nature of the

particles is evident in Figure 5-16(b) and Figure 5-16(d). The coating consists of aggregates of small (<3 nm) titania particles on the primary silica surface. Figure 5-16(c) is a low-magnification TEM, supplementary to Figure 5-15(d) and (f), showing the suppression of secondary nucleation and aggregation among the coated particles. The microfluidic approach allowed tuning of particle size by varying the volumetric flow rate of TEOT (Q_{TEOT}), for a fixed volumetric flow rate of the water-containing silica suspension. Both conditions yielded thick titania coatings (>20 nm). Titania coatings in sample A were, on average, at least 5 nm thicker than sample B.

TEM analysis of particles after calcination at 500 °C is presented in Figure 5-17. There are several observations to be noted. Both samples A and B retain their spherical morphology and narrow size distribution, and remain unagglomerated (Figure 5-17(a),(b)). There is considerable shrinkage in particle size (50-60 nm) in both cases, due to loss of water trapped in the sol-gel network.[25] As seen in Figure 5-17(a) and (c), the coatings in sample A lose conformality with the underlying silica core, while the coatings in sample B adhere to the core particles. While the particles of sample A remain intact, there are void spaces ~10-20 nm in size present between the silica core and titania shell. Such core-shell-shell structures, with an intermediate layer of solvent/air could potentially have interesting optical and catalytic properties. Heat treatment at 500 °C transforms amorphous titania into crystalline anatase.[16] The anatase coating is polycrystalline in nature, with typical crystallite sizes of 10 nm, as seen by the lattice fringes in high-resolution TEM micrographs (Figure 5-17(e)). The crystalline nature of the calcined coating is also confirmed by characteristic rings in the electron diffraction pattern (Figure 5-17(f)). Table 1 summarizes the key measurements of samples A and B obtained from the TEM image analysis, before and after calcination.

Sample	As- synthesized		Post-calcination (500 °C)		
	d_m (nm)	σ (nm)	d_m (nm)	σ (nm)	Shell thickness (nm)
A	266	14	219	11	20
B	253	12	189	11	15

Table 5-1 Summary of measurements from TEM micrographs: Mean particle diameter (d_m), standard deviation in particle diameter (σ) and post-calcination shell thickness. Note: The silica core size before and after calcination is 210 nm ± 10 nm and 157 ± 7 nm respectively.

XPS elemental scans of coated and uncoated particles are presented in Figure 5-18. Si 2p and Si 2s signals are considerably attenuated in the case of coated particles. In addition, a strong characteristic Ti 2p peak is observed for the coated particles (both sample A and B), thus conforming the presence of titanium on the particle surface.
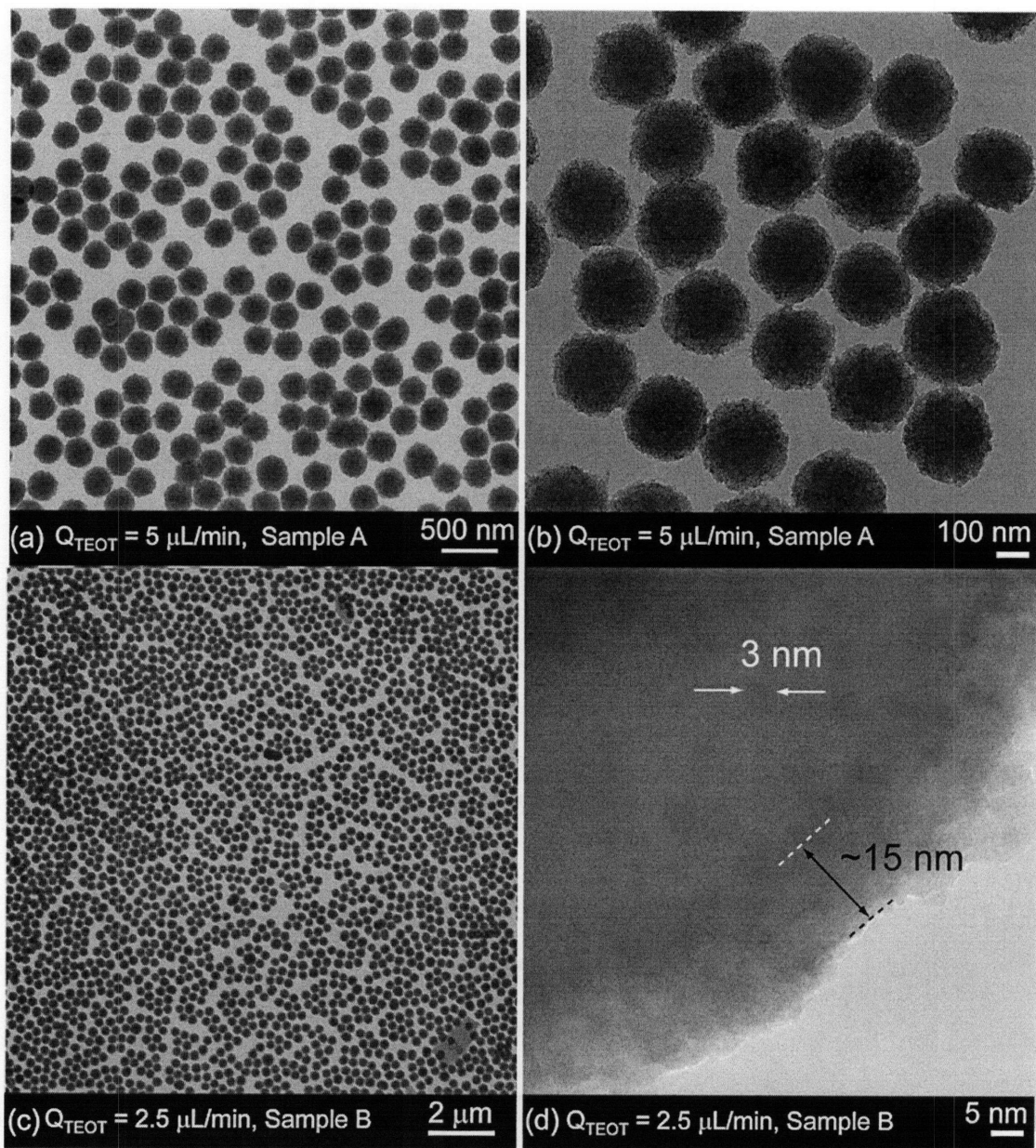
Figure 5-16 TEM analysis of titania-coated silica particles (a),(b) Sample A: Mean diameter (d_m) = 266 nm, Polydispersity (σ/d_m) = 5% (c) Sample B: Mean diameter (d_m) = 253 nm, Polydispersity (σ/d_m) = 5% (d) TEM of core-shell interface: small (<3 nm) nanoparticles are seen on the particle surface.
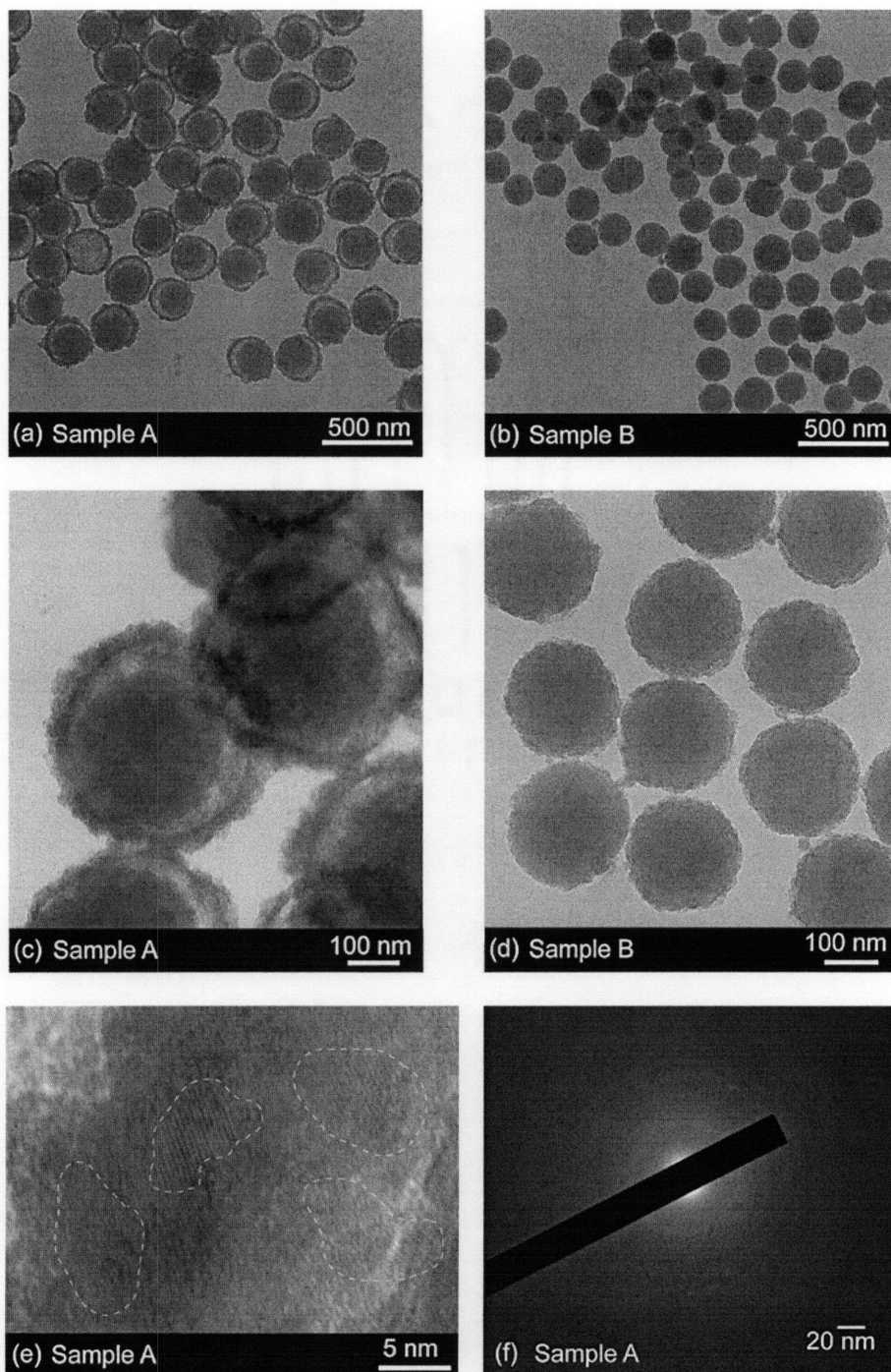
Figure 5-17 TEM analysis of coated particles after calcination at 500 °C (a) Sample A: Mean diameter (d_m) = 219 nm, Polydispersity (σ/d_m) = 5 %. Coatings are not conformal with the silica core, and void spaces are seen. (b) Sample B: Mean diameter (d_m) = 189 nm, Polydispersity (σ/d_m) = 6 %. Conformal coatings are obtained. (c),(d) High magnification images. (e) Polycrystalline coatings: crystallite size typically 10 nm. (f) Electron diffraction pattern indicating polycrystallinity of the calcined shell.
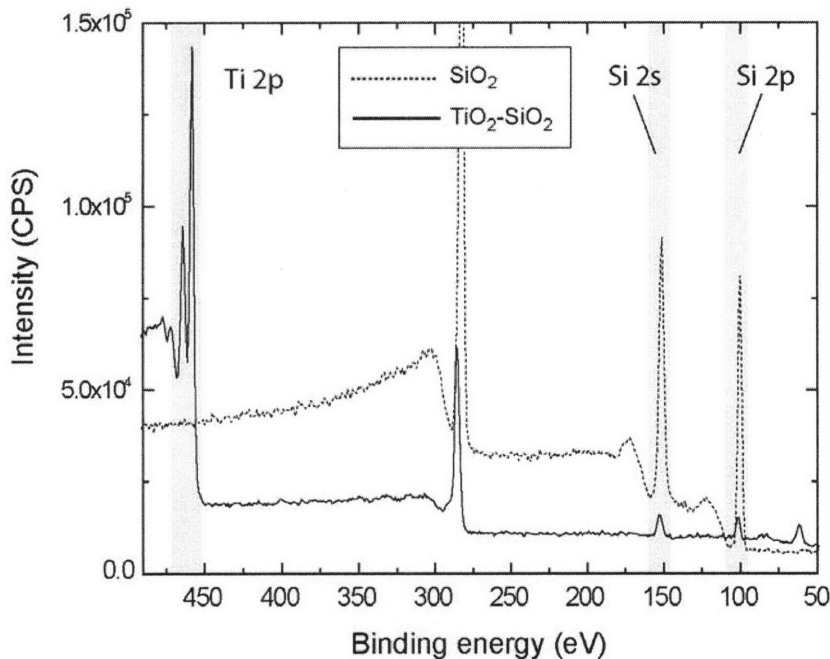
Figure 5-18 XPS elemental scans of the surface of coated particles (scan resolution 1 eV): Strong Ti 2p signal obtained, Si 2s and 2p signals are attenuated compared to the uncoated particle case.

5.4.4 Wall deposition

PDMS was used as a material of construction for the microfluidic reactors. As noted in Chapter 4, particle coating reactions did not lead to catastrophic microchannel blockage and device failure. The particle coating results described in this chapter were obtained when TEOT solution was fed through the side-inlet manifold, and the silica suspension was fed through the main channel inlet. Thin particle coatings (~2 μm) were deposited on the reactor walls over typical reaction runs of 4-6 hours.

In this section, we report interesting particle deposition patterns on the microchannel walls. In particular, we describe the situation when the reactor was operated in non-optimum fashion (with TEOT fed in a single step through one of the main reaction channel inlets instead of the manifold) as described in 5.4.2 and extensive particle deposition was observed. Cross-sectional SEMs of devices obtained after such a reaction run are shown in Figure 5-19. Particles and agglomerates are seen to deposit in islands at the center of the microchannel walls, away from the corners where little deposition is observed. The agglomeration and deposition of particles is due to the high inlet

152

concentration of TEOT in this case, as discussed in 5.4.2. Possible reasons for such deposition patterns could be the breaking of thin liquid films surrounding the gas bubbles (as described in Chapter 2) leading to partial drying of the channel walls, as well as high shear forces in these thin films, that scale inversely with film thickness.
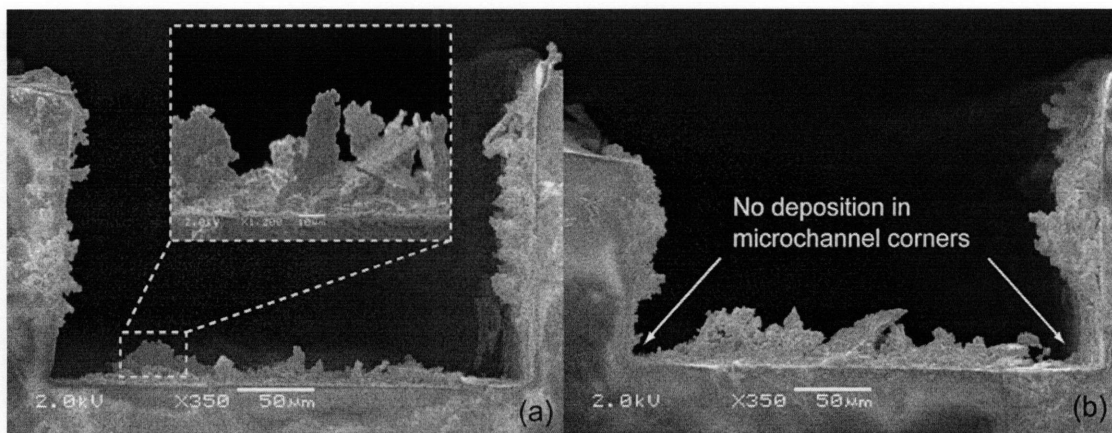
Figure 5-19 Single-step TEOT addition: deposition of particles and agglomerates on channel walls, away from corners.

5.5   Summary

In this chapter we have demonstrated how microfluidics enables creative design of chemical reactors that are difficult to realize using conventional macroscale approaches. We lay out the basic design framework for multi-phase microreactors that accomplish nanoparticle coatings with no secondary nucleation and particle agglomeration. In particular, the design of microfluidic networks with manifolded feed streams is developed through analogy with linear electrical circuits. Such networks enable multi-step addition of secondary reactants along a primary reaction stream, thus maintaining low reactant concentrations throughout the reactor. The operation of such reactors for coating thick titania layers on silica particles is described, along with detailed particle characterization using electron microscopy.

5.6   References

1.   Caruso, F. Nanoengineering of particle surfaces. *Advanced Materials* **13**, 11-+ (2001).

153

2.   Imhof, A. Preparation and characterization of titania-coated polystyrene spheres and hollow titania shells. *Langmuir* **17**, 3579-3585 (2001).

3.   Matijevic, E. Uniform Inorganic Colloidal Dispersions. Achievements and Challenges. *Langmuir* **10**, 8-16 (1994).

4.   Mayya, K. S., Gittins, D. I. & Caruso, F. Gold-titania core-shell nanoparticles by polyelectrolyte complexation with a titania precursor. *Chemistry of Materials* **13**, 3833-+ (2001).

5.   Huang, C. L. & Matijevic, E. Coating of Uniform Inorganic Particles with Polymers .3. Polypyrrole on Different Metal-Oxides. *Journal of Materials Research* **10**, 1327-1336 (1995).

6.   Caruso, F., Shi, X. Y., Caruso, R. A. & Susha, A. Hollow titania spheres from layered precursor deposition on sacrificial colloidal core particles. *Advanced Materials* **13**, 740-744 (2001).

7.   Oldenburg, S. J., Averitt, R. D., Westcott, S. L. & Halas, N. J. Nanoengineering of optical resonances. *Chemical Physics Letters* **288**, 243-247 (1998).

8.   Caruso, R. A. & Antonietti, M. Sol-gel nanocoating: An approach to the preparation of structured materials. *Chemistry of Materials* **13**, 3272-3282 (2001).

9.   Srinivasan, S. et al. The Formation of Titanium-Oxide Monolayer Coatings on Silica Surfaces. *Journal of Catalysis* **131**, 260-275 (1991).

10.   Hsu, W. P., Yu, R. & Matijevic, E. Paper Whiteners I. Titania Coated Silica. *Journal of Colloid and Interface Science* **156**, 56-65 (1993).

11.   Li, Q. & Dong, P. Preparation of nearly monodisperse multiply coated submicrospheres with a high refractive index. *Journal of Colloid and Interface Science* **261**, 325-329 (2003).

12.   Li, H., Han, J., Panioukhine, A. & Kumacheva, E. From heterocoagulated colloids to core-shell particles. *Journal of Colloid and Interface Science* **255**, 119-128 (2002).

13.   Han, J. & Kumacheva, E. Monodispersed silica-titanyl sulfate microspheres. *Langmuir* **17**, 7912-7917 (2001).

14.   Wang, D. Y. & Caruso, F. Polyelectrolyte-coated colloid spheres as templates for sol-gel reactions. *Chemistry of Materials* **14**, 1909-+ (2002).

15.   Nakamura, H., Ishii, M., Tsukigase, A., Harada, M. & Nakano, H. Close-packed colloidal crystalline arrays composed of polystyrene latex coated with titania nanosheets. *Langmuir* **21**, 8918-8922 (2005).

16.   Hanprasopwattana, A., Srinivasan, S., Sault, A. G. & Datye, A. K. Titania Coatings on Monodisperse Silica Spheres (Characterization Using 2-Propanol Dehydration and TEM). *Langmuir* **12**, 3173-3179 (1996).

17.   Holgado, M. et al. Three-dimensional arrays formed by monodisperse TiO2 coated on SiO2 spheres. *Journal of Colloid and Interface Science* **229**, 6-11 (2000).

18. Kim, K. D., Bae, H. J. & Kim, H. T. Synthesis and characterization of titania-coated silica fine particles by semi-batch process. *Colloids and Surfaces a-Physicochemical and Engineering Aspects* **224**, 119-126 (2003).

19. Jiang, X. C., Herricks, T. & Xia, Y. N. Monodispersed spherical colloids of titania: Synthesis, characterization, and crystallization. *Advanced Materials* **15**, 1205-+ (2003).

20. Russell, W. B., Saville, D. A. & Schowalter, W. R. *Colloidal Dispersions* (Cambridge University Press, 1989).

21. Jean, J. H., Goy, D. M. & Ring, T. A. Continuous Production of Narrow-Sized and Unagglomerated Tio2 Powders. *American Ceramic Society Bulletin* **66**, 1517-1520 (1987).

22. Perry, R. H. & Green, D. W. *Perry's Chemical Engineers' Handbook* (McGraw-Hill, 1997).

23. Kreutzer, M. T., Kapteijn, F., Moulijn, J. A. & Heiszwolf, J. J. Multiphase monolith reactors: Chemical reaction engineering of segmented flow in microchannels. *Chemical Engineering Science* **60**, 5895-5916 (2005).

24. Xia, Y. N. & Whitesides, G. M. Soft lithography. *Annual Review of Materials Science* **28**, 153-184 (1998).

25. Brinker, C. J. & Scherer, G. W. *Sol-Gel Science: The Physics and Chemistry of Sol-Gel Processing* (Academic Press, Boston, 1990).

6 Multi-step Processing and Particle Separation

6.1 Introduction

In this chapter, we report steps toward multi-step particle processing. We describe the design, fabrication and operation of two related systems. The first system is an integrated series combination of microreactors for continuous silica synthesis (Chapter 4) and titania overcoating (Chapter 5). The integrated microreactor consists of two stacked layers fabricated in PDMS, the first layer consisting of microchannels for silica synthesis and the second layer consisting of microchannels for titania overcoating using the manifolded microchannel network design of Chapter 5. This system operates with compatible (sol-gel) chemistry in both layers, and hence does not require an intermediate particle separation step between layers. Multi-step processing with incompatible chemistries requires intermediate particle separation and/or solvent change between the different steps in the process. The second system described in this chapter addresses the challenge of *continuous* downstream particle separation. Rapid, transverse free-flow electrophoretic separation is used to 'switch' charged colloidal particles from a reaction stream (containing unreacted precursors and/or other undesired species) to another liquid stream co-flowing parallel to the first. Laminar flow prevents mixing of the two streams, and parallel electrodes enable the application of high DC fields for rapid particle transfer. Finally, we demonstrate simultaneous colloidal silica synthesis and electrophoretic separation in a modular series arrangement of a reactor and separator.

6.1.1 Colloid synthesis and in-situ overcoating

Multi-layered core-shell inorganic oxide particles with high refractive index contrast materials comprising alternate layers in the structure are expected to have interesting photonic properties. The goal of this work is to demonstrate systems that enable synthesis and coating with tunable core and shell sizes, and hence tunable optical properties, as illustrated in Figure 6-1.

156
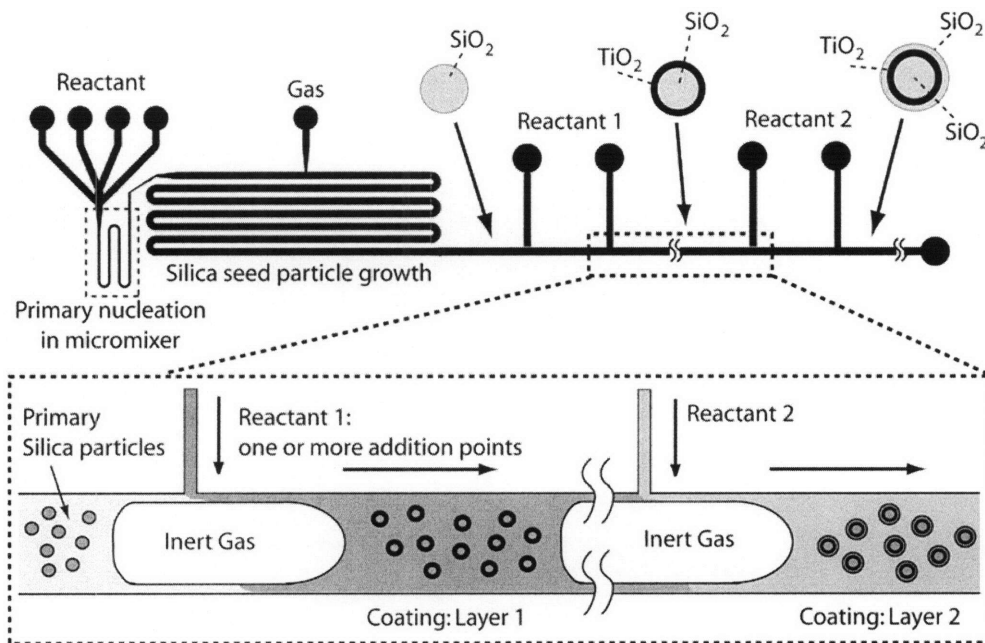
Figure 6-1 Schematic of multi-step core-shell synthesis concept

The motivation for continuous synthesis has been discussed in Chapters 4 and 5. The core-shell particles we are interested in are silica-titania composites. There are several challenges associated with continuous alternating silica and titania sol-gel chemistry without intermediate particle separation. The silica synthesis reaction is typically slow, and requires both dissolved ammonia and excess water (~5 M to 15 M). Titanium alkoxide precursors, on the other hand, rapidly react with water leading to uncontrolled titania precipitation for water concentrations above 1 M. In addition, the particle concentrations obtained from silica synthesis are 5-10 times higher than those required for uniform coatings on unagglomerated particles (Chapter 5). Hence, an integrated reactor that accomplishes series synthesis has to accommodate an intermediate quench/dilution step that adjusts the particle and water concentrations to values that are required for uniform titania (or silica) coatings without secondary precipitation and primary particle agglomeration.

6.1.2   Microfluidic particle separation techniques

Scaling down fluidic channels to micron sizes enables facile manipulation of micro- and nanoparticles using several different fields and forces. For example, high electric field strengths are possible within microchannels with integrated electrodes, even for

small applied voltages. Phenomena such as dielectrophoresis and electrophoresis have been used in microfluidic devices for several diverse applications in 'micro-total analysis systems (μTAS)', such as DNA sequencing[1] and single cell capture and analysis.[2,3] Colloidal particles obtained through sol-gel chemistry have charged surfaces with large zeta potentials (~-50 mV) and high electrophoretic mobilities (~10^{-8} m^2/V/s)), and hence move rapidly under an applied DC electric field.
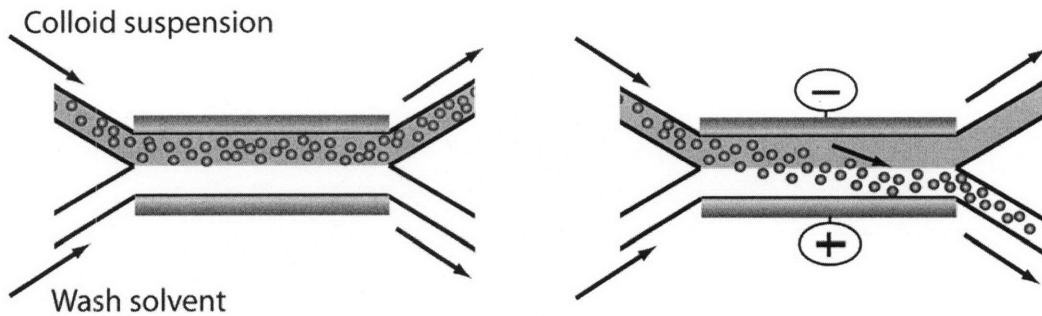
Figure 6-2 Schematic of microfluidic free-flow electrophoresis-based separator

Figure 6-2 illustrates the concept of a continuous electrophoretic particle separator that is the microfluidic analogue of a continuous particle filter in conventional macroscale processing. Colloidal particles suspended in a reaction mixture (containing undesirable species for subsequent steps) enter the first inlet of the microfluidic device. The solvent for the next reaction step, along with one or more reactants, or a wash liquid is delivered to the device from the second inlet. Electrodes for applying a DC voltage are fabricated at the walls of the microchannel, parallel to the co-flowing liquid streams. When a DC voltage is applied at the electrodes (perpendicular to the flow direction), the particles are rapidly transferred from the reaction mixture to the wash stream. In the terminology commonly used in the electrophoresis literature, this mode of operation may be termed as 'free-flow electrophoresis (FFE)', to differentiate it from electrophoresis in gels that is commonly employed for DNA sequencing. FFE was first reported in the literature in the 1960's, and has since found application in chemistry and biochemistry for the separation of proteins, enzymes and cell organelles.[4,5] There are two principal modes of FFE relevant to the above applications: free-flow zone electrophoresis (FFZE), where particles

158

are separated based on their charge to size ratio, and free-flow isoelectric focusing (FFIEF), where separation is based on different isoelectric point (pI) of the species in the sample. Our separator concept, in essence, corresponds to zone electrophoresis (FFZE). However, we are interested in complete transfer of species from one reaction stream to another reaction/wash stream, instead of size/charge-based separation.

There are several time-scales that are important for the design of an FFZE device for complete particle transfer across parallel co-flowing streams. The contact time (τ_C) of the co-flowing streams should be nearly equal to the electrophoretic migration time (τ_M), but much smaller than characteristic diffusion time (τ_D) for the two co-flowing liquid streams. The contact time is the ratio of the microchannel length (L) to the mean flow velocity (U):

$$\tau_C = \frac{L}{U} \tag{6.1}$$

The electrophoretic migration time is given by:

$$\tau_M = \frac{w}{v_M} \tag{6.2}$$

where w is the channel width and v_M is the electrophoretic migration velocity, which depends on particle mobility μ and electric field strength E:

$$v_M = \mu E \tag{6.3}$$

The characteristic diffusion time, as described previously, is given by:

$$\tau_D = \frac{w^2}{D} \tag{6.4}$$

where D is the diffusivity of the suspending liquid (if two different suspending liquids are used, the diffusivity of any one may be used for such a scaling calculation). The collective design criterion is therefore:

$$\tau_M \approx \tau_C \ll \tau_D \tag{6.5}$$

There are several fabrication and operational issues when dealing with microchannel devices for free-flow electrophoresis (μ-FFE). Electrode material selection and fabrication are primary issues. Microfabricated devices that involve electrodes integrated with the microchannel geometry often use metal electrodes fabricated from gold, platinum or indium tin oxide (ITO).[2,3,6-8] Since the electrodes are in direct contact with

159

the (typically aqueous) working liquids, electrolysis and bubble formation under DC voltages is a problem with such an approach, and operating voltages are limited to a few volts or less. Secondly, although planar metal electrode structures are relatively straightforward to fabricate, three dimensional electrode structures typically involve several complex fabrication steps.[2,3,6,9] Several alternative techniques have been reported in the literature to circumvent the above problems associated with metal electrodes. Ion-permeable membrane spacers have been used to isolate the separation channel from the electrode compartments in both macroscale and microscale systems.[4,10] The membrane spacers act as physical barriers to prevent transverse pressure-driven flow, but allow ions to pass through, ensuring electrical connection. Dense channel networks with high hydrodynamic resistance have also been used to separate electrode compartments from the separation chamber in μ-FFIEF devices.[11,12] Such channels networks were observed to have a high electrical resistance, and high voltages were required for efficient separation. Transverse electro-osmotic flow (EOF) caused by the surface charge present at the microchannel walls can hinder the separation process. Dynamic coating of microchannel walls with polymers such as hydroxypropylmethyl cellulose (HPMC) has been used to prevent EOF in μ-FFE devices.[13,14]

We describe two μ-FFE particle separation units with the above general design in this study. The first separator consists of planar metal electrodes in direct contact with the flowing liquids, and the second consists of hybrid electrode structures fabricated with a porous polymer network and microparticles, and isolated from the main separation chamber.

6.2 Design and Fabrication

6.2.1 Two-level stacked reactor design, fabrication and packaging

A design layout for the stacked microreactor is presented in Figure 6-3. It consists of two PDMS microchannel layers. The first layer (Layer 1 in Figure 6-3) is bonded to a glass substrate while the second layer (Layer 2 in Figure 6-3) is bonded to the first. Fabrication and bonding is accomplished using soft lithography techniques described in detail in the previous chapters.
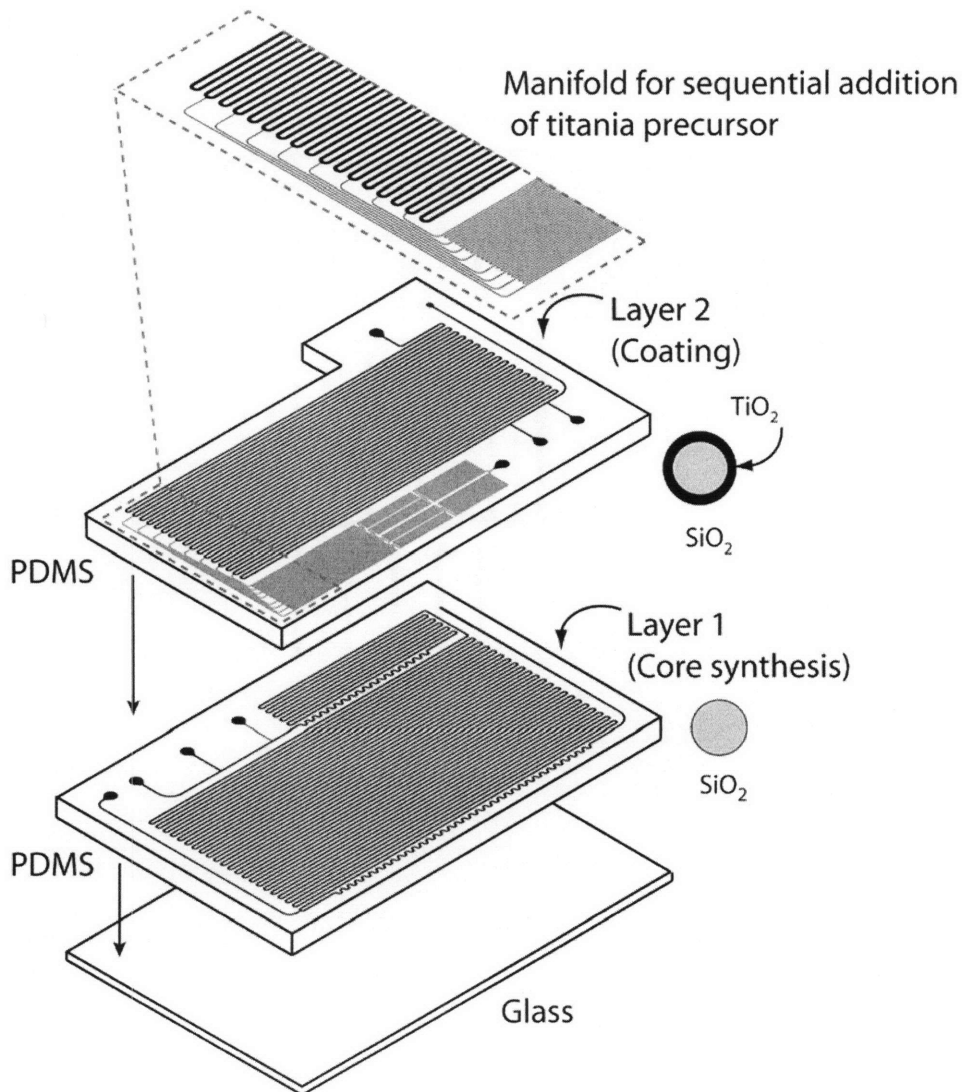
Figure 6-3 Design of stacked two-level microreactor for continuous core-shell synthesis.

Layer 1 consists of microchannels for silica synthesis in a segmented flow microreactor (Design 2 in Chapter 4). The only difference in this case is the presence of meandering channels 5 mm downstream of the reactant and gas inlets to accelerate mixing (Chapter 2), and a quench liquid inlet at the bottom of the reactor to dilute the reaction mixture, thereby reducing particle and water concentration to levels that are acceptable for uniform titania coatings in the subsequent reaction in Layer 2. The quench liquid inlet is also accompanied by downstream meandering channels for rapid mixing. The microchannels in this layer are 300 μm wide and approximately 250 μm deep, and

the reaction channel is 3 m in length. The meandering channels for mixing have a bending radius of 350 µm. Layer 2 consists of the microchannel network described in detail in Figure 5-6 of Chapter 5. All microchannels in Layer 2 are approximately 250 µm deep. Layer 2 is bonded to Layer 1 using the same procedure for bonding PDMS to glass. Both surfaces are activated in an oxygen plasma for 35 seconds and then placing in conformal contact. Figure 6-4(a) and (b) are photographs of the bottom and top of the final fabricated device respectively.

Figure 6-4(c) shows a schematic of the packaging scheme used for this reactor. As shown in the figure, both reactor layers have holes punched in them for insertion of inlet/outlet tubes. The tubes are glued in place using 5-min epoxy (Devcon). Layer 1 and 2 are connected by a small through-hole (~250 µm) punched into Layer 1 at the outlet, using a flat-tipped needle.
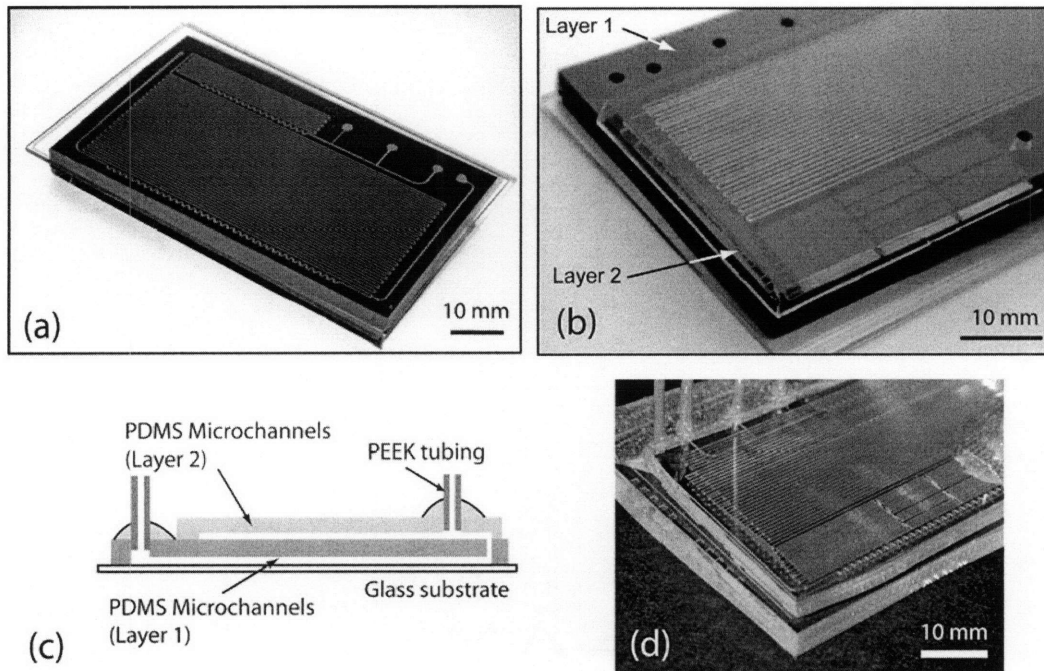
Figure 6-4 (a),(b) Photographs of the final fabricated stacked microreactor before packaging (Layer 1 is colored black by the addition of ~2% w/w carbon black in the PDMS polymer before curing): Holes for Layer 1 inlets and Layer 2 manifold inlet are visible (c) Schematic of packaging scheme and (d) photograph of packaged microreactor (no carbon black added in this case).

6.2.2 Electrophoretic separator with metal electrodes

The fabricated metal electrode-based separator is described in Figure 6-5. It consists of a Pyrex substrate (7740, 150 mm diameter, 0.762 mm thick, Bullen Ultrasonics Inc.) with electron beam deposited and photolithographically defined (by lift off) gold electrodes (200 nm thick gold layer on 10 nm thick Ti adhesion layer). Microfluidic channels in PDMS are fabricated, sealed to the substrate, and packaged using the same techniques as for the microreactors. As shown in the figure, each device consists of one channel that has two inlets and two outlets in a 'Y' configuration. The channel has rectangular cross section, 0.8 mm -1.6 mm wide, 40 μm deep and 11 mm or 22 mm long. Two different electrode configurations are used, as indicated in Figure 6-5(b) and (c). In Figure 6-5(c), electrodes are 200 μm wide lines spaced 600 μm apart, and are 10 or 20 mm long. Wires are glued to the electrodes using silver-containing conductive epoxy (Resin Technology Group).
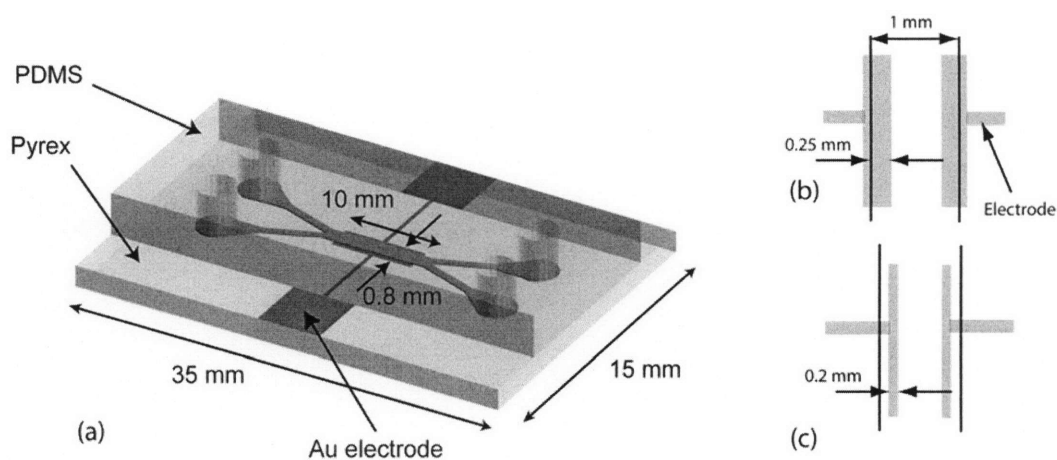
Figure 6-5 (a) Rendered drawing of a metal-electrode based separator (b)(c) Different planar electrode configurations used in the study.

6.2.3 Electrophoretic separator with porous polymer-based electrodes[†]

An alternative to the above design is presented in Figure 6-6. The electrodes in this case are composed of hybrid porous-polymer-PMMA bead monoliths synthesized *in-situ*

[†] This work was performed in close collaboration with Mr. Jacob Albrecht, who at the time was a graduate student in Prof. Jensen's research group.

in a large photolithographically defined PDMS reservoir and are connected to the main separation channel by an alternating network of narrow transverse channels and PDMS posts. The separator channel is 1 mm wide and 10 mm long, and the narrow transverse channels connecting it to the electrode monolith are 10 μm wide and 20 μm long. These transverse channels alternate with PDMS posts that are 20 μm wide and 20 μm long. All channels in the device are approximately 50 μm deep. The porous-polymer-PMMA bead monolith is synthesized *in-situ* inside a large rectangular PDMS reservoir (10 mm x 5 mm) that is also 50 μm deep. Polymerization is carried out using the materials and procedure reported by Peterson et al.[15]
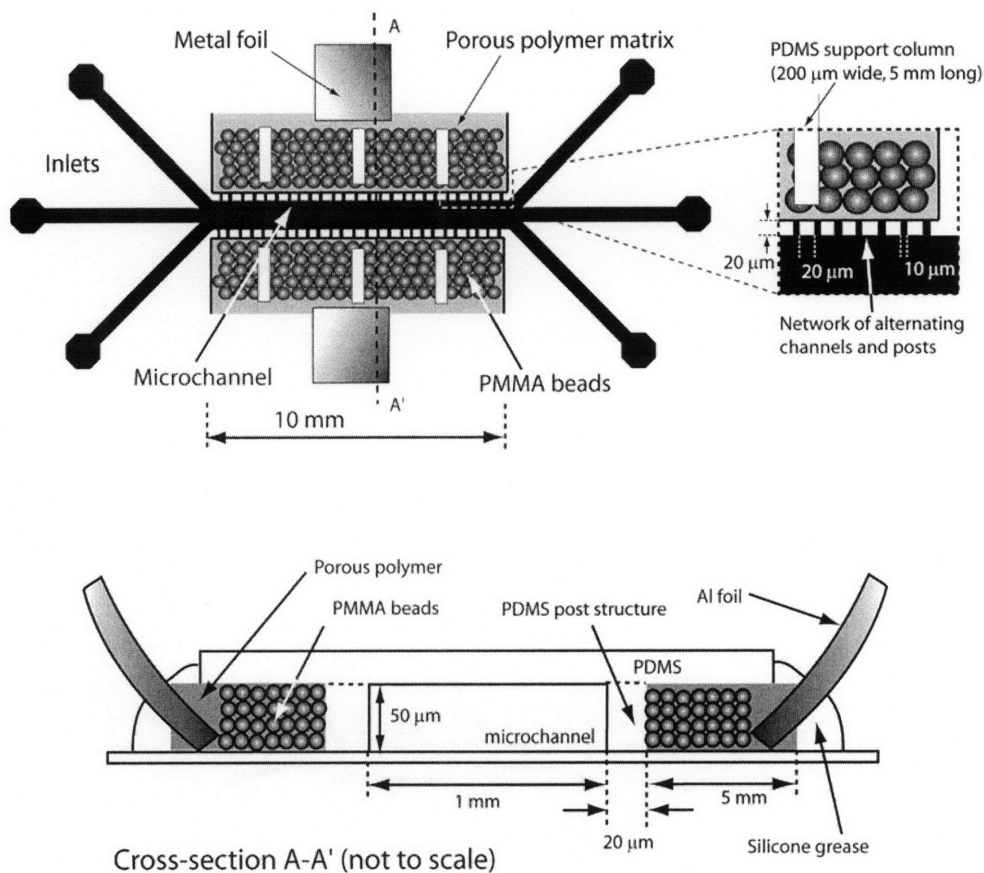
Figure 6-6 Schematic of porous polymer/PMMA-bead hybrid electrode separator concept (not to scale): PMMA beads grafted within a porous poly(butyl methacrylate-*co*-ethylene dimethacrylate) polymer monolith form the electrodes, and are connected to the main separation channel by a network of narrow transverse channels and PDMS posts. Electrical contact is made externally via metal foil pieces in direct contact with the porous polymer and held in place by RTV sealant.

164

6.3 Experimental

6.3.1 Materials and methods

Butyl methacrylate (99%, BuMA), ethylene dimethacrylate (98%, EDMA), 2,2-dimethoxy-2-phenyl acetophenone (99%, DMAP), 1-decanol and cyclohexanol were purchased from Sigma-Aldrich and used without further purification. PMMA beads (5 µm mean diameter, Bangslabs) were first introduced into the PDMS reservoir, which was subsequently filled with the polymerization mixture (Recipe A of Peterson et al.[15]) by capillary action. Polymerization was carried out by direct UV irradiation for 15 minutes.

6.3.2 Stacked multi-step microreactor setup[‡]

The setup for flow characterization experiments for the stacked multi-step reactor (6.2.1) is shown in Figure 6-7. Two syringe pumps (Harvard Apparatus, PHD2000 series) were used to deliver liquids to the reactor, and a gas cylinder (compressed helium, Airgas) was used to deliver the gas through two pressure regulators. The first pressure regulator (VWR Scientific) consisted of two stages, and the outlet pressure of the second stage was set to 10 psig. The outlet of the second pressure regulator (Valco) was set between 2-4 psig for flow characterization and synthesis experiments. An inline pressure gauge (0-10 psig) was used to monitor microreactor gas inlet pressure. As shown in Figure 6-7, two syringe pumps were used for delivering liquids to the reactor. The first syringe pump delivered liquid to the liquid inlets in Layer 1, and the second syringe pump delivered liquid to the quench port of layer 1, and to the manifold inlet of layer 2. Each syringe pump drove two syringes of equal diameter, and hence equal flow rates. Stereomicrographs were taken with a Leica MZ12 stereomicroscope (Diagnostic Instruments, Inc.) interfaced to a digital camera (Nikon CoolPix). A Fiber-Lite PL-800 Lamp (Dolan-Jenner) provided the lighting. Image analysis for determination of bubble and liquid segment length, as well as bubble velocity was carried out using ImageJ software (NIH). For the synthesis experiments, a third syringe pump was used to independently vary the flow rate into the manifold inlet of layer 2.

[‡] This work was done in close collaboration with Ms. Veronique Gondoin, who at the time was a visiting student from ETH (Zürich)
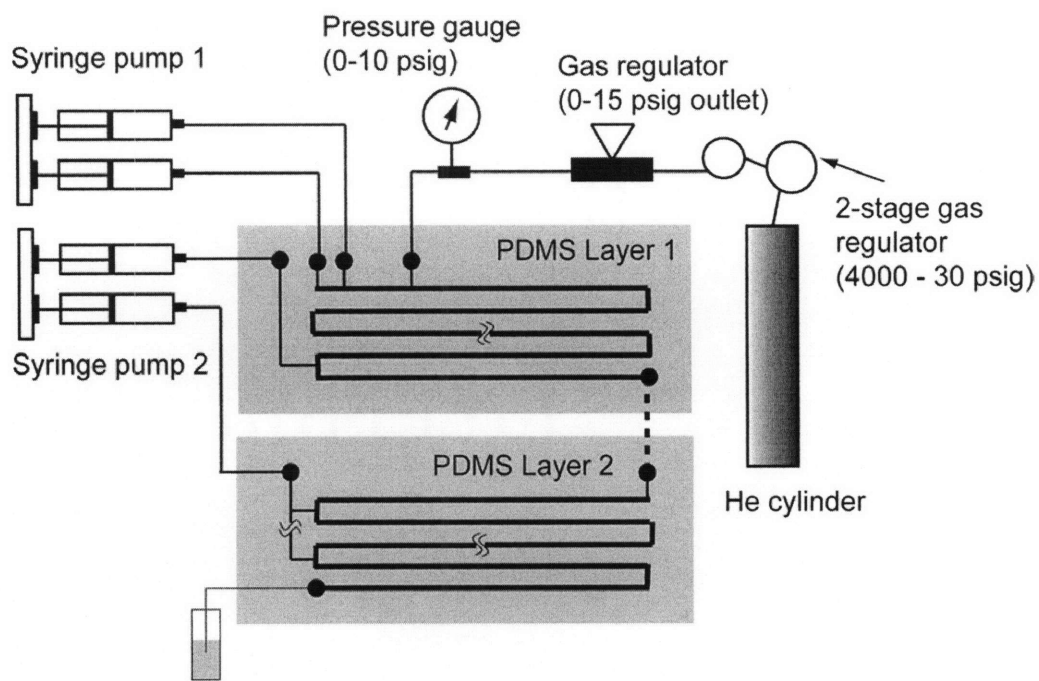
Figure 6-7 Experimental setup for stacked multi-step reactor of 6.2.1

6.3.3 Electrophoretic separator setups

Equal flow rates of two liquid streams were introduced into the separators of 6.2.2 and 6.2.3 using a syringe pump (Harvard Apparatus PHD 2000 series or KD Scientific 9000 series). The first stream contained fluorescent polystyrene particles (700 nm, Molecular Probes) suspended in ethyl alcohol, or silica particles in suspension in the reaction mixture (aged for 4-12 hours) from a batch reactor or a microreactor (Design 1 of Chapter 4), and the second stream contained pure ethyl alcohol. Flow rates of the two streams ranged from 5 μL/min each to 50 μL/min. DC voltages (1-1500 V) were applied across the electrodes using a high-voltage power supply (Fluke, product no. 415B). Photographs were taken with a Leica MZ12 stereomicroscope (Diagnostic Instruments, Inc.) interfaced to a digital camera (Nikon CoolPix), or with an inverted fluorescent microscope (Zeiss) and a CCD camera (LaVision).

166

6.4 Results and discussion

6.4.1 Multi-step microreactor flow characterization

Gas-liquid flow through the stacked microreactor of Figure 6-4 was first tested by running ethyl alcohol-Helium flows at several different conditions. Flow test results are presented in Figure 6-8 and Figure 6-9 for fixed liquid flow rates in layers 1 and 2, and four different gas inlet pressures. The total volumetric flow rate through the liquid inlets in layer 1 was 3 μL/min, while the quench port and manifold flow rates were 27 μL/min each. Under synthesis conditions, these flow rates would thus correspond to a ten-fold dilution of the Stöber reaction mixture, and an equal flow ratio of TEOT precursor and particle suspension in layer 2. Gas inlet pressure to the device was varied from 2.8 psig to 3.5 psig, and bubble and liquid segment lengths and bubble velocities were measured at the top and bottom of layer 1.

Two important observations were made from the results of Figure 6-8 and Figure 6-9. Firstly, large bubble and liquid segment lengths (~10 times the channel width) were obtained under these flow conditions, and could be varied by varying the gas inlet pressure. Thus, bubble lengths could be tuned from 3.5 mm to 4.5 mm and liquid segment lengths could be tuned from 1.4 mm to 1.0 mm. As expected, bubble length increased and liquid segment length decreased with gas inlet pressure. Also, bubble coalescence occurred downstream in layer 1, leading to increase in bubble and liquid segment sizes, as evident in Figure 6-8(a) and (b). Small pressure fluctuations in the gas inlet and the presence of compressible dead volumes (with trapped gas) in the device were possible reasons for the observed coalescence. Dead volumes were present because all the device inlets shown in Figure 6-3 were not utilized in the flow characterization experiments. The inlets that were not used were closed using PEEK plug fittings (Upchurch), and had trapped gas bubbles in the attached tubing at all times. The second important observation, of immediate relevance to synthesis experiments, was that bubble velocity could be tuned by varying inlet gas pressure. As expected, bubble velocity increased with inlet gas pressure (Figure 6-9). This meant that liquid phase residence time (and hence particle growth time) could be tuned to obtain a range of different particle sizes.

167
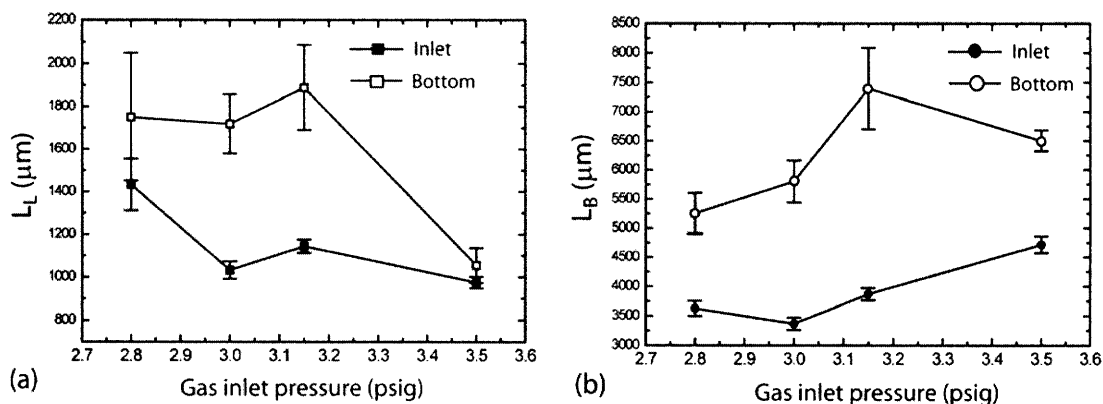
Figure 6-8 Results from flow characterization experiments, Syringe pump 1 (Figure 6-7) flow rate (Q_1) = 1.5 µL/min and syringe pump 2 (Figure 6-7) flow rate (Q_2) = 27 µL/min (a) Liquid segment lengths measured 30 mm downstream of the gas inlet in Layer 1, and at the bottom of layer 1 (before the quench liquid inlet) as a function of gas inlet pressure and (b) Bubble lengths measured at the same locations as a function of gas inlet pressure. Bubbles are seen to coalesce while flowing through the microchannels, leading to a 1.5x-2x increase in bubble and slug length in some cases.
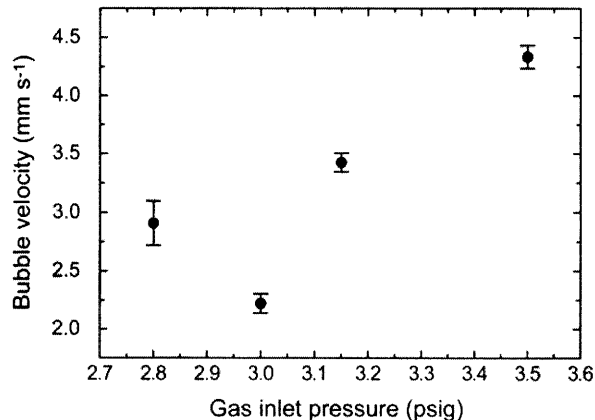
Figure 6-9 Graph of bubble velocity versus gas inlet pressure: Syringe pump 1 (Figure 6-7) flow rate (Q_1) = 1.5 µL/min and syringe pump 2 (Figure 6-7) flow rate (Q_2) = 27 µL/min

6.4.2 Microreactor synthesis and overcoating

The first set of experiments performed with the above microreactor consisted of 'blank' silica synthesis with no overcoating. The important operating parameters were total inlet flow rate of silica reactants into layer 1 (Q_1), the inlet gas pressure and the flow rate of ethanol into the quench inlet of layer 1 (Q_2) and the feed manifold of layer 2 (Q_3).

168

Figure 6-10 shows the results of these experiments along with a comparison with small-scale stirred batch data. The 'Reactor 1' conditions labeled in the figure correspond to Q_1= 2 μL/min and Q_2=Q_3= 18 μL/min, with gas pressure as a parameter to adjust mean residence time. Similarly, 'Reactor 2' conditions labeled in the figure correspond to Q_1= 3 μL/min and Q_2=Q_3= 27 μL/min. As expected, mean particle size increased with residence time in all cases. The microreactor synthesized particle size distributions were wider than the corresponding batch case. We attribute this mainly to the large gas bubble sizes used and some non-uniform mixing of incoming reactants (corresponding to the case of SFR design 2 in Chapter 4). The preparation of silica synthesis solutions and the recipe used (0.2 M TEOS, 2.0 M NH_3, 5.9 M H_2O) are described in detail in Chapter 4. Tunable silica particle synthesis was thus demonstrated in the new microreactor.
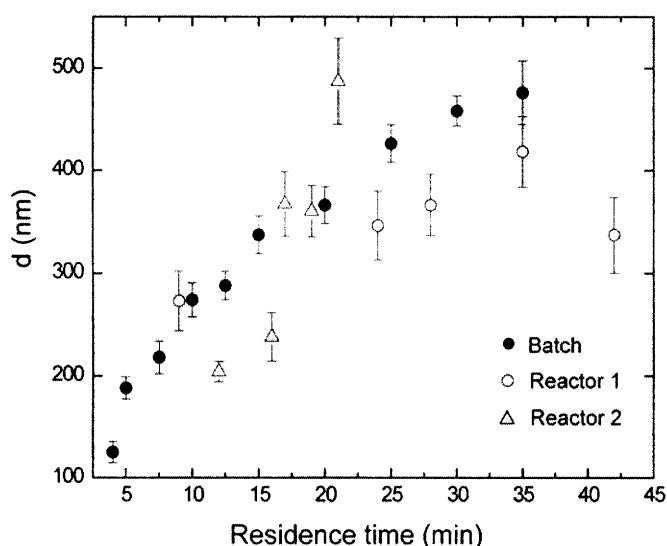
Figure 6-10 Silica synthesis results from the stacked microreactor: Graph of mean particle size 'd' (nm) versus mean residence time (min). Y-axis error bars indicate standard deviation of particle size distribution. Reactor residence time is adjusted by varying gas pressure. (Details in text).

Subsequent experiments were carried out by feeding a 0.03 M TEOT solution through the manifold inlet of layer 2, in addition to the silica reactants and ethanol quench of layer 1. Figure 6-11 contains SEM micrographs of particles synthesized under different conditions (Q_1:Q_2:Q_3). The main observation from these micrographs is that extensive secondary titania precipitation occurs, with (qualitatively) different particle population

distributions for the different synthesis conditions. Both quench and titania feed flow rates are important parameters. Quench liquid flow rate dictates the dilution of both water and silica particle concentration in layer 1. There is therefore a trade-off involved here. Increasing the quench flow rate dilutes the water concentration from the silica synthesis ($\sim$ 1 M) to levels that are acceptable for titania overcoating ($\sim$ 0.1 M). However, this also dilutes the particle concentration which increases the possibility of secondary nucleation. These counteracting considerations lead us to believe that there exists an optimum dilution of the synthesis mixture of layer 1 that will yield uniform titania coatings without secondary nucleation in layer 2. In addition, a smaller flow rate of titanium precursor feed is preferable for uniform titania coatings, as described in Chapter 5. Recommended future efforts include experiments to quantify the particle population distributions and to optimize reactant concentrations and flow rates.
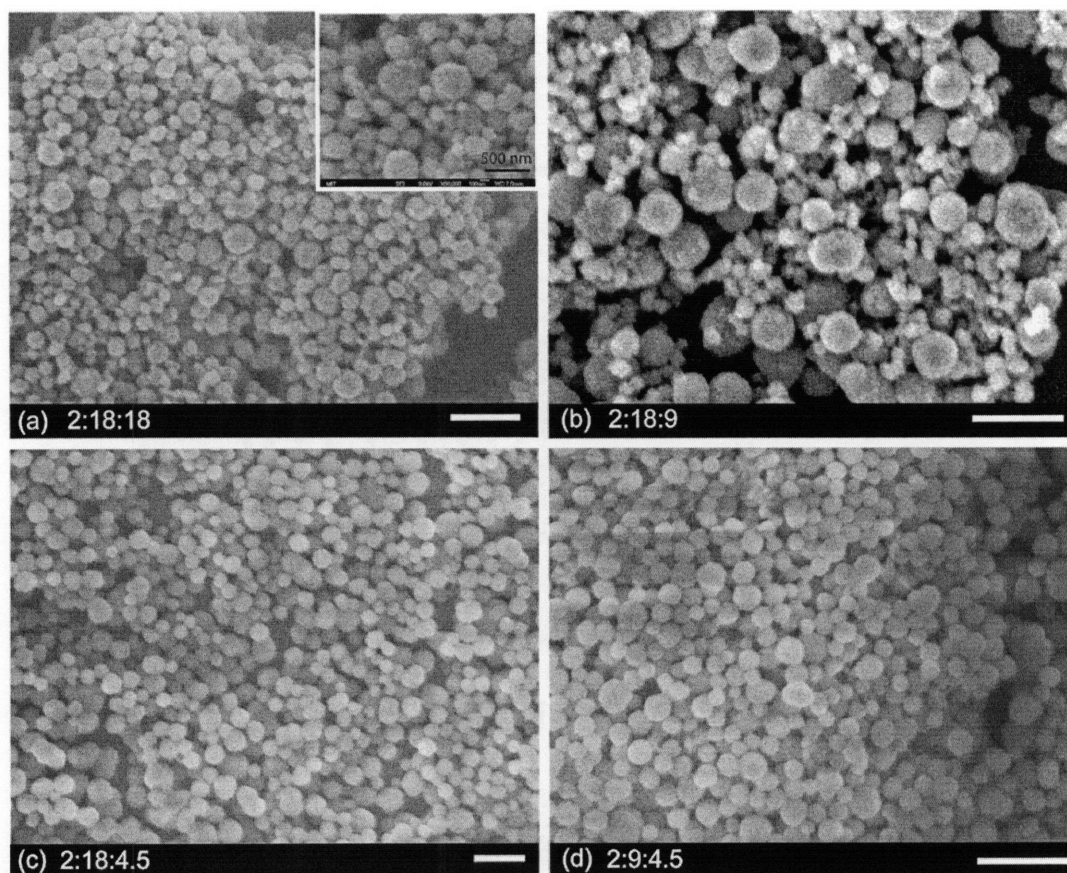
Figure 6-11 SEM micrographs of particles synthesized in the stacked microreactor for several different silica precursor, quench ethanol and titania precursor flow rates $(Q_1:Q_2:Q_3)$. The gas inlet pressure was maintained constant at 1.8 psig. The scale bar in all cases corresponds to 1 μm.

6.4.3   Electrophoretic separation with metal-based electrodes

Two electrophoretic separation experiments with the metal electrode based devices of 6.2.2 are described in this section. The results of these experiments are summarized in Figure 6-12. The first experiment involved transfer of negatively charged fluorescent polystyrene particles (700 nm) suspended in ethyl alcohol to another parallel, co-flowing blank stream of ethyl alcohol. Figure 6-12(a) shows the two co-flowing streams, with a dotted white line indicating the liquid-liquid interface. A small DC voltage (4V) was applied across the electrodes (Figure 6-12(b)), leading to transfer of particles into the blank stream. Complete transfer required the application of higher voltages (≥ 10 V DC). Since there was no dissolved water present in this case, no electrolysis or bubble formation was observed. We expected no interference due to electro-osmotic flow (EOF)

in this case, since ethyl alcohol was the suspending medium, and the walls of the microchannel were presumably uncharged.

The second experiment involved transfer of negatively charged silica particles from a Stöber process reaction mixture to a co-flowing wash stream of ethyl alcohol (Figure 6-12(c) and (d)). Figure 6-12(a) shows the two co-flowing streams, with a white dotted line indicating the colloid suspension-ethyl alcohol interface. The silica suspension had a turbid white color in the stereomicroscope observations. Application of a DC voltage to the electrodes led to transfer of silica particles to the blank ethyl alcohol stream (Figure 6-12). It is important to note that due to the planar nature of the electrodes, the electric field decays rapidly with distance from the electrode, and hence complete transfer of particles is not possible with such a design. In addition, bubbles are rapidly formed at the electrodes due to electrolysis of water present in the reaction mixture. Complete transfer of particles without electrolysis would require closely spaced planar vertical electrodes operating at low DC voltages. However, fabrication of standing metal electrode structures in microfluidic devices requires several complex fabrication steps, and may not be the best solution. In the following section we describe the use of vertical electrode structures fabricated using porous polymer monoliths that allow the application of high electric fields without electrolysis and bubble formation.
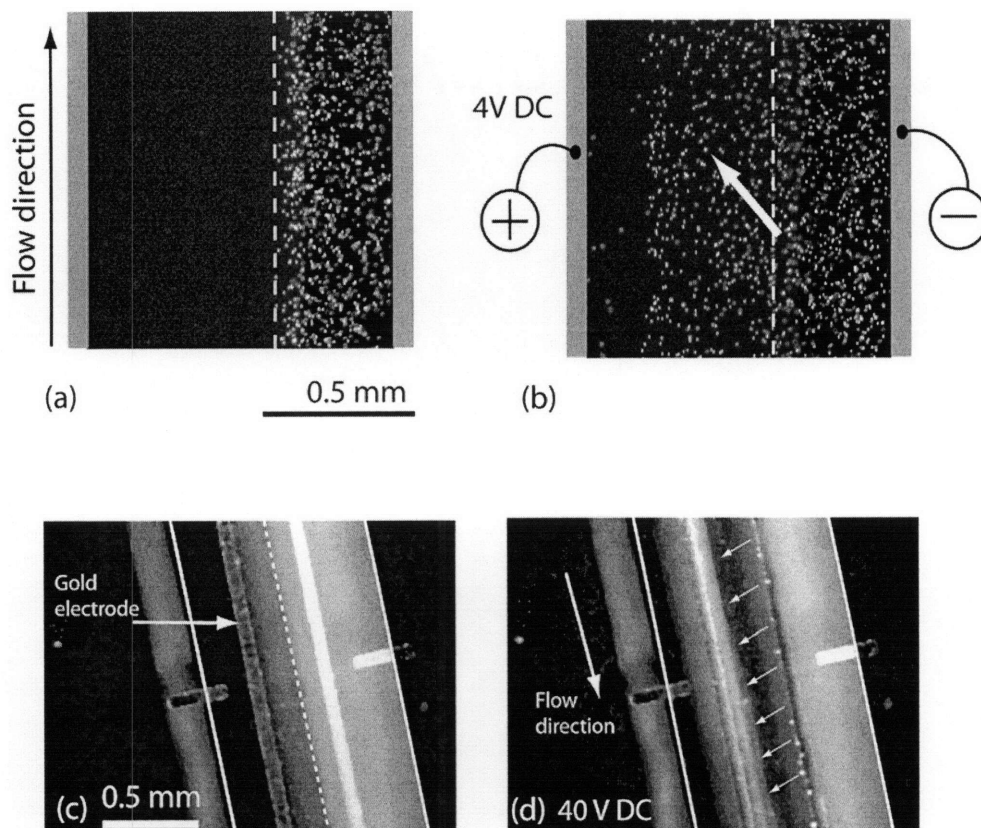
Figure 6-12 Particle separation in metal-electrode based devices (a),(b) Fluorescent polystyrene particles in ethyl alcohol are transferred to a parallel co-flowing stream of ethyl alcohol on application of a DC voltage across the electrodes (c),(d) Silica particles from a suspension (Stöber process reaction mixture) are transferred to a co-flowing stream of ethyl alcohol, small bubbles are formed at the electrodes due to electrolysis.

6.4.4 Porous-polymer/PMMA bead based electrodes

The main idea behind this separation scheme is the use of nanoporous materials as effective electrical interfaces for μ-FFE devices.[16] Packed polymer beads, further immobilized by a grafted polymer monolith are used to isolate the main separation channel from the electrochemical reactions taking place at the metal electrode surface. The polymer-bead monolith nearly eliminates fluid flow into the electrode reservoir, and the high conductivity within the electrode structure enables the application of large homogeneous electric fields without bubble formation problems. Figure 6-13 shows stereomicrographs of the polymer-bead electrode in operation. The clear particle suspension-ethyl alcohol interface is seen to disappear on the application of a DC voltage to the metal foil electrodes (Figure 6-6). In addition, particles are also seen to

agglomerate at the positive electrode over the course of several experiments (dotted ellipses in Figure 6-13(f). No bubble formation due to electrolysis occurs, even at very high applied voltages (1 kV), demonstrating the utility of the electrode structure. A modular series arrangement of a silica synthesis microreactor (Design 1 of Chapter 4) and an electrophoretic separator was also used to synthesize and simultaneously separate silica particles in continuous fashion (Figure 6-13(e) and (f)).

These proof-of-concept demonstrations stimulated further experiments to quantify the separator yield and efficiency under different operating voltages. However, under the current operating conditions (0.1 kV – 1.5 kV), experiments to quantify separator yields with voltages switched on over periods of ~10 minutes led to rapid buildup of particle deposits on the positively charged electrode. In fact, a very small fraction of the separated particles were carried out with the flow. These observations are illustrated in the stereomicrograph pairs in Figure 6-14(a)-(c). There are several points worth noting from these experimental results. Firstly, we note that nearly complete separation was achieved with the current setup. However, at high voltages such as those used in these experiments, the device functioned more as a particle filter than as a continuous particle transfer device, as we intended by design. This fact is illustrated clearly in Figure 6-14(a) where silica particles not only deposit on the electrode-channel barrier, but also migrate into the bead-polymer monolith as seen by the whitish color on the cathode side. The second important observation worth noting is the fact that particle deposition was *reversible*. Reversing electrode polarity led to complete expulsion of all the particle deposits, including those trapped in the bead-polymer monolith. This was in contrast to metal-based electrode devices where particle deposition on the electrodes was nearly irreversible.

Based on these facts, we make recommendations for operation modes of such bead-based electrode devices. The first operating mode would involve low voltages and particle transfer into the solvent stream and subsequent flow out of the device. This would necessarily involve compromising on separation efficiency, and hence would require two or more devices in series for complete particle transfer. The second operation mode would involve high voltages as described above, such that complete particle trapping occurred. However, each device would operate in discrete fashion, with particle

trapping and release steps, and hence would involve operation of two or more devices in parallel for truly continuous operation.
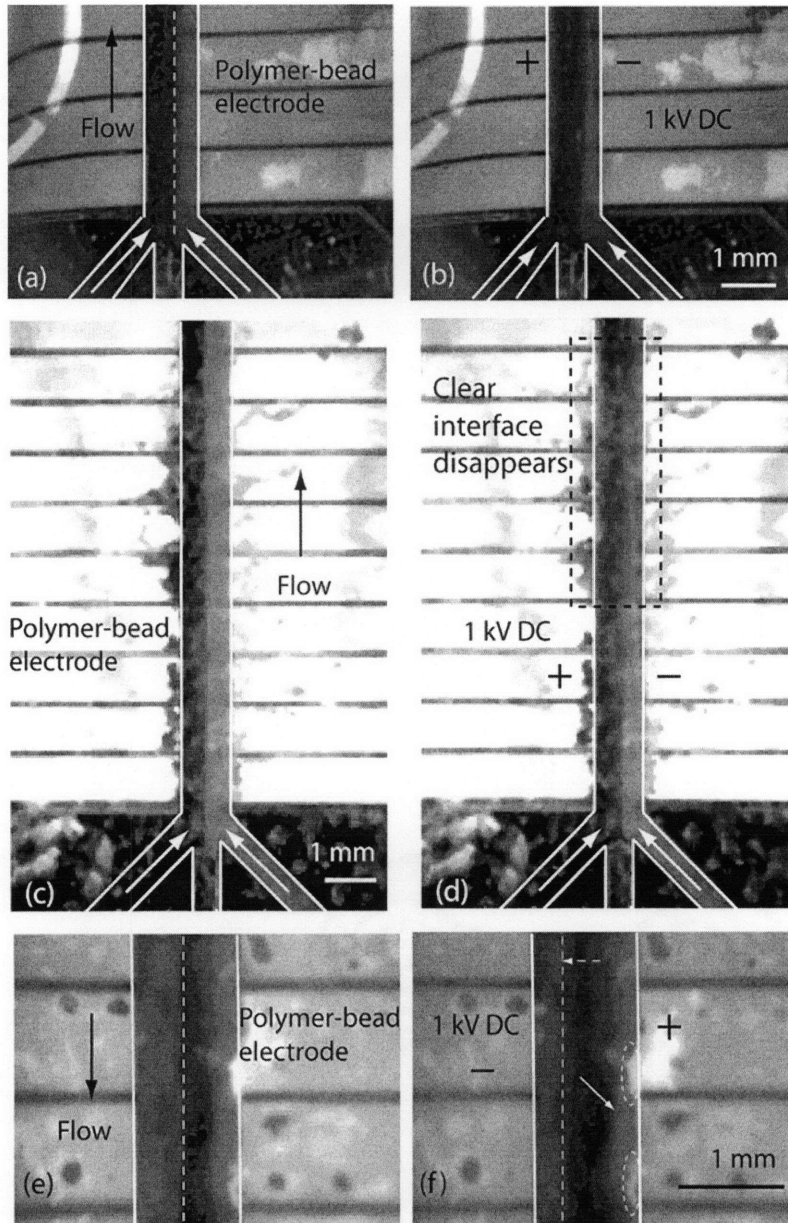
Figure 6-13 Particle separation in polymer-bead hybrid electrode separators: (a),(b),(c) and (d) Silica particle transfer from a Stöber reaction mixture to a blank ethyl alcohol stream.(e),(f) Silica particle transfer from a Stöber reaction mixture from an upstream microreactor connected in series with the separator. Aggregation of silica particles on the oppositely charged electrode, along with some silica migration into the bead-polymer monolith is observed.
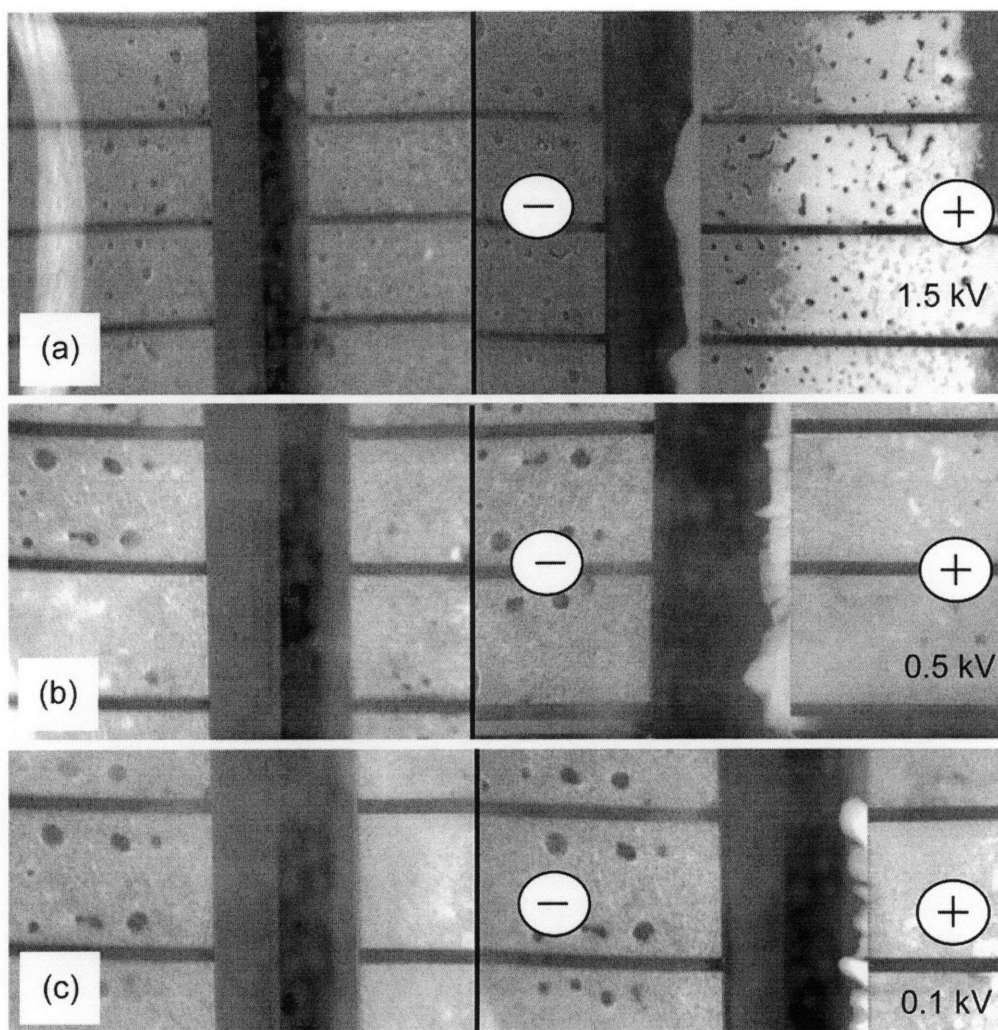
Figure 6-14 Particle deposition in polymer-bead hybrid electrode separators at various operating voltages.

6.5 Summary

Two related steps towards multi-step colloid processing were presented in this chapter. The design, fabrication and flow characterization of a stacked series combination of two reactors for continuous silica synthesis and *in-situ* titania overcoating was described. In addition, continuous particle separation via μ-free flow electrophoresis was demonstrated. Metal-electrode based devices are inherently limited in their scope of operation, since they are in direct contact with the working liquids. Porous polymer-PMMA bead hybrid electrode structures that effectively isolated the separation microchannel from electrochemical reactions at the metal-liquid interface were used to continuously separate

silica particles into ethyl alcohol wash streams. A modular series combination of silica synthesis in a microreactor followed by separation (washing) via electrophoresis was demonstrated using the polymer-bead electrode structures. These initial demonstrations indicate that multi-step microfluidic colloid processing is a potentially viable route for continuous synthesis of core-shell structures.

6.6　References

1.　Manz, A., Graber, N. & Widmer, H. M. Miniaturized Total Chemical-Analysis Systems - a Novel Concept for Chemical Sensing. *Sensors and Actuators B-Chemical* **1**, 244-248 (1990).

2.　Voldman, J., Braff, R. A., Toner, M., Gray, M. L. & Schmidt, M. A. Holding forces of single-particle dielectrophoretic traps. *Biophysical Journal* **80**, 531-541 (2001).

3.　Voldman, J., Toner, M., Gray, M. L. & Schmidt, M. A. Design and analysis of extruded quadrupolar dielectrophoretic traps. *Journal of Electrostatics* **57**, 69-90 (2003).

4.　Hannig, K., Heidrich, H. G., Spiegel, K. & Wirth, H. Analytical Free-Flow Electrophoresis System for Rapid Quantitative-Determination of Electrophoretic Parameters of Proteins and Cells. *Journal of Clinical Chemistry and Clinical Biochemistry* **16**, 203-203 (1978).

5.　Heidrich, H. G. & Hannig, K. Separation of Cell-Populations by Free-Flow Electrophoresis. *Methods in Enzymology* **171**, 513-531 (1989).

6.　Lu, H. et al. in *Micro Total Analysis Systems 2001* (eds. Ramsey, J. M. & van den Berg, A.) 297-298 (Kluwer Academic Publishers, Monterey, CA, 2001).

7.　Lu, H., Jensen, K. F. & Schmidt, M. A. Microfluidic device for sorting cell organelles. (2002).

8.　Lu, H., Schmidt, M. A. & Jensen, K. F. A microfluidic electroporation device for cell lysis. *Lab on a Chip* **5**, 23-29 (2005).

9.　Lu, H., Gaudet, S., Schmidt, M. A. & Jensen, K. F. A microfabricated device for subcellular organelle sorting. *Analytical Chemistry* **76**, 5705-5712 (2004).

10.　Takamura, Y. et al. Low-voltage electroosmosis pump for stand-alone microfluidics devices. *Electrophoresis* **24**, 185-192 (2003).

11.　Raymond, D. E., Manz, A. & Widmer, H. M. Continuous separation of high molecular weight compounds using a microliter volume free-flow electrophoresis microstructure. *Analytical Chemistry* **68**, 2515-2522 (1996).

12.　Zhang, C. X. & Manz, A. High-speed free-flow electrophoresis on chip. *Analytical Chemistry* **75**, 5759-5766 (2003).

13. Cui, H. C., Horiuchi, K., Dutta, P. & Ivory, C. F. Multistage isoelectric focusing in a polymeric microfluidic chip. *Analytical Chemistry* **77**, 7878-7886 (2005).

14. Cui, H. C., Horiuchi, K., Dutta, P. & Ivory, C. F. Isoelectric focusing in a poly(dimethylsiloxane) microfluidic chip. *Analytical Chemistry* **77**, 1303-1309 (2005).

15. Peterson, D. S., Rohr, T., Svec, F. & Frechet, J. M. J. Dual-function microanalytical device by in situ photolithographic grafting of porous polymer monolith: Integrating solid-phase extraction and enzymatic digestion for peptide mass mapping. *Analytical Chemistry* **75**, 5328-5335 (2003).

16. Albrecht, J., Gaudet, S. & Jensen, K. F. in *9th International Conference on Miniaturized Systems for Chemistry and Life Sciences* (eds. Jensen, K. F., Han, J., Harrison, D. J. & Voldman, J.) 1537-1539 (Transducer Research Foundation, Boston, MA, 2005).

7 Summary and Outlook

7.1 Principal Thesis Contributions

This thesis makes several important contributions to the fields of microfluidics, microchemical systems and colloid synthesis. It is one of the first theses to demonstrate the application of microfluidic technology for continuous, controlled synthesis of sub-micron core-shell colloidal particles. The technology developed in this thesis provides a superior, viable and scalable alternative to conventional macroscale particle synthesis techniques that are primarily limited to multi-step batch processes. The principal contributions are the design of microchannel devices for the generation of uniform, segmented gas-liquid microflows, the detailed characterization of multi-phase transport and dynamics in such transient systems, and their application for the synthesis of colloidal core-shell materials. Classical techniques of chemical reaction engineering are applied to design novel microfabricated reactor configurations that cannot be realized easily on the macroscale, and that closely approach theoretical 'idealized' reactor configurations.

Single-phase laminar flow-based chemical synthesis in microchemical reactors is associated with several challenges such as large axial dispersion and wide residence time distributions (RTD), especially for chemical reactions requiring residence time greater than a few seconds. This thesis lays the foundations for designing multi-phase microchemical reactors that elegantly overcome these drawbacks and add new functionalities not possible with single-phase systems. Thus, an important contribution of this thesis is in the field of multi-phase microfluidics, where we demonstrate stable, uniform segmented gas-liquid flows over three orders of magnitude in Capillary number, generally suitable for performing a wide range of chemical reactions. The conditions and design criteria to be met to obtain such flows are laid out in detail. Flow segmentation with inert gas bubbles not only reduces (or eliminates) axial dispersion, but also enables rapid micromixing of incoming reactant streams. This is an important added functionality that is of great value in realizing multi-step chemical syntheses involving colloidal

particles that, due to their inherently low diffusivities, cannot be rapidly mixed by laminar diffusive techniques so popular in the microfluidics community. Although the presented thesis work focuses on cases where the introduced gas is a passive segmentation and micromixing agent, the resultant conclusions and reactor designs are generally applicable even for the cases where the gas takes part in the chemical reaction.

This thesis presents the first demonstration of continuous, tunable microfluidic synthesis of colloidal silica and titania particles by sol-gel chemistry. The microfluidic approach yields particle size distributions comparable to or narrower than the corresponding stirred-flask synthesis, with little agglomeration or shape distortion. Particle sizes can be tuned by simply varying the rates of flow of liquid reactants and gas, or by varying the chip temperature. The reactor designs presented are generally applicable for a wide range of liquid-phase chemistries for nucleation and growth of nanoparticles such as semiconductor nanocrystals (CdSe, ZnSe etc.) or metallic nanoparticles (Au, Ag etc.).

Multi-layered core-shell particle synthesis requires precise control of particle and reactant concentrations to prevent undesirable secondary particle nucleation and primary (core) particle agglomeration. The demonstration of a novel reactor design for continuous synthesis of tunable core-shell silica-titania structures is an important contribution to both the microfluidics and nanomaterials chemistry fields. It illustrates that photolithography-based microfabrication coupled with multi-phase microflows enables unique chemical reactor configurations that cannot be realized on the macroscale, and can be used for controlled synthesis of tailored nanostructures.

Finally, this thesis demonstrates the design and operation of stacked multi-level microfluidic reactors for synthesis of silica particles followed by *in-situ* titania coatings. Multi-step nanomaterials synthesis and surface coating/functionalization with incompatible chemistries requires the development of microfluidic 'unit operations' equivalent to particle filtration. An important contribution of this thesis is the design and development of rapid, continuous microfluidic particle separation using transverse free-flow electrophoresis. Such devices are a critical step towards integrated microsystems for continuous synthesis of multi-level nanomaterials.

7.2 Discussion

7.2.1 Materials and surfaces

Poly (dimethylsiloxane) (PDMS) was used as the primary material of construction for the microfluidic devices fabricated in this thesis. Rapid prototyping of designs using standard soft lithographic techniques was the primary motivation for using this material. However, being a soft cross-linked polymer, PDMS is prone to swelling in solvents over extended periods of time (>8 hours). Partitioning of reactants into the polymer is also a problem, and so is high temperature operation (above 70 °C). PDMS is therefore, not the final material of construction envisioned for the devices and reactors in this thesis. Several other materials such as glass, silicon, and solvent resistant polymers such as COC (cyclic olefin co-polymer) may be used for fabrication of the microchannels.

The use of multi-phase flows coupled with chemistry that generates solids also imposes several requirements on the surface properties of the microchannel walls, as outlined in Chapter 2. Uniform, stable bubble flows require that the liquid phase completely wet the microchannel surfaces, with contact angles as close to 0° as possible. Thin films of particles were observed to form in the center of the microchannel walls for the colloid synthesis experiments, with no particle deposition at the microchannel corners. As discussed in Chapters 4 and 5, the thin liquid films surrounding gas bubbles were observed to break at high gas fractions, leading to partial drying of the microchannel walls. Film breakage was caused primarily by partial wettability (contact angle 'θ'> 0°) of the microchannel wall surfaces towards ethyl alcohol-water mixtures. These observations highlight the critical importance of the molecular structure of the microchannel surfaces in such applications. Engineering the structure of surfaces with tailored wetting properties is one of the key areas of materials research today, and significant research efforts have been directed towards the general area of microchannel surface modification. It is expected that the reactors developed in this thesis will benefit from such research efforts.

7.2.2 Important considerations for integration of units

The microfluidic reactors in this thesis have been designed by taking into consideration potential final integration (monolithic or modular) of individual reactor units. Monolithic integration of two reactor units and modular integration of a reactor and separator were demonstrated in Chapter 6. Monolithic integration requires matching of individual operating ranges such as flow rates and temperatures across individual units. Modular integration for chemical reactors additionally requires special packaging techniques and interconnects to minimize undesirable dead zones. Pressure drop design is critical for the design of microfluidic networks with several entry and exit points for the different phases, as discussed in Chapter 5.

7.2.3 Some comments on scaling for small-scale production

The microreactors we have developed for sol-gel synthesis typically have a volume of 300 μL, and operate with liquid residence times from 5 to 30 minutes. Maximum liquid flow rates used are about 25 μL/min. In the above operating conditions, silica, titania synthesis yields are typically 80% or higher, usually giving 10 mg/mL solids. Each reactor can therefore produce upto 15 mg/hr of solids. The production rates can be increased either by scaling out (i.e. operating multiple units in parallel) the current units or by making longer units (hence with more volume) that can operate at higher flow rates. The important point here is to provide enough residence time for particle growth, whatever the operating flow rates and volumes. One way to do this would be to use large glass plates (of the kind used for DNA electrophoresis) and standard isotropic wet etching techniques to fabricate very long channels with reactors volumes >1 mL (the footprint of such units would be ~30 cm x 10cm), while still keeping the same design features and dimensions. This way each individual unit may be able to produce ~1 g/hr of solids or more. A five unit stack of such reactors can therefore yield ~ 150 g/day of solids (~ 100 lb/year). Design methodologies for such stacked units are reasonably straightforward and follow from single unit design studies. The amounts of solids required depend, of course, on the final application. Nevertheless, the microfluidic reactors are imminently practical as a research tool and, with judicious choice of (niche) application, a practical production tool as well.

182

7.3 Research Opportunities

This work done in this thesis provides the technological base for several high-impact research opportunities in both the microfluidics and nanomaterials synthesis fields. Synthetic applications of microfluidic reactors designed in this thesis can be expanded in a straightforward manner to encompass other liquid-phase chemistries for the synthesis of uniformly sized populations of, for example, metal nanoparticles such as gold or silver. More importantly, precisely tailored optically responsive core-shell nanostructures consisting of alternating dielectric and/or metal layers may be synthesized using microreactors such as those described in Chapter 5. Thus, for example, silica-gold nanoshells or hollow titania particles may be synthesized for ultimate application in biomedical imaging or photonic band-gap materials respectively. In addition, the ability to generate stable, uniform bubble flows over three orders of magnitude in Capillary number is directly useful in several allied areas of microreaction technology, for fundamental kinetics and mass transfer studies in gas-liquid reactions such as oxidations and hydrogenations, and three-phase heterogeneously catalyzed reactions. There is still further room for refinements in the developed technology. Materials selection and engineering of surface properties (such as wettability) of microchannel walls is an important area of research, not only for particle synthesis, but also for generalization of microfluidic tools to include a wider set of chemical reactions. Finally, there exists plenty of opportunity to develop and standardize packaging techniques for effective connection of microfluidic devices integrated in modular fashion with minimized dead volumes.

Appendix A

Process Sequence for SU-8 masters

In this section, we describe the details of the fabrication process for making SU-8 based masters used to mould PDMS microchannels for our reactors. The equipment names in the parentheses refer to machines in the Technology Research Laboratory (TRL) in MIT's Microsystems Technology Laboratories (MTL). The starting substrate is a 4" Silicon wafer (SSP, Test grade). The entire process is code purple. A two layer coating process is used to ensure uniform layer thickness over the entire wafer.

Process Steps

1. Dehydration Bake: Bake the wafers on a hotplate at 200 °C for 20 min. This step removes any adsorbed moisture on the silicon wafer.
2. Spin coating of first SU-8(2050) layer: Transfer the wafers immediately from the dehydration bake hotplate to the spin coater (SU-8 spinner/ TRL) using a metallic wafer carrier. The wafer cools rapidly when placed on the metallic spin coater chuck. Use a nitrogen gun to blow away any dust particles on the wafer. Dispense a small amount (~20 mm diameter circle) of SU-8(2050) (Microchem Corp., MA) onto the wafer and start spinning immediately. SU-8(2050) has a quick evaporating solvent base, therefore immediate spinning is necessary. Spin at 650 rpm for 15s and 1100 rpm for 35s. This yields a layer of thickness ~100-150 μm.
3. Soft-bake of first SU-8(2050) layer: Transfer the freshly coated wafer to a hot plate. Heat at 65 °C for 10 minutes, ramp up to 95 °C and hold for 45 minutes. Cool to at least 65 °C before transferring to the spin coater for the next step.
4. Spin coating of second SU-8(2050) layer: Same sequence of steps as 2.
5. Soft-bake of second SU-8(2050) layer: Same sequence of steps as 3.
6. Photolithography to define microchannel pattern: Interval exposure (5s x 17, 4s interval) (EV1/TRL).
7. Post-exposure bake: Place the freshly exposed wafer to a hot plate. Heat at 65 °C for 10 minutes, ramp up to 95 °C and hold for 30 minutes. Cool to at least 50 °C before transferring for development.
8. Development: Develop in poly(glycol)mono ether acetate (PGMEA, Microchem.) for 45 min, replace with fresh solution every 15 min.
9. Rinse with Isopropyl alcohol and dry under a stream of nitrogen.